# Designing devices using electro-active yield stress fluids

by

Ahmed H. Helal

B.Sc, Ecole Polytechnique (2007)
M.Sc., Ecole Polytechnique (2009)

Submitted to the Department of Mechanical Engineering
in partial fulfillment of the requirements for the degree of

Doctor of Philosophy in Mechanical Engineering

at the

MASSACHUSETTS INSTITUTE OF TECHNOLOGY

June 2016



Author .....
Department of Mechanical Engineering
May 8, 2016

Certified by .....
Anette (Peko) Hosoi
Professor, Department of Mechanical Engineering
Thesis Supervisor

Certified by .....
Gareth H. McKinley
School of Engineering Professor of Teaching Innovation
Department of Mechanical Engineering
Thesis Supervisor

Accepted by .....
Rohan Abeyaratne
Graduate Officer, Professor, Department of Mechanical Engineering
Chairman, Committee on Graduate Students

# Designing devices using electro-active yield stress fluids

by

Ahmed H. Helal

Submitted to the Department of Mechanical Engineering
on May 8, 2016, in partial fulfillment of the
requirements for the degree of
Doctor of Philosophy in Mechanical Engineering

## Abstract

Understanding the rheo-electrical properties of electro-active yield stress fluids (EAYS) lies at the heart of enabling the design of a number of novel applications such as smart valves and semi-solid flow batteries. This thesis explores the rheological and electrical properties of EAYS fluids, with a focus on how the presence of a deformable microstructure, which gives rise to a yield stress at the macroscale, affects the design and performance of the corresponding devices. This thesis will focus on two representative case studies of such devices using EAYS fluids: 1) miniaturized, rapidly-actuated hydraulic valves using electro-rheological fluids applied to centimeter-scale robotics and 2) semi-solid flow batteries using conductive suspensions of percolated carbon black networks flowing in millifluidic channels. Through experimental characterization and modeling of the rheo-electric properties of the materials, this thesis investigates the interplay between the electrical and rheological properties of the EAYS fluids used in these devices. We demonstrate how an improved understanding of the flow of EAYS fluids and the development of device-level predictive models of the key performance metrics leads to a better understanding of the device design and operation space.

In the first part of this thesis, we characterize the field-dependent yield stress of electrorheological fluids at different electric fields and particle volume fractions in wall-driven and pressure-driven flow. We report a yield hardening occurring in pressure-driven flow, as a result of a local increase in particle volume fraction. We propose a phenomenological physical model for the densification process, allowing us to reconcile rheological measurements from wall-driven shear flows e.g. torsional rheometers and in pressure-driven channel flows, that are more applicable to valve applications. Next, we extend this work by introducing the holding pressure drop and power efficiency as key performance metrics for electrorheological valves. Using a custom modular valve design, we investigate the effects of the aspect ratio of the valve and electrode surface roughness on the valve performance. This study enables us to derive design rules for ER valve design and to demonstrate their applicability in robotic applications.

In the second part of this thesis, we characterize the rheological and electrical

properties of carbon black gels under steady and oscillatory shear flow. We assess the influence of design parameters such as the carbon loading, surface material and choice of additives on the rheology and wall-slip behavior of lithium polysuflide semi-solid suspensions. We discuss the design of a new rheo-electric test fixture for controlled-stress rheometers; enabling simultaneous measurements of the rheo-electric properties of strongly conductive materials such as semi-solid flow battery slurries. After careful calibration of the new test fixture, we demonstrate its relevance as a versatile characterization tool by studying the rheo-electric properties of a series of model carbon black gels at rest and under transient and steady shear. Additionally, we show that small amplitude oscillatory shear measurements, performed concomitantly to conductivity measurements on carbon black gels, allow us to precisely extrapolate the conductivity and rigidity percolation thresholds of the carbon black gels. Large amplitude oscillatory shear measurements are also shown to be a useful method to study fatigue in carbon black gels at stresses close to the yield stress. Finally, we introduce a new pumpless design architecture for flow cells: the Gravity-Induced Flow Cell (GIF-cell), that is driven by gravity. We demonstrate how insight into the rheological and wall slip behavior of the lithium polysulfide semi-solid suspensions obtained through careful characterization informs and helps optimize cell design and operation.

Thesis Supervisor: Anette (Peko) Hosoi
Title: Professor, Department of Mechanical Engineering

Thesis Supervisor: Gareth H. McKinley
Title: School of Engineering Professor of Teaching Innovation
Department of Mechanical Engineering

# Acknowledgments

My time at MIT would not have been successful without the support of the many people I was fortunate to meet and work with and to whom I am deeply grateful.

First, I would like to express my gratitude to my advisors, Prof. Gareth H. McKinley and Anette (Peko) Hosoi. I chose to come to MIT because I wanted to work with and learn from you and it has been a privilege to have two of the most brilliant people I know as my mentors. Your constant support, encouragement, and enthusiasm have enabled me to steadily learn and mature as a researcher. I am also grateful for your understanding that life is to be fully enjoyed by pursuing interests inside and outside of the lab and for encouraging me to make the most of my time at MIT. I believe that at the end of a PhD, one inherits the traits of their academic "parents" and I couldn't ask for better ones; I will miss our passionate conversations (scientific or otherwise) that i have become fond of.

I would also like to thank my committee members: Prof. Yet-Ming Chiang and Dr. Murat Ocalan. It has been a privilege working with you. The work presented in this thesis wouldn't be complete without your guidance and advice that helped me connect the disciplines involved.

The financial support from the DARPA M3 project and the JCESR project has made this work possible and I am grateful for their support.

I would like to thank my numerous labmates and collaborators for their support and assistance in this work. I would like to thank Dr. Thibaut Divoux for the many discussions we have had on carbon black; he has been a friend, a mentor and a constant source of encouragement and motivation over the past year. I am blessed our paths have crossed and that I got to learn so much from you on both personal and professional levels. I would like to thank the M3/Squishbot team: Dr. Nadia Cheng, Dr. Maria Telleria, Julie Wang, Sarah Bates, Dr. Bian Qian, Nick Wiltsie, Mike Murphy and Marc Strauss for their assistance on the ER valves project and for their continued support throughout my PhD. I also thank Dr. Xinwei Chen, Frank Fan, Prof. Kyle Smith, Prof. Fikile Brushett, Billy Woodford, Tyler Olsen, Prof. Ken

Kamrin, Brandon Hopkins, Teng-sing Wei, Dr. Brian Solomon, Prof. Jennifer Lewis and Prof. Yet-Ming Chiang for their guidance on the numerous collaborations within the JCESR project. I am also thankful to Philip Rolfe from Malvern Instruments, Aadil Elmoumni from TA instruments and Mark Belanger from the Edgerton machine shop for their help designing the various rheometer test fixtures I worked with.

I am also deeply grateful to all members of "Team Peko", the "Non-Newtonian Fluids Group" and the Hatsopoulos Microfluids Lab. Thank you Dr. Nadia Cheng, Dr. Lisa Burton, Theresa Hoberg, Alice Nasto, Ben Druecke, William Li, Josh Wiens, Dr. Dawn Wendell, Prof. Sunguon Lee, Dr. Jose Alvarado, Dr. Arvind Gopinath, Dr. Justin Kao, Pawel Zimoch, Nathan Tyrell, Jean Comtet, Sarah Fay, Dr. Thomas Ober, Dr. Chris Dimitriou, Dr. Aditya Jaishankar, Allison Yost, Dhananjai Saranadhi, Bavand Keshavarz, Caroline Wagner, Michelle Sing-Ehret, Setareh Shahsavari, Michela Geri, Prof. Vivek Sharma, Dr. Johannes Soulages, Dr. Simon Haward, Dr. Alex Barbati, Shabnam Raayai-Ardakani, Divya Panchanathan, Amir Pahlavan, Dr. Andrew Milne, Yonatan Tekleab, Anoop Rajappan, Athanasios Athanassiadis, Mark Jeunette, Andrew D. Jones and Alisha Schor. It has been a pleasure working with and learning from you in the lab as well as hanging out outside the lab.

My sincere thanks also go to Sean Buhrmester, Debbie Blanchard, Susan Brown, Joan Kravit, Una Sheehan and Leslie Regan in the Mechanical Engineering department for your help and support, for making everything possible when needed, and for being patient and assisting me with my (many) requests.

Thank you Dr. Mirna Slim, Dr. Elan Pavlov, Dr. Thibaut Divoux, Dina El-Zanfaly, Fabián Kozynski, Jenny Wang, Dr. Nadia Cheng, Katia Shtyrkova, Peg Mead, Prof. Amy Bilton, Andrea Carney, Rachael Harding, Allison Yost, Debbie Blanchard, George Lan, Farrah Sabouni, Dr. Ben Scandella, Eric Stanisfer, George Chen, Zelda Mariet, Dr. Gunjan Agarwal, Dr. Armen Mkrtchyan and David Rosen for entertaining long discussions pertaining to my research and work, editing sections of my thesis, and helping me prepare for my defense and the defense celebration.

During my time at MIT, I have been fortunate to be of part a very vibrant

and welcoming graduate community at Sidney-Pacific. Thank you Dottie and Roger Mark, Roland and Annette Tang (and Joshua and Samuel), and Jack and Jean Ahern for opening your hearts and homes to me. You have taken me in your families. Your love, kindness, constant support, and encouragement made me feel at home far away from home. I have had the fortune to work with multiple SP governments and am truly grateful to all of them, particularly my SPEC year (George Lan, Holly Johnsen, George Tucker and Brian Spatocco). It has been a privilege working with you, serving the SP residents and the MIT graduate community. I have been very fortunate to be around such selfless individuals who inspire those around them to be better people. I am also deeply grateful to Peg Mead and Katia Shtyrkova for the time spent on the GradRat committee; it has been great fun working with you during my time at MIT and you continue to inspire me every day. Thank you to Jennifer Hapgood-White and Constance Hemenway for their personal support and encouragement, and for providing the students a voice during the SP HVAC renovation.

I express my deepest gratitude, love, and thanks to the people that made my life and years at MIT enjoyable and possible. Thank you Nadia, Mirna, Farrah, Matt, Dina, Katia, Elan, Burcu, Armen, Dave, Maria, Lisa, Fabián, Jenny, Rachael, Stephanie, Allison, Bernhard, Ben S., Amy, Tim, Chelsea, Jit, George L., Peg, Debbie, George C., George T., Pam, Thibaut, Kendall, Boris, Zelda, Eric, Sherrie, Bomy, Stuart, Caroline, Andrea, Frank, Alex T., Frank, Alice, Athanasios, and Michelle F. Thank you all for always being there and for the unforgettable moments spent together. Thank you for listening to me rant, helping me, procrastinating with me and simply for being there when I needed you. Your friendship is the best thing that happened to me at MIT.

A special thank you goes to my friends overseas who have supported me during my years at MIT: Cesar Roumieh, Amina Nasri, Clement Lix, Antoine Martre, Hichem and Sondes Smaoui, Laure Canis and Amine Naciri. I may be out of sight but I am definitely not out of mind. I am very grateful to all of you for the encouragement and support.

Last but not least, I thank my family, especially my parents Hany and Nahed, my

brother Karim and my uncle Tarek. Your love, encouragement and belief in me have propelled me further than I ever would have thought possible at every step of my life. I wouldn't be here without you and I dedicate this work to you.

# Contents

# List of Figures

# List of Tables

# Chapter 1

# Introduction

## 1.1 Yield stress fluids

In our daily lives, we encounter many materials that are neither perfectly elastic solids nor simple Newtonian fluids, and attempts to describe these materials as being either fluid or solid often fail [1]. From toothpaste and hair gel to whipped cream and chocolate pudding, such complex fluids exhibit a non-Newtonian behavior that is different from simple Newtonian fluids like water or oil. A subset of these complex fluids called viscoplastic or yield stress fluids share a common feature in that they are able to flow only if they are submitted to a stress above some critical value defined as the yield stress; otherwise at rest, they behave mostly like elastic solids and may exhibit some subtle aging properties [2–6]. Many industrial applications involve flow of viscoplastic fluids such as cosmetics (hair gel, toothpaste, shaving cream) [7], food (chocolate, ketchup, mayonnaise, whipped cream [8,9], paper making (pulp suspensions) [3], construction (cement) [10] and the oil industry (waxy crude oil [11,12]) [2]. Biological materials such as mucus can exhibit also viscoplastic behavior making these materials relevant in physiology and biolocomotion [13]. Examples of yield stress fluids present in our daily lives are shown in Fig. 1-1.

The ability of viscoplastic fluids to transition from a solid to a liquid state, and from a liquid to a solid state, in a reversible way results from the interactions between the elements that compose their microsturcture. The microstructure of a viscoplas-

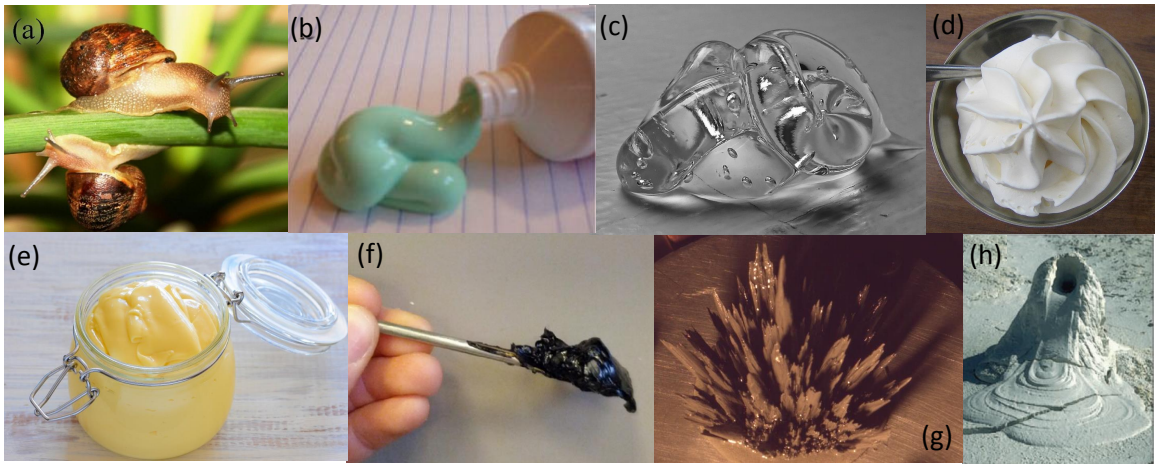


Figure 1-1: Examples of viscoplastic fluids in our daily lives (a) Adhesive locomotion of snails using mucus. Reproduced with permission [14]. (b) A collapsed extrusion of toothpaste [2, 15] (c) Hair gel (Carbopol microgel). Photo credit: Steve Johnson (d) Whipped cream (foam) (e) Mayonnaise (concentrated emulsion). Photo credit: Jules (f). Waxy crude oil. Reproduced with permission [12] (g) MR fluid on a plate with an applied magnetic field. Photo credit: Yonatan Tekleab. (h) A mud volcano. Photograph courtesy of the USGS. [2]

tic fluid can form a jammed system with apparent solid behavior, that breaks if subjected to a large enough stress. Yield stress fluids can be sorted into different categories depending on the nature of the elements forming the microstructure and the interactions between them [16]. Elements forming the microstructure can vary from colloidal-like particles (e.g. carbon black) [17] to volume-filling particles (e.g. swollen microgels like Carbopol) [18–20] to liquid dispersions such as concentrated emulsions [21, 22] or two-phase systems such as foams [23, 24]. Interactions between the different elements can vary from attractive (e.g. carbon black suspensions or clay suspensions) to repulsive (e.g. jammed hard sphere suspensions). A different class of materials are electrorheological (ER) [25–28] and magnetorheological (MR) [29,30] fluids where an electric or magnetic field controls the strength of the interaction between the particles and the fluids consequently develop a field-dependent yield stress. Fig. 1-2 shows some examples of the microstructures present in viscoplastic materials and highlights the diversity in structural elements and interactions that constitute these fluids.

Due to their relevance in the many applications described previously, understand-

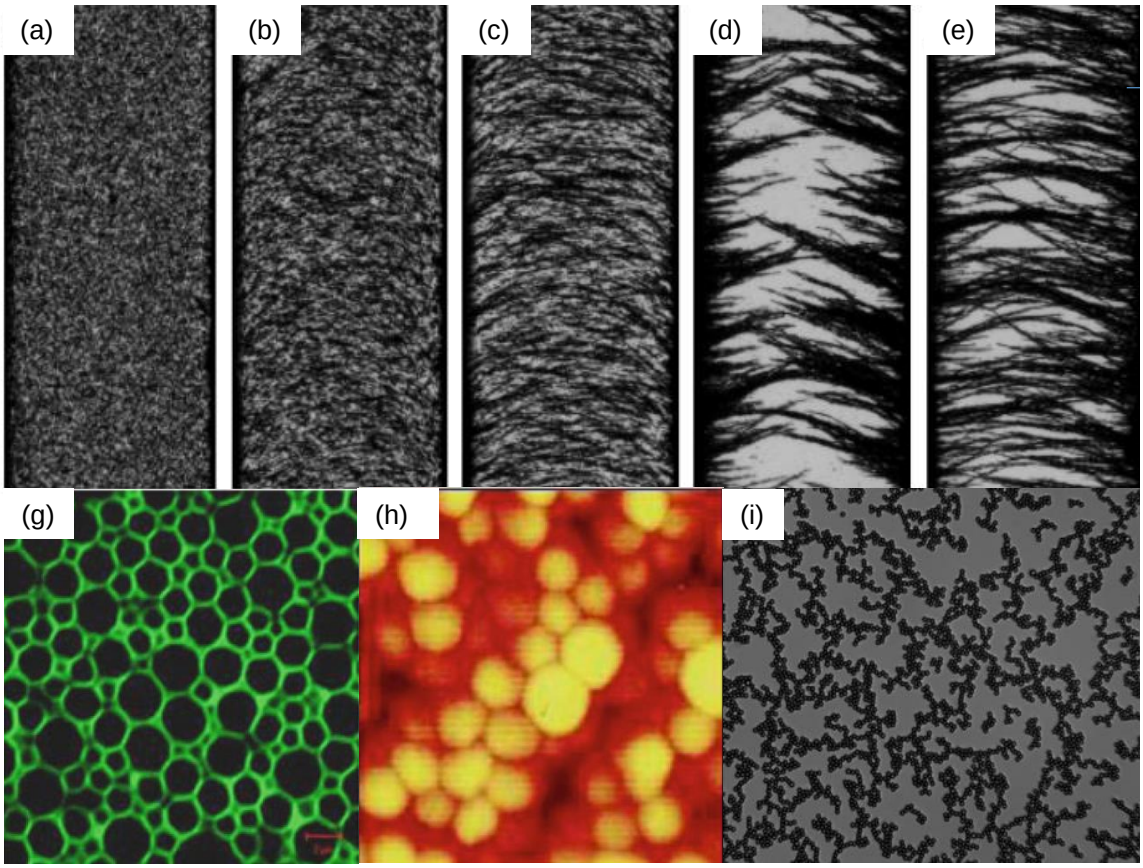


Figure 1-2: Examples of different types of microstructure present in viscoplastic fluids (a-e) Evolution of aggregate microstructure of a magnetorheological fluid [29]. The applied field is off in (a), and increases in strength from (b) to (e). (g) Polyelectrolyte microgels (particle diameter $d \simeq 0.2$ $\mu$m) (Reproduced from [31]) (h) Oil in water emulsion (particle diameter $d \simeq 2$ $\mu$m) (Reproduced from [32]) (i) Percolating 2D colloidal network of aggregated PS spheres destabilized by the addition of salt and surfactant. [17]

ing the flow characteristics of viscoplastic fluids is crucial for their formulation and handling. The flow properties are typically non-linear, shear history-dependent and can be challenging to predict due to the coexistence of solid and liquid regions in the flow [2, 3, 6, 7].

## 1.2 Electro-active complex fluids

In this thesis, our interest lies in studying electro-active yield stress (EAYS) fluids. Here, we define electro-active fluids as conductive or dielectric materials. Conductive

materials contain an electrical-charge carrying species that allow them to conduct current while dielectric materials are insulators that can be polarized upon the application of an electric field. Examples of electro-active materials are electro-rheological fluids, battery slurries, conductive inks, ionic liquids and conductive polymers. The non-linear rheology of these materials, coupled to their electric properties, leads to interesting applications in a wide range of devices, whose design is often consequently challenging. We can classify devices using EAYS fluids into two classes: ones where we control the electrical properties and the mechanical response is the output or the opposite where we specify the rheology of the fluid and monitor its electrical properties. Gaining insight into the rheological and electrical properties of electro-active materials and how they affect device design at the system level is therefore significant for many applications. Here, we choose to focus on two case studies: electro-rheological (ER) fluids and carbon black (CB) gels. These two classes of materials are of practical relevance as we will show in Section 1.3. Additionally, these materials fall at the two extremes of the conductivity spectrum ($\sigma_{ER} \simeq 10^{-6}$ mS/cm and $\sigma_{CB} \simeq 10^{-3} - 10^{1}$ mS/cm [26, 33, 34]) and are useful examples to illustrate the interplay between flow and electrical properties in electro-active fluids and how it affects device design.

### 1.2.1 Electrorheological fluids

Electrorheological (ER) fluids are materials that exhibit a reversible change in rheological properties with the application of a strong external electric field ($E > 1$ kV/mm). They consist, typically, of a suspension of dielectric particles in an insulating carrier fluid ($\sigma < 10^{-13}$ mS/cm) [25, 35]. When an electric field is applied, the particles aggregate and align in the direction of the field, forming columns consisting of chains of particles, which cause the fluid to transition from a liquid-like to a soft solid-like state [27, 28, 36] [Fig. 1-3]. This change in the fluid properties is very rapid ($\delta t_{ER} \sim 10$ ms) and is reversible upon removal of the electric field. From a rheological standpoint, the ER fluid can reversibly transition from a Newtonian fluid when the field is off to a viscoplastic fluid with a field-dependent yield stress when the field

is turned on [26, 37–39] [Fig. 1-3].

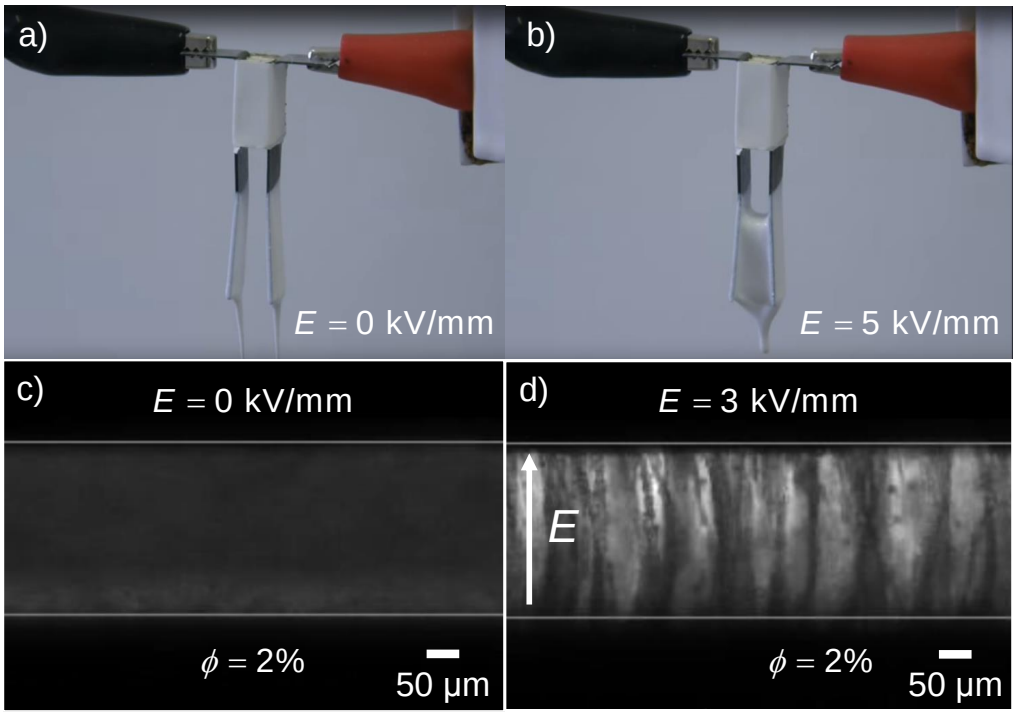


Figure 1-3: An electrorheological fluid based on silicone oil and BaTiO3 particles (40 %wt) with the electric field off (a) and with an applied electric field $E = 5$ kV/mm (Video credit: Tibor Medvegy). Electrorheological fluids have a field-dependent yield stress and can reversibly change from a liquid to solid-like state upon the application of an electric field $E$. Microchannel showing an electrorheological fluid (Rheoil 4.0, $\phi = 2\%$) with the field off (c) and an applied field of $E = 3$ kV/mm (d). The change in the rheological properties of the ER fluid is due to the observed chaining of the particles upon application of the electric field.

These features have made ER fluids a promising candidate for an electrical-mechanical interface and, motivated by applications they have received a great deal of attention since their discovery by Winslow in 1949 [40]. Since then, a wide range of materials have been shown to exhibit an electrorheological effect such as oil-based suspensions containing starch [41, 42], cellulose [43], semiconducting polymers (e.g. polyaniline) [44–46], polymer nanocomposites [47, 48], modified metal oxides [49] and various non-oxide minerals [50,51]. These materials rely on the difference in the dielectric constant between the carrier fluid and the suspended particles to induce electrical

polarization within the particles upon application of the electric field $E$. This type of polarization is denoted as the dielectric electrorheological effect (DER) [52]. Recently, a different type of polarization has emerged using nanoparticles of barium titanate coated in urea where initially randomly oriented molecular dipoles are aligned under the effect of the electric field. This has been dubbed as the giant electrorheological effect (GER) [27, 52]. The GER fluid can exceed by one to two orders of magnitude the yield stress found in ER fluids relying on the induced polarization mechanism (typically a few kiloPascals) [53–55]. Additionally, GER fluids exhibit a linear dependency of the yield stress on the electric field: $\tau_y \propto E$ that is different from that found in conventional DER fluids for which the field-dependent yield stress scales as $\tau_y \propto E^2$ at low fields and as $\tau_y \propto E^{1.5}$ at higher fields [26, 27, 36, 38, 56, 57]. Fig. 1-4 shows a comparison of the field-dependent yield stress in DER and GER fluids.

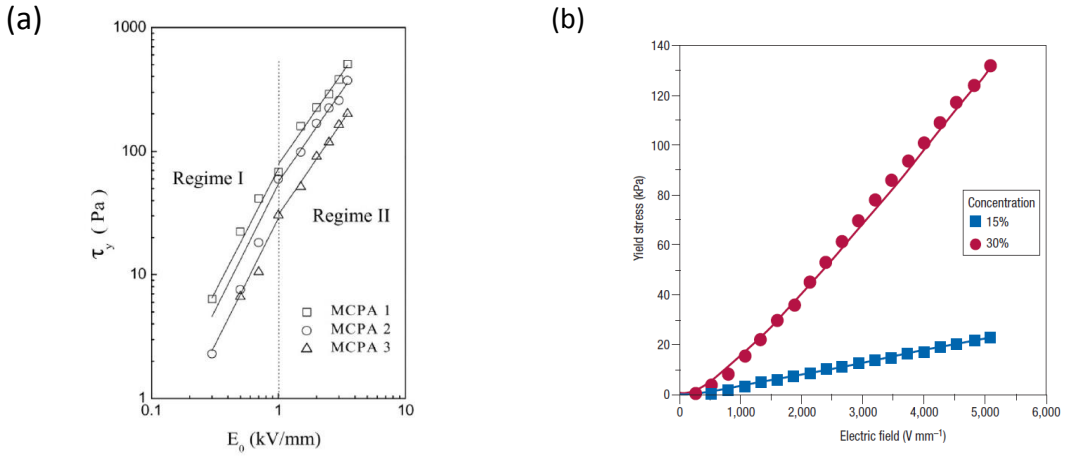


Figure 1-4: Comparison of the field-dependent yield stress in DER and GER fluids. (a) The yield stress $\tau_y$ vs. $E_0$ for 20 wt% suspensions of microencapsulated polyaniline (MCPA) particles encapsulated with melamine-formaldehyde (MF) resin dispersed in silicon oil. The ratios by weight of polyaniline to MF resin are 10/114 (MCPA1), 10/152 (MCPA2), and 10/190 (MCPA3), respectively. Regime I has a quadratic relation region between the yield stress and the electric field strength. In Regime II, the yield stress varies with $E_0^{1.5}$. Reproduced from [56] (b) Yield stress plotted as a function of applied electric field $E$ for two solid concentrations of a GER fluid. (Reproduced from [54])

ER fluids are therefore promising tunable viscoplastic materials for use in a variety of hydraulic components and microfluidic devices including valves, clutches and

Table 1.1: A summary of the different modes of operation of ER devices and their typical engineering applications

| Mode of operation | Illustrative schematic | Applications |
|---|---|---|
| Shear mode | 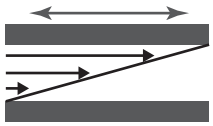 | Clutches, brakes, dampers [62, 69] |
| Flow mode | 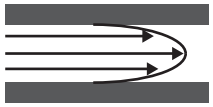 | Valves, vibrators [62, 69, 73–75] |
| Squeeze mode |  | Shock absorbers, dampers [62, 69] |

dampers [58–60]. The operating principle of such devices is based on the controlled resistance to applied force, created by the electrorheological fluid [61]. Devices based on ER fluids can operate under three different modes: shear, flow and squeeze [62]. In shear mode, one of the electrodes is free to move in its plane, and common applications include clutches, brakes and dampers [63–71]. In flow mode, the electrodes are fixed and the pressure drop across the channel is controlled using the electric field. Valves and vibrators are typical applications in which ER fluids are used in flow mode [72–75]. In squeeze mode, the electrode gap is varied and the fluid is compressed in the wall-normal direction. Vibration control, shock absorbers and dampers are examples of application of ER fluids used in squeeze mode [62, 69, 76]. A summary of the different modes of operation and their typical engineering applications is shown in Table 1.1. Other applications of electrorheological fluids include haptic displays [77], micropumps and microfluidic logic gates for microelectromechanial applications [27, 78, 79]. Finally, recent promising applications of ER/MR fluids also include the control of adhesion of an object to a surface using MR fluids [80, 81], polishing of precision optical components [82, 83] and tunable soft grippers for robotics [84].

### 1.2.2 Carbon black gels

Carbon black (CB) refers generically to colloidal soot particles produced from the incomplete combustion of fossil fuels. Three levels of structural hierarchy exist in carbon black system: they are composed of permanently fused "primary" particles or nodules whose diameter is typically about 30 nm [85], to form aggregates of typical size 200-500 nm. Fig. 1-5 shows TEM images of different grades of carbon black that demonstrate these two scales of hierarchal structure. These aggregates display short range attractive interactions of typical strength 30 $k_BT$ [86] and form larger agglomerates of typical size (1-100 $\mu$m) through diffusion limited cluster aggregation (DLCA) [87]. Fig. 1-6 displays the different scales of structural hierarchy and the fractal nature of the network present in carbon black. When dispersed in a liquid hydrocarbon, carbon black agglomerates form a space-spanning percolated fractal network, even at small volume fractions (typically 1 to 5%) [88–90]. The resulting gels are reversible, as they are destroyed by large shear and reform once the flow is stopped [91–93]. This fractal aggregate structure sets carbon black apart from other types of conductive additives such as carbon nanotubes, carbon fibers, graphene sheets, or graphite powder [94].

Carbon black is utilized extensively in a wide variety of industrial applications including batteries, paints, coatings, inks and water treatment [96] as well as filled rubbers and tires [95,97,98]. CB serves as an additive to convey protection from ultra-violet light [99, 100], increase toughness [101], improve processability and to enhance electrical conductivity [97, 102–104]. By changing the primary particle properties and the manufacturing process of the carbon black, the structural properties of the carbon black (such as the fractal dimension of the aggolmerated particles) can be tuned to suit a specific application. For applications requiring a high conductivity, carbon black grades with a small conductive primary nodule manufactured with a highly structured aggregate i.e. with a very large specific surface area are preferred [95]. Additionally, highly porous carbon black grades such as KetjenBlack EC600JD (Akzo Nobel) are also used in high conductivity applications to lower the loading needed to reach a

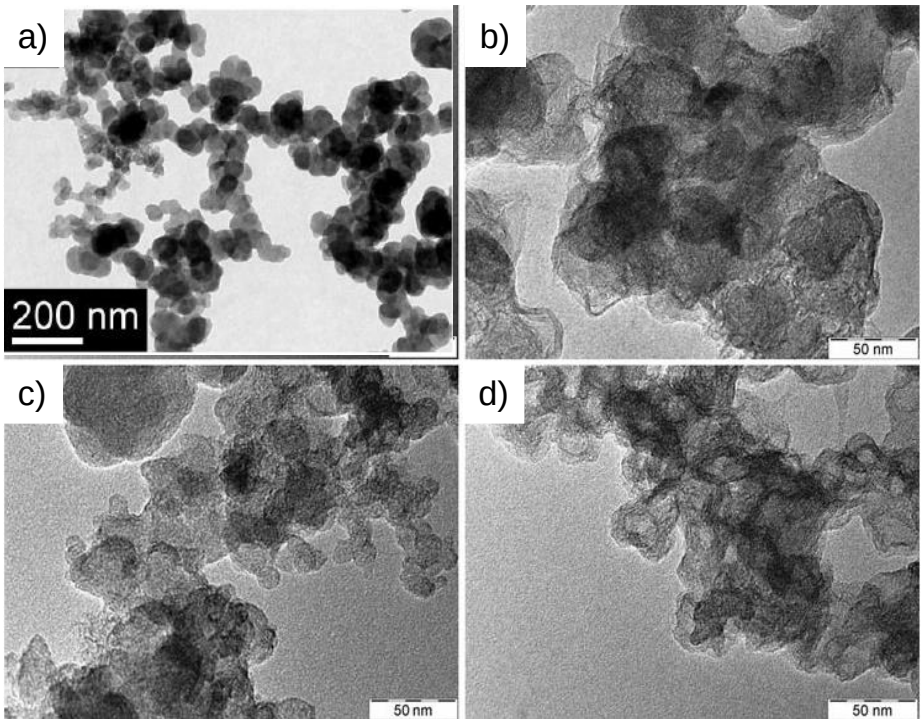


Figure 1-5: TEM images of different carbon blacks: (a) TIMCAL C45 (b) Acetylene Black (c) Vulcan XC72R (d) Ketjen Black EC600JD. Reproduced from [94] and [95].

given conductivity [97]. The specific surface area of some common structured carbon black grades, measured using BET gas adsorption techniques [105], is given in Table 1.2.

Table 1.2: Specific surface area of some common carbon black grades

| **Carbon additive** | **BET surface area ($m^2/g$)** |
|---|---|
| TIMCAL C45 | 45 |
| Acetylene Black | 60 |
| Vulcan XC72R | 250 |
| Ketjenblack EC-600JD | 1453 |

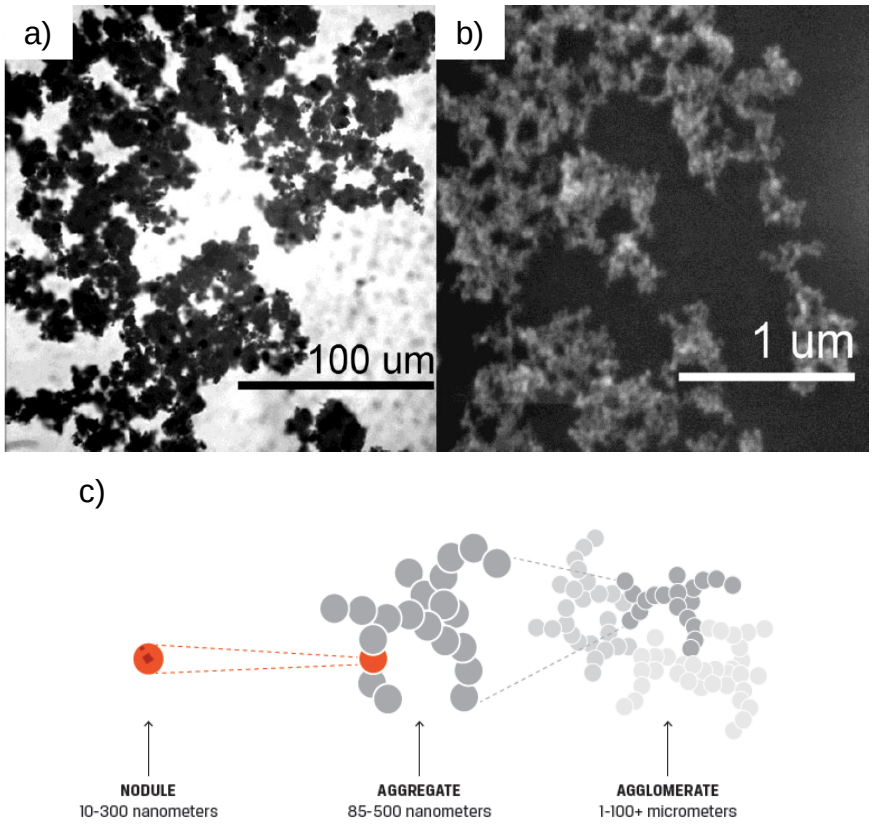


Figure 1-6: (a) Transmission mode optical micrograph of a Ketjenblack gel in SSDE®. SSDE® is a proprietary solution of 1.3 M $LiPF_6$ in a blend cyclic and linear alkyl carbonates produced by Novolyte Technologies. (b) Secondary electron detector image of a Ketjenblack gel in SSDE. Similar, cluster-based structures are observed across length scales differing by two orders of magnitude (Reproduced from [94]). (c) Different scales present in the structural hierarchy of carbon black (Reproduced from [87]).

## 1.3 Devices using electro-active fluids

Among the different applications of electrorheological fluids and carbon black gels, this work will focus on the design of two different devices that make use of these electro-active viscoplastic fluids: smart hydraulic valves for small scale robotics and semi-solid redox flow batteries. These applications will highlight the interplay between the rheological and electrical properties of the viscoplastic materials involved and how an understanding of the flow of these materials can inform device design and optimization.

### 1.3.1 Smart hydraulic valves for small-scale robotics

Hydraulic actuators are promising devices for robotic applications requiring large actuation forces. They provide accurate position and load-invariant control because of the high stiffness present in hydraulic systems, generated by the incompressible nature of the hydraulic fluid [106]. Additionally, the ratio of output power per unit weight is higher than in other systems provided high pressure is supplied, therefore making hydraulic systems an effective way of constructing a compact high-power system [106]. A number of hydraulic robots have shown promise for locomotion on rough terrain, information gathering, search and rescue and payload carrying [107]. The development of small-scale robotics for such applications has the potential to increase their efficacy at accomplishing tasks as well as significantly reduce their cost through mass production.

Due to the number of elements required for a hydraulic circuit such as fluid reservoirs, pumps and valves, making small-scale hydraulic robots is challenging. In particular, despite strong trends towards miniaturization at lower costs in the integrated circuit industry over the last 50 years, as well as the advances in the field of microfluidics in the last decade, valve design has remained relatively unchanged. For small-scale robotics, valves tend to be bulky, heavy and expensive and are often an inhibiting factor in the development and commercialization of this technology.

Drawing inspiration from biological systems, the circulatory system in mammals can be seen as an analog of a "hydraulic" system. In nature, whether the mammal is large (e.g. human) or small (e.g. mouse), the circulatory system is similar and scalable. This is due in part, to the non-Newtonian properties of blood, which confer additional functionality to the system. By analogy, using a non-Newtonian fluid in hydraulic robots, in lieu of a simple Newtonian fluid, can be beneficial and allow the system to scale to a smaller size. In particular, smart fluids such as ER and MR fluids are a promising class of materials for this purpose since they allow control of the properties of the fluid through an electric or magnetic field.

Despite the higher yield stress that can be attained by MR fluids [29], ER fluids are

more promising for small-scale valve applications [108–114]. By leveraging advances in printed circuit boards (PCB) and microelectromechanical systems (MEMs) technology, scaling down electrical circuits is straightforward while miniaturized magnetic circuits are still a challenge today. Composed of a pair of electrodes and a spacer, ER valves form a mechanically simple system with no moving parts. By making use of PCB technology and commercial off-the-shelf hardware, ER valves are easy and inexpensive to fabricate. The system requires the use of high electric fields ($E > 1$ kV/mm) but uses very low current ($I \simeq$ 1-10 $\mu$A) and therefore consumes little power (typically on the order of a few mW). Finally, the electric field provides a means to control the system with fast switching times thanks to the fast response time of ER fluids ($\delta t_{ER} \sim 10$ ms). These features make ER valves a promising low-cost technology for small-scale hydraulic robots compared to existing hydraulic valve technology as shown in Fig. 1-7.

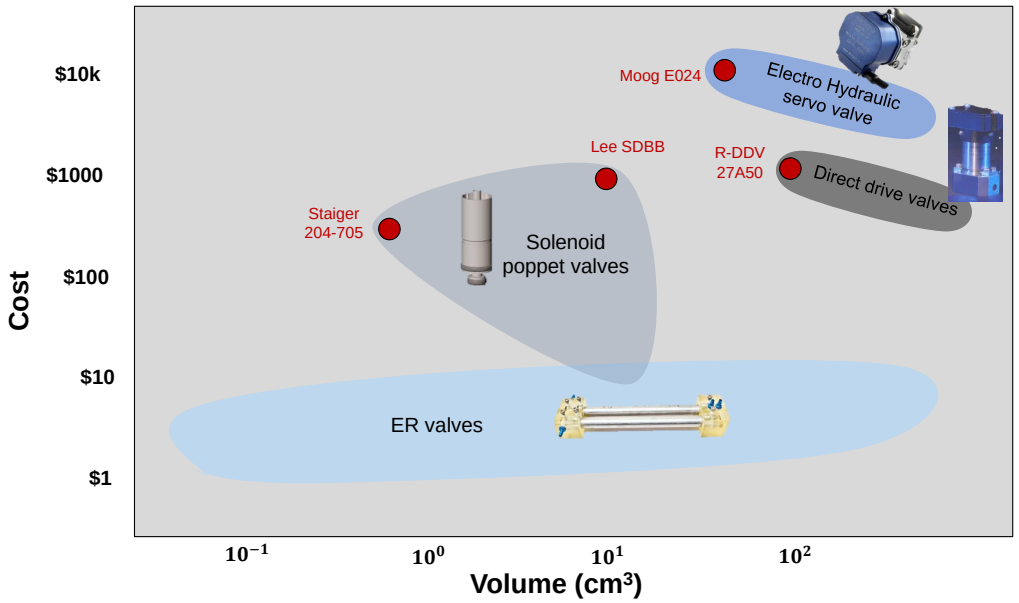


Figure 1-7: Cost vs volume of existing hydraulic valve technology at the small scale. ER valves are a promising technology for small cheap hydraulic valves.

### 1.3.2 Semi-solid redox flow batteries

The rapidly increasing integration of renewable energy sources such as wind and solar into the electric power infrastructure has resulted in an urgent need for low-cost, scalable energy storage for load balancing [115–120]. Currently, the vast majority of energy storage occurs via pumped hydro installations, a technology that is mature, cost effective, and efficient, but limited in applicability by geographic constraints [121]. Alternative modes of energy storage that can be deployed in a distributed manner include batteries, compressed air, thermochemical energy, and flywheels; but today only a small fraction of the world's energy storage uses these technologies [121]. Various novel energy storage technologies have been proposed to improve grid reliability and utilization, including high energy density flow batteries [121–125], aqueous Li-ion [126], Na-ion [127–129], and K-ion batteries [130, 131].

Flow batteries are a type of rechargeable battery consisting of tanks of anolyte and catholyte that are pumped past a membrane between two electrodes [34, 121]. They represent a promising technology for reaching the 100 $/kWh cost target needed for grid-level energy storage [132]. This is due to their low manufacturing cost considerations and their design flexibility and scalability, allowing the decoupling of power (stack size) and energy (tank size) [94, 133–135]. Many aqueous solution-based flow battery chemistries are known, all of which have historically been used in some variant of the same basic flow cell architecture and typically operate at less than 1.2 V cell voltage and low molarities [135]. In conventional flow batteries, a Newtonian electrolyte is pumped through a stationary porous conductive carbon felt that enables charge transfer from the bulk of the electrode to the current collectors. Increases in solution molarity and therefore in energy density, especially for large molecules, are accompanied by higher viscosities leading to higher driving pressures, greater flow resistance and lower energy efficiency [34].

A new approach proposed by Duduta et al. [121] and Fan et al. [34] is the semi-solid flow battery. In semi-solid flow batteries, a nanoconductor (e.g. carbon black) is directly mixed in with the electrolyte to form a conductive suspension and the

suspension as a whole is pumped through the cell. Increasing the carbon black loading yields a higher electronic conductivity of the slurry therefore leading to better electrochemical cycling, but also increases the yield stress therefore requiring higher pressures to flow. The optimal amount of carbon black needs to be mixed in to strike a balance between flowability and charge transfer in the suspension, thus demonstrating the importance of understanding the trade-offs in the design space of these devices [136]. Fig. 1-8 shows a schematic of a flow battery and a comparison between conventional and semi-solid flow battery architectures. Recent work by Darling et al. [132] shows that aqueous and non-aqueous flow batteries are promising technology platforms capable of achieving the low costs (100$/kWh target) required for their widespread implementation. They showed that non-aqueous systems enable higher cell voltages than their aqueous counterparts but also require higher active material solubility to offset higher electrolyte costs. In particular, their work showed that lithium polysulfide flow batteries are able of reaching the target of 100 $/kWh due to the low cost of sulfur.

## 1.4 Scope of the thesis

The goal of this thesis is to explore the design space of devices using electro-active yield stress fluids and how the interplay between rheological and electrical properties affects their design and operation. We aim to develop design rules and performance metrics for devices using EAYS fluids, with a focus on how an added structure at the microscale, corresponding to the existence of a yield stress at the macroscale, affects the performance of the devices. This thesis will focus on two representative case studies of such devices using viscoplastic fluids: 1) small rapidly-actuated hydraulic valves using electrorheological fluids applied to centimeter-scale robotics and 2) semi-solid flow batteries using suspensions of percolated networks of carbon black flowing in millifluidic channels. Using these two examples, this thesis strives to improve the fundamental understanding of the electrical and rheological properties of the electro-active yield stress materials used in these devices through experimental

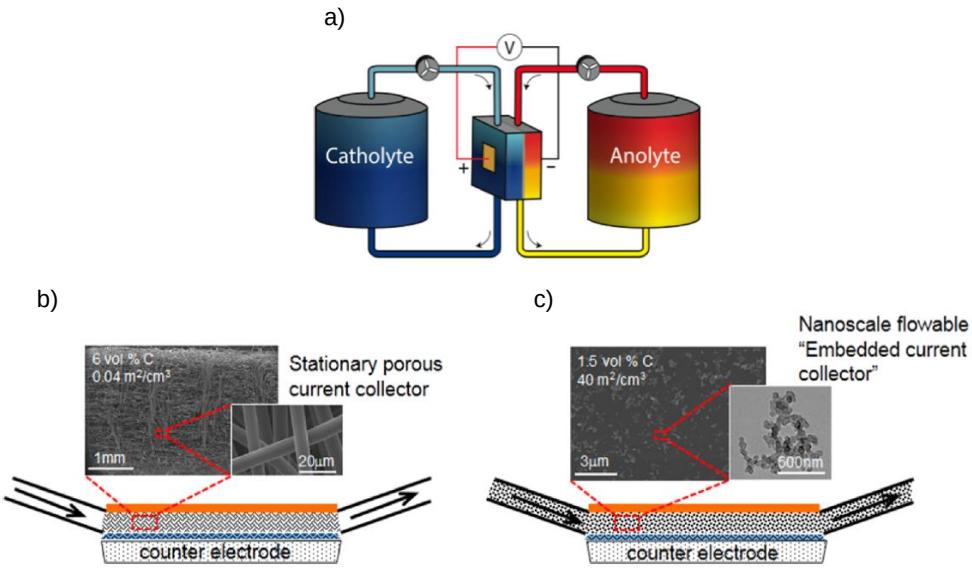


Figure 1-8: Conventional vs. semi-solid flow battery architecture (a) Flow batteries combine a current-extracting stack, through which redox active solutions flow, with storage tanks and pumps. (b) Conventional flow cell architecture using stationary carbon fiber current collector and an electronically insulating Newtonian flow electrode (in white on the figure). (c) Semi-solid flow cell architecture relying on viscoplastic electronically conductive flowing redox electrodes, composed of nanoscale percolating networks of conductor particles such as carbon black. Reproduced from [34].

characterization and modeling of the properties of the materials. A new test fixture for simultaneous measurements of rheo-electric properties is introduced and we discuss how rheo-electric measurements can give insight into the flow behavior of the fluid. Finally, we demonstrate how to translate the material models developed to device/system level predictive models of the key performance metrics of the devices.

This thesis is composed of two main parts: Chapters 2 and 3 will focus on ER fluid characterization and ER valve design, while Chapters 4-8 will discuss the rheological and electrical characterization of carbon black gels and their application to semi-solid flow batteries.

In chapter 2, we discuss the rheological and electrical characterization of electrorheological fluids. In particular, we perform a comparison of the yield stress obtained in pressure-driven channel flow and in wall-driven flow. We show that an increase in the yield stress (yield hardening) occurs in pressure-driven flow that can

be explained by a local increase in volume fraction and we propose a phenomenological physical model for the process. This allows us to reconcile rheological measurements taken in wall-driven flows (e.g. torsional rheometers) and in pressure-driven channel flow, a flow configuration that is more applicable to valve applications.

In chapter 3, we introduce performance metrics for ER valves, and by using a custom modular valve design, we study the effects of the geometry and surface roughness of the electrodes on the ER valve performance. This allows us to derive some design rules for ER valve design and we demonstrate the applicability of ER valves in robotic applications.

Chapter 4 focuses on the rheological and wall slip characterization of carbon black gels in steady shear. We study the effect of important material properties and operating parameters, such as the carbon black loading, mixing protocol and surface material, on the rheology and wall slip behavior of the material. In addition, we demonstrate the effect of incorporating additives such as polymers or active energy storage particles on the rheology and conductivity of the gels.

Chapter 5 introduces a novel test fixture for stress-controlled rheometers to perform simultaneous measurements of rheo-electric properties of strongly conductive complex fluids. Using benchmark and calibration experiments, we demonstrate the ability of this setup to perform simultaneous rheo-electric measurements on different classes of conductors and we derive expressions for extracting conductivity in plate-plate and cone-plate geometries.

In chapter 6, we aim to illustrate the relevance of this novel apparatus on a class of strongly conductive complex fluids, namely carbon black gels. We simultaneously measure the electrical and mechanical properties of carbon black gels at rest, under creep and during steady shear flow. We show that the corrections first introduced for mechanical measurements extend to electrical measurements and enable accurate conductivity measurements under shear. As an illustrative example, we examine the rheo-electric properties constitutive of five carbon black gels of different grades, and demonstrate the relevance of the novel rheo-electric apparatus as a versatile characterization tool for strongly conductive complex fluids and their applications.

In chapter 7, we discuss small and large oscillatory measurements performed on carbon black gels. Small amplitude oscillatory shear measurements, performed concomitantly to conductivity measurements on carbon black gels of different concentrations, allow us to extrapolate the conductivity and rigidity percolation of carbon black gels. Additionally, large amplitude oscillatory shear measurements are shown to be a useful metric to study fatigue in carbon black gels.

Chapter 8 introduces a new pumpless design architecture for flow cells that is driven by gravity. We demonstrate how insight into the rheological and wall slip behavior of the semi-solid suspensions obtained through careful characterization can inform and help optimize cell design and operation.

In the last section, concluding remarks on electro-active fluids are made and perspectives for future work are considered.

## 1.5 Measuring the yield stress

Throughout this work, we discuss, in part, characterizing the shear flow behavior of viscoplastic materials. In this section, we introduce some of the relevant methods available for this purpose as well as various models that represent their flow behavior.

### 1.5.1 Rheometry methods

The most common instrument for characterizing the rheology of a material is a rheometer, which allows the user to perform simple steady shear measurements and extract material properties. Our interest lies in the shear rheology of viscoplastic materials. Two classes of shear rheometers are most commonly used: torsional rheometers and capillary rheometers [137, 138].

Torsional rheometers rely on placing the material in a thin gap between two geometries and rotating one or both of them to shear the material. Torsional rheometers can be divided into two classes: stress-controlled and strain-controlled rheometers. Stress-controlled rheometers impose the torque $\mathcal{M}$ and measure the displacement and the angular rotation speed $\Omega_{rot}$ while, conversely strain-controlled rheometers impose

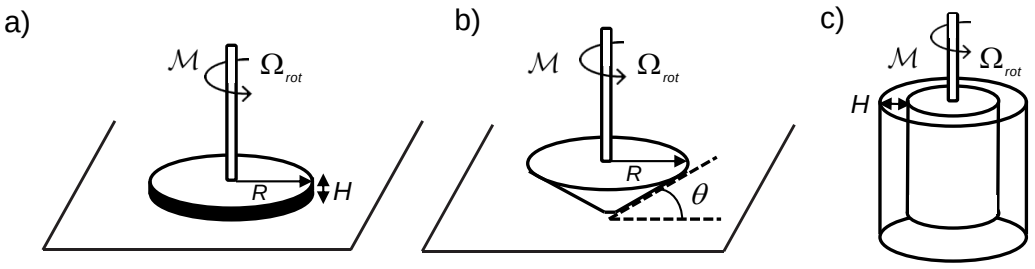


Figure 1-9: Typical geometries used in torsional rheometers. a) Parallel plate geometry b) Cone-plate geometry c) Couette geometry. In stress-controlled rheometers, the torque $\mathcal{M}$ is imposed and the angular velocity $\Omega_{rot}$ is measured. In strain-controlled rheometers, the angular velocity $\Omega_{rot}$ is imposed and the torque $\mathcal{M}$ is measured. Reproduced from [98].

the displacement and measure the resulting torque $\mathcal{M}$. In both cases, one can extract the shear stress and shear strain acting on the material and derive material functions relevant to the flow of the material (e.g. the flow curve defined as the shear stress $\tau$ vs. the shear rate $\dot{\gamma}$) [138]. In torsional rheometers, if the gap between the geometries (between which the material is sheared) is small, the shear stress is homogeneous across the gap, and therefore, torsional rheometers are often used to obtain viscometric measurements. Different geometries most commonly used are shown in Fig. 1-9.

Figure 1-9 (b) shows a cone-plate geometry, in which a truncated cone with a small truncation gap and small angle ($\theta \leq 4°$) is typically used. The cone-plate geometry has the advantage of imposing a homogeneous shear rate distribution across the radius of the fixture, allowing for controlled precise measurements. Only small volumes $Vo$ of sample are needed for this geometry ($Vo = 2\pi R^3\theta/3$, typically 30-1500 $\mu$L), which is useful when samples are scarce. However, due to the small truncation gap $h_{trunc} = 50 - 150$ $\mu$m), it can be challenging to use with suspensions of particles, where the particles are of similar size to the truncation gap. In this geometry, the shear rate is given by $\dot{\gamma} = \Omega_{rot}/\theta$ and the shear stress is given by $\tau = 3\mathcal{M}/2\pi R^3$ where $R$ is the radius of the cone.

Figure 1-9 (a) shows a plate-plate geometry, in which the sample is confined between two parallel plates. This geometry allows for a variable sample thickness

($0 \leq H \leq 2000$ $\mu$m), which is useful to accommodate dispersions with different particle sizes. Similarly to the cone-plate geometry, only a small volume is needed in this geometry ($Vo = \pi R^2 H$). The parallel plate configuration also allows for relatively straightforward control of the surface treatment (roughness, chemistry, texture), therefore resulting in better control over wall slip. Additionally, using measurements at multiple gaps, corrections for wall slip can be performed and its effect decoupled from the rheology of the material [139]. Wall slip and parallel plate corrections will be discussed further in section 1.5.3. Finally, the parallel plate geometry can be used to impose a constant electric field across the sample, which will prove advantageous in this work as discussed in chapters 2 and 5. However, unlike the cone-plate geometry, the shear rate is not homogeneous in the radial direction $r$ but varies as $\dot{\gamma}(r) = \Omega_{rot} r/H$ where $H$ is the gap between the plates. As a consequence, the stress also depends on the radius $r$ and extraction of the relationship between shear stress and shear rate is more complicated. Typically, the shear stress at the rim (radius $R$) $\tau_R$ is derived using the following relationship :

$$\tau_R = \frac{\mathcal{M}}{2\pi R^3}\left[3 + \frac{d\ln \mathcal{M}/2\pi R^3}{d\ln \dot{\gamma}_R}\right] \tag{1.1}$$

where the shear rate at the rim $\dot{\gamma}_R$ is given by $\dot{\gamma}_R = \Omega_{rot} R/H$. In this work, the parallel plate geometry will often be the geometry of choice for the aforementioned reasons and further discussion on this geometry is provided in chapter 5.

Figure 1-9 (c) shows a Couette geometry, where the sample is inserted between two concentric cylinders. Due to its large surface area, this geometry is often used for low viscosity samples or for high shear rates where centrifugal forces could be an issue for cone-plate or plate-plate geometries. However, larger volumes of sample are needed and the larger inertia of the geometry can complicate measurements for certain applications e.g. small amplitude oscillatory shear (SAOS).

An alternative geometry used to measure the yield stress of viscoplastic is the vane geometry in which a thin-bladed vane is introduced into the fluid with the minimum amount of disturbance to the sample [140, 141]. It is a particularly useful geometry

for fluids that display large slip effects at smooth walls but is relatively difficult to use with EAYS fluids to apply an electric field or measure electrical properties.

On the other hand, capillary rheometers rely on flow of the fluid through thin capillaries to characterize its rheology. While velocity profiles in torsional rheometers are linear in the gap direction (Couette flow), in capillary rheometers, the flow is more complex e.g. parabolic Poiseuille flow. Consequently, the stress is not homogeneous across the capillary tube and more complex relationships are needed to extract material functions from capillary measurements. In the capillary rheometer, for a capillary of length $L$ and radius $R$, the flow rate $Q$ and the pressure drop $\Delta P$ are measured and the stress at the wall and the apparent shear rate are given by $\tau_R = \Delta PR/2L$ and $\dot{\gamma}_a = 4Q/\pi R^3$. For non-Newtonian fluids, a Weissenberg-Rabinowitsch-Mooney (WRM) correction accounts for the non-parabolic velocity profile and the true shear rate is given by $\dot{\gamma}_t(\tau_R) = \frac{Q}{\pi R^2}\left[3 + \frac{d\ln\dot{\gamma}_a}{d\ln\tau_R}\right]$ [137]. However, flow through capillaries or microchannels is often closer to flow in real applications, which can provide additional insight on the flow behavior of the fluid but larger sample volumes are needed, in general [6].

Our approach in this work will focus on characterizing viscoplastic fluids using torsional rheometers, in particular the parallel plate geometry. Using the parallel plate geometry, we can perform viscometric tests, apply a constant electric field and perform wall slip corrections, which will prove useful in the context of this work. Two types of tests will be of interest: steady-shear tests and oscillatory tests. In steady-shear tests, the fluid is sheared at a constant shear rate or shear stress and the flow curve of shear stress $\tau$ vs shear rate $\dot{\gamma}$ is derived. Apparent viscosity $\eta \equiv \tau/\dot{\gamma}$ is defined as the ratio of stress to shear rate. Fig. 1-10 shows examples of flow curves for typical viscoplastic materials. Newtonian fluids have a constant viscosity, while more complex fluids such as viscoplastic materials typically have a viscosity that is dependent on shear rate. Viscoplastic flow models are described in section 1.5.2. We define the static yield stress as the stress needed to initiate flow from rest while the dynamic yield stress is obtained by extrapolation from the flow curve when starting from a fluidized initial state at high shear rate. The existence of separate dynamic

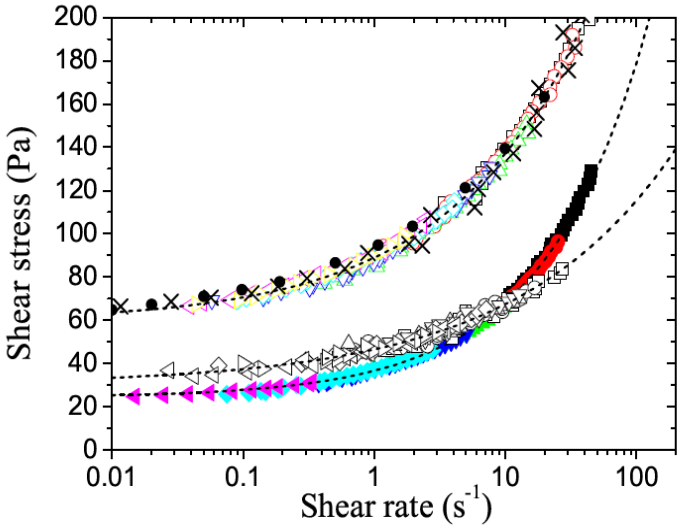


Figure 1-10: Flow curves of typical viscoplastic materials. Constitutive laws of (from bottom to top) a concentrated emulsion, a foam, and a Carbopol gel, measured locally in a wide gap Couette cell using MRI techniques. Macroscopic data measured in the Carbopol gel in the Couette geometry (crosses) and in a cone and plate geometry (filled circles) are also shown. The dotted lines are Herschel-Bulkley fits to the data [Eq. 1.3]. The emulsion is composed of 6.5 $\mu$m diameter silicone oil droplets dispersed at a 75% volume fraction in a mixture of 50 wt% glycerine and 50 wt% water stabilized by Brij and trimethyl tetradecyl ammonium bromide at a 1 wt% concentration. The foam is composed of 45 $\mu$m diameter bubbles at a 92% volume fraction in a Sodium Laureth Sulfate (SLES) foaming solution. The gel is a hair gel (Vivelle Dop, France), which is mainly composed of Carbopol in water. Reproduced from [142].

and static yield stresses in the same material is known in bentonite, paints and waxy crude and fuel oils and more generally in thixotropic materials [143,144]. In oscillatory shear, the shear rate is sinusoidal with frequency $\omega$ and the viscoelastic moduli $G'(\omega)$ and $G''(\omega)$, representing respectively the elastic and loss components extracted from the resulting stress signal, are derived. Oscillatory measurements will be discussed in more detail in Chapter 7.

### 1.5.2 Viscoplastic flow models

To quantify the steady-state flow properties of non-Newtonian fluids requires the measurement of an entire function: the flow curve. The flow curve is a representation

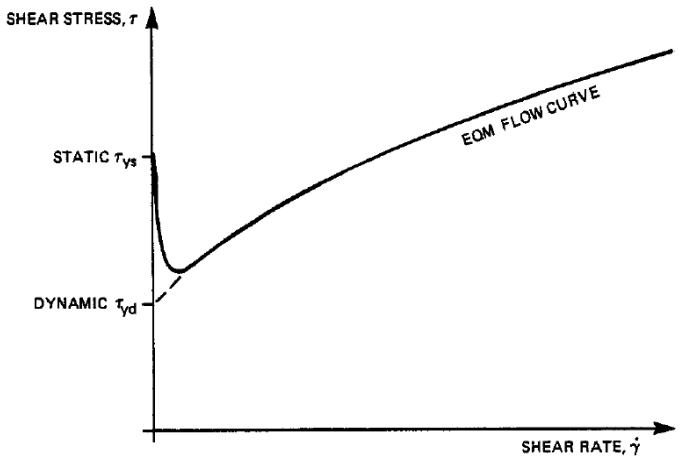


Figure 1-11: Static vs. dynamic yield stress. The static yield stress is defined as the stress needed to initiate flow from rest. The dynamic yield stress is obtained by extrapolation from the flow curve when starting from a fluidized initial state at high shear rate. Reproduced from [143].

of the dependence of the shear stress $\tau$ on the shear rate $\dot{\gamma}$. For a Newtonian fluid, these functions are linearly related $\tau = \mu\dot{\gamma}$, where $\mu$ is a constant viscosity. Unlike Newtonian fluids where the shear viscosity is constant, viscoplastic fluids have a shear-rate dependent viscosity $\eta(\dot{\gamma})$ and the flow curve is not a simple straight line passing through the origin. The fluid only flows above a critical stress $\tau_y$ called the critical stress. The simplest model capturing the existence of a finite yield stress is the Bingham model [145]:

$$\begin{aligned} \dot{\gamma} &= 0 \quad \text{if} \quad \tau < \tau_y \\ \tau &= \tau_y + \mu_p\dot{\gamma} \quad \text{if} \quad \tau > \tau_y \end{aligned} \tag{1.2}$$

where $\tau_y$ is the yield stress and $\mu_p$ is the plastic viscosity. In general, the Bingham model does not give a good fit to experimental data when fitted over more than two decades of shear rates but it is useful for modeling purposes due to its simplicity. A

popular generalization to the Bingham model is the Herschel-Bulkley model [146]:

$$\begin{aligned} \dot{\gamma} &= 0 \quad \text{if} \quad \tau < \tau_y \\ \tau &= \tau_y + K\dot{\gamma}^n \quad \text{if} \quad \tau > \tau_y \end{aligned} \tag{1.3}$$

where $\tau_y$ is the yield stress, $K$ is the consistency and $n$ is the flow index. For $n < 1$, the Herschel-Bulkley model allows for a shear-thinning behavior post-yield. Across a large number of viscoplastic fluids, the shear-thinning exponent $n$ is found to have a value in the range $n = 0.2 - 0.8$ [3]. The case $n = 1$ corresponds to the Bingham fluid described in Eq. 1.2 and can be seen as the simple case of a constant plastic viscosity post-yield. A useful non-dimensional number is the Bingham number, which is defined as the ratio of yield stress to the plastic flow stress [147]:

$$Bn = \tau_y / K\dot{\gamma}^n \tag{1.4}$$

The Bingham number gives some measure of the relative importance of the solid and liquid regions in the fluid. A schematic of representative flow curves for different viscoplastic models is shown in Fig. 1-12. We note that the Bingham and Herschel-Bulkley models do not distinguish between static and dynamic yield stress and more sophisticated models are sometimes needed to investigate these parameters [7, 148].

### 1.5.3 Wall slip in yield stress fluids

The flow behavior of yield stress fluids is often found to depend not only on their rheological bulk properties but also on the nature of the confining surfaces. The interaction of the fluid with the wall i.e. whether the material sticks or not, has a great importance on its flow behavior [7, 16, 149, 150]. In particular, the contact angle of the fluid on the surface has been shown to affect the slip behavior of a number of Newtonian fluids [151, 152]. Wall slip is ubiquitous in many viscoplastic fluids such as concentrated particulate suspensions [153, 154], flocculated suspensions [155, 156], colloidal gels [157, 158], suspensions of fillers in polymer matrices [159, 160],

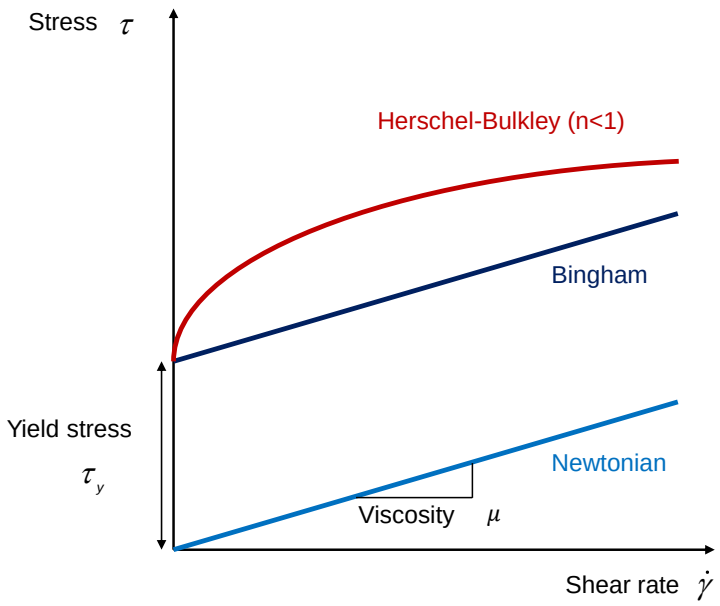


Figure 1-12: Schematic of representative flow curves for different viscoplastic models.

concentrated emulsions [161, 162], foams [163], microgel suspensions [12, 32, 164], and many other complex fluids [165, 166]. Due to the presence of a thin layer of solvent near the wall (wall depletion), the velocity and the local shear rate near the wall are much larger than in the bulk [149]. This flow can essentially be modeled as a velocity discontinuity between the fluid and the wall as shown in Fig. 1-13. This effect is dubbed "apparent" slip and is common in most yield stress materials.

In his review on slip, Barnes [149] discusses the use of a slip law to relate the velocity discontinuity at the wall-fluid interface $V_s$, to the shear stress within the fluid $\tau$. A general form for slip law is given by the following equation:

$$V_s = \beta(\tau - \tau_c)^n \tag{1.5}$$

where $V_s$ is the slip velocity, $\beta$ is the slip coefficient (with $\beta = 0$ corresponding to no slip) and $\tau_c$ is the critical stress for onset of slip. The case of $n = 1$ and $\tau_c = 0$ is the linear slip law often referred to as the Navier slip law. $V_s$ has been shown to display a nearly quadratic scaling, i.e. $n \simeq 2$ in the case of attractive/non-wetting

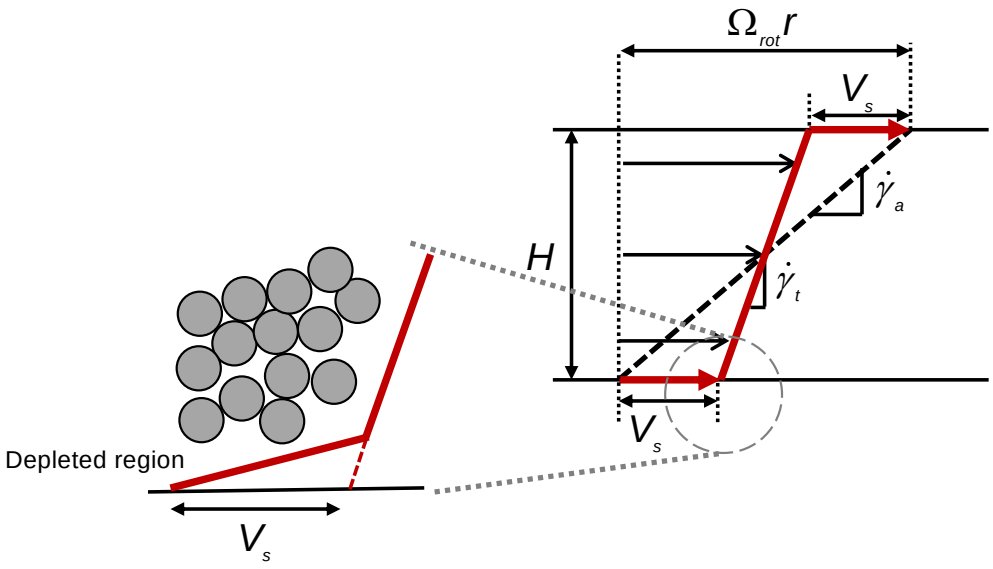


Figure 1-13: Wall slip in a plate-plate geometry at a radius $r$. Figure is adapted from Yoshimura & Prud'homme [139].

surfaces, whereas $n = 1$ has been found for repulsive and/or wetting walls as shown in Fig. 1-14(b) [3, 164, 167].

Wall slip has important consequences with respect to the rheological characterization, flow and processing of yield stress materials. A direct manifestation of wall slip in yield stress fluids is that a yield stress fluid can flow steadily (possibly as a plug), even if subjected to stresses lower than the yield stress as shown in Fig. 1-14(a) [7, 16]. This can have a large effect on the shape of the flow curves and the values of the yield stress could be underestimated if slip is not accurately taken into account. In general, the best way to minimize or eliminate wall slip is to use rough wall surfaces, with a roughness adapted to the sample microstructure or to use serrated plates [7, 32, 149, 168].

Common methods used to reveal the existence of wall slip include injecting a line of dye at the surface of the material [153, 157, 159], MRI imaging techniques [165, 169, 170], dynamic light scattering [171], ultrasonic velocimetry [172, 173], direct observation via PIV [12, 32, 174, 175], or confocal microscopy [176–179]. Yoshimura and Prud'homme [139] introduced useful rheometric techniques which can be used to

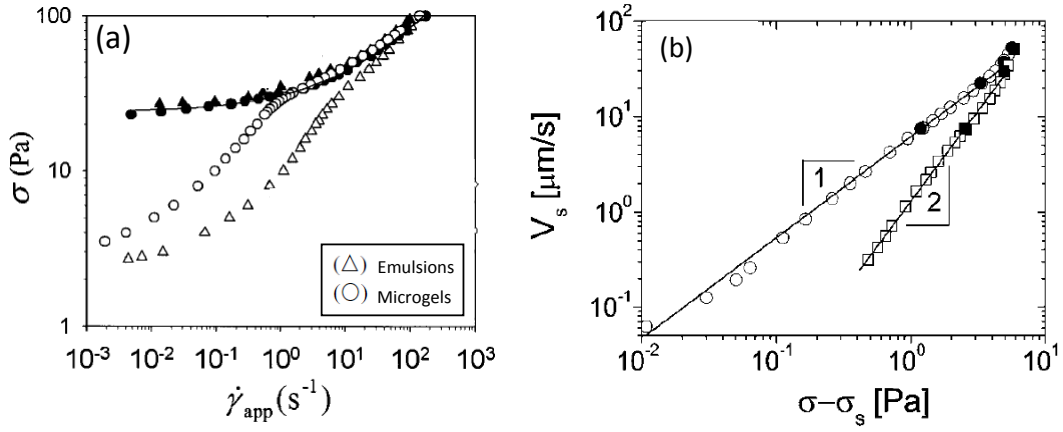


Figure 1-14: (a) Shear stress vs. the apparent shear rate for a microgel paste (circles) and an emulsion (triangles) of packing fraction $\phi \simeq 0.77$ obtained in a cone-and-plate device for smooth (open symbols) and rough (closed symbols) surfaces. Figure is adapted from [32]. (b) Slip velocity vs. the excess stress (defined as the difference between the stress and the critical stress for onset of slip) in a dense emulsion for stresses below the yield stress in a plate-plate geometry. The plates are either coated with a weakly adhering polymer surface (squares) or a non-adhering glass surface (circles). The wetting properties of the boundary conditions strongly impact the scaling of the slip velocity. Extracted from [167].

determine slip laws such as Eq. 1.5, without having to resort to direct measurements of the slip velocity [180]. In particular, assuming equal slip at both walls, they show that in a parallel-plate geometry the following kinematic relation can be derived for each value of the imposed rim shear stress $\tau_R$:

$$\dot{\gamma}_a(\tau_R) = \dot{\gamma}_t(\tau_R) + \frac{2V_s(\tau_R)}{H} \tag{1.6}$$

where $\dot{\gamma}_a(\tau_R) = \Omega_{rot}R/H$ and $\dot{\gamma}_t(\tau_R)$ are the apparent and true shear rates experienced by the fluid at the rim $r = R$ and associated with the stress $\tau_R$, $H$ is the gap between the plates and $V_s(\tau_R)$ is the slip velocity at the imposed stress $\tau_R$. Using Eq. 1.6 and measurements at multiple gaps, the true flow curve can be decoupled from the wall slip effects and the slip law can be derived. This method will be employed and discussed further in chapter 4.

# Chapter 2

# Rheological & Electrical Characterization of Electrorheological Fluids

## 2.1 Introduction

Electrorheological (ER) fluids are materials that exhibit a reversible change in rheological properties with the application of an external electric field [40]. They consist, typically, of a suspension of dielectric particles in an insulating carrier fluid. When an electric field is applied, the particles aggregate and align in the direction of the field, forming columns consisting of chains of particles, which cause the fluid to transition from a liquid-like to a soft solid-like state. This change in the fluid properties is very rapid (on the order of tens of milliseconds) and is reversible upon removal of the electric field. These features have made ER fluids promising candidates for use in a variety of hydraulic components and microfluidic devices including valves, clutches and dampers. Devices based on ER fluids can operate under three different modes: shear, flow and squeeze [62]. In shear mode, one of the electrodes is free to move in its plane, and common applications include clutches, brakes and dampers [69]. In flow mode, the electrodes are fixed and the pressure drop across the channel is

controlled using the electric field. Valves and dampers are typical applications in which ER fluids are used in flow mode [73–75]. In squeeze mode, the electrode gap is varied and the fluid is compressed in the wall-normal direction. Vibration control, shock absorbers and dampers are examples of application of ER fluids used in squeeze mode [62, 69]. For each mode of operation, the particle interaction and the particle structures that are formed affect the mechanical properties of the ER fluid; most notably its yield strength, thus an understanding of the microstructures that form is crucial to predicting the mechanical performance of devices utilizing ER fluids. In shear mode, shear-induced lamellar structures are known to form while in flow mode, the microstructure tends to contain clusters and aggregates [181–183]. In addition, an enhancement in the shear yield strength has been shown in magnetorheological fluids as the fluid is compressed in the direction orthogonal to shear [30] and a strengthening of the microstructure of ER fluids has also been shown in squeeze mode by Tian et al [184].

The rheological response of ER fluids under shear is traditionally modeled using a continuum approach with a Bingham plastic model, where the application of the field induces a field-dependent yield stress [73]. The rheological constitutive relation for the ER fluid is typically expressed as:

$$\begin{aligned} \dot{\gamma} &= 0 \quad \text{if} \quad \tau < \tau_y(E, \phi) \\ \tau &= \tau_y + \mu\dot{\gamma} \quad \text{if} \quad \tau > \tau_y(E, \phi) \end{aligned} \tag{2.1}$$

where $\tau$ is the shear stress, $\dot{\gamma}$ the shear rate, $\mu$ the plastic viscosity and $\tau_y(E, \phi)$ is the field-dependent yield stress, $E$ the electric field and $\phi$ the particle volume fraction. ER fluid applications, in both shear and flow modes, have been successfully modeled using Eq.2.1 and it has been demonstrated that experimental results align well with this model [185–187].

For regular yield stress fluids, knowledge of the rheological constitutive relation in one mode can be used to predict the flow performance in a different mode. However, recent studies [187–189] have indicated that there is a difference in the dynamic

response of ER fluids in shear and flow modes. Lee et al. [187] have compared the rheological properties of an ER fluid in both modes and observed that the Bingham yield stress is higher in flow mode. Nam et al. [189] have studied the dynamic response of an ER fluid in steady pressure-driven flow and found that the response in flow mode is dominated by a densification process, in which the competition between particle interaction and hydrodynamic forces on the incoming particles leads to cluster formation. On the other hand, in shear mode, they note that aggregation of chains into columns is the dominant process. This is in agreement with recent studies by Qian et al. [190] on structure evolution in channel flow of ER fluids.

In order to accurately model systems which utilize ER fluids, particularly ER valves, there is a need for a better understanding of how the yield-hardening behavior observed in channel flow, differs from the rheological response observed in shear mode. Yield-hardening in flow mode is dominated by a densification process, which in turn depends on the initial volume fraction of particles in the fluid. In general, understanding the effect of particle volume fraction on the response of ER fluids has proven to be challenging. For a given electric field, a linear dependence of the yield stress with increasing particle volume fraction has been observed [26, 38, 53]. However, at higher volume fractions, some report the presence of a maximum in the yield stress [26, 38] while others observe an exponential-like growth [53]. A first step to resolve this discrepancy is to perform a systematic study comparing the effects of the particle volume fraction on the response of the ER fluid in the two different flow modes.

In the present study, we take this first step by experimentally investigating the yielding properties of ER fluids with different particle volume fractions under both wall-driven flow and pressure-driven channel flow with a constant electric field. Values of Bingham yield stress are extracted from the data by regression to Eq.2.1 and a comparison between the fluid responses in these two modes can then be performed. Finally, we present a model that captures the experimentally observed dependence of the fluid rheology on particle volume fraction in shear, as well as a phenomenological model that rationalizes the densification process and consequent yield hardening

measured in channel flow. Our interest lies in using these densification models to predict the yield pressure of rapidly-actuated hydraulic devices such as ER valves from viscometric measurements performed on a torsional rheometer.

## 2.2 Materials and Methods

ER fluids with different particle volume fractions ($0 \leq \phi \leq 0.55$) were prepared from a stock solution of a commercially-available ER fluid (Fludicon, RheOil4). The stock solution has a particle volume fraction $\phi = 0.41$ and is made of a colloidal suspension of polyurethane (PUR) particles doped with $Li^+$ (mean diameter of $1.4 \pm 0.6$ $\mu$m) with silicone oil as a carrier fluid [191–193]. An SEM showing the morphology of the ER particles is shown in Fig. 2-1. This class of ER fluids containing polymer particles doped with salt and/or polar organic dopants have been shown to exhibit a low base viscosity and a relatively high yield stress while having low current density. In addition, they also show good sedimentation and re-dispersion properties, a short response time (1-10 ms) and long-term stability making them a promising candidate for practical applications using electrorheological fluids [185, 194]. Particle volume fractions lower than the stock solution were obtained by dilution with 100 cSt silicone oil while higher particle volume fractions were obtained by centrifuging the stock solution and removing a known volume of carrier fluid using a micropipette and then re-suspending the centrifugate using an ultrasonic bath.

The rheological response of the ER fluid under shear mode was measured using an AR1000N stress-controlled rotational rheometer, with a custom-made ER fixture which applies a uniform electric field between two aligned parallel plates. The connection to the rotating shaft is done through a salt solution that closes the electric circuit. Steady shear flow tests with decreasing shear rates varying from $4 \geq \dot{\gamma} \geq 0.1$ $s^{-1}$ were performed using a parallel-plate geometry with a gap of 300 $\mu$m. This procedure, analogous to that described by [195], has been shown to insure that a reproducible value of the dynamic yield stress is reached at steady-state for a similar class of materials. The maximum shear rate applied was chosen to be $\dot{\gamma} \leq 4s^{-1}$ to minimize formation of

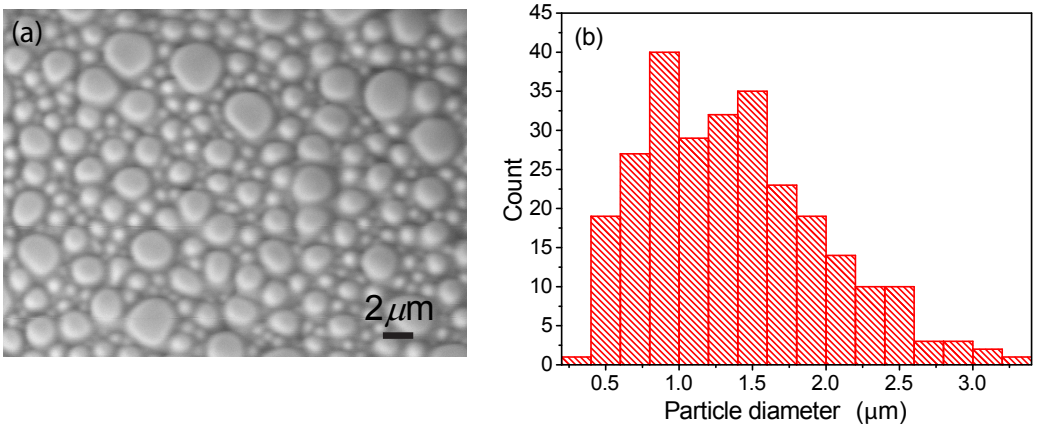


Figure 2-1: Morphology of Rheoil 4.0 ER particles. (a) SEM image showing the morphology of the polyurethane particles contained in the ER fluid. b) Histogram of particle size distribution in the ER fluid.

shear-induced lamellar structures during the steady shear flow tests that tend to be associated with a non-monotonic flow curve [181,182]. This insures that the ER fluid remained homogeneous during the steady shear flow tests and that modeling using the Bingham model (Eq.2.1) as well as comparison to flow data obtained from microchannels is applicable. The tests were performed at constant temperature $T = 22°\text{C}$ and constant particle volume fraction $\phi = 0.41$ with different electric fields as well as constant electric field $E = 3$ kV/mm for fluids with different particle volume fractions. The electric field $E = 3$ kV/mm was chosen because it is of particular interest in valve applications: This electric field is high enough for potential engineering applications and for dielectrophoretic effects to be negligible and low enough to avoid electrical breakdown if an air bubble passes through the microchannel.

To measure the rheological response under flow mode, a rectangular microchannel was fabricated [190], (shown in Fig.2-2). The microchannel consists of three regions: a test section with electrically conductive side walls through which the field is applied, and two auxiliary sections with non-conductive side walls at the inlet and outlet to minimize effects due to the curvature of the streamlines. The two electrode side walls are made out of a conductive copper film (250 $\mu$m thick, 10 mm long) and separated by a 250 $\mu$m gap. For the non-conductive walls, a polyether ether ketone film of

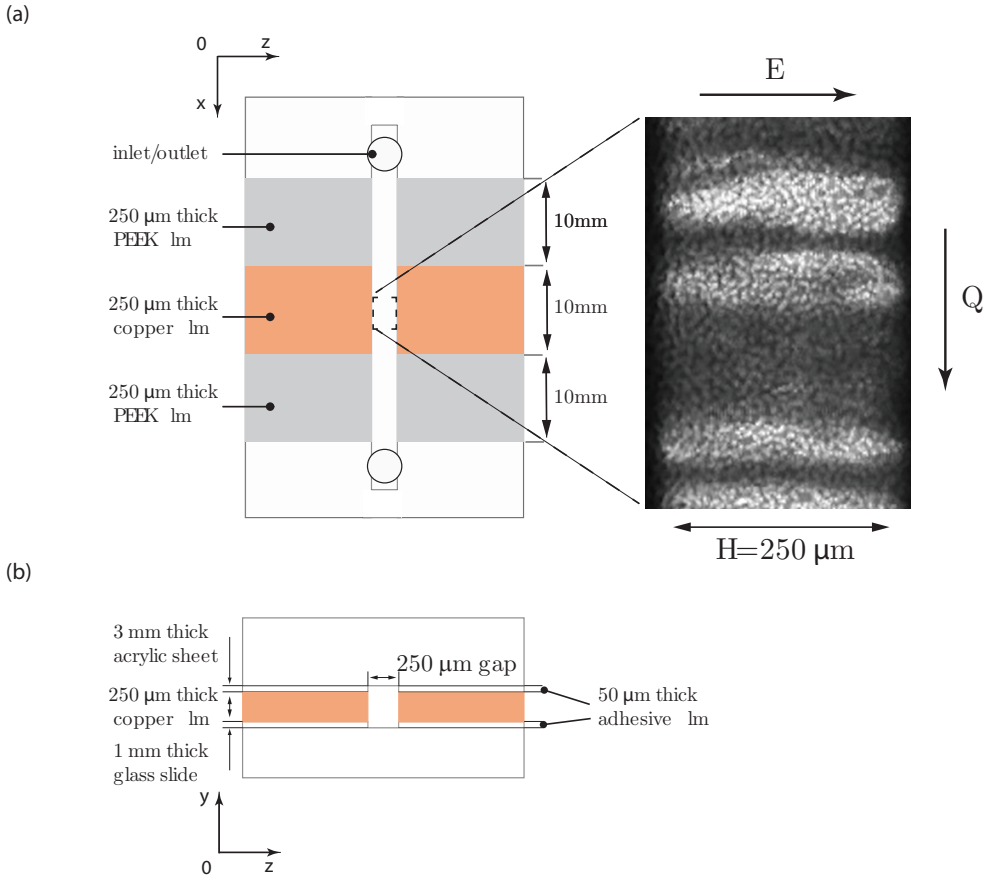


Figure 2-2: (a) Schematic of a microchannel fabricated for pressure measurements in flow mode. Also shown is a top view showing the microstructures that develop upon application of an electric field $E = 4$ kV/mm for $\phi_0 = 0.02$ (b) Cross-sectional view of the microchannel in the flow direction.

similar dimensions was used. To seal the microchannel, a 50 $\mu$m thick adhesive film (3M, 966) bonded the films to a 1 mm thick glass slide and a 3 mm thick acrylic sheet with tapped holes for the inlet and outlet adapters. The portion of the microchannel, over which an electric field can be applied, has the dimensions $L = 10$ mm, $W = 350$ $\mu$m, $h = 250$ $\mu$m. The conductive side walls were connected to a high voltage power supply (Stanford Research Systems PS350) via a driver circuit board. ER fluids were injected into the channel using a gas-tight glass syringe (Hamilton, 1005TLL) that was connected to the microchannel with stainless steel tubing (ID=1.6 mm). The flow rate $Q$, of the fluid was controlled by a syringe pump (Harvard Apparatus, PHD Ultra) and operated within the range of $30 \leq Q \leq 60$ $\mu$L/min. The pressure drop

between the entry and exit of the channel was measured using a differential pressure sensor (Honeywell, 26PCBFA6D) with a measurement range of $0 \leq \Delta P \leq 35$ kPa; the signal was amplified and acquired using a DAQ board (National Instrument, DAQ1200). In the microchannel, gravity plays a negligible role and the settling of the particles can be neglected. A lower bound on the characteristic time scale for settling is given by $t_{settling} \sim \mu h/(\rho_p - \rho_f)ga^2$ where $a$ is the average particle diameter and $\rho_p$, $\rho_f$ are the densities of the particles and the fluid respectively. We estimate $t_{settling} \sim 5000$ s, which is much larger than the time scales in our study and therefore, settling can be considered negligible.

## 2.3 Rheo-electric characterization: wall-driven flow

Flow curves of the measured shear stress vs. imposed shear rate curves, for the stock solution ($\phi = 0.41$) at different electric fields, obtained in shear mode are presented in Fig. 2-3 and the data was fit with the Bingham model (Eq. 2.1). We observe that in the absence of an electric field, the ER fluid behaves like a Newtonian fluid of viscosity $\mu = 31$ mPa.s. When an electric field is applied for $E \geq 1.5$ kV/mm , the ER fluid develops a field-dependent yield stress as shown in Fig. 2-3b. Fig. 2-4 shows the Bingham yield stress $\tau_y$ and leakage current density $j$ vs. the applied electric field $E$. We observe that the yield stress scales as $\tau_y \simeq E^{1.5}$ for $E \geq 2$ kV/mm, while the current density is found to be in good agreement ($R^2 = 0.98$) with a quadratic fit of the form $j = AE + BE^2$ for $A = (9.0 \pm 2.0)\ 10^{-13}$ mS/cm and $B = (7.9 \pm 1.2)\ 10^{-16}$ mS/kV. These scalings are in agreement with functional forms reported in the literature for various types of ER fluids [26, 27, 38, 56].

The flow curves for the solutions with different particle volume fractions at $E =$ 3 kV/mm, obtained in shear mode are presented in Fig.2-5. This data was fit with the Bingham model of Eq. 2.1. While some applications operate at high shear rates with an electric field applied (e.g. dampers and vibration control devices), for valve applications, our interest lies solely in the yield pressure of the valve and thus in the shear yield stress extracted from the Bingham model fit. For each volume fraction,

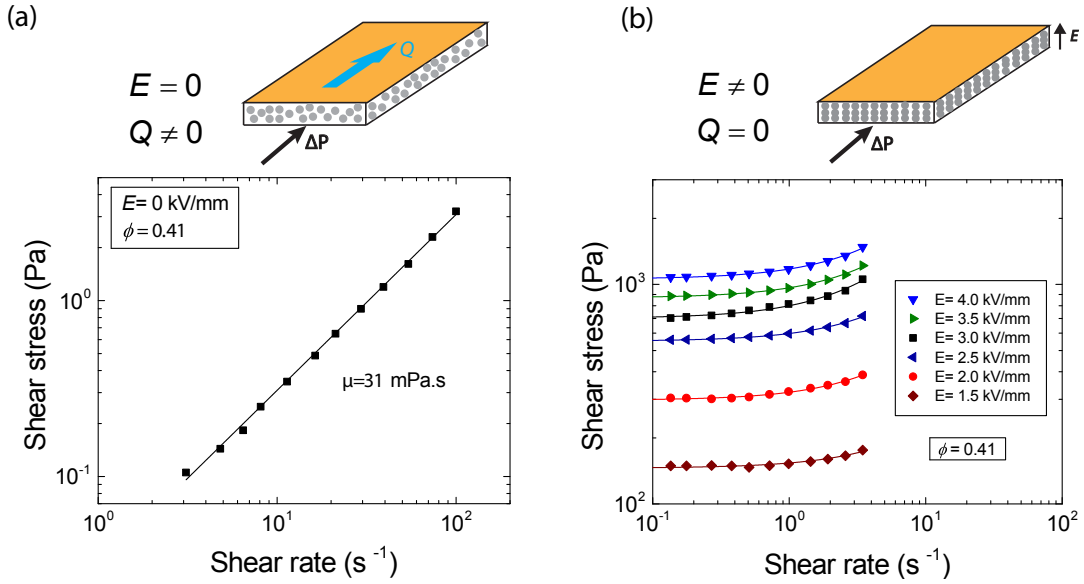


Figure 2-3: (a) Shear stress vs. shear rate curves for different electric fields obtained from steady shear flow tests on the AR1000N rheometer with a custom ER parallel plate fixture ($R = 20$ mm, $H = 0.3$ mm) for $\phi = 0.41$. The lines indicate fits of the data with the Bingham model [Eq. 2.1]. (a) Field off case ($E = 0$ kV/mm): The ER fluid is Newtonian and flows through the microchannel (b) Field on case ($E > 0$ kV/mm): The ER fluid has a field-dependent yield stress and flow can only occur in the microchannel if the applied pressure drop exceeds the yield pressure drop.

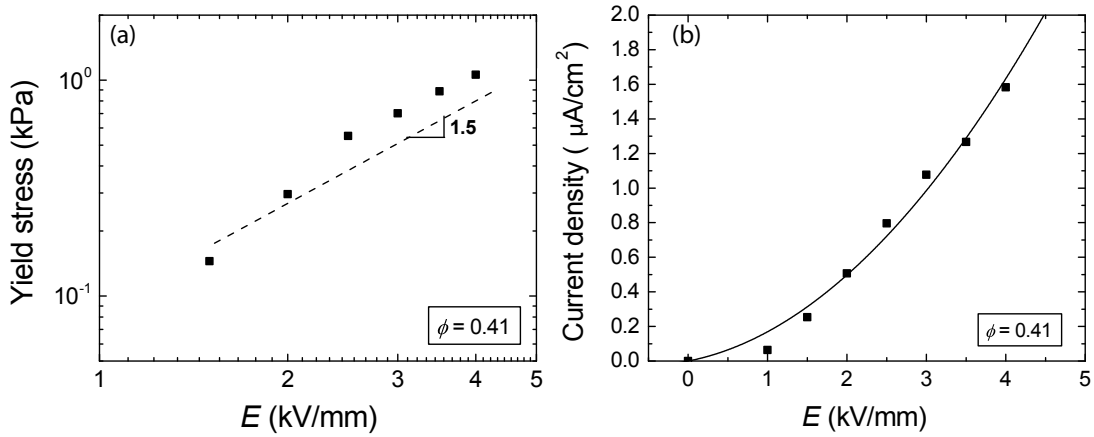


Figure 2-4: Bingham yield stress $\tau_y$ (a) and leakage current density $j$ (b) vs. applied electric field $E$ for Rheoil 4.0 at $T = 22°$C. The black solid line is a quadratic fit of the form $j = AE + BE^2$ to the current density data.

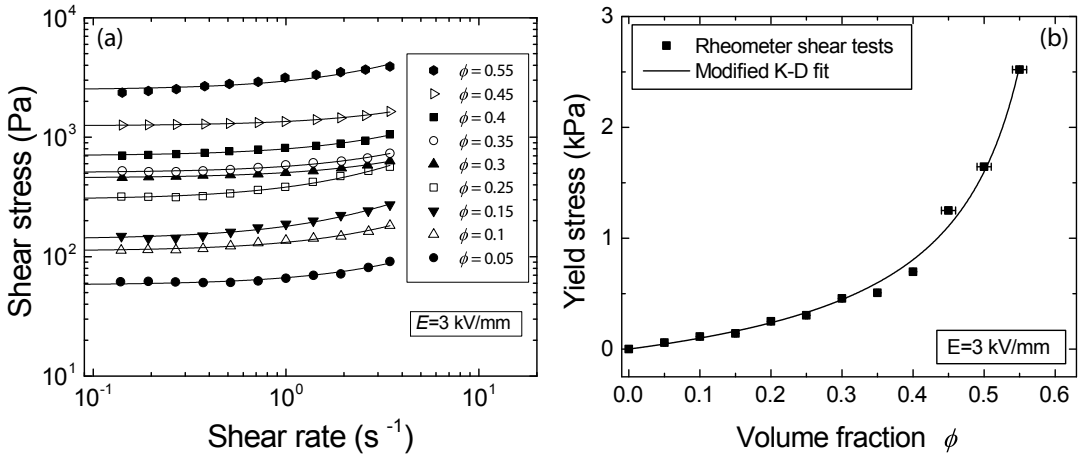


Figure 2-5: (a) Shear stress vs. shear rate curves for different particle volume fractions obtained from steady shear flow tests on the AR1000N rheometer with a custom ER parallel plate fixture ($R = 20$ mm, $H = 0.3$ mm) at $E = 3$ kV/mm. The lines indicate select fits of the data with the Bingham model [Eq. 2.1]. (b) Yield stress extracted from rheometry shear tests vs. the particle volume fraction $\phi$. The black solid line shows the fit of the modified Krieger-Dougherty model [Eq. 2.3] to the viscometric data.

the Bingham yield stress was extracted from the fit to be compared to the yield stress obtained from flow mode measurements. In steady shear, the yield stress is found to increase linearly with particle volume fraction at low volume fractions and then more rapidly at higher volume fractions.

Previous studies have shown that the yield stress of ER fluid in wall-driven shear flow exhibits a maximum [26,38], while others show a monotonic increase of the yield stress with volume fraction [196–198]. In our case, no maximum in yield stress was observed within the range of volume fractions studied. Based on the chain model, the influence of the particle volume fraction on the yield stress of ER fluids is often described using a power law or exponential model over the volume fractions studied [26,53,199]. These models fail to capture the effects observed here, namely a linear dependence at low volume fractions and a diverging behavior as the volume fraction approaches the maximum packing fraction (expected to be $\phi = 0.64$ for a random close packing of spherical monodisperse particles). The observed results are more akin to results obtained for concentrated suspensions of solid particles in yield stress flu-

ids. For such suspensions, the viscometric properties (viscosity, shear modulus, yield stress) are often modeled using an empirical Krieger-Dougherty model [8, 200, 201]:

$$\frac{\tau_y(\phi)}{\tau_0} = \left(1 - \frac{\phi}{\phi_m}\right)^{-K\phi_m} \tag{2.2}$$

where $K$ is a coefficient that quantifies the initial linear increase in yield stress at low volume fractions, $\tau_0$ is a characteristic yield stress and $\phi_m$ is the maximum packing fraction. $K$ is analogous to the Einstein coefficient or intrinsic viscosity when the shear viscosity of a suspension is fitted to this model. We propose to model the influence of the particle volume fraction on the yield stress of the ER fluid by using a modified form of this relationship to account for the absence of a yield stress when no particles are present ($\phi = 0$) :

$$\frac{\tau_y(\phi, E)}{\tau_0(E)} = \left[(1 - \frac{\phi}{\phi_m})^{-K\phi_m} - 1\right] \tag{2.3}$$

In this model, $\tau_0(E)$ is a characteristic field-dependent yield stress that reflects the strength of the attractive interaction between the particles. $K$ is expected to be independent of the electrical field $E$ for $E \geq 1.5$ kV/mm where dielectrophoretic effects are negligible. As the field $E$ increases, it is expected that the structures that form remain structurally similar while the strength of the attractive interaction increases, leading to an increase of $\tau_0(E)$. A fit of this model to the yield stress in shear vs. volume fraction curve is shown in Fig.2-5 and the coefficient of determination is found to be $R^2 = 0.98$ for $K = 1.23$ , $\tau_0(E = 3kV/mm) = 700$ Pa and $\phi_m$=0.63. A similar model was used by Mueller et al. [202] and Heymann et al. [203] to fit the yield stress of suspensions of solid spheres with $K\phi_m = 2$. We expect that this divergence from the case of solid suspensions is due to the fact that ER fluids are active materials that do not exhibit a yield stress in the absence of an electric field, but rather develop this property through the aggregation of particles into chains and columns [73, 189] and can form ordered lamellar structures upon the application of the electric field [181, 182].

## 2.4 Rheological characterization: pressure-driven flow

Fig. 2-6a shows a sample output for the pressure drop measured in a flow-mode experiment as a function of time at two different particle volume fractions ($\phi = 0.05, 0.4$) with an imposed flow rate $Q = 50$ $\mu$L/min. The observed curves all indicate an initial pressure rise followed by a series of oscillations. At the beginning of each test, the electric field is activated causing the ER fluid initially present in the microchannel to block the flow. As the syringe pump displaces the fluid, the effective "lumped" compressibility $\beta = \frac{-1}{V}\frac{\partial V}{\partial P}$ of the entire microfluidic system (consisting of the syringe, tubing, channel and fluid contained therein) comes into play and the pressure rises. For a given flow rate, the slope of the pressure rise is the same for different volume fractions and can be used to estimate this lumped compressibility $\beta$ of the system ($\Delta P = -1/\beta \ln(1 - Qt/V_0)$ where $V_0$ is the volume of the system, $\beta = 5$ MPa$^{-1}$). When the imposed pressure difference exceeds a critical value, the ER microstructure yields, enabling the ER suspension to flow, thereby resulting in a drop in pressure. Since the electric field is still present in the channel, at a second critical pressure, the flow is arrested once more and the compression cycle starts again, hence the observed oscillations. By averaging over a series of peaks, we obtain an average value of the yield pressure differential for the channel at each imposed mass flow rate. In the lubrication limit ($L \gg h, W$), the field-dependent pressure difference at yield $\Delta P_y(E, \phi)$ can be related to the Bingham yield stress using the following relation obtained via a global force balance on the system [137, 190]:

$$\Delta P_y(E, \phi) = \frac{2\tau_y L(h + W)}{hW} \tag{2.4}$$

where $L$ is the length of the channel over which the field is applied and $h$ is the gap between the electrodes. Using this relation, we can compute the Bingham yield stress $\tau_y(E, \phi)$ from the measured yield pressure for each flow rate and particle volume fraction.

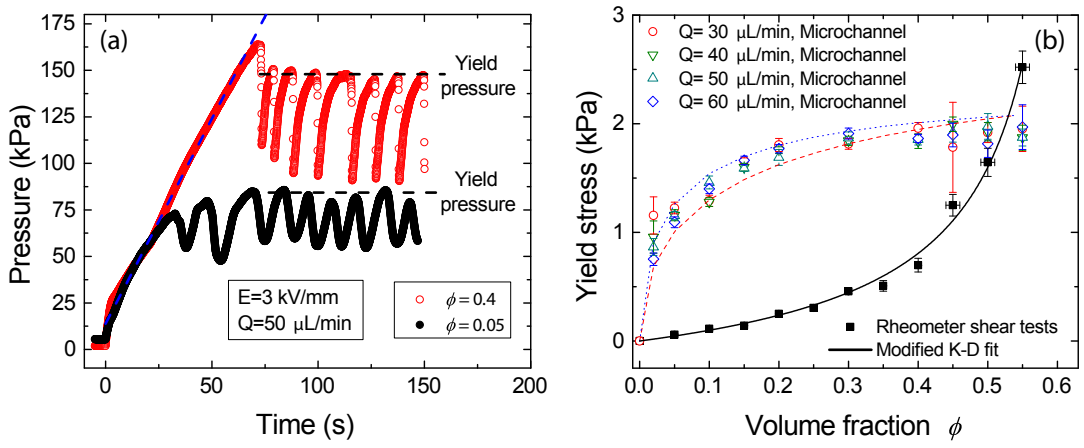


Figure 2-6: (a) Pressure drop across the microchannel for two different particle volume fractions ($\phi = 0.05, 0.4$) as a function of time for an electric field of $E = 3$ kV/mm and an imposed flow rate $Q = 50$ $\mu$L/min. The dashed lines represent the peaks of the curve which are averaged to determine the yield pressure of the ER valve at each applied field strength, volumetric flow rate and fluid volume fraction. The overall system compressibility $\beta$ estimated from the slope $[\Delta P = -1/\beta \ln(1 - Qt/V_0)]$ (blue dotted line) of the pressure rise is $\beta = 5$ MPa$^{-1}$. (b) Comparison of the yield stress extracted from the viscometric tests in the rheometer [Fig. 2-5] and from the yield pressure in the microchannel flow setup for flow rates $Q$ ranging from 30-60 $\mu$L/min as a function of the particle volume fraction for $E = 3$ kV/mm. The black solid line shows the fit of the modified Krieger-Dougherty model [Eq. 2.3] to the viscometric data. The red and blue dashed lines show the fit of the proposed model, obtained by combining Eq. 2.3 and Eq. 2.7, with the microchannel data for $Q = 30$ $\mu$L/min and $Q = 60$ $\mu$L/min respectively.

The yield stress data extracted from the tests in shear and flow modes are shown in Fig.2-6b as a function of the particle volume fraction. We observe that, for all the flow rates tested, the yield stress computed in flow mode is a weak function of the flow rate, but is consistently greater than the one extracted from the steady-shear experiments. In channel flow, we observe that after an initial increase the extracted yield stress reaches a plateau value above a composition of $\phi \approx 0.25$. This plateau intersects the yield curve obtained from shear tests at $\phi = 0.54 \pm 0.01$.

To rationalize these results, we note that in the steady shear experiments, the system is closed and the volume fraction of particles in the sample is fixed; whereas in channel flow, the system is open and new particles are continuously convected into the microchannel thus potentially increasing the local volume fraction if the fluid exiting the channel is depleted in particles. Since the yield strength of the ER fluid is determined by its microstructure, which in turn depends on the local volume fraction of particles, the higher value of yield stress observed in channel flow, and the saturation of the yield stress at higher volume fractions, are both consistent with an increase of the local volume fraction in the channel to a maximum value of $\phi_M \approx 0.54$. These results are consistent with the densification process described qualitatively by Nam et al. [189]. Light transmission measurements performed by Qian et al. [190] show cluster formation in pressure-driven flow and the formation of a compaction front at the entrance of the microchannel that is associated with an increase in volume fraction. In addition, images taken by Tang et al. [182] show that after densification, at sufficiently high pressures, fingers appear near the inlet as the material yields. This behavior is reminiscent of fluidization in jammed granular media [204] where compaction fronts and finger formation at sufficiently high pressures are known to occur. In granular systems where the interstitial fluid is compressible e.g. air, diffusive propagation of the overpressure can play a role in the compaction process. However, in our system the fluid is incompressible and such effects do not play a significant role in the dynamics of the system.

## 2.5 Importance of wall slip in wall-driven and pressure-driven flows

Yield stress fluids including ER fluids, particularly at high particle volume fractions, are prone to wall slip during viscometric and channel flow. To correct for slip in the parallel plate geometry on the rheometer, the protocol proposed by Yoshimura and Prud'homme was followed [139]. The sample was tested at two different gaps ($H = 0.5$ mm, 0.3 mm respectively) to probe and correct for slip effects. If the flow curves at different gaps superimpose, then the wall slip is negligble. If gap-dependent rheology is observed, a correction needs to be applied to extract the true shear rate applied on the sample at each value of the applied stress. The flow curves for $\phi = 0.41$ and $E = 3$ kV/mm at two different gaps are shown in Fig.2-7a and show that wall slip plays a negligible role in the steady shear flow tests performed on the rheometer. For the corresponding case of pressure-driven channel flow, a supporting video (Fig.2-7b) demonstrates the absence of slip at the walls for a low volume fraction fluid ($\phi = 0.02$) at an applied field of $E = 4$ kV/mm and an imposed flow rate $Q = 30$ $\mu$L/min.

## 2.6 Modeling the yield hardening in pressure-driven flow

### 2.6.1 Modeling approach

As discussed, ER fluid flow in a channel is characterized by a densification process that is manifested as an increase in the local volume fraction of particles in the channel and in the overall pressure differential. Unlike wall-driven flow, the measured yield function is not a material property of the fluid but rather a complex function of the fluid and channel properties. Consider an ER fluid of initial volume fraction $\phi_0$ that is pumped at a constant flow rate $Q$ into an ER valve that is activated with a constant transverse electric field $E$. Due to the electrostatic interactions, stable microstructures are formed in the channel through chaining and aggregation of particles. Eventually,

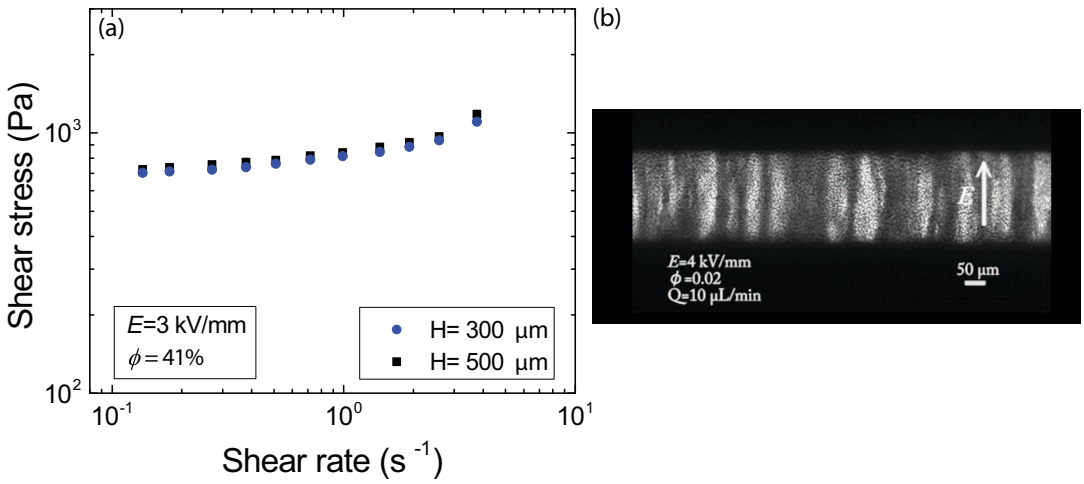


Figure 2-7: (a) Shear stress vs. shear rate curves for different rheometer gaps obtained from steady shear flow tests on the AR1000N rheometer with a custom ER parallel plate fixture ($R = 20$ mm) for $\phi = 0.41$ and $E = 3$ kV/mm. The flow curves obtained at different gaps superimpose showing that wall slip plays a negligible role in the steady shear flow tests performed on the rheometer. (b) Video 1 taken using the imaging setup described by Qian et al [190]) demonstrating the absence of slip at the walls for a low volume fraction fluid ($\phi = 0.02$) at an applied of field of $E = 4$ kV/mm and an imposed flow rate $Q = 30$ $\mu$L/min.

these particulate chains may span the channel width and then become immobilized in the channel while the suspending solvent continues to flow out of the channel exit. The evolution of the structures formed during flow, and thus the particle volume fraction in the channel, is a complex function of $\phi_0$, $Q$ and $E$.

We characterize the structures formed in the ER channel using the concept of hydraulic permeability $\kappa$ which must satisfy the following conditions as shown in Fig. 2-8. First, at large flow rates $Q \to \infty$ or small initial volume fraction $\phi_0 \to 0$ , all structures are unstable as the hydrodynamic forces acting on the chains dominate over the electrostatic forces. We expect no particles to be retained in the channel and thus a flow mobility $M_0 = \frac{QL}{Wh\Delta P}$ that is given by standard equations for viscous flow in a channel. Under the lubrication approximation $W \gg h$, $M_0 = \frac{h^2}{12\mu}$ where $h$ is the electrode thickness (which forms the channel separation), $W$ the width of the channel and $\mu$ the viscosity of the fluid. The flow mobility can be related to an effective permeability $\kappa_0$ via the Darcy equation for flow in porous media and we

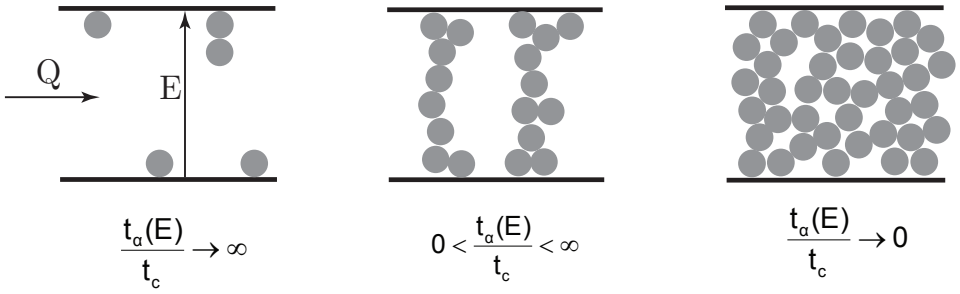


Figure 2-8: Schematic of the chained microstructures built in the channel as a function of the non-dimensional ratio of the aggregation time $t_\alpha(E)$ to the convective time $t_c(Q, \phi_0) = \frac{LA}{Q}\frac{(\phi_M - \phi_0)}{\phi_0}$. As the ratio $\frac{t_\alpha(E)}{t_c(Q,\phi_0)}$ gets smaller, the residence time in the channel becomes longer, there is less frustration and the structures can anneal to a higher packing fraction $\phi_M$.

can define the permeability in this limit as $\kappa_0 = M_0\mu$. Second, in the limit $Q \to 0$, hydrodynamic forces are small and the particles reach a maximum packing volume fraction $\phi_M$ and the chained microstructure that is formed by the ER suspension has a permeability $\kappa_M$. We note that the structure formed under dynamic flow conditions may be trapped at a maximum packing volume fraction $\phi_M$ that is lower than the maximum possible packing fraction reached under static conditions $\phi_m$. These conditions are in agreement with the experimental observations of Tang et al. [182] and Nam et al [189] that show that cluster size observed in channel flow decreases with the imposed flow rate. The existence of several time scales in the evolution of the structure of ER fluids has been shown in previous reports [182, 189, 190, 205, 206]: a short time scale related to the aggregation of particles into chains and a longer time scale associated with cluster formation. Following the work by Qian et al. [190], the electric field sets a time scale for aggregation $t_\alpha(E)$ while the structure formation is governed by the ratio of the convective time scale for the flowing suspension $t_c$ to the aggregation time scale $t_\alpha(E)$. The convective time scale $t_c(Q, \phi_0)$ is given by $t_c(Q, \phi_0) = \frac{LA}{Q}\frac{(\phi_M - \phi_0)}{\phi_0}$ and represents the time needed to fill a channel of length $L$ and cross-section $A$ to the maximum volume fraction $\phi_M$ when starting from an initial volume fraction $\phi_0$.

We propose the following permeability function $\kappa_s$ that defines the overall mi-

crostructure formed within the channel.

$$\kappa_s = \kappa_M + (\kappa_0 - \kappa_M)(1 - e^{-\frac{t_\alpha(E)}{t_c(Q,\phi_0)}}) \tag{2.5}$$

This function satisfies the experimental observations described above and physically corresponds to the fact that under "fast" flow rates or small initial volume fractions, the structure formed will be more permeable than at "slow" flow rates. As the flow rate is reduced, the suspended particles have more time to rearrange and reach the maximum packing fraction $\phi_M$ without getting trapped in a frustrated or jammed state at a lower volume fraction. An analogous functional form was proposed by Nakano et al. [188] to model the dependence of the pressure drop for flow of ER fluids in a rectangular channel on the flow rate, and shown to agree with their experimental results.

To relate permeability and average volume fraction in the channel at any given time, we use the simple relation proposed by Qian et al. [190]

$$\kappa = \kappa_0(1 - \phi)^n \tag{2.6}$$

where $\phi$ is the average volume fraction in the channel and $n$ is an empirical parameter found to be $n = 6$ by Qian et al [190]. This functional form is chosen because it was shown experimentally using optical transmissivity measurements that it provides a good approximation to the evolution of the permeability in an ER channel. In addition, it is readily invertible thus providing an exact expression for the average volume fraction of particles in the channel for a given permeability. A more in depth discussion, comparing permeability models from the literature and this model, is provided in section 2.6.2. Combining equations 2.5 and 2.6, we can compute the average volume $\phi_s$ fraction of the assembled microstructures built in the channel during shear flow :

$$\phi_s(E, Q, \phi_0) = 1 - \left[\frac{\kappa_M}{\kappa_0} + \left(1 - \frac{\kappa_M}{\kappa_0}\right)\left(1 - e^{-\frac{t_\alpha(E)}{t_c(Q,\phi_0)}}\right)\right]^{\frac{1}{n}} \tag{2.7}$$

By combining Eq. 2.3 and Eq. 2.7, the yield stress of the permeable microstructure that assembles in the channel is then given by $\tau_y(\phi_s)$ where $\tau_y(\phi)$ is the material function that was measured independently under wall-driven shear flow in the rheometer and discussed earlier in Eq. 2.3.

Fig. 2-6b shows the experimental data and the model predictions of the yield stress in our channel geometry, obtained by combining Eq. 2.3 and Eq. 2.7, for $t_\alpha(E) = 3.5$ ms and a maximum packing fraction $\phi_M = 0.54$ for two different flow rates: 30 and 60 $\mu$L/min. The model demonstrates the ability to capture the experimental observation discussed earlier for ER fluids in pressure-driven microchannel flow: a sharp increase of the yield stress at low initial volume fractions, followed by saturation at high initial volume fractions and a weak dependence of the measured results on the flow rate. The fitted value found for the aggregation time scale $t_\alpha(E) = 3.5$ ms is within the range reported in the literature for electrorheological fluids [26, 74, 185, 189]. The analysis performed does not depend sensitively on the choice of the permeability model, provided the permeability of the chained microstructure in the channel is a monotonically decreasing function of particle volume fraction (as would be expected). This simple two-parameter phenomenological model, thus offers a simple, yet rich, physical mechanism to model the yield hardening observed in channel flow. Previous work has focused on showing that each mode of shear has to be characterized separately experimentally to model the performance of ER fluids in devices of interest. Using our model and the physical understanding of the densification that occurs in channel flow, we have demonstrated that we are able to model and predict the rheological performance in channel flow using an independent characterization of the dependence of the yield stress on particle volume fraction performed in wall-driven flow (Eq. 2.3). This allows us to reconcile the discrepancies observed in the two modes of flow.

### 2.6.2 Influence of the choice of the permeability model

In this section, we discuss the sensitivity of our densification model to the choice of the permeability model. As suspended particles flow into the channel, chain-like

microstructures are built dynamically, first forming chains then coarsening them [26, 38]. Due to the complex dynamic nature of this process, it is difficult to make a comparison to traditional permeability models in porous media that are based on a pre-exisiting static structure. Nonetheless, we compare in this section the model used by Qian et al. [190] to permeability models from the porous media literature that characterize flow past an array of cylinders [26, 190]. Despite the fact that in our system, a wide range of different column sizes will form during flow and assembly, we will make the comparison of our chosen model [190] to models with an array of columns of fixed diameter $d$ (Ergun [207] and Tamayol et al. [208]). Physically, this would correspond to approximating flow in the channels to flow through the largest pores/structures in our structures that would have an average diameter size on the order of $d$.

The total hydraulic resistance in a microfluidic channel partially filled with ER particles can be modeled as the open channel and the chained microstructures in series and thus the overall permeability is given by $\kappa = \frac{\kappa_p \kappa_0}{\kappa_p + \kappa_0}$ where $\kappa_0$ is the open channel permeability and $\kappa_p$ the permeability of the static microstructure.

The expressions for $\kappa_p$ for the different models are given below:

$$\kappa_{p,Ergun} = \frac{d^2}{150} \frac{(1-\phi)^3}{\phi^2} \tag{2.8}$$

$$\kappa_{p,Tamayol} = 0.16 \alpha d^2 \frac{(1 - \sqrt{\frac{\phi}{\alpha}})^3}{\phi \sqrt{1-\phi}} \tag{2.9}$$

where $\alpha = \frac{\pi}{4}$ for a square packing of cylinders and $\alpha = \frac{\pi}{2\sqrt{3}}$ for a hexagonal packing. We note that the model proposed by Ergun et al. [207] has the same functional dependence on volume fraction as the Carman-Kozeny classical relation for a random packing of spheres [209, 210].

We compare the overall permeability given by these models to the simple expression given by Qian et al. [190] $\kappa = \kappa_0 (1-\phi)^n$ where $\kappa_0$ is the open channel permeability ($\kappa_0 = 4.510^2$ $\mu$m$^2$) and $n$ is an empirical parameter found to be $n = 6$. As shown in Fig. 2-9, the permeability predicted by the different models is in good

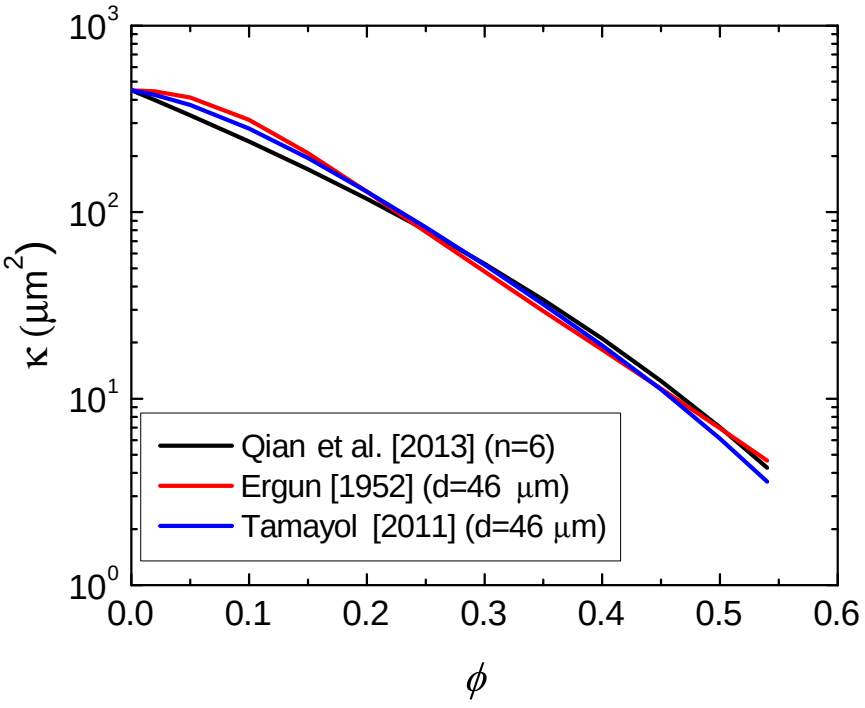


Figure 2-9: Comparison of the overall system permeability $\kappa$ predicted by Qian et al. with $\kappa_0 = 4.5\ 10^2\ \mu\text{m}^2$ and $n$=6, Ergun and Tamayol et al. For $d = 46\ \mu$m, the permeability is predicted to be very similar for all three models.

agreement for an average column diameter $d = 46\ \mu$m. This size is reasonable for the typical length scale of the structures in the channel as the particles (with an average diameter of 2.5 $\mu$m) are convected into the channel and jam dynamically under flow.

## 2.7 Conclusions

In summary, when designing devices using active suspensions such as electrorheological or magnetorheological fluids in flow mode, the phenomenon of yield hardening must be considered. Specifically, the local densification in the suspension microstructure reported here, must be taken into account in systems modeling, since it controls the magnitude of the yield pressure in the device. In the present work, we have shown that the complex interdependencies between the electrostatic interactions, the hydrodynamic forces and the channel geometry can be modeled by understanding the ratio

of the particle aggregation time scale to the convective flow time scale and linked to the permeability of the chained microstructures that assemble in the channel, when a transverse electric field is applied to the flow. The understanding of flow-induced densification and saturation is important in optimizing parameters such as channel length and switching time in ER-fluidic valve design. With the physical understanding of the densification that occurs in channel flow, we can model and predict the performance in channel flow using a characterization of the dependence of the yield stress on particle volume fraction performed in wall-driven flow, thus allowing us to reconcile the discrepancies observed in the two modes of flow.

# Chapter 3

# Design of Electrorheological Valves

## 3.1 Introduction

Due to their reversible viscoplastic behavior discussed previously, ER fluids are considered as smart "auto-valving" fluids and are promising for applications requiring small valves [108–114]. By leveraging advances in PCB and MEMs technology, scaling down electrical circuits is straightforward. Composed of a pair of electrodes and an insulating spacer as shown in Fig. 3-1(a), ER valves form a mechanically simple system with no moving parts. By making use of PCB technology and commercial off the shelf hardware, they are easy and inexpensive to fabricate. The system requires the use of high electric fields ($E > 1$ kV/mm) but uses very low current ($I \simeq$ 1-10 $\mu$A) and therefore consumes little power (on the order of a few mW). Finally, the electric field provides a means to control the system with fast switching times thanks to the fast response time of ER fluids ($\delta t_{ER} \sim 10$ ms). These features make ER valves a promising low-cost technology for small-scale hydraulic robots compared to existing hydraulic valves.

Despite the demonstration of the feasibility of ER valves and their impact as well as a large body of literature on the subject [72, 75, 108, 111, 112, 211–217], the use of ER valves in small robotic applications remains limited. A systematic analysis of the design space of ER valves and the effect of the various design parameters on their performance remains lacking. In this chapter, we define performance metrics for ER

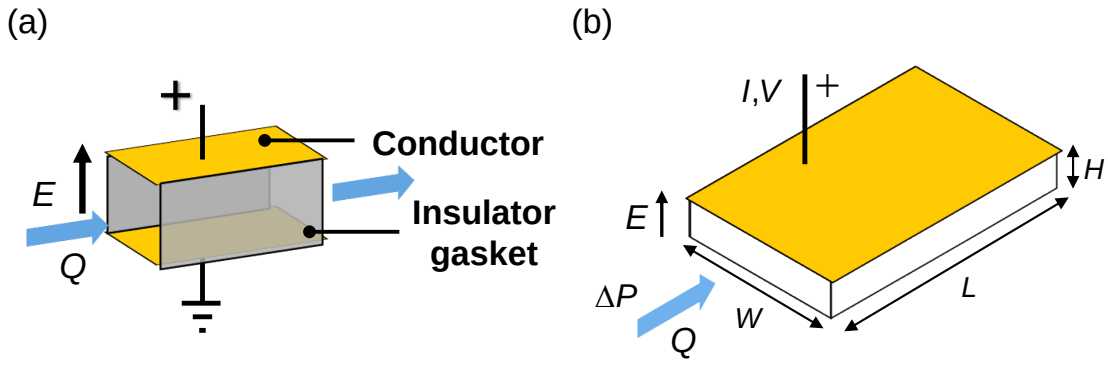


Figure 3-1: (a) Schematic of the design of an ER valve. The design is composed of a microchannel with two conductive sides and an insulating gasket in between. (b) Schematic of an ER defining the relevant parameters affecting the valve performance.

valves and investigate the effects of the electric field, geometry of the valve and the electrode surface roughness on the valve performance. This study aims at providing design rules for ER valves to guide the design of ER valve prototypes given a desired application. Finally, we discuss the application of ER valves to robotic applications and showcase prototypes developed by Boston Dynamics using ER valve technology.

## 3.2 Performance metrics for ER valves

In this section, we define two performance metrics for ER valve and discuss their dependence on the valve design parameters. ER valves can be fabricated in a concentric cylindrical [108–110, 218] or rectangular geometry [74, 79, 108, 114, 188]. We focus on a rectangular channel design to leverage existing PCB and MEMs manufacturing technology in fabricating small valves for robotic applications. The geometry of the valve and the parameters that define it are described in Fig. 3-1(b). Of interest to our study are the following parameters: the length of the channel $L$, its aspect ratio $\Psi = W/H$, the surface roughness of the electrode $R_q$, the electric field $E = \mathcal{V}/H$, the current density $j = I/WL$, the applied pressure drop $\Delta P$ and the volumetric flow rate across the valve $Q$.

We define two states for the ER valve: an "off" state in which the field $E$ is

turned off and the fluid flow through the valve is Newtonian and an "on" state in which the field $E$ is applied and there is no flow through the valve ($Q = 0$). We assume Bingham rheology for the fluid with a field-dependent yield stress $\tau_y(E)$ as described in Eq. 2.1. The first performance metric of interest for ER valves is the holding pressure drop per unit length $\Delta P_y/L$ in conjunction with the device length $L$. This defines the maximum pressure the valve can hold before yielding and therefore sets the system pressure used in the desired applications.

In the on state, the balance of forces on an element of fluid in the channel at the yield point gives

$$2\tau_y(E)L(H+W) = \Delta P_y HW \tag{3.1}$$

which yields the holding pressure per unit length of the valve for an applied field $E$

$$\boxed{\frac{\Delta P_y}{L} = \frac{2\tau_y(E)}{D_H}} \tag{3.2}$$

where $D_H = WH/(W+H)$ is the hydraulic diameter. Eq. 3.2 shows that the holding pressure of the valve is expected to scale linearly with the yield stress, therefore as $E^{1.5}$. We also observe that the holding pressure scales as the inverse of the hydraulic diameter $D_H$, therefore for a fixed electrode gap $H$, the holding pressure drop per unit length scales as $\frac{\Delta P}{L} \sim \left(1 + \frac{1}{\Psi}\right)$. This analysis shows that low aspect ratio channels ($\Psi \ll 1$) are preferable to achieve higher holding pressures in the valve. However, as the aspect ratio $\Psi$ decreases, we expect that the viscous dissipation in the off state will increase and the valve will have high viscous losses.

This leads us to define the second performance metric for ER valves: the power efficiency $\eta_W$ defined as

$$\eta_W \equiv \frac{\dot{W}_{Mech}^{max}}{\dot{W}_{Mech}^{max} + \dot{W}_{Elec}} \tag{3.3}$$

where $\dot{W}_{Mech}^{max}$ is the maximum mechanical power that can be extracted from the valve and $\dot{W}_{Elec}$ is the electric power needed to turn the valve on or off. The power efficiency represents a ratio of the max mechanical power gained from the valve to the overall power of the valve represented by the sum of the mechanical and electric

contributions. In the off state, the flow through the valve is Newtonian and can be modeled using Eq. 3.4 assuming lubrication conditions ($L \gg W, H$). The flow rate $Q$ in the off state is given by:

$$Q = \frac{WHD_H^2}{12\mu}\frac{\Delta P}{L} \tag{3.4}$$

where $D_H$ is the hydraulic diameter, $\mu$ the viscosity of the fluid in the off state and $\Delta P$ the pressure drop across the valve.

The mechanical power of the valve is defined as $\dot{W}_{Mech} = \Delta P * Q(\Delta P)$ where $\Delta P$ is the pressure drop across the valve and $Q(\Delta P)$ is the flow rate through the valve at that pressure drop. Assuming the system pressure (maximum pressure available in the system) to be equal to the holding pressure of the valve $P_{sys} = \Delta P_y$, the pressure in the valve can therefore be varied from 0 to $\Delta P_y$ and the flow rate $Q$ can varied from 0 to $Q_{max} = Q(\Delta P_y)$. As shown in Fig. 3-2, the mechanical power of the valve (black line) reaches a maximum for $\Delta P = \Delta P_y/2$ and $Q = Q(\Delta P_y)/2$ and we obtain

$$\dot{W}_{Mech}^{max} = \frac{\Delta P_y * Q(\Delta P_y)}{4} = \frac{\tau_y(E)^2 WHL}{12\mu} \tag{3.5}$$

.

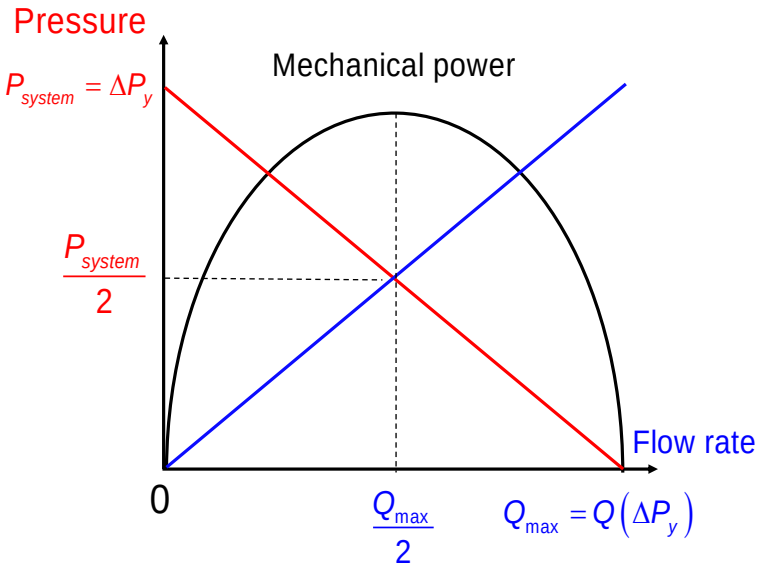


Figure 3-2: Definition of the system mechanical power. The peak mechanical power that can be extracted from the valve is $P_{system} * Q_{max}/4$.

The electrical power needed to activate the valve is the sum of the electric losses in the ER fluid and the static losses in the other static components of the valve (e.g leakage current in the gasket) and is given by

$$\dot{W}_{Elec} = I\mathcal{V} = \dot{W}_{elec}^{static}(E) + Ej(E)LWH \tag{3.6}$$

where $\mathcal{V}$ is the imposed voltage, $I$ is the current measured in the valve, $j(E)$ is the current density and $\dot{W}_{elec}^{static}(E)$ are the parasitic static electrical losses in the valve components outside of the fluid.

The power efficiency of the valve is then given by

$$\eta_W = \frac{\Psi}{\Psi\left(1 + \frac{Ej(E)12\mu}{\tau_y(E)^2}\right) + \frac{\dot{W}_{elec}^{static}(E)12\mu}{LH^2\tau_y(E)^2}} \tag{3.7}$$

and we observe that as the aspect ratio $\Psi = W/H$ increases, the power efficiency of the valve increases. Consequently, there is a trade-off in terms of aspect ratio between designing an efficient valve and one that has a large holding pressure. We also note that the static electrical losses can significantly affect the power efficiency of the valve and careful design to minimize these losses is recommended.

## 3.3 Valve prototype design and testing

In this section, we discuss the design of rapid valve prototypes to experimentally characterize the effect of design parameters on the two performance metrics described in section 3.2. We also aim to validate the conclusions on the effect of the aspect ratio on the valve performance discussed in section 3.2.

A CAD drawing of the valve design is shown in Fig. 3-3(a). Conductive copper tape (McMaster, 0.001" thick, $R_q = 0.2$ $\mu$m) is used for the electrodes of the valve. Rubber polyurethane gasket (Mcmaster, 0.02" thick) is used to seal the channel and avoid leaks during operation of the valve. A plastic shim (thickness 0.02") allows precise control of the electrode as the valve is sealed to avoid errors on the field

imposed. The channel is made out of acrylic and all parts (acrylic, gasket, plastic shim) are laser-cut to the specified dimensions therefore allowing for rapid prototyping and quick sweep of the design parameter space. The valve is assembled using bolts that allow the valve to operate at high pressures without leakage. A picture of an assembled valve is shown in Fig. 3-3(b). For this study, the electrode gap was fixed at $H = 0.5$ mm and the length of the channel was chosen to be $L = 20$ mm. The width of the channel $W$ was varied between 0.7 mm $\leq W \leq$ 8 mm, therefore varying the aspect ratio $\Psi$ between $1.4 \leq \Psi \leq 16$. A commercially-available ER fluid (Fludicon, RheOil4) described in section 2.2 was used to operate the ER valves.

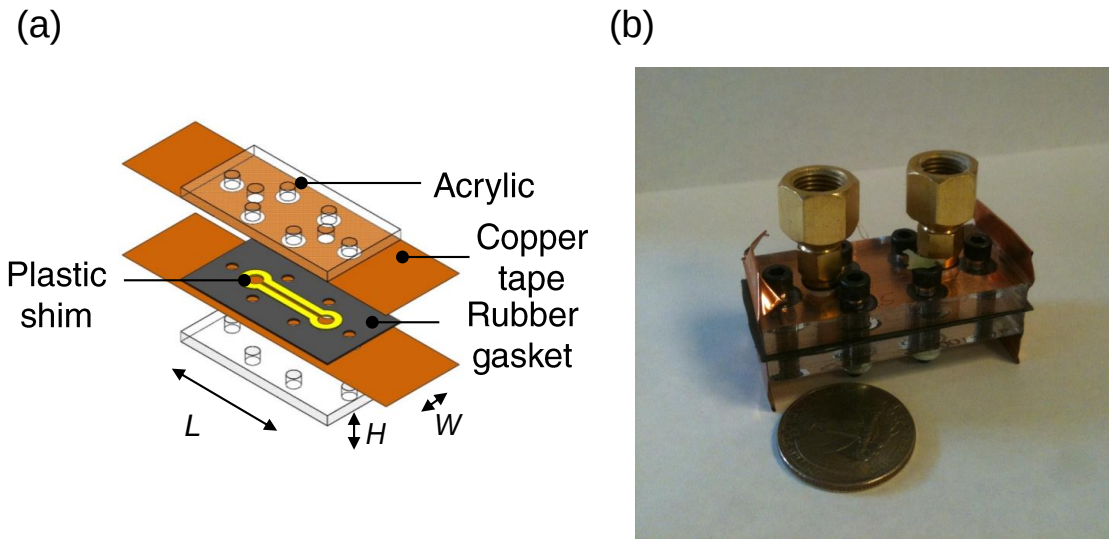


Figure 3-3: (a) CAD of the prototype of the modular ER valves allowing straightforward modification of the design parameters. The plastic shim allows for precise control of the electrode gap. (b) Picture of an assembled ER valve next to a quarter.

The conductive copper electrodes were connected to a high voltage power supply (Stanford Research Systems PS350) and the voltage $\mathcal{V}$ was controlled using a DAQ that also measured the current $I$ needed to operate the valves. The setup used to test the valves uses pressurized air to apply pressure across the valves. Pressure sensors were connected to each end of the valve and used to measure the pressure difference applied across the valve. A gear flow rate meter (G004, Max Machinery Inc) with a minimum resolution of 0.5 cc/min was used to measure the flow rate through the

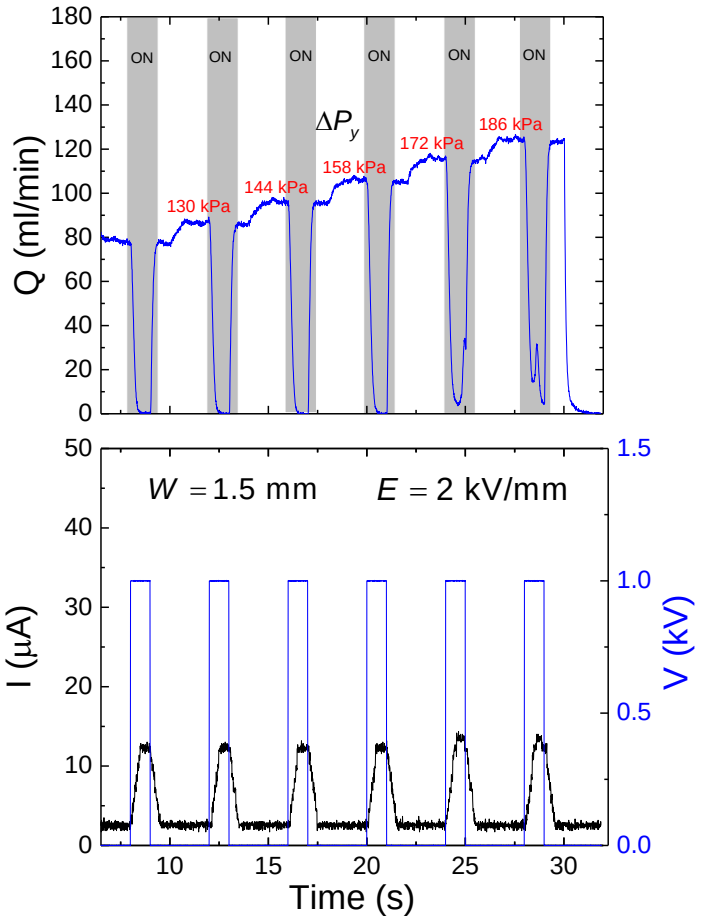


Figure 3-4: Typical output from the valve testing setup for a valve with $H = 0.5$ mm, $W = 1.5$ mm and $L = 20$ mm. For each pressure drop $\Delta P$ imposed across the valve, the flow rate $Q$ is measured for 6 s with $E = 0$ kV/mm. The field is then turned on and the flow rate $Q$ and current $I$ are measured. The valve is considered closed if $Q = 0$ ml/min within 0.5 s of the switching of the field. The holding pressure drop $\Delta P_y$ is the last pressure drop for which the valve remained closed and did not yield.

valve. For a given applied pressure difference, the flow rate $Q$ was measured for 6 s with the field turned off. This duration was found to be sufficient for the flow rate to reach steady state. The field $E$ is then turned on and the flow rate and current are measured. The valve is considered closed if the flow rate drops to zero within 0.5 s of the switching of the field, implying the valve did not yield. If the valve did not yield, the applied pressure is ramped up and the protocol is repeated until the valve yields. The holding pressure drop $\Delta P_y$ is then defined as the last pressure drop for which the valve remained closed and did not yield. The measured flow rate in the off state at the holding pressure differential allows us to define the max mechanical power of the valve given by $\dot{W}_{Mech}^{max} = Q(\Delta P_y) * \Delta P_y/4$. The electrical power consumed by the valve is given by $\dot{W}_{Elec} = I\mathcal{V}$. An example of a typical output from the valve testing setup is shown in Fig. 3-4. Using this setup, we seek to explore the effect of the electric field $E$, the valve aspect ratio $\Psi = W/H$ and the electrode surface roughness on the two performance metrics of interest: the holding pressure drop per unit length and the power efficiency of the valve.

## 3.4 Effect of the valve aspect ratio

In this section, we focus on the effect of the electric field $E$ and the valve aspect ratio $\Psi$ on the performance metrics of the valve defined in section 3.2. The holding pressure per unit length $\Delta P_y/L$ is measured for different electric fields 2 kV/mm $\leq E \leq$ 4 kV/mm for two valves with $H = 0.5$ mm, $L = 20$ mm and $W = 1$ mm and $W = 4$ mm respectively. The results are shown in Fig. 3-5. We observe that the holding pressure per unit length of the valve increases with the electric field. Power law fits to data ($\Delta P/L \sim E^n$) show good agreement with an exponent $n = 1.5$ for the two valves studied. This result validates the expected scaling of the holding pressure with the electric field $E$ discussed in Eq. 3.2.

The holding pressure drop per unit length $\Delta P_y/L$ is plotted against the aspect ratio $\Psi = W/H$ in Fig. 3-6(a) for different electric fields 2 kV/mm $\leq E \leq$ 4 kV/mm for valves with $H = 0.5$ mm, $L = 20$ mm. For all the electric fields tested, the holding

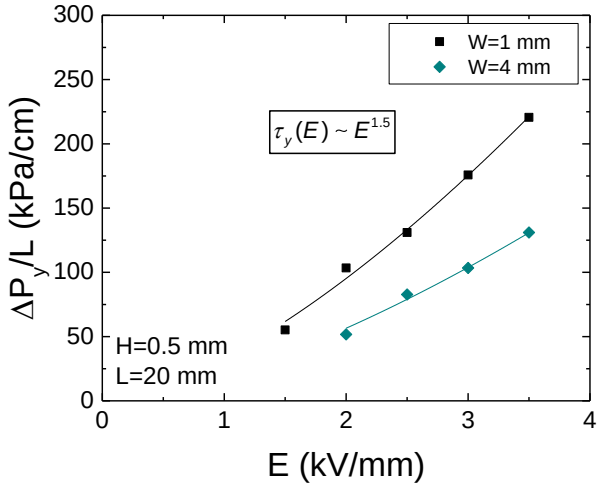


Figure 3-5: Holding pressure drop per unit length $\Delta P_y/L$ vs. the imposed electric field $E$ for valves with $H = 0.5$ mm, $L = 20$ mm and $W = 1$ mm (black squares) or $W = 4$ mm (cyan diamonds). The solid lines are power law fits to the data with an exponent $n = 1.5$.

pressure per unit length decreases with increasing aspect ratios $\Psi$ in accordance with the trend discussed in section 3.2.

We define a normalized holding pressure drop $\mathcal{P} = \Delta P_y H/2\tau_y(E)L$ and plot it against the aspect ratio $\Psi$ for all the electric fields tested in Fig. 3-6(b). The data for the all electric fields collapses onto a single master curve. A fit to the data of the form $\mathcal{P} = (1+1/\Psi)^n$ is found to be in good agreement for $n = 1.5$. This scaling is different from the predicted exponent $n = 1$ obtained from the analysis in section 3.2 and indicates that the yield stress $\tau_y(E)$ also has a weak dependence on the aspect ratio $\Psi$: $\tau_y(E, \Psi) \sim \sqrt{1 + 1/\Psi}$. A possible explanation for this scaling is the densification process described in chapter 2 that would result in a higher yield stress in low aspect ratio channels compared to high aspect ratio channels due to the decrease in the convection time scale $t_c$ with smaller $\Psi$.

The measured power efficiency $\eta_W$ of the valves is shown in Fig.3-7(a) for different electric fields 2 kV/mm $\leq E \leq$ 4 kV/mm and valve aspect ratios $\Psi$ for $H = 0.5$ mm and $L = 20$ mm. We report an increase of the power efficiency of the valves with the

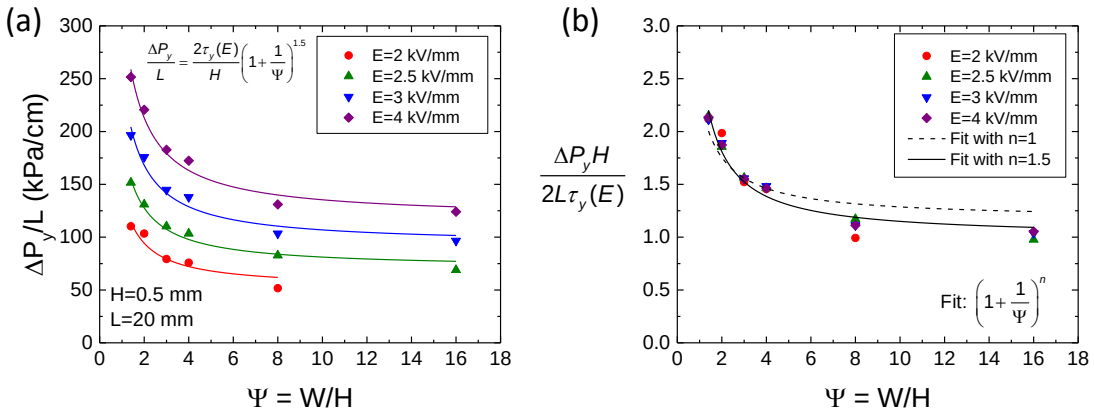


Figure 3-6: (a) Holding pressure drop per unit length $\Delta P_y/L$ vs. the channel aspect ratio $\Psi = W/H$ for valves with $H = 0.5$ mm, $L = 20$ mm and $E = 2$, 2.5, 3, 4 kV/mm. The solid lines are fits of the data to the model described in the figure. (b) Normalized holding pressure drop $\mathcal{P}$ vs. the channel aspect ratio $\Psi$. The solid and dashed lines represent fits of the data to the equation shown in the figure with $n = 1.5$ and $n = 1$ respectively.

aspect ratio $\Psi$; in agreement with the trends discussed in section 3.2. Additionally, the power efficiency has a weak dependence on the electric field: as the electric field increases, the power efficiency increases as well. Overall, the power efficiency $\eta_W$ of the valve prototypes is relatively high ($\eta_W \geq 0.75$). In general, the power efficiency can be improved by reducing the static electrical losses in the design by limiting the electrodes to the channel region only and minimizes ohmic losses in the rubber gasket.

Fig. 3-7(b) shows both the normalized holding pressure and the power efficiency as a function of the aspect ratio $\Psi$ for different electric fields $E$. The trade-off between power efficiency and higher holding pressure in terms of aspect ratio is evident in this representation. While valves can be specifically designed to have a high efficiency (high aspect ratio) or high holding pressure (low aspect ratio), in general an aspect ratio $\Psi \simeq 2.5$ is optimal to obtain efficient valves with relatively high holding pressures.

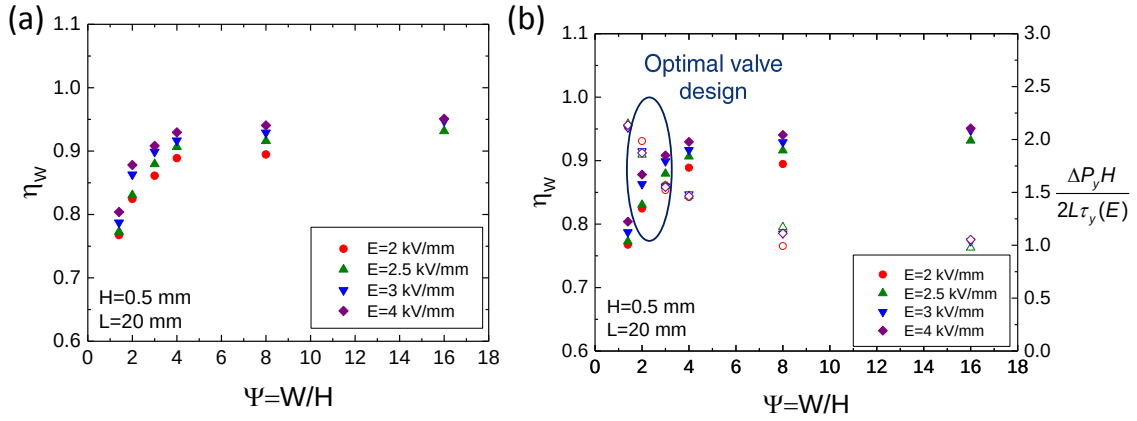


Figure 3-7: (a) Power efficiency $\eta_W$ vs. the channel aspect ratio $\Psi = W/H$ for valves with $H = 0.5$ mm, $L = 20$ mm and $E = 2,\ 2.5,\ 3,\ 4$ kV/mm. (b) Power efficiency and normalized holding pressure drop $\mathcal{P}$ vs. the channel aspect ratio $\Psi$. An aspect ratio $\Psi \simeq 2.5$ is in general optimal for ER design as it combines a high yield pressure drop $\Delta P$ and high power efficiency $\eta_W$.

## 3.5 Effect of electrode surface roughness

In this section, we explore the effects of electrode surface roughness on the performance of ER valves. Electrode shape and surface roughness has been reported to affect the holding pressure of ER valves [219, 220] but further understanding of this effect and how it affects the performance of the valves remains of interest. The copper tape was roughened by pressing it over grit 400 sandpaper using an Instron machine at 19,000 lbs. A comparison of the smooth and roughened surfaces using optical and SEM images is shown in Fig 3-8. Surface profilometry using a Mitotoyo SJ200 contact profilometer was performed on the electrode surfaces and the results are shown in Fig. 3-9. The RMS roughness $R_q$ of the smooth and rough surfaces was found to be $R_q^s = 0.19$ $\mu$m and $R_q^r = 4.0$ $\mu$m respectively.

The holding pressure per unit length $\Delta P_y/L$ and the power efficiency are plotted against the applied electric field $E$ for smooth and roughened valves of dimensions $H = 0.5$ mm, $W = 1$ mm and $L = 20$ mm. We observe that the roughened valves have a higher holding pressure per unit length and power efficiency for all electric fields tested. This is in contrast to the effect of the aspect ratio $\Psi$ where there

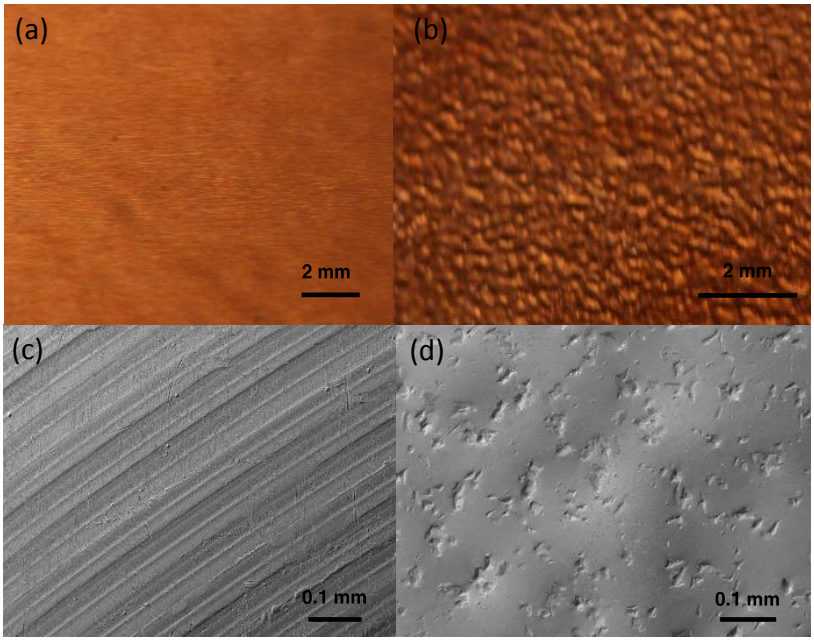


Figure 3-8: Optical images of the smooth (a) and roughened (b) copper surface used as electrodes in the valve. SEM images of the smooth (c) and roughened (d) copper surface used as electrodes in the valve.

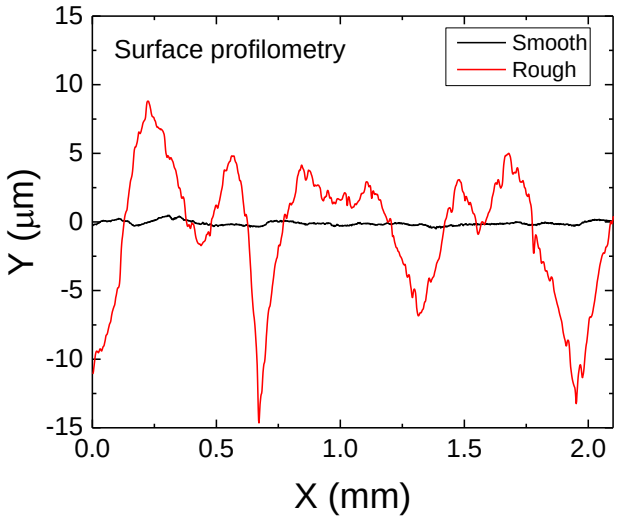


Figure 3-9: Surface profiles obtained by contact profilometry of the smooth and roughened copper surfaces shown in Fig. 3-8. The RMS roughness $R_q$ was found to be $R_q = 0.19$ $\mu$m and $R_q = 4.0$ $\mu$m for the smooth and roughened surface respectively.

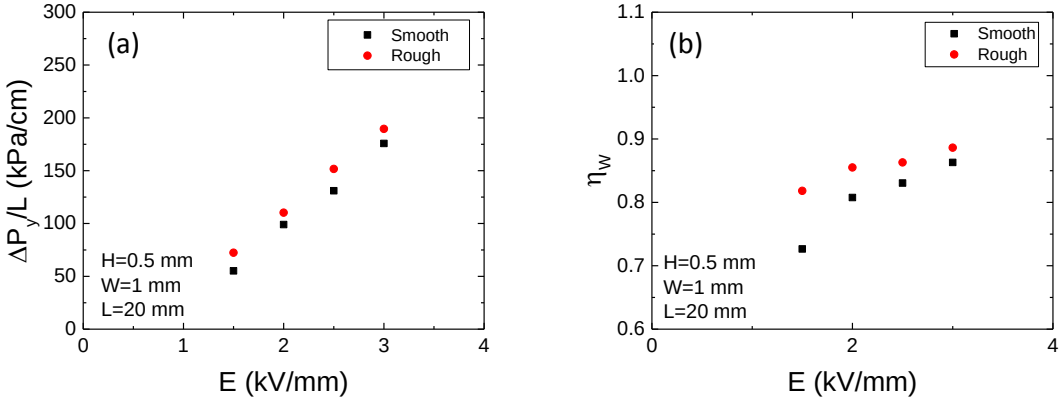


Figure 3-10: Holding pressure drop per unit length $\Delta P_y/L$ (a) and power efficiency $\eta_W$ (b) vs. the imposed electric field $E$ for valves with $H = 0.5$ mm, $L = 20$ mm and $W = 1$ mm and smooth (black squares) or rough electrodes (red circles).

exists a trade-off between efficiency and the holding pressure. Here, increasing the surface roughness improves the holding pressure and power efficiency of the valve. The increase in holding pressure with surface roughness can be interpreted as a delay of the adhesive failure at the electrode wall. This effect is expected to be largest when the roughness size is on the scale of the ER particle diameter. A more systematic study of the effect of roughness is still needed to derive the scaling of the valve performance metrics with the surface roughness. Using our rapid valve prototypes and the testing platform described previously, we will focus on studying this effect in future work.

## 3.6 Applications of ER valves to robotics

With an understanding of design rules for ER valves, we focus on applications of ER valves to robotics in this section. In collaboration with Boston Dynamics, ER valve prototypes (shown in Fig. 3-11(a)) were manufactured using printed circuit board (PCB) technology and applied to build small hydraulic robots. PCB manufacturing methods allow for easy control of the valve geometry and size. An example of a soft robotic gripper using ER valve technology is shown in Fig. 3-11(b). ER valves allow for precise control of the gripper's shape through control of the flow rate and pressure drop in each digit while miniaturizing the size of the gripper.

To conclude, this study focused on exploring the design space of ER valves with a focus on defining performance metrics for the valves and understanding how design parameters such as the electric field, channel aspect ratio and electrode surface roughness affect the valve performance. We demonstrated that a trade-off exists between power efficiency and holding pressure in terms of valve aspect ratio. We also showed that the electrode surface roughness can improve both the efficiency and holding pressure of the valve and can be an interesting area for further study. This work paves the way for the use of ER valves in small hydraulic robotic applications.

(a)

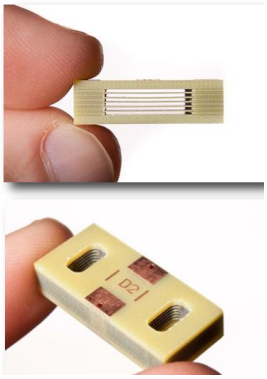

(b)

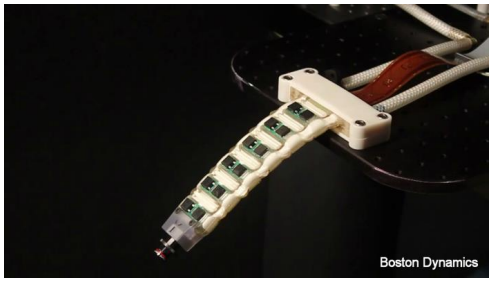


Figure 3-11: (a) Pictures of small ER valves designed by Boston Dynamics using PCB manufacturing methods. (b) Soft robotic gripper designed by Boston Dynamics using small ER valves.

# Chapter 4

# Rheological & Wall Slip Characterization of Conductive Semi-solid Flow Electrodes

## 4.1 Introduction

In semi-solid flow batteries, a nanoconductor such as carbon black is mixed in with the electrolyte and the storage material species to form a conductive suspension and as a whole it is pumped through the cell [34,121]. The storage material species can take the form of a dissolved substance such as Lithium polysulfide (Li-PS) [34] or solid particles such as Lithium Iron Phosphate (LFP) or Lithium Titanate (LTO) [121,125,221]. Fig. 4-1 shows the different components that compose semi-solid suspensions used in flow batteries. The semi-solid suspensions exhibit a yield stress and viscoplastic behavior and accurate characterization of their rheology and wall-slip behavior is crucial for modeling flow when designing flow cell prototypes. Smith et al. [222] have demonstrated the importance of plug flow in maximizing the energetic efficiency of semi-solid flow cells. In their work, they highlight the role of wall slip and the degree of yielding of the suspension on achieving plug flow and reaching higher energy efficiencies in the cells. With precise characterization of the rheology and wall-slip behavior of the

suspensions, flow modeling can guide mechanical design of the cells to achieve the desired design targets. This chapter focuses on methods to precisely characterize the rheological and wall slip behavior of semi-solid carbon black suspensions in steady shear using the parallel plate geometry. Using these methods, we then explore the impact of different design parameters such as carbon loading, surface properties, state of charge and additives on the rheology of the suspensions and their slip behavior. These results combined with flow models will aid design and selection of semi-solid suspensions for flow cell prototypes as discussed further in Chapter 8.

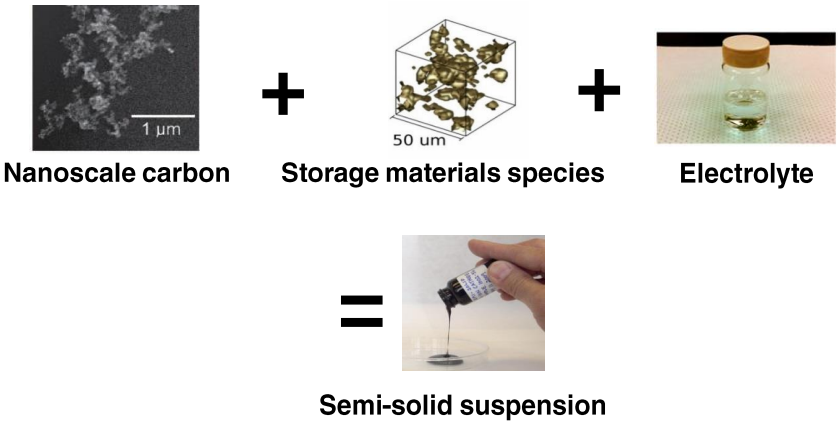


Figure 4-1: Composition of conductive semi-solid carbon black gels for flow battery applications. The semi-solid suspension contains a Newtonian electrolyte, a storage material species (in the form of a dissolved species or solid particles) and a nanoscale electronic conductor such as carbon black.

## 4.2 Materials and Methods

We focus on two different types of high energy density semi-solid flow electrodes using different energy storage species (Lithium polysulfide solutions and LFP/LTO suspensions) and containing carbon black (KetjenBlack ECJD600, Akzo Nobel) as the nanoscale electronic conductor. These materials have been previously studied and good flow cell performance has been demonstrated by Ho et al. [94] and Fan et al. [34].

In the case of Lithium polysulfide suspensions, an electrolyte solution was formulated by adding 1 wt% of Lithium Nitrate ($LiNO_3$, Sigma-Aldrich) and 0.5 M lithium Bis(Trifluoromethanesulfonyl)imide (LiTFSI, Sigma-Aldrich) to tetraglyme (TEGDME) or triglyme (Sigma-Aldrich) electrolyte solvents. The addition of $LiNO_3$ improves the passivation of lithium metal by forming a non-reactive surface to dissolved polysulfides on the Lithium, which reduces capacity fading. The catholyte was then prepared in the following steps. Lithium sulfide ($Li_2S$, Alfa) and Sulfur (Sigma-Aldrich) was added to the electrolyte solution to prepare a sulfur concentration of 2.5 M in the solution. The mixture was stirred mechanically in an argon gas-filled glove box at a temperature of 60°C for 12 hours to obtain a dark brown lithium polysulfide ($Li_2S_8$) solution. Conductive carbon black (KB, Ketjenblack, EC600JD, specific surface area of 800-1200 $m^2.g^{-1}$, Azko Nobel Polymer Chemicals LLC, Chicago, Illinois, US) was used to provide an electronic conducting network to the otherwise insulating sulfur species. KB was weighed and mixed in a 20 mL glass vial. Half of the $Li_2S_8$ solution was added to the vial. KB was then added after which the remaining $Li_2S_8$ solution was added. This method of mixing was found to yield a more uniform suspension than by adding the solution directly to KB. The suspension mixed in this manner exhibits a lower yield stress under the same viscometric testing conditions as shown in section 4.4.3. The resulting suspension was then sealed in a vial by black insulating tape and removed from the glove box. The vial was subjected to sonication in an ultrasonic bath for 60 min to obtain a homogeneous suspension of the catholyte.

In the case of LFP/LTO suspensions, the active materials consist of a carbon-coated $LiFePO_4$(LFP) powder (M121, Advanced Lithium Electrochemistry Co., Ltd., Taoyuan, Taiwan) with a mean particle size of 4 $\mu$m, a specific surface area of 13 $m^2.g^{-1}$, and a density of 3.551 $g.cm^{-3}$ and carbon-coated $Li_4Ti_5O_{12}$ (LTO) powder (LTO-1, BTR NanoTech Co., Shenzhen, China) with a mean particle size of 1.1 $\mu$m, a specific surface area of 10.68 $m^2.g^{-1}$, and a density of 3.539 $g.cm^{-3}$. The conductive material consists of a Ketjenblack (KB) carbon black powder described previously. Lithium bis(trifluoromethane)sulfonamide (LiTFSI), propylene carbonate (PC), and polyvinylpyrrolidone ( $M_W$ = 40,000 $g.mol^{-1}$) are acquired from Sigma-

Aldrich. Electrode suspensions are prepared in an Argon-filled glovebox. All dry materials are heated at 120°C overnight under vacuum to remove moisture. First, 250 mL HDPE bottles are filled with 5 mm (200 g) and 0.5 mm (100 g) yttrium stabilized zirconia (YSZ) milling beads. Next, PC (50 g), PVP (0.3 g), and LFP or LTO powder (10 g) are added. The bottles are sealed and the suspensions are ball-milled under ambient conditions for 24 h. The suspensions are then filtered through 20 $\mu$m stainless steel sieves in the argon-filled glovebox. The filtered suspensions are then sealed and centrifuged at 12 500 g in the glove box for 1 h to collect the dispersed particles. After removing the supernatant, the dense sediment (typically 70 wt% solids) is collected and homogenized using a planetary mixer (Thinky AR-100). Additional PC and 1% PVP/PC solution are added, followed by ultra-sonication and homogenization. LiTFSI is then added to achieve a 1 M electrolyte concentration. Finally, KB powder is added and homogenized.

The viscometric behavior of the different solutions and semi-solid suspensions was measured using a Malvern Kinexus Pro torsional rheometer enclosed in an Argon glovebox (MBRAUN, Newburyport, MA, US) with $H_2O$ & $O_2$ levels below 1 ppm. Steady shear viscometry tests were performed using a smooth stainless steel parallel plate geometry ($D$ = 40 mm; mean roughness $R_a$ = 0.36 $\mu$m). All tests were performed at $T$ = 25°C and the temperature was regulated with a Peltier plate system. Steady shear tests were performed with decreasing applied shear rates as described by Ovarlez et al. [223] to insure the existence of a simple yield stress for the material and avoid possible transient shear banding. In addition, following the protocol proposed by Yoshimura and Prud'homme [139], the same sample was tested at three different gaps to probe and correct for slip effects. If the flow curves at different gaps superimpose, the material does not slip. If gap-dependent rheology is observed, a correction needs to be applied to extract the true shear rate applied on the sample at each value of the applied stress. All samples were presheared for 1 min at 100 $s^{-1}$ and the stress was allowed to relax for 2 min before each test.

The flow curves of solutions containing 2.5, 5 and 7 M sulfur as $Li_2S_8$ in TEGDME with 0.5 M LiTFSI supporting electrolyte were measured at $T$ = 25°C and exhibited

Newtonian liquid behavior with constant viscosity as shown in Fig. 4-2(a) and no slip at the wall. The viscosity of the Lithium polysulfide solutions increases rapidly with sulfur molarity $c$ as shown in Fig. 4-2(b). An exponential fit of the form $\mu = \mu_0 \exp(Bc)$ with $\mu_0 = 7.8$ mPa.s and $B = 0.4$ M$^{-1}$ is in good agreement with the measured data ($R^2 = 0.988$). This Newtonian behavior of the Lithium polysulfide solutions prior to the incorporation of the carbon black is in contrast with the non-Newtonian behavior of the LFP/LTO suspensions [125, 221].

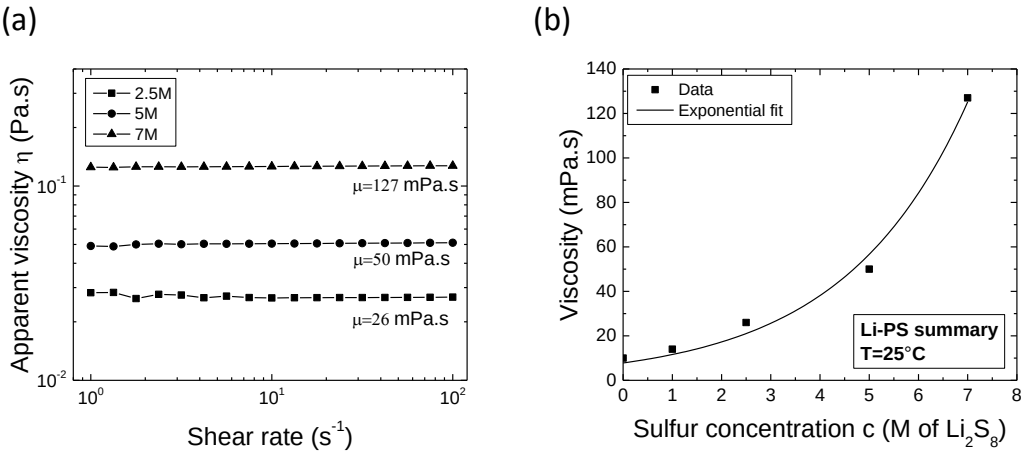


Figure 4-2: Viscosity of Lithium polysulfide solutions in TEGDME of different Suflur molarities at $T = 25$°C. (a) Apparent viscosity $\eta$ vs shear rate $\dot{\gamma}$ for Lithium polysulfide solutions in TEGDME containing 2.5, 5, 7 M Sulfur as $Li_2S_8$. The solutions are Newtonian with constant viscosity over the range of shear rates studied. (b) Viscosity of the Lithium polysulfide solution vs Sulfur molarity. The solid line represents an exponential fit to the data of the form $\mu = A \exp(Bc)$ with $A = 7.8$ mPa.s and $B = 0.4$

## 4.3 Steady shear flow curves & wall slip correction

Apparent flow curves of a 2.5M Lithium polysulfide solution in TEGDME with 1.5 vol% KB at different gaps $H$ =1, 0.75, 0.5 mm are shown in Fig. 4-3. The dependence of the flow curve on the gap $H$ as well as the kink in the flow curve at shear rates of about 1 s$^{-1}$ are indications of the presence of wall slip [7, 16].

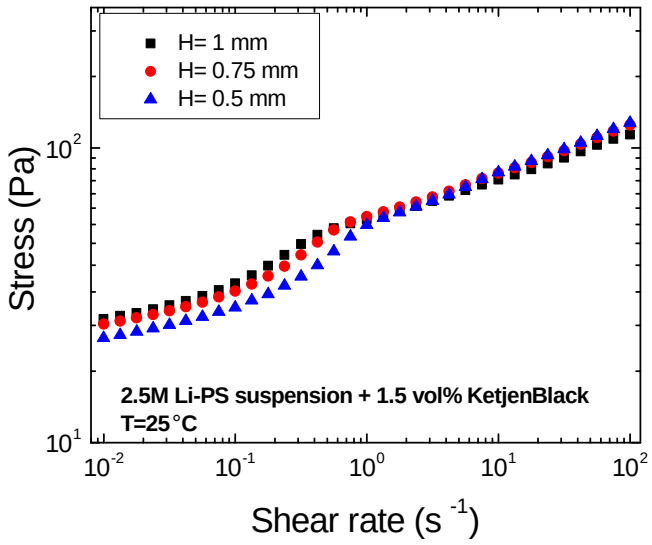


Figure 4-3: Apparent flow curves of a 2.5M Lithium polysulfide solution in TEGDME with 1.5 vol% KB at different gaps $H$ =1, 0.75, 0.5 mm. The dependence of the flow curve on the gap $H$ as well as the kink in the flow curve at shear rates of about 1 $s^{-1}$ are indications of the presence of wall slip.

Following the slip correction protocol proposed by Yoshimura and Prud'homme [139] and described in section 1.5.3, for each stress $\tau$, the apparent shear rate $\dot{\gamma}_a$ is plotted against the inverse of the gap $H$ and a fit to the data is performed using the kinematic relation described by Eq. 1.6. The intercept and slope of the fitting line allow us to extract the true shear rate $\dot{\gamma}_t$ and slip velocity $V_s$ associated with the stress $\tau$. Fig. 4-4 shows an example of this slip analysis. The measured slip velocity $V_s$ is shown as a function of the applied stress $\tau$ in Fig. 4-4(b). We observe a linear increase of the slip velocity with stress above a critical stress $\tau_c \simeq 25$ Pa. The presence of a critical stress for the onset of slip is associated with the external work that must be applied for adhesive failure at the wall.

A linear slip law with critical slip described by Eq. 4.1:

$$V_s = \beta(\tau - \tau_c) \tag{4.1}$$

where $V_s$ is the slip velocity, $\beta$ is the linear slip coefficient and $\tau_c$ is the critical stress for onset of slip; was fit to the data and was found to be in good agreement for

$\beta = 6.8 \pm 0.2$ $\mu$m/(Pa.s) and $\tau_c = 25.6 \pm 0.2$ Pa. Characterization of the slip velocity is challenging at higher stresses because once the material yields, the contribution of wall slip to the overall velocity becomes less and less important compared to the viscoplastic deformation and errors on the slip velocity become increasingly large.

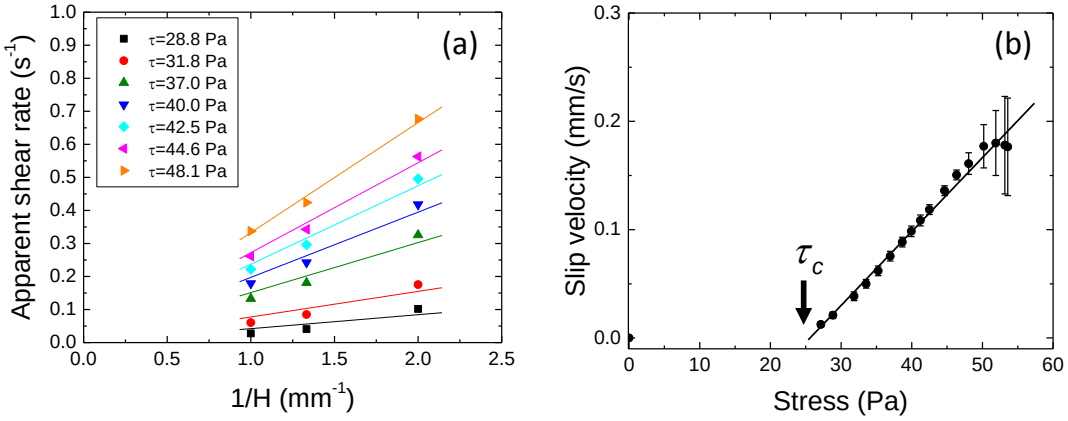


Figure 4-4: (a) Slip analysis of the data shown in Fig. 4-3 following the wall slip correction method proposed by Yoshimura and Prud'homme [139]. The solid lines represent linear fits to the data following Eq. 1.6. (b) Measured slip velocity vs applied stress below yield. The solid line represents a linear fit to the data following the critical slip model shown in Eq. 4.1.

Fig. 4-5 shows the true flow curve for the 2.5M Lithium polysulfide suspension containing 1.5 vol% KB before and after correction for wall slip. We observe three distinct regions in the apparent flow curves shown in Fig. 4-3. First, for $\tau \leq 25$ Pa, the fluid doesn't flow i.e. it is truly an unyielded solid, then for 25 Pa $\leq \tau \leq 40$ Pa, the fluid slips at the wall and flows as an unyielded plug. Finally, for $\tau \geq 40$ Pa, the suspension yields and undergoes pseudo-plastic flow. These results demonstrate the importance of accounting for wall slip when measuring the rheology of semi-solid suspensions to enable accurate characterization of the rheology of the slurry.

Suspensions containing carbon black can be modeled as yield stress materials using for instance the Bingham plastic (Eq. 1.2) or Herschel-Bulkley models (Eq. 1.3). Ovarlez et al. [195] have also shown that such suspensions can exhibit more complex rheology such as time-dependent effects but for the purpose of this analysis, to a first order, this effect has been neglected. The semi-solid suspension rheology can be

modeled by the Herschel-Bulkley model with a yield stress $\tau_y = 41.7$ Pa, a consistency $K = 19.0$ Pa.s$^n$ and a power-law index $n = 0.31$ ($R^2 = 0.99$). Alternatively, for simpler flow analysis, the Bingham model with a yield stress $\tau_y = 64.6$ Pa and a plastic viscosity $\mu_p = 0.71$ Pa.s, also provides a reasonable fit ($R^2 = 0.8$).

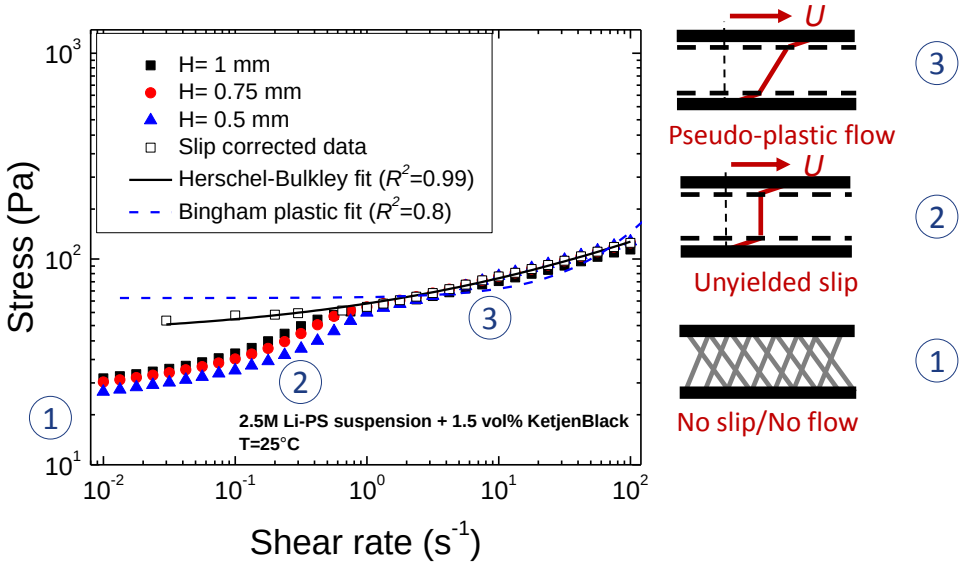


Figure 4-5: Flow curve of a 2.5M Lithium polysulfide solution in TEGDME with 1.5 vol% KB measured at different gaps ($H$=1 mm, 0.75 mm, 0.5 mm) as well as the slip-corrected true flow curve. Fits to the Herschel-Bulkley model and the Bingham plastic model are shown by the black solid line and the blue dashed line. Three regimes are visible on the apparent flow curves and are depicted in the schematics to the right of the figure. As the stress increases, the gel starts to slip and flows as a solid plug then yields and undergoes pseudo-plastic flow.

## 4.4 Influence of design parameters on the rheology and wall slip of semi-solid suspensions

With an understanding of the role of wall slip in the rheological measurements and how to correctly characterize the rheology of semi-solid suspensions, we investigate the effect of different design parameters on the rheology and wall slip of semi-solid suspensions. In particular, we are interested in the role of the carbon black loading, surface properties, mixing protocol and state of charge on the rheology and wall slip

of Lithium polysulfide suspensions. In addition, we will explore the role of additives such as polymers on the rheology of LFP and LTO suspensions.

### 4.4.1 Influence of CB volume fraction

In this section, we investigate the role of the volume fraction of carbon black on the rheology of Lithium polysulfide suspensions. We prepared suspensions containing 2.5 M Sulfur as $Li_2S_8$ in TEGDME and containing Ketjenblack (KB) with nominal volume fractions $0\% \leq \phi \leq 1.5$ %. The slip-corrected flow curves of the suspensions are shown in Fig. 4-6(a). As carbon black is added, the fluid becomes viscoplastic and develops a yield stress even at volume fractions as low as $\phi = 0.25$ %. Fits to the Herschel-Bulkley model are performed and the measured yield stress is plotted against the volume fraction of carbon $\phi$ in Fig. 4-6(b).

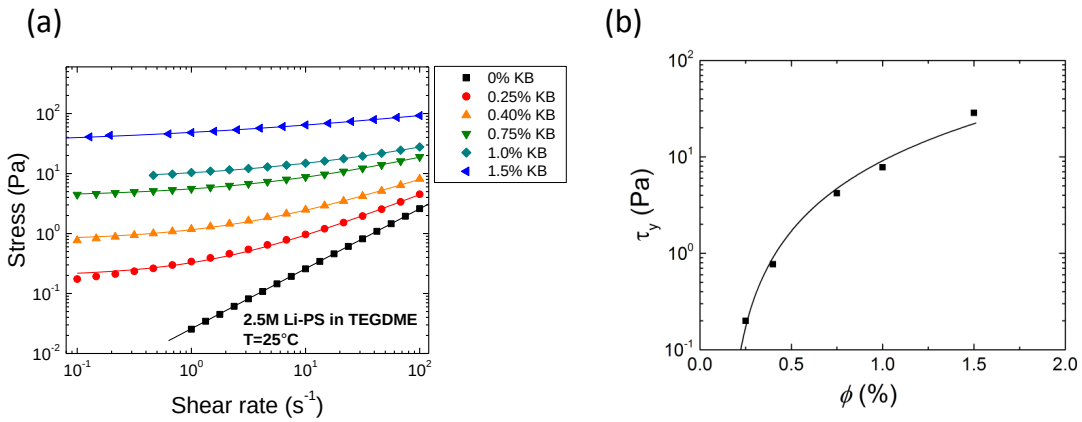


Figure 4-6: Influence of the carbon black loading on the rheology of 2.5M Lithium polysulfide (Li-PS) suspensions in TEGDME. (a) Slip-corrected flow curves for the Li-PS suspensions with carbon black nominal volume fractions varying from $\phi$=0% to $\phi$=1.5% in volume. Fits to the Herschel-Bulkley model are shown by the solid lines. (b) Yield stress $\tau_y$ vs carbon black nominal volume fraction $\phi$. The solid line represents a power law fit to the data of the form $\tau_y = \tau_0(\phi - \phi_p)^\alpha$ where $\tau_0 = 13.3 \pm 0.8$ Pa, $\phi_p = 0.14 \pm 0.07$ % and $\alpha = 2.32 \pm 0.14$.

The yield stress is found to increase as a power law of the carbon volume fraction. A fit of the form $\tau_y = \tau_0(\phi - \phi_p)^\alpha$ was fit to the data and good agreement was found

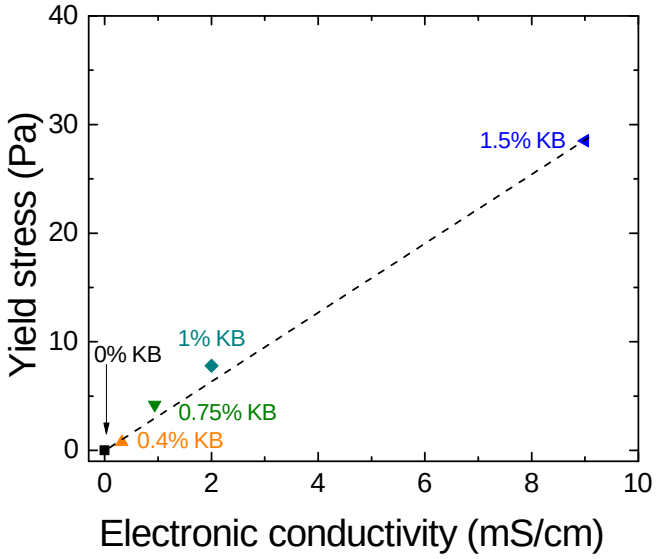


Figure 4-7: Ashby plot showing yield stress vs electronic conductivity for 2.5M Lithium polysulfide suspensions in TEGDME containing different loadings of KB. The dashed line represents a linear fit to the data of slope 3.21 Pa.cm/mS ($R^2 = 0.99$).

for$\tau_0 = 13.3 \pm 0.8$ Pa, $\phi_p = 0.14 \pm 0.07$ % and $\alpha = 2.32 \pm 0.14$. This results shows that KetjenBlack percolates at a very low volume fraction $\phi_p \simeq 0.14\%$. The exponent $\alpha = 2.32$ is in agreement with previous results ($\alpha = 2.4$) on carbon black stabilized suspensions reported by Godfrin et al. [224].

For material design purposes, we construct an Ashby plot [225] showing the yield stress vs. the electronic conductivity for the Lithium polysulfide suspensions in TEGDME containing different loadings of KB. The results are shown in Fig. 4-7. We observe a linear correlation between the yield stress of the suspension and its electronic conductivity (slope: 3.21 Pa.cm/mS, $R^2 = 0.99$). Additionally, increasing the carbon loading by a small amount can change its yield stress and conductivity by an order of magnitude. This type of representation is useful for design of the semi-solid flow electrodes and guide the cell design given a specified conductivity or yield stress. An example of semi-solid flow electrode design using Ashby plots is discussed in section 8.3.

### 4.4.2 Influence of surface properties

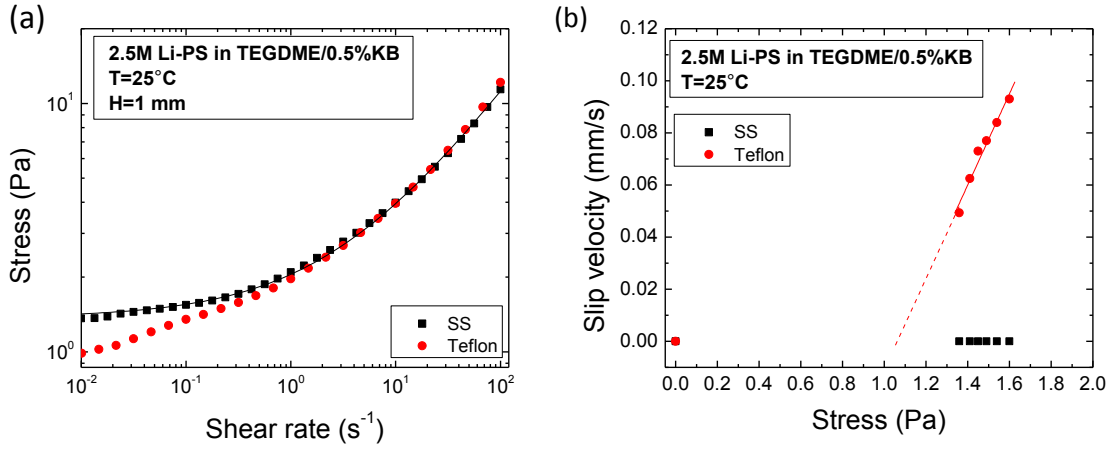


Figure 4-8: Influence of the surface properties on the rheology and wall slip of a 2.5M Lithium polysulfide suspension in TEGDME with 0.5% KB. (a) Apparent flow curves for a gap $H = 1$ mm on Stainless Steel (SS) and Teflon surfaces. The solid black line represents a fit of the Herschel-Bulkley model to the data. (b) Measured slip velocity vs applied stress on stainless steel and Teflon surfaces. The solid line represents a linear fit to the data following the critical slip model shown in Eq. 4.1.

Given the importance of plug flow and slip on the energetic efficiency of flow cells [222], we investigate the effect of the surface properties of different materials on the rheology and wall slip behavior of a Lithium polysulfide suspension in TEGDME with 0.5% KB. Two surfaces of interest were investigated: a Teflon surface ($R_q = 210$ nm) and a stainless steel surface ($R_q = 145$ nm). The parallel plate geometry enables easy modification of the surface properties as a different flat surface can be easily glued to the plates. The apparent flow curves for a Lithium polysulfide suspension in TEGDME with 0.5% KB measured at $H = 1$ mm are shown in Fig. 4-8 (a). We observe a difference between the two flow curves below stress $\tau \leq 3$ Pa, indicating that slip is playing a role in the rheology measurements. By running tests at different gaps and using the multiple gap correction method for wall slip described previously, we can characterize the slip velocity on the two surface at the imposed stress. The measured slip velocity is shown for both the stainless steel surface and the Teflon surface in Fig. 4-8(b). We note that within the range of stress covered in the measurement, the stainless steel surface acted as a no-slip surface while the Teflon surface displayed

slip at the wall for the Lithium polysulfide suspension in TEGDME with 0.5%KB. The critical slip model described in Eq. 4.1 was fit to the data and good agreement was found for $\beta = 0.17 \pm 0.01$ mm/(Pa.s) and $\tau_c = 1.02 \pm 0.1$ Pa. These results confirm that Teflon is a high slip surface for the Lithium polysulfide suspensions and these measurements allow us to quantatively model the slip in the system as discussed further in section 8.4.

### 4.4.3 Influence of the mixing protocol

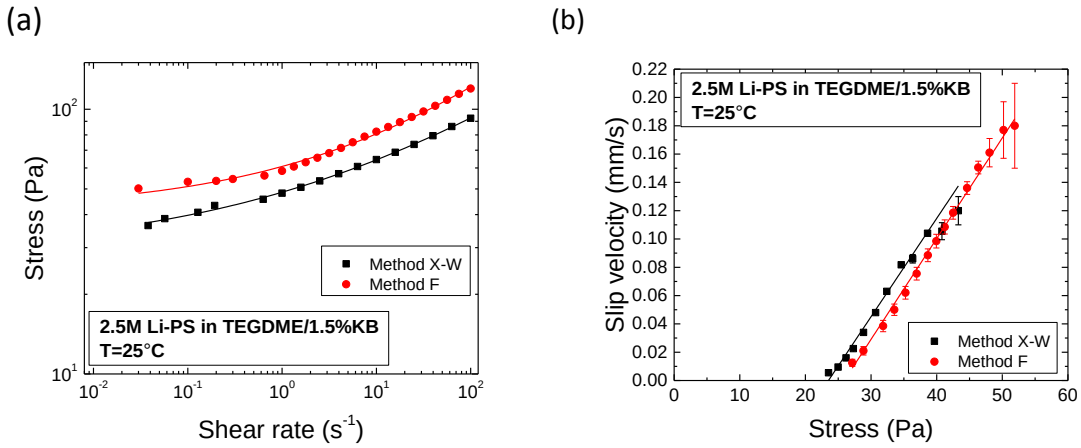


Figure 4-9: Influence of the mixing protocol on the rheology and wall slip of a 2.5M Lithium polysulfide suspension in TEGDME with 1.5% KB.(a) Slip-corrected flow curves for two different mixing protocols dubbed "F" and "X-W". The solid lines represent fits of the Herschel-Bulkley model to the data. (b) Measured slip velocity on SS vs applied stress for the two mixing protocols. The solid lines represent linear fits to the data following the critical slip model shown in Eq. 4.1.

In this section, we emphasize the importance of the mixing protocol of the Lithium polysulfide suspensions on their rheology. The mixing protocol defined in section 4.2 uses a two-step mixing process of the KB. This method of mixing dubbed "X-W" will be compared to a one step mixing process of the KB dubbed "F". In the one step mixing method, the KB is added directly to the Li-PS suspension and mixed and sonicated for the same amount of time as the "X-W" two-step mixing method. The slip-corrected flow curves and the slip velocity on smooth stainless steel for a 2.5M Lithium polysulfide suspension in TEGDME with 1.5% KB mixed using the two

aforementioned methods are shown in Fig. 4-9. We observe that the slip behavior remains relatively unchanged between the two suspensions but the flow curves exhibit a different yield stress. To quantify this effect, the Herschel-Bulkley model (Eq. 1.3) was fit to the flow curve data and good agreement was found for the following parameters: $\tau_{XW} = 28.5 \pm 0.8$ Pa, $\tau_F = 41.7 \pm 1.7$ Pa, $K_{XW} = 20.0 \pm 1.1$ Pa.s$^n$, $K_F = 19.1 \pm 1.6$ Pa.s$^n$, $n_{XW} = 0.25 \pm 0.02$, $n_F = 0.32 \pm 0.02$ where the subscripts XW and F denote the mixing method. Additionally, the critical slip model (Eq. 4.1) was fit to the slip velocity data and the following parameters were extracted: $\tau_{c,XW} = 23.5 \pm 0.7$ Pa, $\tau_{c,F} = 25.8 \pm 0.6$ Pa, $\beta_{XW} = 6.9 \pm 0.2$ $\mu$m/(Pa.s), $\beta_F = 7.1 \pm 0.1$ $\mu$m/(Pa.s). These results show that the mixing method affects the yield stress of the suspension but does not strongly affect its shear thinning behavior after yielding or its slip behavior at the wall. These measurements highlight the importance of controlling the mixing protocol for carbon black suspensions designed to be used in battery applications in order to obtain reproducible flow behavior in cell prototypes.

### 4.4.4 Influence of the state of electrical charge

In this section, we discuss the effect of the state of electrical charge on the rheology of the 2.5M Lithium polysulfide suspension in triglyme solvent containing 0.75% KB. The sulfur flow electrode does not contain solid elemental sulfur but rather contains $Li_2S_8$, which is completely soluble in the solvent. Fig. 4-10(a) shows the voltage-capacity behavior of the Li-$Li_2S_8$ couple when operated over a complete galvanostatic charge-discharge cycle in a stationary cell. As the state of charge is increased, the composition of the sulfur species transitions from the soluble $Li_2S_8$ to $Li_2S_6$ then to the precipitated and insoluble $Li_2S$ state. By discharging the electrode to the insoluble $Li_2S$, the capacity of the flow cell can reach $\sim$ 1000 mAh/g compared to $\sim$ 200 mAh/g if the cycling is restricted to the soluble regime. It is therefore important to understand the change in rheology of the semi-solid electrode as the state of charge is varied and characterize the flow behavior in the insoluble regime. To capture the precipitation mechanism as closely as possible to a real flow cell, the Lithium sulfur electrode ($Li_2S_8$) was discharged to the desired capacity in a stationary cell then the

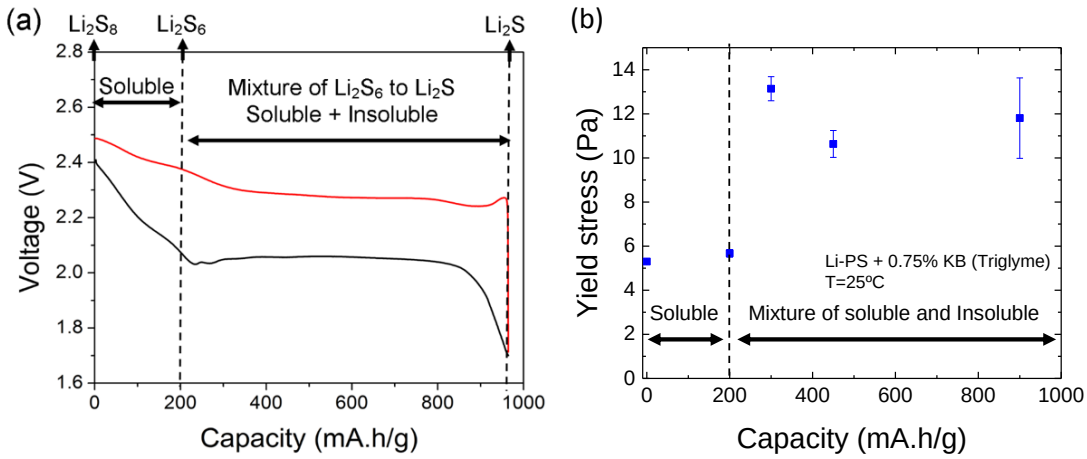


Figure 4-10: Influence of the state of charge on the rheology of a 2.5M Lithium polysulfide suspension in triglyme with 0.75% KB, 0.5 M LiTFSI, and 1wt% $LiNO_3$. (a)The Li-$Li_2S_8$ reaction during the first galvanostatic cycle in a Swagelok half-cell configuration at a C-rate of 1/50 $h^{-1}$. The lithiation of soluble Li-PS species from $Li_2S_8$ to $Li_2S_6$ is reflected by the first 200 mAh/g of capacity, during which the voltage decreases from 2.4 to 2.05 V. Further lithiation of the Li-PS results in precipitation of insoluble $Li_2S$ at a near-constant voltage of 2.05 V. (b) Yield stress as a function of the discharge capacity of the cell.

suspension was collected and subsequently tested. The yield stress of the suspension as a function of the capacity of the cell is shown in Fig. 4-10(b). We observe that as the transition to the insoluble regime occurs, the yield stress of the suspension increases by a factor of two. This indicates that precipitation of the insoluble species $Li_2S$ affects the connectivity of the percolated carbon black network and changes the rheology of the suspension. This result demonstrates that for flow modeling in cell prototypes, the effect of state of charge has to be carefully taken into account.

### 4.4.5 Effect of dispersants on the rheology of semi-solid electrodes

In this section, we discuss the effect of dispersants on the rheology of semi-solid electrodes namely LFP or LTO based ones. To fully optimize semi-solid flow cells using these electrodes, the flowing electrodes must have high active material content coupled with an adequate conductive network to overcome the resistive nature of

most electrochemically active Li-ion compounds such as LFP or LTO. However, as their solids loading increases, dramatic changes in their rheological properties ensue, which inhibit flow. The key to maximizing active material content while retaining satisfactory flowability and conductivity, is to simultaneously tailor the respective interactions between all particles present within these electrode suspensions.

Here, we discuss the design of biphasic semi-solid flow electrodes with high energy density, fast charge transport, and low-dissipation flow. To create these biphasic mixtures [226, 227] the interactions were tailored to be repulsive between the active particles (LFP or LTO), attractive between the conductive carbon black (Ketjen-Black ECJD600) and repulsive between the LFP/LTO-KB. These two particle populations are suspended and mixed sequentially in propylene carbonate (PC) with 1 M of lithium bis(trifluoromethane)sulfonamide (LiTFSI). Colloidal particles tend to rapidly aggregate when suspended in polar solvents under high ionic strength conditions due to van der Waals interactions [228]. We introduce a nonionic polymeric dispersant, polyvinylpyrrolidone (PVP), with appropriate amount to selectively stabilize the LFP or LTO particles fully, but not the KB particles. PVP has been shown to sterically stabilize colloidal particles in both aqueous [229–231] and non-aqueous [232] media leading to well dispersed suspensions. PVP is especially useful for SSFC electrodes as it confers stability even in systems with high salt concentrations that undergo electrochemical charging and discharging.

To explore dispersant effects on flow behavior, we carried out shear viscometry on biphasic and purely attractive LFP and LTO electrode suspensions with the following compositions: 20%LFP/1.25%KB/ 0.3%PVP, 20%LFP/1.25%KB/ 0%PVP, 20L%TO/1.5%KB/0.3%PVP and 20L%TO/1.5%KB/0%PVP. Their measured flow curves are shown in Fig. 4-11. Here the flow curves for biphasic LFP and LTO suspensions are slip-corrected and exhibit nearly identical behavior over multiple gap heights indicating the absence of wall slip as shown in Fig 4-12. The inhomogeneity of the purely attractive electrode suspensions makes slip correction difficult. Their flow curve, which represents a lower bound, is acquired at a gap height $H = 0.8$ mm. We observe that the flow curve of the biphasic system is nearly an order of magnitude

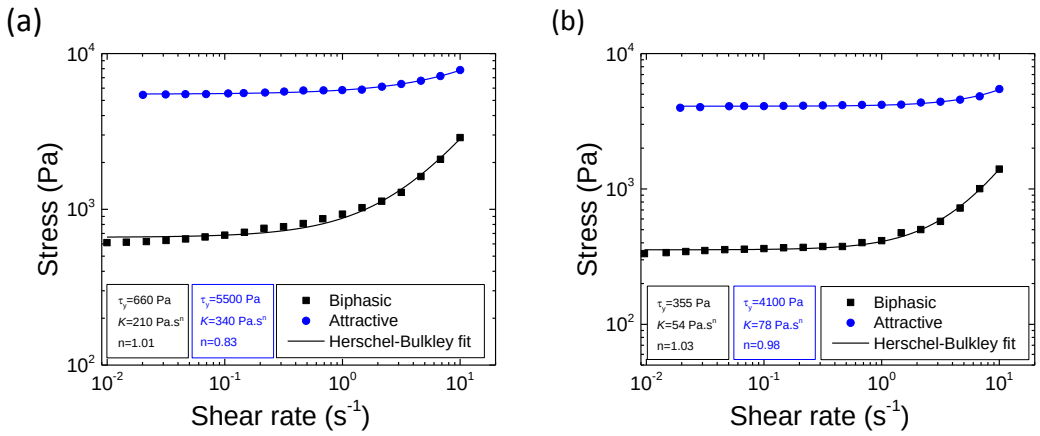


Figure 4-11: Flow curves for biphasic (0.3 wt% PVP) and purely attractive (0 wt% PVP) electrode suspensions composed of (a) 20 vol% LFP and 1.25 vol% KB and (b) 20 vol% LTO and 1.5 vol% KB. The solid lines represent fits of the Herschel-Bulkley model to the experimental data.

lower than its purely attractive counterpart at all shear rates in both the LFP and LTO system. This is also true for shear yield stress, which is an order of magnitude lower for the biphasic LFP and LTO suspensions. Fits to the Herschel-Bulkley model (Eq. 1.3) are shown in Fig. 4-11 and regression to the experimental data gives an extrapolated yield stress of 660 and 5500 Pa for the biphasic and purely attractive LFP suspensions respectively, and 360 and 4100 Pa for the biphasic and purely attractive LTO suspensions, respectively. These results highlight the impact of the addition of a small amount of dispersant in the suspension on its rheology and flowability.

Additional results obtained in collaboration with Wei et al. [221] show that once a critical amount of PVP (0.3 wt%) is introduced to the suspension to stabilize the particles, both electronic conductivity and yield stress vary minimally with further addition of PVP. These results demonstrate that optimizing biphasic electrode suspensions for use in semi-solid flow cell batteries is not straightforward. Both their ability to charge/discharge efficiently and flow readily through the cell is important. These criteria are often in conflict, since the carbon black network gives rise to both the desired electronic conductivity (which facilitates charge transfer) and a yield stress (which increases pumping pressure).

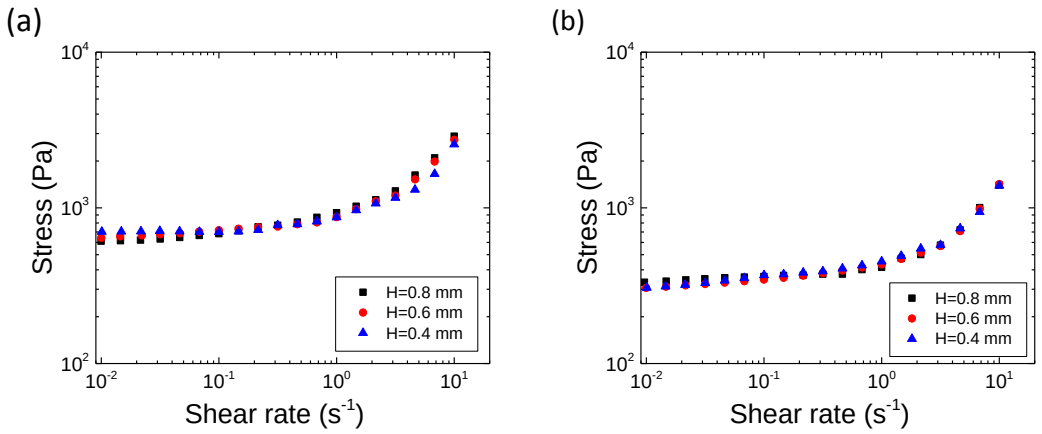


Figure 4-12: Flow curves for the (a) biphasic LFP suspension (20%LFP/1.25%KB/0.3%PVP) and (b) biphasic LTO suspension (20L%TO/1.5%KB/0.3%PVP) suspensions measured at $T = 25°C$ at different gaps ($H = 0.8$, 0.6 and 0.4 mm) against a smooth stainless steel surface (roughness $R_q = 145$ $\mu$m). The overlapping flow curves indicate no-slip boundary conditions at the surface.

In summary, we have discussed methods to characterize the rheology and wall slip of semi-solid flow electrodes. We emphasized the importance of wall slip correction in obtaining accurate rheology data and slip laws and explored the impact of various design parameters on the rheology and slip of the suspensions. Quantifiying the rheology and wall slip behavior of the flow electrodes is crucial for flow modeling in cell prototypes as discussed further in Chapter 8.

# Chapter 5

# Test Fixtures for Simultaneous Rheo-electric Measurements using Stress-controlled Rheometers

## 5.1 Introduction

From wormlike micellar fluids to colloidal glasses, complex fluids encompass a wide array of soft materials that all display a deformable and reconfigurable microstructure, which gives rise to intermediate mechanical properties between that of liquids and solids [2, 233, 234]. Under shear, the microstructure can rearrange and interact with the flow, which may in turn feed back on the flow itself triggering instabilities [10]. As such, complex fluids can exhibit a host of non-linear effects such as shear banding instabilities [235, 236] as well as shear localization [223], wall slip [149, 150, 160, 237], macroscopic fractures [157, 158], shear-induced structuration [91, 92, 238–240], etc. The use of complementary local measurements such as X-ray scattering [241] and Neutron spectroscopy [242] to extract structural information on the one hand, or MRI [169,243], particle tracking [179], dynamic light scattering and ultrasound imaging [172, 244] to extract velocity profiles on the other hand, has provided valuable insights about complex fluid rheology through time-resolved measurements of the

microstructure evolution under shear.

Another microstructural probe, less frequently employed, is measurement of the electrical properties of the fluid (e.g. conductivity $\sigma$, permittivity $\epsilon$), which coupled with standard rheological measurements also provides additional information on the evolution of the fluid microstructure under flow [33, 245–250]. Previous rheo-electric studies have focused mostly on dielectric complex fluids such as polymeric materials [251–253], liquid crystals [247], colloidal suspensions [248] and electrorheological fluids [198], as well as weakly conductive materials ($\sigma \ll 1$ mS/cm) such as CNT nanocomposites [245, 246, 254–258] and weakly conductive carbon black gels [249,250,259–262]. Typical commercial rheo-electric platforms involve the use of a rheometer coupled with an electrical measuring system such as an LCR meter that measures electric or dielectric constants simultaneously. In some studies, electrical measurements are performed using Alternating Current (AC) to extract the complex permittivity of the material [247,249,261,263] while other studies have focused on the use of Direct Current (DC) measurements to characterize the conductivity of weakly conductive materials under flow [245,246,250,255,258]. However, rheo-electric studies of complex fluids are rare as they typically require the use of less common and expensive strain-controlled rheometers in which the rotary drive and stationary torque sensor are separate. Furthermore, most previous studies assume homogeneous flows and neglect non-linear kinematic phenomena discussed above such as slip and shear banding that regularly occur in conductive complex fluids [264, 265], and can lead to misinterpretation of rheological data [259, 262, 263].

Characterizing the electrical properties of strongly conductive complex fluids ($\sigma >$ 1 mS/cm) under flow is of practical relevance for numerous applications among which the large-scale manufacturing of conductive nanocomposites [245, 246, 258, 266] and the design of semi-solid flow battery electrodes [34, 121, 127, 259] are particularly noteworthy. For instance, the use of an embedded dispersed nanoconductor, such as carbon black, as an additive in semi-solid flow cells has been shown to increase the electrochemical activity throughout the volume of the cell, leading to higher rate performance and higher energy densities at lower cost [34, 221, 259]. As such,

characterizing the evolution of the conductivity of battery slurries under imposed shear is crucial to optimize the design and operation of semi-solid flow cell [222].

## 5.2 Rheo-electric test fixture: parallel plate

Rheo-electric platforms typically involve coupling an electrical measuring system to a conventional torsional rheometer that is used to measure the rheological properties of the materials under investigation. In previous work, a number of different two-electrode geometries have been used including cylindrical Couette [33, 249, 250], plate-plate [247, 256, 262, 263], ring geometries [245, 246, 254, 255] and pipe flow [248]. The difficulty inherent in performing simultaneous rheo-electric measurements lies in the additional friction caused by the electrical connection to the rotating electrode (typically through a slip ring), which can induce large errors in the measurement of the torque, when measured at the same electrode. Controlled-rate rheometers are therefore generally preferred for this class of measurements as they allow the user to measure torque on the stationary electrode, thus decoupling the electrical and rheological measurements. However, rate-controlled rheometers are more expensive and less common than stress-controlled rheometers and less well-suited for measuring yielding transitions that are common in highly filled conductive materials. These limitations motivate the development of a new apparatus.

A schematic and picture of the experimental test fixture used to perform the simultaneous rheo-electric measurements are shown in Fig. 5-1. The apparatus is built around two parallel plates (of radius $R = 20$ mm, and surface roughness $R_a = 0.1$ $\mu$m, as determined by a Mitutoyo surface profilometer) that form a two-electrode cell separated by a distance $H$ with the conductive sample sandwiched between them. The upper rotating plate is connected to a stress-controlled torsional rheometer (TA instruments, AR-G2) that applies a torque and measures the resulting shear strain. The plate-plate geometry is chosen here as it allows for a homogeneous electric field and can be used to correct for wall slip effects through measurements at multiple gap settings [139]. However, the shear rate $\dot{\gamma}$ is not homogeneous in the parallel

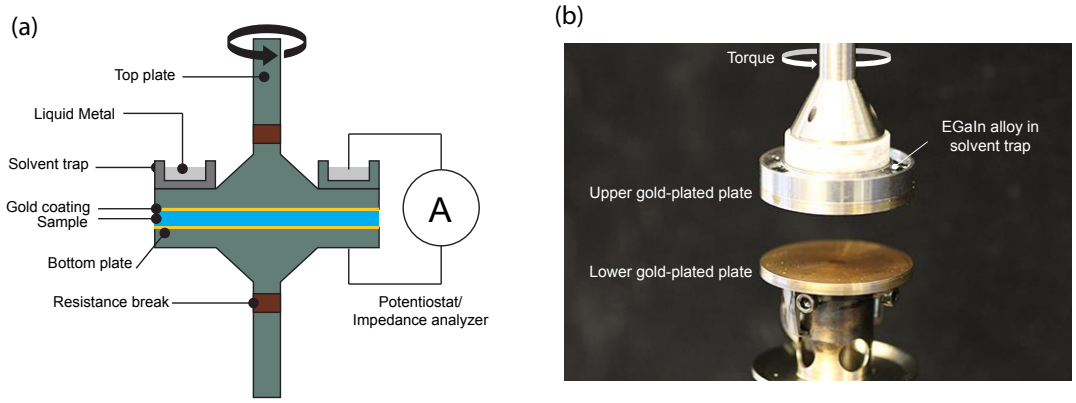


Figure 5-1: Schematic (a) and picture (b) of the EGaIn rheo-electric test fixture. The sample is sandwiched between two parallel plates ($R = 20$ mm) that form a two-electrode closed electrical circuit. The rotating upper plate is driven by a stress-controlled rheometer that applies stress and measures strain. Liquid metal (EGaIn) in the solvent trap provides a low-friction electrical contact to the rotating shaft. The plates are sputter-coated in gold to reduce contact resistance.

plate geometry and depends on the radial position $r$, as follows: $\dot{\gamma}(r) = r\Omega_{rot}/H$, where $\Omega_{rot}$ denotes the angular velocity of the upper plate. The impact of such inhomogeneity on the rheological measurements is taken into account and discussed in section 5.3. The geometry forms a closed electrical circuit that incorporates $(i)$ the conductive sample, $(ii)$ the plates, $(iii)$ the electrical measuring system formed by a potentiostat (Solartron SI1287) with an Impedance Analyzer (SI1266) and $(iv)$ the solvent trap (constructed from a machined annulus of SS316) filled with eutectic gallium-indium liquid metal (EGaIn, from GalliumSource). EGaIn is a liquid metal at room temperature which provides a safe non-hazardous alternative to other liquid metals such as mercury [253] and is used to create a low-friction continuous electrical connection to the rotating shaft. Finally, to reduce the contact resistance, the plates are sputter-coated with gold using a Pelco SC-7 sputterer for 10 min. Unless otherwise noted, all rheo-electric tests were performed at a temperature $T = (23.0 \pm 0.3)°C$, with a gap $H = 750$ $\mu$m. A laser-cut acrylic enclosure was designed to surround the test fixture to contain the liquid metal in case of accidents or spills. A photo showing

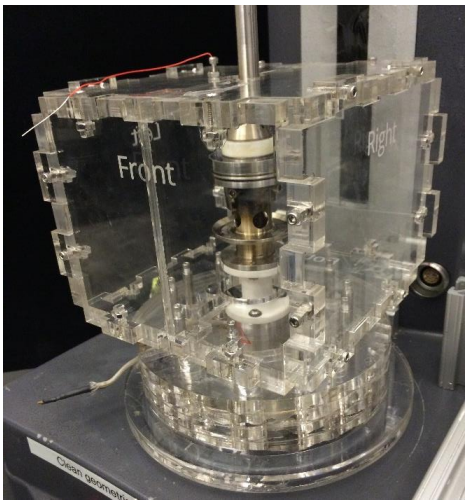


Figure 5-2: Picture of the acrylic enclosure surrounding the test fixture. The enclosure allows the containment of the liquid metal in case of a spill.

this enclosure is shown in Fig. 5-2.

Under static conditions, two types of electrical conductivity measurements are of interest: DC and AC tests. In a DC test, a constant potential $\phi_0 = 100$ mV is applied and the corresponding current $I$ is measured. The apparent DC conductivity $\sigma_a$ is then given by

$$\sigma_a = \frac{H}{\pi R^2}\frac{I}{\phi_0} \tag{5.1}$$

where $H$ is the sample gap imposed by the rheometer. In an AC test, a sinusoidal potential $\phi = \phi_0 \sin(\omega t)$ is applied and the corresponding alternating current is measured. The complex impedance is defined as

$$Z^*(\omega) = \frac{\phi}{I} = Z' - iZ'' \tag{5.2}$$

where $Z'$ and $Z''$ are, respectively, the real and imaginary contributions to the impedance. Note that $Z'$ and $Z''$ are the electrical analog of the real and imaginary contributions ($\eta'$ and $\eta''$ respectively) to the complex viscosity $\eta^*(\omega)$ in rheology, which will be of interest in section 5.2.2 [267, 268]. Finally, the complex impedance is

related to the complex dielectric permittivity through the following expression [269]:

$$\epsilon^* = \frac{H}{Z^* i\omega\epsilon_0 \pi R^2} \tag{5.3}$$

In both AC and DC measurements, it is important to note that the measured resistances and impedances correspond to a sum of two contributions: a bulk resistance due to the sample resistance, and an interfacial contact resistance representing how readily the electrons can flow through the interface between the sample and the plates so that:

$$\mathcal{R}_{measured} \equiv \frac{\phi_0}{I} = \mathcal{R}_{contact} + \frac{H}{\sigma_{bulk}\pi R^2} \tag{5.4}$$

Traditionally, by conducting measurements at different gaps, the contribution of the contact resistance can be calculated in conjunction with Eq. (5.4) and corrected for [269]. For strongly conductive fluids, the relative contribution of the contact resistance becomes increasingly important as the bulk conductivity increases and cannot be neglected if accurate measurements are desired. Unless stated otherwise, the conductivity and impedance discussed hereafter correspond to the apparent quantity defined respectively in Eq. (5.1) and (5.2).

### 5.2.1 Mechanical and electrical calibration

We first discuss the mechanical calibration of the rheo-electric test fixture, and justify the preferential use of liquid metal in the electrical circuit compared to two other techniques, namely a gold spring and a salt solution that are commonly used in other existing rheo-electric configurations. On stress-controlled rheometers, friction acting on the rotating shaft during electrical measurements under shear can impede simultaneous rheological measurements. To quantify such friction, we have performed measurements of the torque $\mathcal{M}$ associated with the friction inherent to different electrical couplings: EGaIn, a gold leaf spring, and a salt solution. Results are reported as a function of the angular velocity $\Omega_{rot}$ of the upper plate in Fig. 5-3(a). The friction due to the liquid metal lies two orders of magnitude below that of the gold spring, and

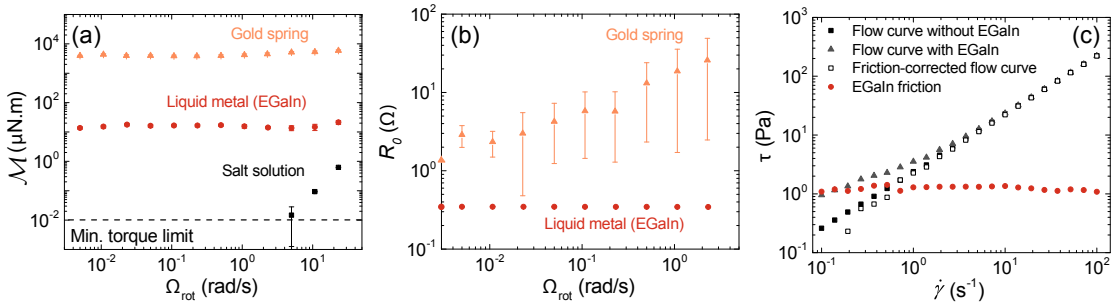


Figure 5-3: (a) Total measured torque $\mathcal{M}$ due to the friction of the electrical connection to the rotating shaft as a function of the angular velocity $\Omega_{rot}$ of the upper plate. Measurements are conducted in the absence of a sample and for different electrical contacts: a gold leaf spring, liquid metal (EGaIn) and a salt solution. (b) Setup DC resistance $\mathcal{R}_0$ measured in the absence of a sample as a function of $\Omega_{rot}$ for two electrical conductors: either a gold leaf spring or a liquid metal (EGaIn). Error bars are determined by calculating the standard deviation of the temporal signal over 180s. The use of a salt solution as a conductor does not allow for DC measurements as the ionic species will only polarize under DC current. (c) Measured flow curves showing shear stress $\tau$ vs shear rate $\dot{\gamma}$ for a Newtonian calibration oil and illustrating the friction correction due to EGaIn. Red filled circles represent the friction calibration performed with EGaIn in the absence of a sample prior to the flow curve measurement. Green triangles and black squares represent respectively the flow curves measured with and without the liquid metal. Open black squares represent the final corrected flow curve.

is constant over four decades of angular velocity, thus leading to a straightforward correction for mechanical friction. This constant friction arises primarily from the thin oxide layer that forms on top of the liquid metal when in contact with air [270]. Furthermore, a signature of the existence of the oxide layer is the temporal fluctuations of the friction contribution to the stress shown in Fig. 5-4. These fluctuations can be neglected during simultaneous measurements in general, when operating at stresses larger than the background friction level.

Regarding the electrical calibration, the DC resistance $\mathcal{R}_0$ of the test fixture in the absence of any sample is measured as a function of angular velocity $\Omega_{rot}$ for a closed electrical circuit using either EGaIn or a gold spring [Fig. 5-3(b)]. The liquid metal leads to a low resistance $\mathcal{R}_0 = 0.3\ \Omega$ that is independent of angular velocity, which makes the contribution to the electrical resistance from the test cell easy to take into

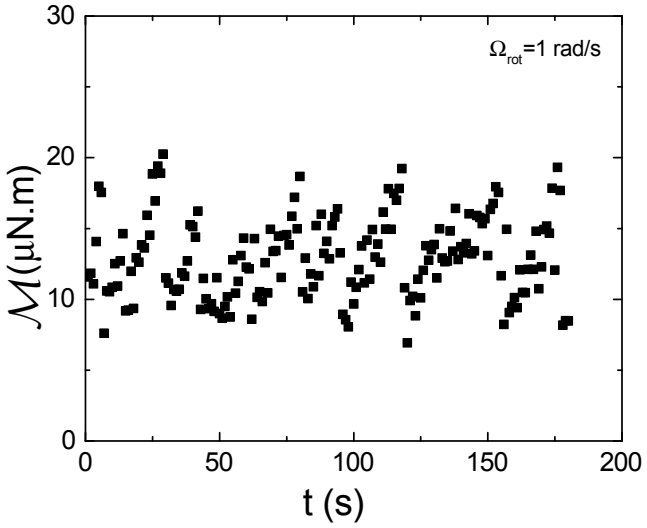


Figure 5-4: Typical fluctuations of the frictional torque $\mathcal{M}$ from the EGaIn alloy as a function of time. Data recorded in steady state for an angular velocity $\Omega_{rot} = 1$ rad/s of the upper plate, and with the liquid metal (EGaIn) ensuring the electrical contact. Such data are representative of the noise level associated with the rheological measurements when simultaneously conducting electrical measurements with the rheo-electric setup. For applied torques sufficiently large compared to $15 \pm 5$ $\mu$N.m, i.e. for stresses here larger than about $1.2 \pm 0.4$ Pa, such temporal fluctuations can be neglected.

account. On the contrary, the configuration involving the gold leaf spring shows a larger and much noisier resistance that increases with the plate rotation speed. We also emphasize that the use of a salt solution only allows for AC measurements at low potentials ($\phi_0 \leq 10$ V) and tends to have a complex electrical signature due to ion mobility that can complicate electrical corrections [269].

From both a mechanical and electrical standpoint, the test configuration using EGaIn is the most suitable for rheo-electric measurements on stress-controlled rheometers. As a result of the low friction, we are able to perform simultaneous measurements of rheology and conductivity, an example of which is shown in Fig. 5-3(c) on a calibration oil (N1000, Cannon Instrument Company). The additional friction due to the EGaIn is constant at about 1.2 Pa. By subtracting the latter value from the flow curve measured using the same experimental fixture, one recovers with high accuracy the true flow curve of the calibration oil measured in the absence of the electrical connections, at least for shear stresses $\tau \geq 1.2$ Pa. For shear stresses

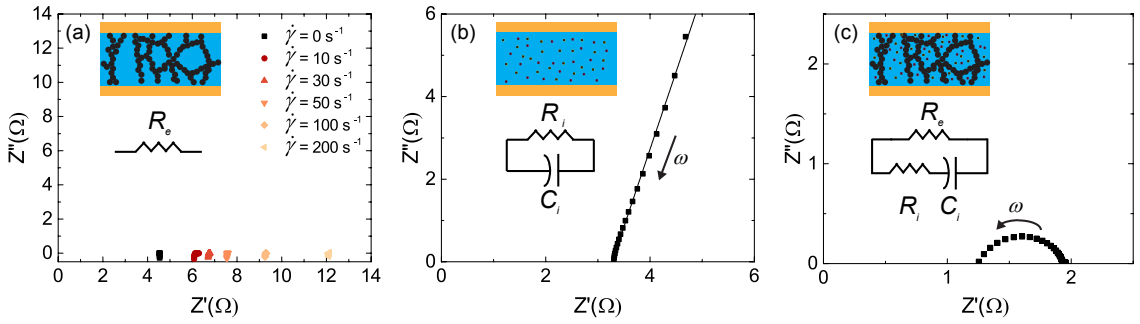


Figure 5-5: Nyquist plots of complex impedance for three different classes of conductive complex fluids and their corresponding equivalent circuits: (a) Electronic conductor: suspension of attractive soot particles (carbon Black, VXC72R) dispersed in mineral oil at 8% wt.. The conductivity is measured at different shear rates coded in color: $\dot{\gamma} = 0$, 10, 30, 50, 100 and 200 s$^{-1}$ from dark to light color; (b) Ionic conductor (Oakton 2764 $\mu$S/cm KCl solution) measured under static conditions for $H = 750$ $\mu$m. The linear fit corresponds to the model blocking circuit shown in the inset. (c) Mixed conductor: Lithium polysulfide suspension containing 2.5M $Li_2S_8$, 0.5M LiTFSI and 1M $LiNO_3$ with 1.5 vol% Ketjenblack carbon measured under static conditions. AC tests were performed for $10^2 \leq \omega \leq 10^4$ Hz.

$\tau < 1.2$ Pa, the corrected data departs appreciably from the constitutive equation showing that although conductivity measurements may still be performed, stress measurements should be conducted separately in this low stress range, i.e. without the upper electrode immersed in the liquid metal (EGaIn).

### 5.2.2 Benchmark electrical measurements

To illustrate the ability of the EGaIn rheo-electric fixture to perform accurate conductivity measurements, we conducted a series of benchmark AC measurements ($\phi_0 = 100$ mV, $10^2 \leq \omega \leq 10^4$ Hz) on different classes of conductive complex fluids, namely electronic, ionic and mixed conductors. The AC response of these fluids are reported in Fig. 5-5, where the imaginary part $Z''$ of the complex impedance is plotted vs the real part $Z'$ of the complex impedance. Such a representation, also known as a Nyquist plot [269], is analogous to a Cole-Cole plot for rheological measurements. First, we report the response of an electronic conductor, here a suspension of attractive soot particles (carbon black VXC72R, Cabot) dispersed in mineral oil at 8% wt. that is measured under steady simple shear flow. The electrical resistance

of this suspension is well represented by a pure ohmic resistor and corresponds to a series of points that sit on the horizontal axis of the Nyquist plot [Fig. 5-5(a)]. As the shear rate is increased, the resistance increases approximately three-fold due to the disruption of the floculated carbon black network under shear. Second, we report an example of an ionic conductor (Oakton 2764 $\mu$S/cm KCl solution, Cole-Parmer) measured under static conditions for $H = 750$ $\mu$m and at $T = 25.0$°C [Fig. 5-5(b)]. This suspension is represented by an ohmic resistor in parallel with an imperfect capacitor $[Z^*(\omega) = \mathcal{R}_i + 1/(i\omega C_i)^\alpha]$, represented by a constant phase element of phase $\alpha$. In the Nyquist plot, it appears as a line of slope $\tan(\alpha\pi/2)$ that intercepts with the horizontal axis at $Z' = \mathcal{R}_i$, which represents the ionic resistance of the solution. The experimental data are indeed well described by a blocking circuit [black fit in Fig. 5-5(b)]. Measurements at various gaps shown in Fig. 5-6 used in conjunction with Eq. (5.4) allow us to correct for the contact resistance and thus infer the bulk conductivity of the ionic solution. The contact resistance and bulk conductivity are found to be respectively $\mathcal{R}_c = 0.94\ \Omega$ and $\sigma_b = (2.76 \pm 0.01)$ mS/cm at $T = 25.0$°C, in excellent agreement with the value provided by the manufacturer ($\sigma = 2.764$ mS/cm). Finally, we consider a third sample which is an example of a semi-solid battery material that consists of a mixed conductor (Lithium polysulfide suspension containing 2.5M $Li_2S_8$, 0.5M LiTFSI and 1M $LiNO_3$ with 1.5vol% Ketjenblack EC600JD carbon black). Its equivalent circuit, which is the mechanical analog of the Jeffreys model in rheology [137], corresponds to a depressed semi-circle that intersects the horizontal axis at $Z' = \mathcal{R}_e\mathcal{R}_i/(\mathcal{R}_e + \mathcal{R}_i)$ and $Z' = \mathcal{R}_e$ respectively. The Nyquist plot of this slurry, determined under static conditions using the rheo-electric fixture is shown in Fig. 5-5(c). The ionic and electronic conductivities are estimated to be $\sigma_i = 2.6$ mS/cm and $\sigma_e = 3.7$ mS/cm respectively, in agreement with measurements previously reported on the same material [34].

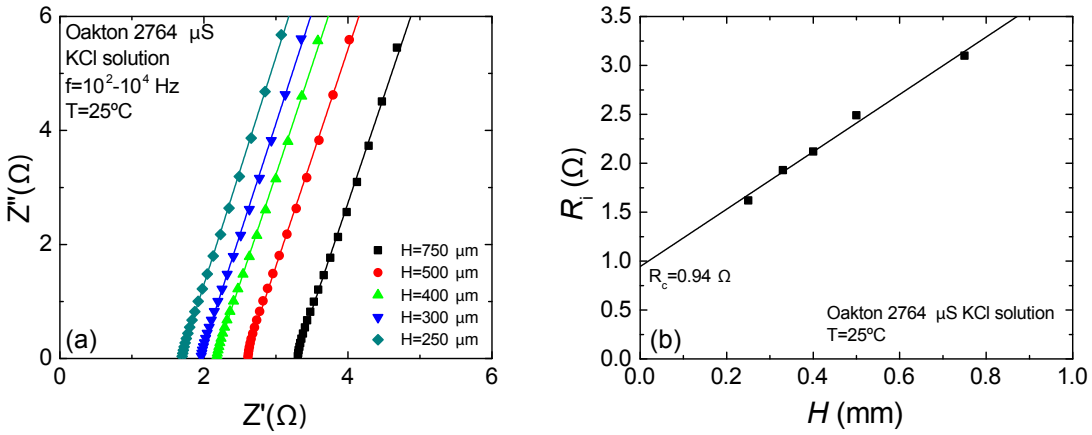


Figure 5-6: (a) Nyquist plot of the complex impedance for an ionic conductor (Oakton 2764 $\mu$S/cm KCl solution) measured under static conditions for various gap heights $H = 750, 500, 400, 330$ and 250 $\mu$m. This suspension is characterized by an ohmic resistor in parallel with an imperfect capacitor $[Z^*(\omega) = \mathcal{R}_i + 1/(i\omega C_i)^\alpha]$, represented by a constant phase element of phase $\alpha$ and which appears in the Nyquist plot as a line of slope $\tan(\alpha\pi/2)$ that intercepts with the horizontal axis at $Z' = \mathcal{R}_i$. Color lines pictured here correspond to the best linear fit of the data for each gap setting. (b) Ionic resistance $\mathcal{R}_i$ as determined in (a) vs the gap height $H$. The present data set shows that the sample resistance is divided into two contributions: a contact resistance $\mathcal{R}_c$ which corresponds to the intercept, and a bulk resistance associated with the slope; see Eq. (4) in the main text. The black line is the best linear fit of the data and leads to: $\mathcal{R}_c = 0.94\ \Omega$ and $\sigma_b = (2.76 \pm 0.01)$ mS/cm.

## 5.3 Derivation of electrical corrections in the parallel plate

In this section, we discuss corrections for the effects shear inhomogeneity and contact resistance on the measured conductivity in the parallel plate geometry. The demonstration of the importance of these corrections is discussed in section 6.4.

### 5.3.1 Shear inhomogeneity: Derivative method

In a parallel plate geometry, the shear rate $\dot{\gamma}$ is not homogeneous across the gap, but depends on the radial position $r$ as $\dot{\gamma}(r) = r\Omega_{rot}/H$, where $\Omega_{rot}$ is the angular velocity of the upper plate, and $H$ is the sample gap. Shear inhomogeneity can be corrected by means of the shear rate at the rim $\dot{\gamma}_R = R\Omega_{rot}/H$ and computing the stress at the

rim $\tau_R$ using the following expression [137]:

$$\tau_R(\dot{\gamma}_R) = \frac{\mathcal{M}}{2\pi R^3}\left[3 + \frac{d\ln \mathcal{M}/2\pi R^3}{d\ln \dot{\gamma}_R}\right] \tag{5.5}$$

where $\mathcal{M}$ denotes the torque applied on the upper plate. A similar expression can be derived for electrical measurements. Indeed, the total current $I$ that is measured is given by the following expression:

$$I = \frac{\phi_0}{H} 2\pi \int_0^R \sigma_a(r) r dr \tag{5.6}$$

where $\phi_0$ is the applied potential and $\sigma_a$ is the apparent conductivity. By changing the integration variable from $r$ to $\dot{\gamma}$, we obtain

$$I = \frac{\phi_0}{H}\frac{2\pi R^2}{\dot{\gamma}_R^2}\int_0^{\dot{\gamma}_R} \sigma_a(\dot{\gamma})\dot{\gamma} d\dot{\gamma} \ . \tag{5.7}$$

Differentiating this result with respect to $\dot{\gamma}_R$, while using the Leibniz formula leads to

$$\frac{dI}{d\dot{\gamma}_R} = \frac{-2I}{\dot{\gamma}_R} + \frac{\phi_0}{H}\frac{2\pi R^2}{\dot{\gamma}_R}\sigma_{a,R}(\dot{\gamma}_R) \ , \tag{5.8}$$

that can be rewritten into:

$$\sigma_{a,R}(\dot{\gamma}_R) = \left(\frac{H}{2\pi R^2}\frac{I}{\phi_0}\right)\left[2 + \frac{d\ln\left(\frac{H}{2\pi R^2}\frac{I}{\phi_0}\right)}{d\ln \dot{\gamma}_R}\right] \tag{5.9}$$

The latter expression relates the apparent conductivity at the rim of the plate $\sigma_{a,R}$ to the macroscopic current $I$ measured at a shear rate $\dot{\gamma}_R = R\Omega_{rot}/H$. Eq. (5.9) allows us to correct for the radial shear inhomogeneity in the parallel plate geometry.

### 5.3.2 Shear inhomogeneity: Single-point method

The single-point correction method relies on the Gaussian quadrature of moments equation which takes the following form [271]:

$$\int_0^1 f(x)x^k dx = \sum_{i=1}^{n} w_i f(x_i) \tag{5.10}$$

where $k$ and $n$ denote integer larger than 1 and the pairs $\{w_i,x_i\}$ are given in [272] In the parallel plate geometry, the torque $\mathcal{M}$ can be expressed as an integral:

$$\mathcal{M} = 2\pi \int_0^R \tau(r) r^2 dr \tag{5.11}$$

The integral can be non-dimensionalized by replacing the integration variable $r$ by $x = \dot{\gamma}/\dot{\gamma}_R = r/R$. We obtain

$$\mathcal{M} = 2\pi R^3 \int_0^1 \tau(x) x^2 dx \tag{5.12}$$

By using Eq. (5.10) with $n = 1$ and $k = 2$, we compute $\{w_i,x_i\}$= $\{1/3,3/4\}$, which leads to:

$$\mathcal{M} \simeq 2\pi R^3 \frac{\tau(3/4)}{3} \tag{5.13}$$

otherwise written as:

$$\boxed{\tau\left(\frac{3\dot{\gamma}_R}{4}\right) \simeq \frac{3\mathcal{M}}{2\pi R^3}} \tag{5.14}$$

Eq. (5.14) links the stress at $r = 3R/4$ to the torque $\mathcal{M}$. The error associated with Eq. (5.14) is generally less than 5% for Bingham plastic and Newtonian fluids [271]. Moreover, an expression similar to Eq. (5.12) can be derived for electrical measurements. Indeed, we can express the macroscopic current as follows:

$$I = \frac{\phi_0 2\pi R^2}{H} \int_0^1 \sigma_a(x) x dx \tag{5.15}$$

Using again Eq. (5.10) with $n = 1$ and $k = 1$, we find $\{w_i,x_i\}$= $\{1/2,2/3\}$ and thus

that

$$I \simeq \frac{\phi_0 \pi R^2}{H} \sigma_a(2/3) \tag{5.16}$$

which leads to the following expression:

$$\boxed{\sigma_a(\frac{2\dot{\gamma}_R}{3}) \simeq \frac{IH}{\phi_0 \pi R^2}} \tag{5.17}$$

which relates the apparent conductivity at $r = 2R/3$ to the macroscopic current $I$ at a rotation rate $\Omega_{rot}$ and a gap $H$. The static apparent conductivity given by the value of $(IH/\phi_0 \pi R^2)$ is thus associated with the shear rate $2\dot{\gamma}_R/3 = 2\Omega_{rot}R/3H$.

### 5.3.3 Contact resistance correction

Viscometric corrections for wall slip can be performed by conducting rheological measurements at different gaps [139, 273, 274]. If the flow curves obtained at various gaps superimpose, the material does not slip, whereas a gap-dependent rheology is the signature of wall slip. Assuming symmetric slip at both walls, the following kinematic relationship can be derived for a given imposed stress $\tau$ [139]:

$$\dot{\gamma}_a(\tau) = \dot{\gamma}_t(\tau) + \frac{2V_s(\tau)}{H} \tag{5.18}$$

where $\dot{\gamma}_a$ is the apparent shear rate, $\dot{\gamma}_t$ the true shear rate and $V_s$ denotes the slip velocity. In the case of a static measurement of conductivity, the apparent conductivity $\sigma_a$ measured experimentally is the sum of a bulk contribution $\sigma_b$ and a contact resistance $\mathcal{R}_c$ originating from the two interfaces:

$$\mathcal{R}_{measured} \equiv \frac{\phi_0}{I} = \frac{H}{\sigma_a \pi R^2} = \mathcal{R}_c + \frac{H}{\sigma_b \pi R^2} \tag{5.19}$$

To extend the latter correction to a sample flowing in the parallel plate geometry, we consider an annulus of width $\mathrm{d}r$ at a radius $r$ and define the specific contact resistance at radius $r$ as $\rho_c(r) = (\partial \mathcal{R}_c(r)/\partial j)$, where $\mathcal{R}_c$ is the contact resistance at a radius $r$ and $j = I/\pi R^2$ is the current density. In this annular ring, the incremental

conductance can be written as

$$d\mathcal{G}(r) = \frac{2\pi r \mathrm{d}r}{\rho_c(r)} + \frac{\sigma_b(r) 2\pi r \mathrm{d}r}{H} \tag{5.20}$$

and the current as

$$dI(r) = \phi_0 d\mathcal{G}(r) = \frac{\phi_0 r \mathrm{d}r}{\frac{\rho_c(r)}{2\pi} + \frac{H}{\sigma_b(r) 2\pi}} \tag{5.21}$$

Summing the above expressions, the resistance of each component adds in parallel and the macroscopic current measured reads

$$I = \int_0^R \frac{2\pi\phi_0 r \mathrm{d}r}{\rho_c(r) + \frac{H}{\sigma_b(r)}} \tag{5.22}$$

Furthermore, following the same derivation as for the mechanical correction [see Eq. (5.6), (5.7) and (5.8)] we obtain

$$\sigma_{a,R} = \frac{H}{2\pi R^2} \frac{I}{\phi_0} \left[ 2 + \frac{d \ln \left( \frac{H}{2\pi R^2} \frac{I}{\phi_0} \right)}{d \ln \dot{\gamma}_R} \right] = \frac{1}{\frac{\rho_{c,R}}{H} + \frac{1}{\sigma_{b,R}}} \tag{5.23}$$

In summary, by analogy to the slip correction in Eq. (5.18), for a given imposed stress at the rim $\tau_R$ as defined by Eq. (5.5), we can decouple the bulk contribution from the surface contribution to the conductivity as follows:

$$\boxed{\frac{1}{\sigma_{a,R}(\tau_R)} = \frac{\rho_{c,R}(\tau_R)}{H} + \frac{1}{\sigma_{b,R}(\tau_R)}} \tag{5.24}$$

Alternatively, if we use single-point determination methods to compute the apparent conductivity, we can derive the following relation:

$$\boxed{\frac{1}{\sigma_a[\tau(\frac{2\dot{\gamma}_R}{3})]} = \frac{\rho_c[\tau(\frac{2\dot{\gamma}_R}{3})]}{H} + \frac{1}{\sigma_b[\tau(\frac{2\dot{\gamma}_R}{3})]}} \tag{5.25}$$

We note that the use of Eq. (5.25) is only useful if the full flow curve is known (e.g. from a stress sweep) as information about the quantity $\tau(\frac{2\dot{\gamma}_R}{3})$ at a shear rate $\dot{\gamma} = 2\dot{\gamma}_R/3$ is unknown *a priori* since $\tau(\frac{3\dot{\gamma}_R}{4})$ is the quantity obtained from the single-

point determination method applied to the rheological data.

## 5.4 Rheo-electric test fixture: cone-plate

Unlike the parallel plate geometry, the cone-plate geometry has the advantage of having a homogeneous shear rate distribution across the radius, allowing for controlled precise measurements. Shear inhomogeneity can sometimes lead to complex experimental artefacts, in particular when conducting large amplitude stress-controlled oscillatory measurements (LAOStress) [275, 276]. For LAOStress measurements, it is challenging to derive the viscoelastic compliances in a parallel plate geometry due to the radial shear inhomogeneity. To our knowledge, there are only approximate methods for performing theses measurements in parallel plate geometries [276, 277]. For cases such as LAOStress measurements, it is therefore useful to derive the conductivity of complex fluids in a cone-plate geometry. This section introduces an alternative rheo-electric test fixture that is more suitable for oscillatory measurements and we discuss derivations for conductivity measurements in a cone-plate geometry in the presence, and absence, of contact resistance effects.

### 5.4.1 Alternative rheo-electric test fixture for oscillatory measurements

Rheo-electric measurements can alternatively be performed using a standard dielectric geometry where a wire is connected to the upper plate through the center of the shaft. In this case, only oscillatory measurements are possible due to the finite length of the wire and the motion of the shaft is generally limited to two rotations in either direction. However, this allows for simultaneous rheo-electric measurements at stresses lower than those attainable with the test fixture using liquid metal, which is of interest for small amplitude oscillatory measurements. We note that the choice of the geometry (cone or plate) is independent from the choice of the rheo-electric test fixture. Here, we calibrate an alternative rheo-electric setup using a cone-plate

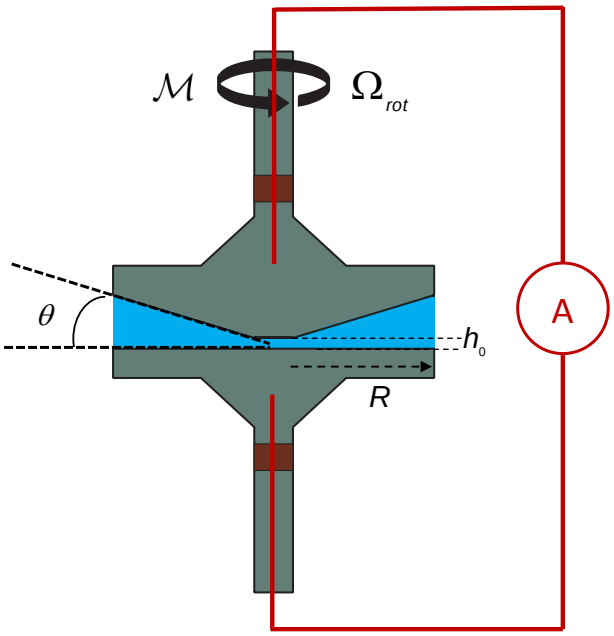


Figure 5-7: Schematic of a cone-plate geometry in an alternative rheo-electric test fixture using wires connected to the center of the rheometer shafts. The angle $\theta$ is typically small ($\theta \leq 4°$). The A in the circle represents the potentiometer and impedance analyzer used to apply and measure the voltage and current for electrical measurements.

geometry but results shown here are applicable to a parallel plate geometry as well. Similarly, a cone-plate geometry could potentially be used in the liquid metal rheo-electric test fixture as well.

Fig. 5-7 shows a cone-plate geometry in a rheo-electric test fixture using wires connected to the center of the rheometer shafts. The truncated cone has a small truncation gap $h_0$ and a small angle $\theta$ ($\theta \leq 4°$). In this geometry, the shear rate is given by $\dot{\gamma} = \Omega_{rot}/\theta$ and the shear stress is given by $\tau = 3\mathcal{M}/2\pi R^3$ where $R$ is the radius of the cone.

Similarly to the corrections performed for the liquid metal test fixture in section 5.2.1, we performed mechanical and electrical calibration measurments for the test fixture using wires (Copper, gauge 30). Fig. 5-8 shows the viscoelastic moduli for a strain amplitude sweep at $\omega = 6.28$ rad/s measured using the wire rheo-electric test fixture in the absence of a sample in the rheometer. These measurements demonstrate

that the tension in the wire has a signature on the shear oscillatory measurements, primarily in the form of a finite and constant contribution of $G' \simeq 30$ Pa at small amplitudes. This sets the limit of viscoelastic moduli that can be measured simultaneously with the conductivity using this test fixture. Electrical calibration measurements were also performed and the wire resistance was found to be $\mathcal{R}_{wire} = 0.3\ \Omega$ independently of the angular displacement of the upper plate. Rheo-electric measurements using this test fixture are discussed further in Chapter 7.

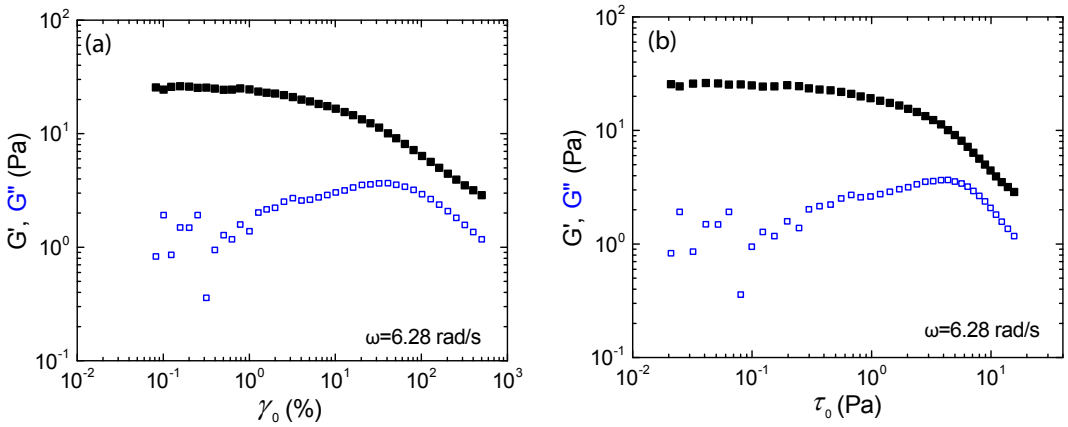


Figure 5-8: Mechanical calibration of the rheo-electric test fixture using wires connected to the center of the rheometer shafts. Viscoelastic moduli $G'$ (closed symbols) and $G''$ (open symbols) vs. strain amplitude $\gamma_0$ (a) and stress amplitude $\tau_0$ (b) obtained from a strain amplitude sweep at $\omega = 6.28$ rad/s using the wire rheo-electric test fixture in the absence of a sample in the rheometer.

### 5.4.2 Benchmark in the absence of contact resistance

In this section, we derive the relationship between the measured current $I$ and the conductivity $\sigma$ in a DC potentiostatic test with an applied potential $\Phi_0$ for a fluid placed in a cone-plate geometry. We assume that the contact resistance is negligible at first and will discuss the effects of contact resistance on the measurement in section 5.4.3. The angle of the cone $\theta$ is assumed small, therefore the height at each radius $r$ is $H(r) = r\theta$ and we can define the truncation radius $r_0$ as $r_0 = h_0/\theta$ where $h_0$

is the truncation gap. Due to the assumption of a small cone angle, we make the approximation that the electric field lines are perpendicular to the bottom plate and are similar to field lines found in a parallel plate geometry. We define annuli of radius $r$, width $dr$ and height $H(r)$ and compute the incremental conductance outside of the truncation region as

$$d\mathcal{G}(r) = \sigma \frac{2\pi r dr}{H(r)}. \tag{5.26}$$

By summing the incremental conductances inside and outside the truncation region, the resistance of each annuli adds in parallel and the macroscopic current measured reads

$$I = \sigma\phi_0\Big(\int_{r_0}^{R} \frac{2\pi dr}{\theta} + \frac{\pi r_0^2}{h_0}\Big) \tag{5.27}$$

which yields

$$\boxed{I = \frac{2\pi\sigma\phi_0}{\theta}\big(R - \frac{r_0}{2}\big) \simeq \frac{2\pi R\sigma\phi_0}{\theta}} \tag{5.28}$$

Eq. 5.28 relating current and conductivity in a cone-plate geometry is consistent with solving the Laplace equation $\nabla^2\phi = 0$ in the cone plate geometry with the boundary condition $\nabla_r\phi(H) = 0$. This boundary condition is equivalent to the vertical electric field lines approximation described previously. This relationship remains true as the cone rotates and the material is sheared since the shear rate is homogeneous in the cone-plate geometry. For a carbon black gel (VXC72R, Cabot in mineral oil) at 6% wt. at $T = 23°$C, the conductivity measured using a cone-plate geometry of radius $R = 25$ mm, angle $\theta = 4°$ and truncation gap $h_0 = 55$ $\mu$m is found to be $\sigma_{cone} = 0.75 \pm 0.04$ mS/cm while the conductivity measured in the parallel plate geometry ($R = 20$ mm, $H = 0.75$ mm) is found to be $\sigma_{plate} = 0.86 \pm 0.03$ mS/cm. This discrepancy is possibly related to contact resistance contributions that could play a larger role in a cone-plate geometry due to the presence of a smaller distance between the electrodes where the contact resistance might dominate the bulk resistance.

### 5.4.3 Effect of contact resistance on conductivity measurements

In this section, we introduce a specific contact resistance $\rho_c$ and compute its contribution to the overall measured apparent conductivity and current. Using the same summation method as Eq. 5.28, the measured current reads

$$I = \phi_0 \left( \int_{r_0}^{R} \frac{2\pi r dr}{\rho_c + \frac{r\theta}{\sigma}} + \frac{\pi r_0^2}{\rho_c + \frac{r_0\theta}{\sigma}} \right). \tag{5.29}$$

By computing the different terms in the integral in Eq. 5.29, we obtain the following expression for the measured current:

$$\boxed{I = \frac{2\pi\sigma\phi_0}{\theta} \left( R - r_0 + \frac{r_0}{2(1 + \frac{\rho_c\sigma}{\theta r_0})} + \frac{\rho_c\sigma}{\theta} \ln \left( \frac{1 + \frac{\theta r_0}{\rho_c\sigma}}{1 + \frac{\theta R}{\rho_c\sigma}} \right) \right)} \tag{5.30}$$

We observe that the contribution of the contact resistance can be significant and is a function of the non-dimensional numbers $\frac{\rho_c\sigma}{\theta r_0}$ and $\frac{\rho_c\sigma}{\theta R}$. In the cone-plate geometry, the gap reaches relatively small values compared to the parallel plate geometry and therefore the contact resistance has a larger contribution, particularly close to the truncation region. A specific contact resistance $\rho_c = 5\ \Omega.\text{cm}^2$ is sufficient to account for the discrepancy between the conductivity measurements in the parallel plate and cone-plate geometries on the 6% wt carbon black gel discussed in section 5.4. This value for the specific contact resistance is consistent with other measurements on this class of materials as shown in section 6.4 . These results indicate that contact resistance can strongly affect the measurement of conductivity in a cone-plate geometry. Due to this effect, when using a cone-plate geometry, the reported conductivity values may be systematically biased towards lower values, the parallel plate geometry, a convenient method for contact resistance correction is challenging to perform. However, in cases when the contact resistance is negligible or when our interest lies in the relative evolution of the conductivity between a sheared and a static state, cone-plate fixtures can be used as a rheo-electric geometry with homogeneous shear rate.

To conclude, the use of gold-sputtered plates and EGaIn to close the electrical

circuit allow for accurate electrical measurements on a wide variety of strongly conductive complex fluids, which demonstrate the versatility of the EGaIn rheo-electric test fixture. More generally, the low friction rheo-electric apparatus we have designed for stress-controlled rheometers paves the way for a wider use of rheo-electrical measurements in the broad soft matter community. In particular, the EGaIn apparatus enables two-electrode electrochemical tests to be performed under flow, which is of primary importance for flow batteries, where the systematic characterization of cell performance under flow in a controlled environment is crucial for cell design and optimization. In addition, we introduce an alternative rheo-electric test fixture using wires connected to the center of the rheometer shafts that is more suitable for oscillatory measurements. We derive, for the first time, expressions to calculate the conductivity of a fluid in a cone-plate geometry for rheo-electric tests where a homogeneous shear rate is desired (e.g. LAOStress). We show however that contact resistance can decrease the accuracy of the conductivity measurements in this geometry. In chapter 6, we employ the EGaIn rheo-electric fixture to investigate in detail one of the afore-mentioned model systems, namely carbon black gels.

# Chapter 6

# Rheo-electrical Study of Carbon Black Gels

## 6.1 Introduction

In this section, we aim at illustrating the relevance of this apparatus on a class of strongly conductive complex fluids, namely carbon black gels. We focus on carbon black dispersions as a case study of a strongly conductive complex fluid to illustrate the additional insight that can be gained from this rheo-electric apparatus. Carbon black (CB) which refers generically to colloidal soot particles produced from the incomplete combustion of fossil fuels, is utilized extensively in a wide variety of industrial applications including batteries, paints, coatings as well as filled rubbers and tires. CB serves as an additive to convey protection from ultra-violet light, increase toughness, improve processability and to enhance electrical conductivity [97, 104]. Composed of permanently fused "primary" particles whose diameter is about 30 nm [85], CB particles are of typical size 200-500 nm and display short range attractive interactions of typical strength 30 $k_BT$ [86]. When dispersed in a liquid hydrocarbon, carbon black particles form a space-spanning network, even at small volume fractions (typically 1 to 5%) [88, 90]. The resulting gels are reversible, as they are destroyed by large shear and reform once the flow is stopped. The elastic modulus and yield stress depend on the flow history which can be used to tune

the solid-like properties of the gel at rest [92, 195]. Finally, shear-induced changes in microstructure are known to strongly affect the electrical properties of carbon black gels as the percolated network ruptures under shear [33, 250, 266]. Depending on the choice of the carbon black, the conductivity of the gel either decreases by several orders of magnitude as the material is sheared and undergoes a conductor to insulator transition [33], or, in the case of more conductive samples, the conductivity only decreases by a small factor under shear [250].

In this work, a number of CB dispersions are prepared in the absence of any additional dispersant by mixing CB particles of different grades [VXC72R, Monarch 120 and Elftex 8 from Cabot chemicals (Billerica, MA), and KetjenBlack EC600 from Akzo Nobel (USA)] into a light mineral oil (Sigma, density 0.838 g/cm$^3$, viscosity 20 mPa.s) as described in ref. [264] at weight concentrations $c$ ranging from 4 to 15% wt. The samples are sonicated for 4 hours and mixed thoroughly prior to any use. In the following sections, we mainly report data obtained with a 8% wt. carbon black gel (VXC72R) which has been extensively studied in the literature [92, 239, 265, 278]. Such a gel is used here as a model conductive complex fluids as it shows neither chemical aging nor any evaporation, and allows for reproducible measurements over long durations. Furthermore, the VXC72R carbon black has been specifically developed for high conductivity applications and is an ideal system to explore the rheo-electric properties of strongly conductive complex fluids. For this chapter, all measurements will be conducted using the parallel plate geometry.

Fig. 6-1 shows an example of a simultaneous rheo-electric measurement in a 8% wt. VXC72R carbon black gel using the rheo-electric test fixture. The gel is repeatedly subjected to cycles of imposed constant shear rate $\dot{\gamma}_0 = 100$ or 10 s$^{-1}$ for 5 min followed by an imposed zero stress *tau* for 5 min. We observe that we are able to temporally resolve both the apparent conductivity and the stress under flow. The results in Fig. 6-1(a) shows that while the stress reaches steady state rapidly, the conductivity takes a few minutes to reach steady state. Additionally, when the imposed shear rate is sufficiently high i.e. $\dot{\gamma}_0 = 100$ s$^{-1}$, the conductivity is constant and repeatable for cycle to cycle. This indicates that this shear rate is sufficiently high to fluidize

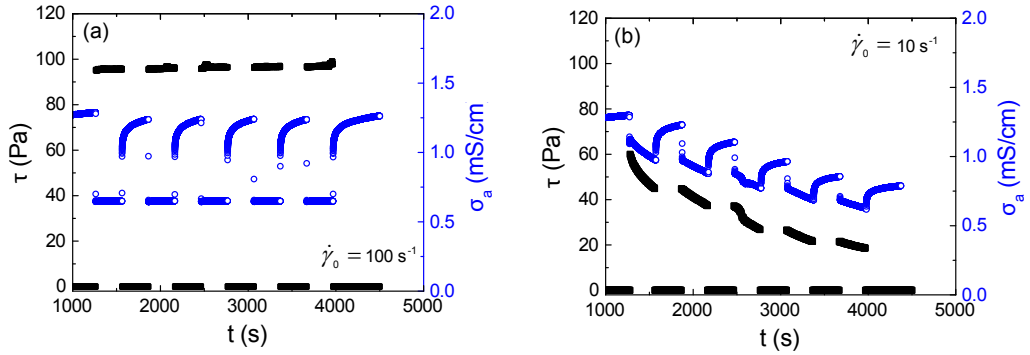


Figure 6-1: Stress $\tau$ (black squares) and apparent conductivity $\sigma_a$ (blue circles) vs time $t$ measured in a 8% wt. VXC72R carbon black gel. The gel is repeatedly subjected to cycles of imposed constant shear rate $\dot{\gamma}_0$ for 5 min followed by an imposed zero stress $tau$ for 5 min. In (a), $\dot{\gamma}_0 = 100\ s^{-1}$ while in (b), $\dot{\gamma}_0 = 10\ s^{-1}$

the gel completely and erase any memory of the shear history of the sample. This result will be useful during our measurements as generally, we will choose pre-shear rates $\dot{\gamma}_p \leq 100\ s^{-1}$ to erase any shear history of the sample. However, as seen in Fig. 6-1(b), for an imposed shear rate $\dot{\gamma}_0 = 10\ s^{-1}$, we observe irreversible phenomena from cycle to cycle. Both the stress and the conductivity decrease during the shearing cycles, a reflection of the existence of complex flow phenomena such as wall slip or structuration during those measurements. This behavior demonstrates the rheological complexity in CB gels and the need for a closer investigation and will be discussed further in section 6.4.

Using the rheo-electric test fixture characterized in Chapter 5, we first determine the electrical and mechanical solid-like properties of the CB gel at rest, which is brought to rest through different flow cessation protocols (section 6.2). We then focus on transient flows and perform creep experiments to study the yielding behavior of the CB gel from an electrical perspective (section 6.3). Finally, we report an extensive study of steady shear flows of the CB gel, and show how electrical measurements allow us to detect flow heterogeneities and wall slip (section 6.4). To conclude, a discussion section including a quantitative comparison of the rheo-electric properties of CB gels, prepared with different grades of CB, shows how the nature of the CB particles greatly affects the ensuing rheo-electric properties of the gels. Such analysis, made

possible with the rheo-electric fixture introduced here, is key for numerous applications where the selection of an appropriate conductive sample should obey specific design constraints on both the mechanical and electrical properties (section 6.5).

## 6.2 Tuning rheo-electric properties of carbon black gels using shear history

Recent studies have shown that the mechanical properties of weak attractive gels can be tuned by controlling their shear history [104, 142, 279]: abrupt flow cessation or "quenching" leads to highly elastic gels, whereas slow cessation of shear leads to weak solids characterized by a vanishingly small yield stress for decreasing flow cessation rate. In this subsection, we investigate the evolution of the electrical properties concomitantly to the elastic properties of the gel prepared by flow cessation experiments at various cessation rates. Ramps of decreasing stress from $\tau = 100$ Pa to $\tau = 0$ Pa bringing the sample at complete rest are performed in $N = 100$ successive steps. The upper stress value is applied for 5 min before the start of each decreasing ramp, and is chosen to be large enough to ensure the sample is fully fluidized and that any previous flow history is erased. The flow cessation rate is controlled through the duration of each step $\Delta t$, that is varied in each test from 1 s to 120 s. The resulting flow and conductivity curves are plotted in Fig. 6-2. As the stress is ramped down, the shear rate decreases and the conductivity concomitantly increases. Such results coincide with the fact that the gel transitions from a fully fluidized state at high shear rates to a solid-like state at rest. The gels structure builds up, forming a percolated network which accounts for the solid-like behavior and the conductivity increase. For $\dot{\gamma}_a > 30$ s$^{-1}$, the flow and conductivity curves obtained at different cessation rates collapse, indicating that in this region the gel is fully fluidized, and not sensitive to the flow history. At lower shear rates, both the flow and conductivity curves become strongly sensitive to the flow cessation rate: slower ramps (or increasing shearing durations $\Delta t$ spent at each rate) lead to lower yield stress (defined as the stress ex-

trapolation for vanishing shear rates) and lower apparent conductivity. These results are associated with the growth of a solid-like structure as the gel comes to a stop, whose formation kinetics are strongly affected by $\Delta t$.

To characterize the final state of the gel once the stress ramp is over, we record both the terminal value of the conductivity $\sigma_0$, and the linear elastic moduli $G'_0$ determined by oscillations of small amplitude ($\gamma = 0.2\%$) at $f = 1$ Hz. These measurements are performed 90 min after the end of the stress ramp to ensure that mechanical and electrical equilibrium is reached as shown in Fig. 6-3. Repeating the experiment for various step durations $\Delta t$ allows us to extract a series of pairs $\{G'_0,\ \sigma_0\}$ that are plotted in Fig. 6-4. The elastic modulus $G'_0$ displays a power-law increase with the apparent conductivity at rest ($\sigma_0$) showing that there is a correlation between the mechanical and electrical properties of the gel at rest: slower ramps lead to softer and less conductive gels, a signature of lower connectivity in the sample-spanning network of CB aggregates. The latter results hold true at lower concentrations of carbon black particles. Data obtained following the same protocol with 4% wt. and 6% wt. carbon black gels [respectively (▲) and (•) in Fig. 6-4] show the same result and collapse on a master curve for $\sigma_0 \geq 0.1$ mS/cm, where $G'_0 \propto \sigma_0^{\alpha}$, with $\alpha = 1.65 \pm 0.04$. The latter result hints at a unique gelation scenario kinetically driven by shear and not sensitive to the particle concentration, at least for strong enough gels with $G'_0 \gtrsim 10$ Pa.

Finally, we have also performed sudden quenches, that is the CB gel is brought from $\tau = 100$ Pa to $\tau = 0$ Pa within 1 s. In that case, the conductivity is comparable to that obtained with the fastest ramp previously explored (of total duration 100 s), but the elastic modulus is much larger so that the rheo-electric properties at rest [open symbols in Fig. 6-4] do not fall onto the same master curve as the ramp tests of longer duration. However, we emphasize that the terminal elastic modulus still appears to grow as a power-law function of the conductivity, and the exponent is compatible (within error bars) with the value determined for softer flow cessations. For the three concentrations examined, abruptly stopping the shear flow leads to a gel of enhanced elasticity which hints at a specific gel microstructure that is well adapted to sustain shear and yet not more conductive (hence percolated) than gels formed in

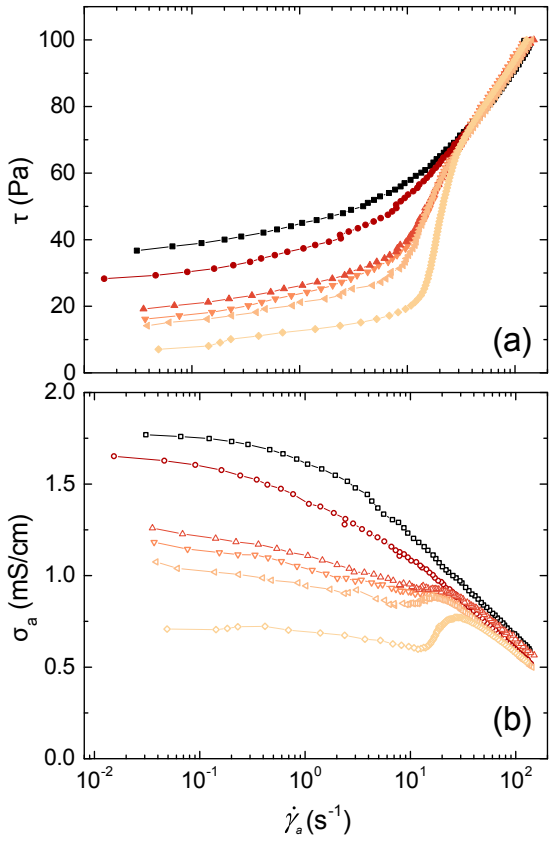


Figure 6-2: (a) Stress $\tau$ vs apparent shear rate $\dot{\gamma}_a$ (b) Apparent conductivitiy $\sigma_a$ vs the apparent shear rate $\dot{\gamma}_a$ measured in a 8% wt. VXC72R carbon black gel during decreasing ramps of stress from $\tau = 100$ Pa to $\tau = 0$ Pa. Each test was performed in $N = 100$ steps of 1 Pa each and different duration per point $\Delta t$ was used for each experiment. From top to bottom: $\Delta t = 1, 6, 15, 21, 30$ and 120 s.

a fast ramp of 100 s. These results show that the electrical properties of carbon black gels can be tuned through the shear history in parallel to the mechanical properties.

## 6.3 Stress-induced yielding in creep measurements

In this section, we turn to the transient behavior of carbon black gels and investigate the evolution of the rheo-electric properties of the 8% wt. CB gel (VXC72R) during its stress-induced yielding transition. Prior to each creep experiment, the CB gel is presheared at $\dot{\gamma} = 200$ s$^{-1}$ for 5 min to erase previous flow history, and left to rebuild for 20 min at $\tau = 0$ Pa. A constant stress is then applied from $t = 0$ and

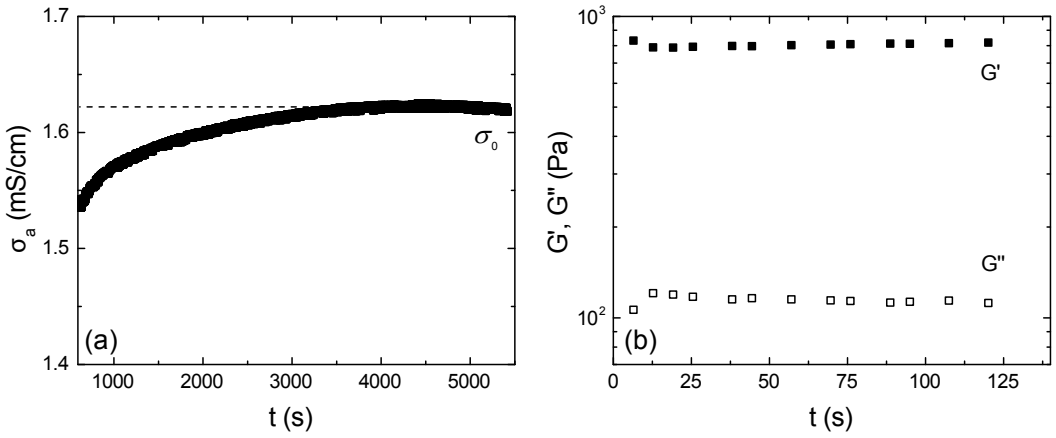


Figure 6-3: (a) Temporal evolution of the apparent conductivity $\sigma_a$ in a 8% wt. carbon black gel (VXC72R) during the 90 min recovery period that follows a decreasing ramp of stress, from $\tau = 100$ Pa to $\tau = 0$ Pa. The stress and conductivity data associated with the ramp are pictured in Fig. 4 in the main text (duration per point $\Delta t = 6$ s). The conductivity reaches a steady-state value $\sigma_0$ =1.62 mS/cm after about an hour. (b) Viscoelastic moduli $G'$ and $G''$ vs. time, measured with oscillations of small amplitude ($\gamma_0 = 0.2$ %) at $\omega = 6.3$ rad/s, after the 90 min recovery period pictured in (a). The viscoelastic moduli are constant with values $G'_0 = 805 \pm 4$ Pa, and $G''_0 = 114 \pm 6$ Pa. The values of $\sigma_0$ and $G'_0$ are reported in Fig. 5 in the main text, and further determined systematically for different ramp durations $\Delta t$ in carbon black gels of various concentrations to assemble the data set reported in Fig. 5 in the main text.

the resulting shear-rate response $\dot{\gamma}(t)$ and apparent conductivity response $\sigma_a(t)$ are monitored simultaneously. Results for different applied shear stresses are reported in Fig. 6-5.

All the creep experiments display three characteristic regimes that we illustrate in Fig. 6-6(a) for the case of an experiment conducted at $\tau = 22$ Pa. (*i*) First, for $t < 3800$ s the shear rate decreases as a power law: $\dot{\gamma}(t) \sim t^{-0.9}$ while the apparent conductivity increases as a weak power law: $\sigma_a(t) \sim t^{0.035}$. Fig. 6-6(b) shows a logarithmic plot of the same data to emphasize the power law characteristics of the primary creep regime. (*ii*) Second, for 3800 s $\leq t \leq$ 4600 s, a jump in the shear rate is observed and the apparent conductivity drops concomitantly by half and fluctuates. (*iii*) Third, for $t > 4600$ s, the shear rate undergoes a second steep increase while the apparent conductivity drops, before both observables tend towards

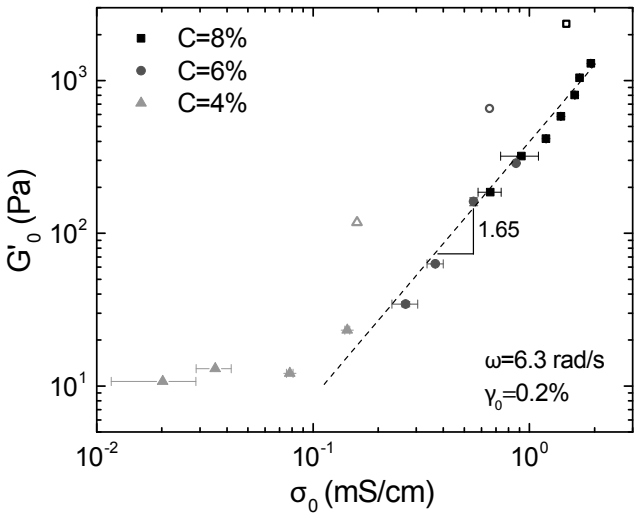


Figure 6-4: Elastic modulus $G_0'$ of carbon black gels vs conductivity $\sigma_0$ measured at rest, 90 min after the end of a decreasing stress ramp from 100 Pa to 0 Pa and composed of 100 steps. Each point corresponds to different step durations $\Delta t$ during the ramp, from $\Delta t = 1$ s to 120 s, while symbols stand for different concentrations of carbon black (VXC72R): $c$ =4% wt. (▲), 6% wt. (●) and 8% wt. (■). Open symbols stand for an instantaneous quench from $\tau = 100$ Pa to $\tau = 0$ Pa. Data for the 8% wt. gel corresponds to the experiment reported in Fig. 6-2. Oscillatory measurements were performed at a strain $\gamma_0 = 0.2\%$ and a frequency $f = 1$ Hz. The dashed line corresponds to the best power-law fit of the data for $\sigma_0 \geq 0.1$ mS/cm, i.e. $G_0' = \tilde{G_0'}\sigma_0^{\alpha}$, with $\tilde{G_0'}$ =400 Pa.(cm/mS)$^{\alpha}$ and $\alpha = 1.65 \pm 0.04$.

a final steady-state value. The mechanical response alone of this "delayed yielding" has been previously reported in a Couette geometry [264, 265]. Coupled with time-resolved velocimetry, the latter studies have shown that the three regimes can be interpreted as a succession of $(i)$ homogeneous deformation above the micron scale followed by $(ii)$ a total wall slip regime associated with the first rapid increase of $\dot{\gamma}(t)$, and the growth of a transient shear band [second increase of $\dot{\gamma}(t)$] to finally reach $(iii)$ a homogeneous flow.

The unique signature of these regimes also appears in the apparent conductivity response which provides further insights into the yielding behavior. Indeed, in the first regime, the increase in apparent conductivity clearly demonstrates that either the bulk microstructure of the sample, or the number of contacts between the sample and the wall, is evolving. The latter result highlights the high sensitivity of the

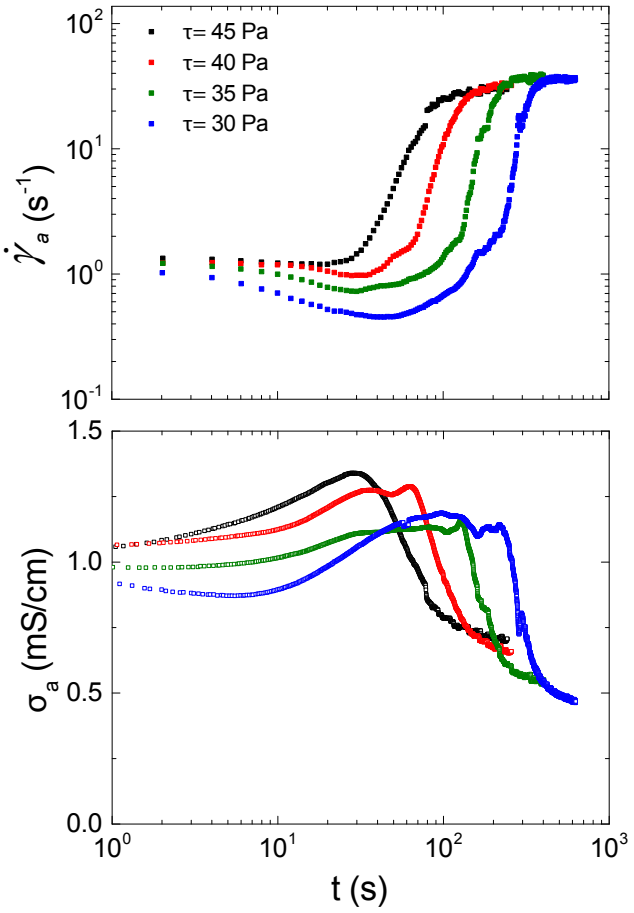


Figure 6-5: Creep experiments in a 8% wt. carbon black gel (VXC72R) at various stresses $\tau = 45, 40, 35$ and 30 Pa. (a) Shear-rate response $\dot{\gamma}_a(t)$ and (b) apparent conductivity response $\sigma_a(t)$. Before each experiment, the gel is presheared at $\dot{\gamma} = 200$ s$^{-1}$ for 5 min to erase previous flow history, and then left to restructure for a waiting time $t_w = 1200$ s at $\tau = 0$ Pa.

rheo-electric test fixture in the first regime where the sample deformation remains extremely low [$\gamma \lesssim 4\%$ for $t$ <3800 s] and where other techniques, including ultrasonic velocimetry [265], fail to provide time-resolved data due to a lack of resolution. In the intermediate regime, the decrease in the apparent conductivity is compatible with the onset of slip which is expected to increase the electrical resistance at the interface. Moreover, the oscillations observed in the apparent conductivity are strongly reminiscent of the stick-slip like motion of the carbon black gel reported in ref. [265], where alternating plug and shear flow regions have been observed. Finally, in the third regime, the conductivity reaches its lower, constant value – which is in

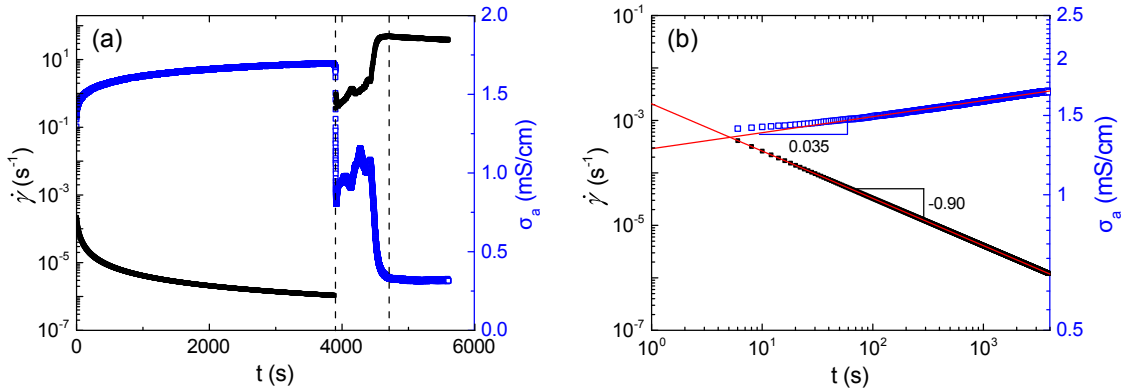


Figure 6-6: Creep experiment in a 8% wt. carbon black gel (VXC72R) at $\tau = 22$ Pa. (a) Shear rate response $\dot{\gamma}(t)$ and apparent conductivity response $\sigma_a(t)$. The shear rate was derived numerically from the strain measured by the rheometer to increase the precision. The jump observed in the curves at $t = 3800$ s marks the onset of a total wall slip regime followed by the growth of a transient shear band [265] before the sample reaches a homogeneous steady state. The vertical dashed line marks the three different flow regimes discussed in the text: primary creep, heterogeneous flow and steady-state flow. (b) Apparent shear-rate response $\dot{\gamma}_a(t)$ and apparent conductivity response $\sigma_a(t)$ on doubly-logarithmic scales to emphasize the power law characteristics of the primary creep regime. The same data is shown as that presented in Fig. 6(a) in the main text. The shear rate was calculated numerically from the strain measured by the rheometer to increase the precision. The red lines correspond to the best power-law fits of the data that leads to $\dot{\gamma}_a(t) = At^{\alpha}$ with $A = (2.3 \pm 0.1)\ 10^{-3}$ s$^{-\alpha-1}$ and $\alpha = -0.90 \pm 0.02$ and the $\sigma_a(t) = Bt^{\beta}$ with $B = 1.26 \pm 0.01$ mS.s$^{-\beta}$/cm and $\beta = 0.035 \pm 0.002$. We note that the power law fit of the conductivity is hardly distinguishable from a logarithmic fit $\sigma_a(t) = C\ln(t) + D$ for the data under study with $C = 0.0560 \pm 0.0005$ mS/cm and $D = 1.23 \pm 0.01$ mS/cm.

agreement with a fully fluidized sample, that makes uniform electrical contact with the wall, flowing homogeneously in steady state .

A cross-plot of the apparent conductivity $\sigma_a$ vs strain $\gamma$ is shown in Fig. 6-7. In this representation, the delayed yielding and the three regimes discussed above are readily observed. In the primary creep regime, we observe a linear increase of apparent conductivity with strain, a signature of the increase of connectivity within the carbon black network in bulk or at the interface. In the intermediate regime, wall slip and shear banding result in the sudden decrease of apparent conductivity with strain as the sample fails at the interface, increasing the contact resistance. Finally, in the third regime, the apparent conductivity reaches a constant value as the strain

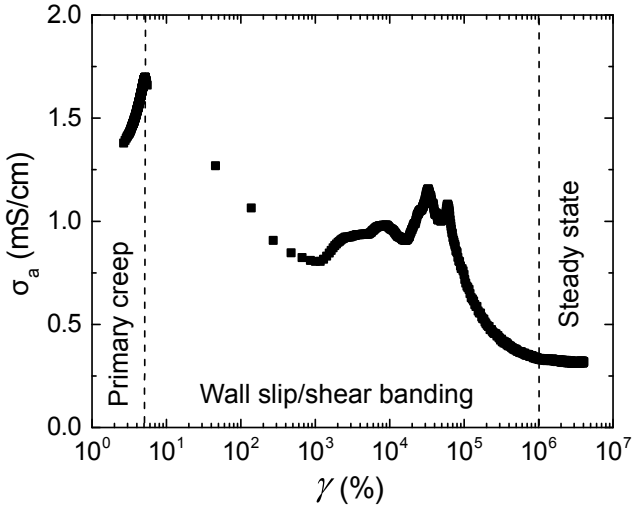


Figure 6-7: Creep experiment in a 8% wt. carbon black gel (VXC72R) at $\tau = 22$ Pa. Apparent conductivity $\sigma_a$ vs strain $\gamma$. The vertical dashed line marks the three different flow regimes discussed in the text: primary creep, heterogeneous flow and steady-state flow.

increases, an indication that the system is fully fluidized and has reached steady state.

Finally, to determine whether the increase of the conductivity during the primary creep regime is associated with bulk rearrangements, or with the evolution of the sample in the vicinity of the plates, we have performed supplemental creep experiments at $\tau = 30$ Pa for gaps of different height $H = 660$, 500 and 330 $\mu$m. The corresponding shear rate and apparent conductivity responses are shown in Fig. 6-8. For the three gaps studied, the shear-rate responses display a similar evolution indicating that the material is subjected to the same delayed yielding scenario in time [Fig. 6-8(a)]. However, the various apparent conductivity responses exhibit significant differences: in the early stage of the experiment, all the apparent conductivity responses start at the same value, but the conductivity measured for larger gaps increases more rapidly [Fig. 6-8(b)]. To determine the bulk contribution, we estimate the contact resistance by extrapolating the apparent conductivity in the limit $t = 0$ s. Then, using Eq. (5.4), we compute the bulk conductivity $\sigma_b$ for each experiment. This is then further normalized by the gap height $H$ [inset in Fig. 6-8(b)]. In the entire primary creep regime ($t \lesssim 50$ s), we observe that $\sigma_b/H$ is independent of the

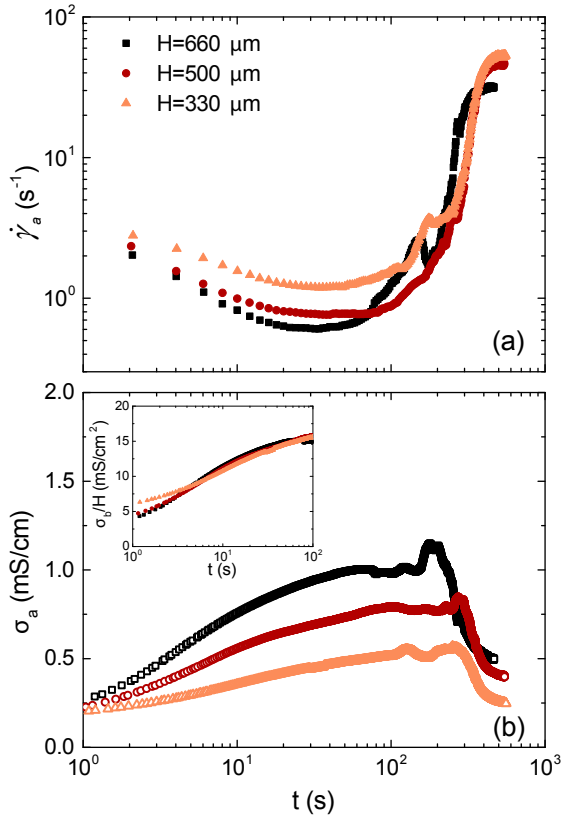


Figure 6-8: Creep experiment in a carbon black VXC72R suspension ($c = 8\%$ wt.) at $\tau = 30$ Pa for different gaps ($H = 660, 500$ and $330$ $\mu$m). (a) Shear rate response $\dot{\gamma}(t)$ (b) Apparent conductivity response $\sigma_a(t)$. The inset shows the estimated bulk conductivity $\sigma_b(t)$ normalized by the gap $H$. The contribution of the contact resistance was estimated using Eq. (5.4) and the measurements at multiple gaps for $t = 0$ s.

gap height, which demonstrates that the increase in apparent conductivity during the primary creep regime is due to a change in bulk of the sample properties. The deformation of the sample microstructure under external stress appears sufficient to trigger the pairing of attractive CB particles leading to an enhanced connectivity and thus a larger conductivity. In that framework, the faster increase of the conductivity at a larger gap can be interpreted as an increasing rate of plastic rearrangements for larger gaps.

To conclude this section, simultaneous time-resolved rheo-electric measurements provide a more detailed picture of the yielding scenario which is in general agreement with previous velocimetry measurements [264, 265]. As a key novel result, time-resolved measurements of the conductivity during the primary creep regime allow

us to reveal the existence of stress-induced bulk rearrangements in the sample microstructure, which correspond to very small values of the macroscopic imposed strain.

## 6.4 Steady-state measurements

After studying the transient rheo-electric behavior of CB gels, we now focus on steady-state shear measurements. The determination of the true constitutive equation is crucial for numerous applications, where the true bulk behavior must be accurately modeled [34, 121, 127, 245, 246, 258, 259], whereas numerous studies in the literature report only approximative or apparent flow curves [259, 262, 263]. In this last section, we take advantage of the rheo-electric test fixture to characterize accurately the constitutive rheological behavior together with the conductivity of CB gels under flow by taking into account the inhomogeneity inherent to the parallel plate geometry, the slip of the sample at the wall and the contact resistance. A stress ramp of decreasing values from $\tau$ =100 Pa to 0 Pa and composed of $N = 100$ steps, each of duration $\Delta t = 30$ s is performed on a 8% wt. CB gel (VXC72R). The choice of ramping the stress downwards and at a slow enough pace is made to insure that the rheological and electrical properties are close to steady state at all shear rates explored. The resulting flow and conductivity curves, as well as the effects of the different corrections detailed below, are shown in Fig. 6-11(a).

We first discuss the mechanical corrections. The shear rate $\dot{\gamma}$ is not homogeneous across the parallel plate, but depends on the radial position $r$ as $\dot{\gamma}(r) = r\Omega_{rot}/H$, where $\Omega_{rot}$ is the angular velocity of the upper plate. The corrected flow curve can be obtained using the apparent shear rate at the rim $\dot{\gamma}_{a,R} = R\Omega_{rot}/H$ and by computing the stress at the rim $\tau_R$ by means of the following expression [137]:

$$\tau_R(\dot{\gamma}_{a,R}) = \frac{\mathcal{M}}{2\pi R^3}\left[3 + \frac{d\ln \mathcal{M}/2\pi R^3}{d\ln \dot{\gamma}_{a,R}}\right] \tag{6.1}$$

where $\mathcal{M}$ denotes the torque applied on the upper plate. The corrected flow curve,

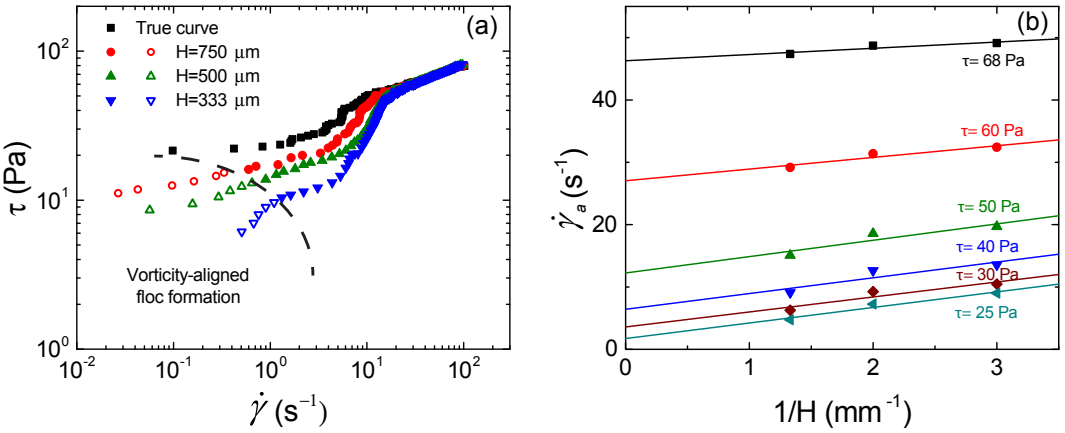


Figure 6-9: (a) Flow curves of a 8% wt. carbon black gel (VXC72R) measured for various gap heights $H = 750, 500$ and 330 $\mu$m together with the true flow curve corrected for slip. The open symbols indicate the region associated with the formation of vorticity aligned flocs. The boundary for the onset of this regime is given by $\dot{\gamma}_c = 3650/H^{1.4}$ with $H$ given in $\mu$m, independently of the CB concentration [239]. (b) Plot of the measured values of apparent shear rate $\dot{\gamma}_a$ vs. $1/H$ for various imposed stresses $\tau = 68, 60, 50, 40, 30$ and 25 Pa. Colored lines correspond to the best linear fits of the data and allow us to extract the true shear rate $\dot{\gamma}_t$ and the slip velocity $V_s$ for each imposed stress $\tau$ using Eq. 6.2.

pictured as filled triangles (▲) in Fig. 6-11(a) appears shifted towards lower stresses for $\dot{\gamma} \leq 7$ s$^{-1}$. Alternatively, single-point determination methods can also be used to correct for shear inhomogeneity to avoid additional noise associated with numerical calculation of the derivative in Eq. (6.1) [271,280]. These methods rely on calculating the apparent Newtonian viscosity at the rim $\eta_N = 2\mathcal{M}H/\pi R^4\Omega_{rot}$ which is then associated with a lower shear rate, equal to approximately three quarters of the rim shear rate. For Bingham plastic and power-law materials, the error associated with performing this single-point correction is typically less than 2% [271,280]. Indeed, the result of the latter method is barely distinguishable from that of the derivative method [(▼) in Fig. 6-11(a)]. Finally, correction for slip can be performed by conducting rheological measurements at different gaps [139,273,274]. If the flow curves obtained at various gaps superimpose, the material does not slip, whereas a gap-dependent rheology is the signature of wall slip. Assuming symmetric slip at both walls, the

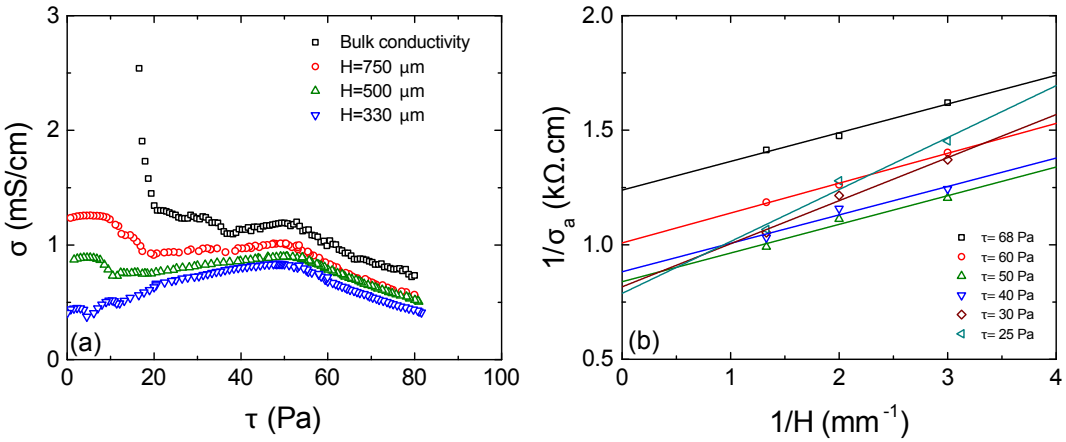


Figure 6-10: (a) Conductivity curves of a 8% wt. carbon black gel (VXC72R) measured for various gap heights $H = 750, 500$ and 330 $\mu$m together with the bulk conductivity curve. (b) Inverse of the apparent resistivity $1/\sigma_a$ vs $1/H$ for various stresses $\tau = 68, 60, 50, 40, 30$ and 25 Pa. Color lines correspond to the best linear fits of the data and allow to extract the bulk resistivity $1/\sigma_b$ and the specific contact resistance $\rho_c$ for each stress $\tau$ using Eq. 6.4 in the main text.

following kinematic relationship can be derived for a given imposed stress $\tau$ [139]:

$$\dot{\gamma}_a(\tau) = \dot{\gamma}_t(\tau) + \frac{2V_s(\tau)}{H} \tag{6.2}$$

where $\dot{\gamma}_a$ is the apparent shear rate, $\dot{\gamma}_t$ the true shear rate and $V_s$ the slip velocity. Experiments conducted at different gaps shown in Fig. 6-9 together with Eq. (6.2) allow us to compute the true flow curve of the carbon-black gel [(■) in Fig. 6-11(a)]. The corrections reveal that the gel exhibits a critical shear rate of about 1 $s^{-1}$ below which no homogeneous flow is possible (see additional discussion below about the formation of log-rolling flocs) and that, for shear stresses larger than 50 Pa, the shear rate was underestimated prior to the shear inhomogeneity correction.

We now turn to the electric measurements, and discuss the corrections to the apparent conductivity defined in Eq. (5.1) which is observed to decrease for increasing shear rate [Fig. 6-11(b)]. First, as shown in section 5.3, following a calculation analogous to the one that leads to Eq. (6.1), a correction for shear inhomogeneity can be derived for the conductivity which reads for the apparent conductivity $\sigma_{a,R}$ at the

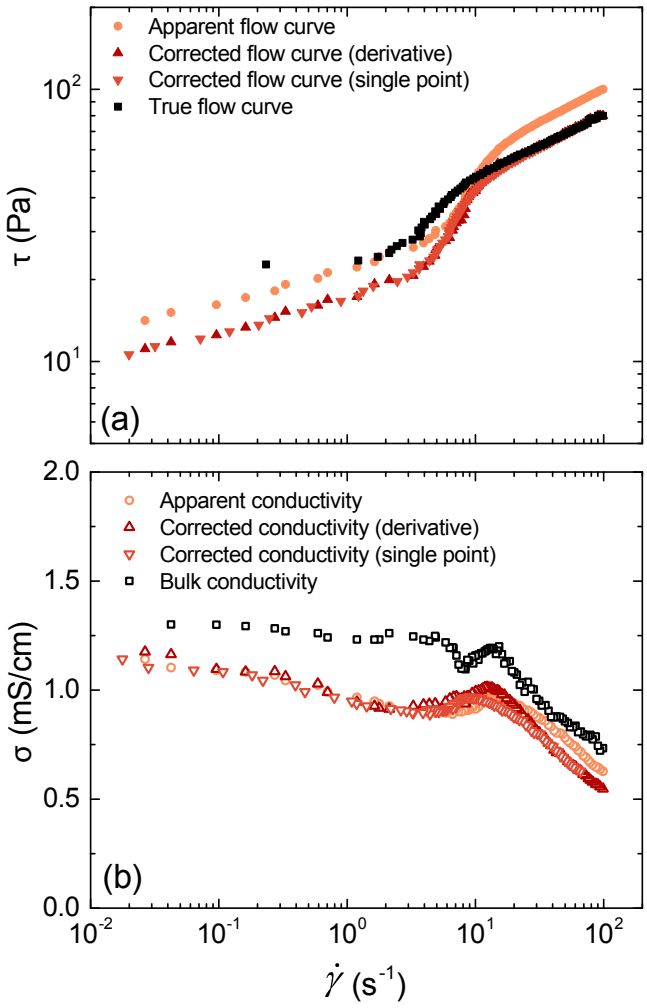


Figure 6-11: Steady-state flow and conductivity curves in a 8% wt. carbon black gel (VXC72R). (a) Flow curves showing the effects of the shear inhomogeneity correction (derivative and single point methods) as well as the slip correction. The "corrected" flow curves are obtained after correcting for shear inhomogeneity alone, while the true flow curve is obtained after correcting for both shear inhomogeneity and slip effects. (b) Conductivity curves showing the effects of the shear inhomogeneity correction as well as the contact resistance correction. The "corrected" conductivity curves are obtained after correcting for shear inhomogeneity alone, while the bulk conductivity curve is obtained after correcting for both shear inhomogeneity and contact resistance effects.

rim:

$$\sigma_{a,R}(\dot{\gamma}_{a,R}) = \frac{I}{\phi_0}\frac{H}{2\pi R^2}\left[2 + \frac{d\ln\left(\frac{I}{\phi_0}\frac{H}{2\pi R^2}\right)}{d\ln\dot{\gamma}_{a,R}}\right] \tag{6.3}$$

where $I$ denotes the measured current and $\phi_0$ the applied potential. Corrected data appears as simply shifted along the shear-rate axis [(△) in Fig. 6-11(b)]. Moreover, an analogous calculation to the single-point determination method described in [271,280], leads to a similar expression for the conductivity as shown in section 5.3. The apparent conductivity as defined in Eq. (5.1) is associated with a lower shear rate, equal to approximately two thirds of the shear rate at the rim. Here again, similarly to the rheological correction, the result of this method is barely distinguishable from that of the derivative method [(▽) in Fig. 6-11(b)]. Finally, we have shown in section 5.3 that the expression for the contact resistance shown in Eq. (5.4), which is the electrical equivalent to the correction for slip [Eq. (6.2)] can be extended to a sample under flow. For a given stress at the rim $\tau_R$, one can thus write the resulting resistivity as:

$$\frac{1}{\sigma_{a,R}(\tau_R)} = \frac{1}{\sigma_{b,R}(\tau_R)} + \frac{\rho_{c,R}(\tau_R)}{H} \tag{6.4}$$

where $\sigma_{a,R}$ denotes the measured apparent conductivity derived in Eq. (6.2) and $\sigma_{b,R}(\tau_R)$ is the bulk conductivity at the level of imposed stress $\tau_R$. Finally, $\rho_{c,R}$ is the specific contact resistance at the rim expressed in $\Omega.\text{cm}^2$ and defined as $\rho_{c,R}(\tau_R) = (\partial\mathcal{R}_c/\partial j)_R(\tau_R)$ where $\mathcal{R}_c$ is the contact resistance and $j$ is the current density. By introducing the specific contact resistance, Eq. (6.4) takes into account the potential variation of the contact resistance with the radius $r$ and hence its dependence on both the shear rate and shear stress. Ultimately, we find that the fully corrected conductivity curve shows the same trend as the raw data but is quantitatively shifted towards larger conductivities [(□) in Fig. 6-11(b)].

Experiments conducted at different gaps shown in Fig. 6-10 together with Eq. (6.4) allow us to compute the bulk conductivity of the carbon-black gel [(□) in Fig. 6-11(b)]. Let us now discuss the quantities extracted from both the mechanical and electrical corrections of the flow curve, i.e. the slip velocity $V_s$, the bulk conductivity

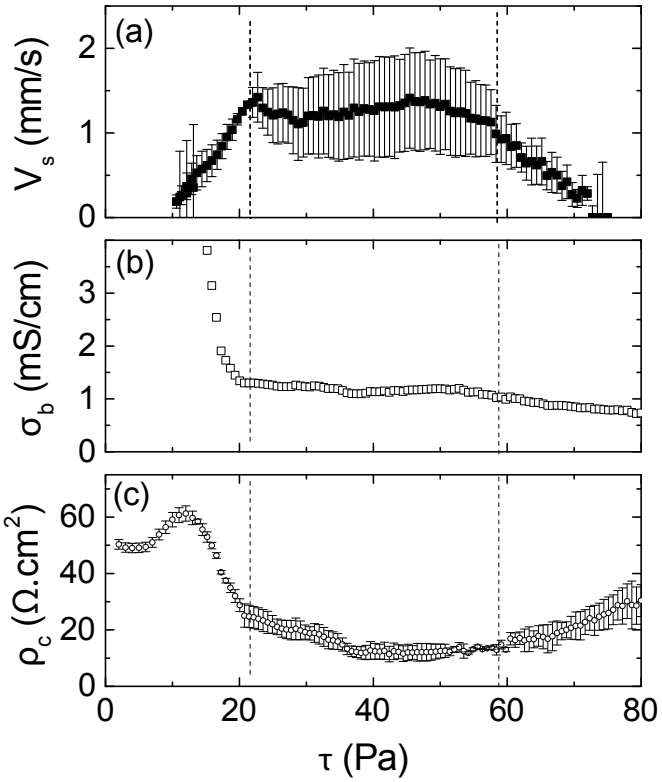


Figure 6-12: Slip velocity $V_s$, bulk conductivity $\sigma_b$ and specific contact resistance $\rho_c$ obtained from the slip and contact resistance corrections performed on the steady state flow curves in a 8% wt. carbon black gel (VXC72R). The vertical dashed lines indicate the limits of the three regimes discussed in the text. From large to low stresses: fully fluidized regime for $\tau \geq 55$ Pa, plug flow with slip at the walls for 55 Pa $\geq \tau \geq$ 20 Pa and shear-induced structuration (formation of vorticity-aligned flocs) for $\tau \leq 20$ Pa. (a) Slip velocity $V_s(\tau)$ (b) Bulk conductivity $\sigma_b(\tau)$ (c) Specific contact resistance $\rho_c(\tau)$.

$\sigma_b$ and the specific contact resistance $\rho_c$. These quantities are reported as a function of the applied stress $\tau$ in Fig. 6-12 during the flow cessation of a 8% wt. CB gel (VXC72R). In consequence, the graphs in Fig. 6-12 should be read from right to left. At large stresses, i.e. $\tau \geq 75$ Pa, the slip velocity is negligible, and the bulk resistance and specific contact resistance are constant, in agreement with a fully fluidized sample that is sheared homogeneously. As the stress is ramped down to $\tau \simeq 55$ Pa, the bulk conductivity slowly increases and the slip velocity becomes positive while the specific contact resistance decreases. These evolutions reflect the aggregation of the CB particles into larger flocs which better conduct the current

and display an increasing amount of slip at the wall. Such aggregates experience more contact with the wall than individual CB particles, hence the decrease in $\rho_c$. From $\tau \simeq 55$ Pa to 20 Pa, both $\sigma_b$ and $V_s$ are roughly constant while $\rho_c$ slowly increases as the stress is ramped down. These results strongly suggest the appearance of thin lubrication layers at both walls, mainly composed of oil, and isolating a bulk percolated structure of CB particles, that is only weakly sheared. Moreover, assuming a slip layer of thickness $\delta$ and viscosity $\eta_s$ that is equal to the value for the matrix phase, the stress at the wall reads [149]: $\tau_w = \eta_s V_s/\delta$, where $V_s/\delta$ denotes the shear rate inside the slip layer. As both $V_s$ and $\delta$ remain constant while decreasing the stress, one should expect the thickness $\delta$ of the slip layer to progressively increase from $\delta \simeq$ 400 nm to 1 $\mu$m. And indeed, the specific contact resistance increases concomitantly with the stress decrease. Finally, for $\tau \leq 20$ Pa, both the bulk conductivity and the contact resistance show a dramatic increase which is the signature of strong changes in the sample microstructure that we interpret as the formation of vorticity-aligned flocs [91, 93, 239]. Indeed, the formation of log rolling flocs has been reported in confined geometries for shear rates lower than a critical value $\dot{\gamma}_c$ that scales for VXC72R CB gels as $\dot{\gamma}_c = 3650/H^{1.4}$ with $H$ given in $\mu$m, independently of the CB concentration [239]. For $H = 750$ $\mu$m, one calculates $\dot{\gamma}_c \simeq 1.2$ s$^{-1}$ which, according to the true flow curve of the gel [Fig. 6-11(a)], corresponds to $\tau_c \simeq 25$ Pa, in good agreement with the transition observed in Fig. 6-12, at $\tau \simeq 20$ Pa. Therefore at low shear rates, the rheo-electric measurements reflect the growth of a shear-induced structure which is otherwise hard to visualize at such large concentrations of CB [239].

The above analysis shows that conclusions drawn from rheo-electric measurements must be considered with care, and, we have highlighted the importance of corrections for shear inhomogeneity in parallel plate geometry, wall slip and contact resistance, which are often overlooked in the study of strongly conductive complex fluids. Application of these corrections also provides quantitative values for important quantities, namely the slip velocity, bulk conductivity and specific contact resistance which, once combined, provide a more complete picture of the flow profile in the conductive gel at steady state over a large range of stress values.

## 6.5 Discussion

The rheo-electric apparatus described in chapter 5 provides robust measurements for highly conductive materials at rest, during transient flows and under steady-state shear.

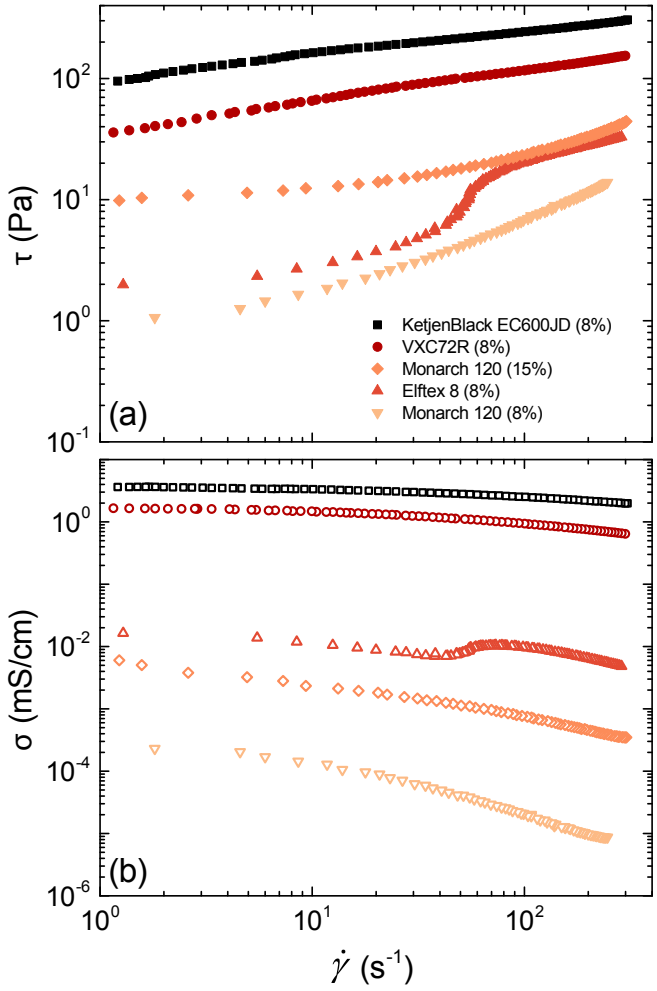


Figure 6-13: Sets of corrected (a) flow curves and (b) conductivity curves for carbon black gels made with carbon black particles of different grades: KetjenBlack EC600JD, VXC72R, Elftex 8 at weight concentration $c = 8\%$ wt., and Monarch 120 at $c = 8\%$ wt. and 15% wt.

Flow cessation experiments on carbon black gels reported in section 6.2 have

revealed that the sample shearing history tunes concomitantly the elastic and the electric properties of these attractive gels. Progressive stress decrease down to $\tau =$ 0 Pa leads to a more solid-like gel whose elastic modulus $G'_0$ varies as a power-law function of the conductivity $\sigma_0$ for increasing quenching speed: i.e. $G'_0 \propto \sigma_0^{\alpha}$, with $\alpha = 1.65 \pm 0.04$. Previous measurements on gels formulated with exact same carbon black powder from Cabot at various volume fractions $\phi$ have shown that: $G'_0 \propto (\phi - \phi_c)^{\nu}$, with $\nu = 4.0 \pm 0.1$, where the exponent $\nu$ is consistent with percolation theory [88]. Assuming that the electrical and elastic percolation occurs at the same volume fraction $\phi_c$, one can expect from the measurements reported here that: $\sigma_0 \propto (\phi - \phi_c)^t$, with $t = \alpha/\nu = 2.4 \pm 0.1$ [1]. Interestingly, this value is quantitatively outside the range of values predicted by percolation theories $1.5 \leq t \leq 2$ [281–283], and larger than values recently reported for other carbon black gels: Ketjen Black ($t = 1.9$) and Super C-45 ($t = 1.7$) dispersed in an organic solvent [259]. Our measurements strongly suggest that the VXC72R carbon black gel exhibit an anomalous conductivity dependence. Such conclusions are strikingly similar to that obtained in Cabot carbon-black polymer composite, where CB particles are embedded in an insulating plastic [284]. Indeed, composites loaded with the Cabot carbon black show an exponent larger than 2, ($t = 2.8 \pm 0.2$ for CB particles embedded in polyvinylchloride) which has been interpreted as the consequence of a more compact network, due to the less tortuous shape of these particles [285, 286]. Our result shows here that such an exceptional behavior of the VXC72R also extends to carbon-black networks embedded in a non-aqueous solvent.

We have also shown in section 6.3 that the rheo-electric apparatus is well adapted to probe the evolution of the gel structure under weak deformations and provides much higher sensitivity for monitoring the evolution of the microstructure compared to other techniques such as velocimetry [265]. Indeed, applied to creep experiments, rheoelectric measurements reveal that the power-law response of the carbon black gel during the primary creep regime is associated with an increase in the network con-

[1] Here, the variable $t$ denotes the critical exponent associated with the electrical percolation and not time.

nectivity and conductivity of the gel. Power-law responses to creep tests have been reported already for numerous other soft materials such as microgels [287], polycrystalline surfactant hexagonal phases [288], core-shell colloidal particles [289] and protein gels [290, 291]. However, the present measurements are among the first to illustrate the existence of simultaneous rearrangements of the sample in bulk. At the strand level, such rearrangements may likely correspond to the net creation of new bonds due to the presence of attractive van der Waals forces between the soot particles. Indeed, recent numerical simulations on model colloidal gels have revealed that imposed macroscopic deformation leads to the formation of new bonds even at low strain [292], which may account for the increase of conductivity reported in Fig. 6-8. More simulations under applied shear stress conditions are needed to clarify the evolution of the sample network connectivity during primary creep. In steady shear, we have shown in section 6.4 that performing corrections for shear inhomogeneity, wall slip and contact resistance are crucial to correctly determine the electrical and mechanical constitutive behavior of CB gels under flow. As a result, we can now safely compare the rheo-electric properties of CB gels made from different grades of carbon black. We examine 8% wt. CB gels made of respectively: VXC72R, Monarch 120, Elftex 8 (Cabot) and KetjenBlack EC600JD (Akzo Nobel), as well as a 15% wt. dispersion made of Monarch 120 (Cabot). Similarly to the experiments reported in Fig. 6-2, ramps of decreasing stress from $\tau = \tau_{max}$ down to $\tau = 0$ Pa and composed of $N = 100$ steps each of duration $\Delta t = 15$ s are applied to each gel. The value of $\tau_{max}$, which ranges between 15 Pa and 300 Pa depending on the type of CB gels, is chosen such as the corresponding shear rate is 300 $s^{-1}$ for all samples (Fig. 6-13). The rheo-electric properties of the different 8% wt. CB gels span over several orders of magnitude both in conductivity and stress. On the one hand, CB gels made with KetjenBlack EC600JD and VXC72R show a high conductivity larger than 1 mS/cm that is weakly sensitive to shear, which is indeed why these CB were initially designed. Such properties are intimately linked to their large specific surface area of about 200 $m^2/g$ for the VXC72R sample [293,294] and 1400 $m^2/g$ for the Ketjenblack EC600JD [34,121,293]. On the other hand, CB gels made with Elftex 8 and Monarch

120 display a much lower conductivity that is also more strongly sensitive to shear. Correspondingly, these CB have a lower specific surface area of about 75 $m^2/g$ [295] and 29 $m^2/g$ [296] respectively. Such CB are typically used for color as pigments where CB conductive properties are less crucial. Finally, we note that the electrical properties of these CB dispersions are strongly related to the individual properties of the CB particles. In particular, increasing the concentration in CB does not compensate for low conductivity values or shear sensitivity, as illustrated by the results for a gel made of 15% wt. of Monarch 120. These measurements illustrate how the rheo-electric fixture can be used to compare, rank and select the desired properties of highly conductive complex fluids.

## 6.6 Conclusion

We have introduced a new rheo-electric apparatus designed for conventional stress-controlled rheometers. This apparatus can be used to accurately measure the conductivity of strongly conductive materials under flow at the same time as the viscometric properties of the gel are measured. Benchmark tests on CB gels have allowed us to illustrate the high sensitivity of the apparatus even at low strains, and to determine the transient and steady-state behavior of CB gels by comparing the simultaneous electrical and mechanical response. Furthermore, by taking into account shear inhomogeneity, wall slip and the existence of a measurable contact resistance, we have shown that the correction methods first introduced to extract true bulk mechanical measurements from parallel plate rheometry data can be formally extended to analyze electrical data. The latter analysis should be used as a reference for future electrical characterization of conductive complex fluids such as conductive silver pastes, carbon nanotube nanocomposites, conductive inks, etc.

# Chapter 7

# Rheo-electrical Characterization of Carbon Black Gels under Oscillatory Shear

## 7.1 Introduction

In this Chapter, we explore the use of oscillatory measurements to characterize the rheo-electrical properties of carbon black gels. In particular, we explore the use of small amplitude oscillatory shear measurements (SAOS) measured simultaneously to conductivity measurements to extrapolate the electrical and rigidity thresholds for percolation in carbon black gels. Additionally, we investigate the use of large amplitude oscillatory stress measurements (LAOStress) to understand cyclic fatigue in carbon black gels under repeated loading.

## 7.2 Probing the percolation of CB gels using oscillatory shear

### 7.2.1 Small amplitude oscillatory shear (SAOS) measurements

In oscillatory shear, a sinusoidal strain is imposed with frequency $\omega$ :

$$\gamma(t) = \gamma_0 \sin(\omega t) \tag{7.1}$$

and the resulting shear stress $\tau(t)$ is measured. For small strain amplitudes i.e. in the linear viscoelastic regime, the in-phase storage modulus $G'(\omega)$ and the out-of-phase loss modulus $G''(\omega)$ are given by

$$\tau(t) = \gamma_0[G'(\omega)\sin(\omega t) + G''(\omega)\cos(\omega t)]. \tag{7.2}$$

A purely elastic material with a shear elastic modulus $G$ results in $G'(\omega) = G$ and $G''(\omega) = 0$ while a purely viscous Newtonian fluid of viscosity $\eta$ results in $G'(\omega) = 0$ and $G''(\omega) = \eta\omega$. In general, most viscoelastic materials exhibit a behavior that is a combination of these two limiting cases, resulting in more complex dependence of the viscoelastic moduli with the angular frequency $\omega$ [137].

### 7.2.2 Electrical and rigidity percolation in CB gels

Suspensions of colloidal particles such as CB gels exhibit a diverse range of rheological properties, varying from simple viscous fluids to highly elastic pastes. Control over the rheology is achieved by adjusting the interparticle interactions and the particle volume fraction. A highly dispersed fluidized phase of particles undergoes a jamming transition and is transformed into a jammed solid network by increasing $\phi$. We can define two percolation thresholds: an electrical percolation and a rigidity percolation threshold. The electrical percolation corresponds to the geometrical percolation that occurs when a space-spanning network if first formed. On the other hand, we identify the rigidity percolation by the existence of a stress-bearing network, which results

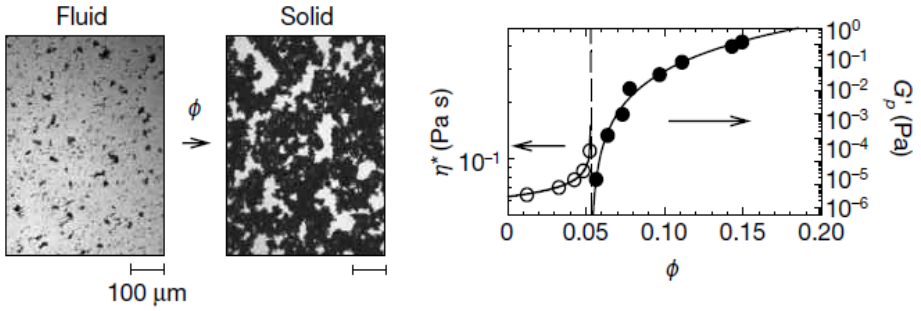


Figure 7-1: Mechanical percolation of carbon black gels. As the volume fraction of carbon black is increased, at the percolation threshold, the viscosity of the gel diverges and it develops a finite elastic modulus. Reproduced from Trappe et al. [89]

in a plateau of the elastic modulus, $G'_0$ at low frequencies. As shown in Fig. 7-1, as the particle volume fraction of carbon black increases, a well-defined transition from fluid-like to solid-like behavior can be found [86,88,89]. The viscosity $\eta$ diverges as some critical value is approached, whereupon the elastic modulus $G'$ increases sharply. Trappe et al. [88] have also shown that the strength of the interaction energy between the particles $U$ influences the rigidity percolation threshold and the rheological behavior of the gel.

Close to the percolation threshold, both the conductivity and the elastic modulus have been shown to exhibit critical-like power law behavior [88,259,285,286,297–299],:

$$G' \sim (\phi - \phi_r)^{\nu} \tag{7.3}$$

$$\sigma \sim (\phi - \phi_c)^{s} \tag{7.4}$$

where $\nu$ and $s$ are the rigidity and conduction critical exponents respectively and $\phi_r$ and $\phi_c$ are the rigidity and conduction percolation thresholds. These parameters are set by the dimensionality of the network (2 or 3D), the fractal dimension of the particle clusters and the strength of the interparticle interaction. The rigidity critical exponent $\nu$ has been found to vary between 3.6 and 4.1 in three dimensional lattices [88,259,298,299]. The conduction critical exponent $s$ [1] has a larger spread in

[1] traditionally the variable $t$ is used but we choose to use $s$ to avoid confusion with the time

the reported values in the literature. It has been demonstrated to be different than the rigidity critical exponent $\nu$ [297–299], showing that the electrical and rigidity percolation belong to different universality classes. Classical percolation theories predict $1.5 \leq s \leq 2$ [281–283, 297, 300]. However, work by Balberg et al. [284–286,301,302] has shown that in carbon black gels, electron tunneling can lead to non-universal exponents that are larger than the ones expected from classical percolation theory. For instance, composites loaded with Cabot carbon black show an exponent larger than two, ($s = 2.8 \pm 0.2$ for CB particles embedded in polyvinylchloride) which is a result of a more compact network, due to the less tortuous shape of these particles [285, 286]. In general, Balberg et al. [285] have shown that higher structure in carbon black particles yields a lower percolation threshold $\phi_c$ and a lower critical exponent $s$ that is close to the classical percolation theory value of two, due to the more tortuous nature of the particles. On the other hand, lower structure in carbon black particles yields a higher $\phi_c$ and an anomalous critical exponent that is higher than two.

While the rigidity and conduction critical exponents have received a great deal of attention, the percolation thresholds have not been as widely studied. In particular, we are interested in understanding whether the rigidity and conduction percolation thresholds are the same. One expects that the two thresholds could differ because the conductivity does not strongly depend on the shape of the chains in the network (but on the path of least resistance), while the elastic modulus strongly depends on both the geometry and the structure of the chains and in particular, the presence of load-bearing chains.

To that end, we simultaneously measure the viscoelastic moduli measured under SAOS and the DC conductivity of gels composed of VXC72R carbon black particles (Cabot) in mineral oil at different carbon mass fractions ranging from $0\% \leq \phi_m \leq 8\%$wt. Here, we choose to work with mass fractions as opposed to the nominal volume fraction $\phi$ used in Chapter 4 because mass fractions represent more accurately the amount of carbon black introduced in the suspension. The SAOS measurements

variable

were performed using a DHR-3 stress controlled rheometer (TA instruments) with a stainless steel parallel plate geometry coated in gold ($R = 20$ mm, and surface roughness $R_a = 0.1$ $\mu$m) at a gap $H = 0.75$ mm and at a temperature $T = 23°$C. The rheo-electric test fixture using a wire running through the center of the rotating shaft and described in Section 5.4.1 was used to measure the conductivity of the gel in-situ. The conductivity was measured at two different gaps $H = 0.75, 0.50$ mm for each sample to enable correction of the contact resistance in each measurement. For each sample, the gel was pre-sheared at 100 $s^{-1}$ for 30 s then rapidly brought to $\tau = 0$ Pa and left to equilibrate for 15 min. Frequency sweeps were performed at small amplitudes in the linear viscoelastic region then, the conductivity and the viscoelastic moduli at $\omega = 6.28$ rad/s were measured for 5 min before disconnecting the wire and measuring the viscoelastic moduli at $\omega = 6.28$ rad/s in the absence of the wire. This protocol allows us to correct for the contribution of the tension of the wire (described in section 5.4.1) to our rheological measurements, which is of particular importance for weakly elastic samples. We emphasize that this protocol allows the measurement of the rheological and electrical properties *in situ* on the same gel under the same shear history, therefore eliminating errors induced by user handling if the tests were done separately.

The frequency-dependent linear viscoelastic storage and loss moduli $G'(\omega)$ and $G''(\omega)$ of the CB gels are shown in Fig. 7-2. We observe that at high mass fractions $\phi_m \geq 3$%wt., the suspension is a viscoelastic gel with the storage modulus $G'(\omega)$ almost independent of the angular frequency $\omega$ and substantially larger than the loss modulus $G''(\omega)$. At low mass fractions ($\phi_m \leq 1.25$%wt), we observe a stronger dependence of the viscoelastic moduli with frequency and for $\phi_m \leq 1.00$%wt, $G''(\omega) > G'(\omega)$. This highlights the transition from a fluidized phase to a jammed solid where a plateau in the elastic modulus is observed. For low volume fractions, rheological measurements are challenging because the inertia of the instrument tends to dominate the torque measurement [14, 137, 138, 275].

By limiting our extraction of the elastic moduli to the jammed regime with a plateau in the elastic modulus, we plot the elastic modulus $G'$ obtained for $\omega =$

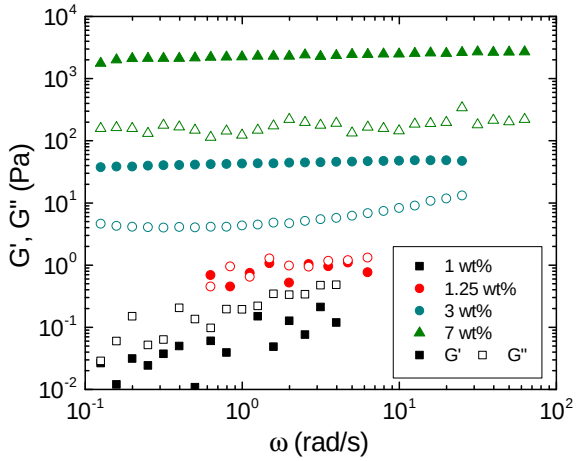


Figure 7-2: Viscoelastic moduli $G'(\omega)$ and $G''(\omega)$ as a function of angular frequency $\omega$ for different mass fractions $\phi_m$ of carbon black (VXC72R) in mineral oil at $T = 23°\text{C}$.

6.28 rad/s against the mass fraction of carbon black $\phi_m$ in Fig. 7-3(a). As expected, we observe that the elastic modulus increases with increasing loading of carbon black. A power-law fit of the form $G' = \tilde{G}'_0(\phi_m - \phi_{m,r})^\nu$ is found to be in good agreement with the data for $\tilde{G}'_0 = 2.18 \pm 1.64$ Pa, $\phi_{m,r} = 0.46 \pm 0.27$ wt% and $\nu = 3.68 \pm 0.33$. This exponent $\nu$ is consistent with those typically seen for elasticity percolation in three dimensions [298, 299] and in agreement with values previously reported for this grade of CB gels [88, 89]. The high value reflects the strong increase in the modulus that results upon addition of a very small number of new bonds, which significantly increases the elasticity of the network [88].

The measured conductivity $\sigma$ is plotted against the mass fraction $\phi_m$ in Fig. 7-3(b). We observe that the conductivity increases with the loading in carbon black. A power-law fit of the form $\sigma = \tilde{\sigma_0}(\phi_m - \phi_{m,c})^s$, with $\tilde{\sigma_0} = 0.013 \pm 0.002$ mS/cm, $\phi_{m,c} = 0.43 \pm 0.02$ wt% and $s = 2.66 \pm 0.07$ is found to be in good agreement with the data. Here, the exponent $s$ deviates from the classical percolation theory value of 2.0 [281–283, 297, 300] but is consistent with values reported for medium structure Cabot black composites [285, 286]. The error bars on the conductivity exponent and percolation thresholds are smaller than those found for the rheological measurements because we are able to perform conductivity measurements closer to the percolation

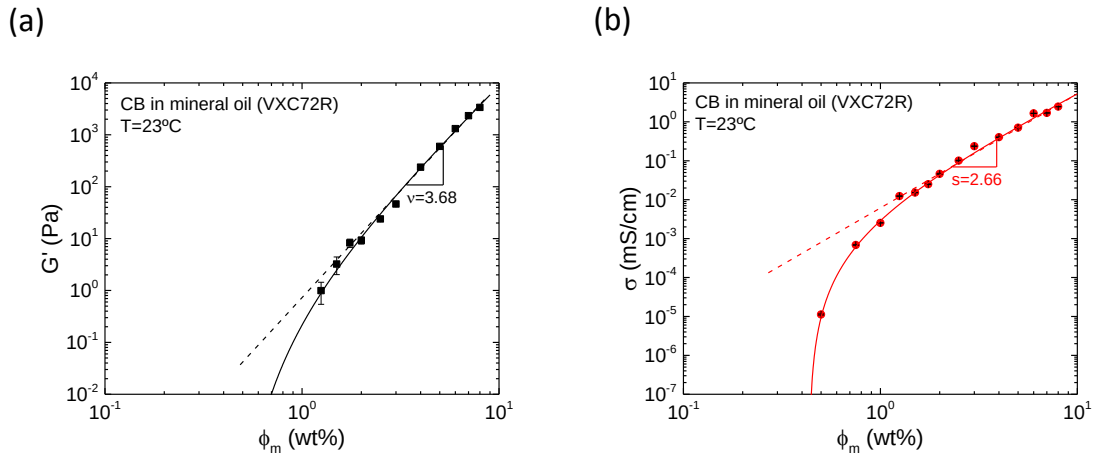


Figure 7-3: (a) Elastic modulus $G'$ vs mass fraction of carbon $\phi_m$ in carbon black gels (VXC72R). The solid line corresponds to a power-law fit of the data of the form $G' = \tilde{G}'_0(\phi_m - \phi_{m,r})^\nu$, with $\tilde{G}'_0 = 2.18 \pm 1.64$ Pa, $\phi_{m,r} = 0.46 \pm 0.27$ wt% and $\nu = 3.68 \pm 0.33$. The elastic modulus is reported for $\omega = 6.28$ rad/s. For mass fractions below 1 wt%, inertia dominates the measurement and accurate determination of the elastic modulus is challenging. (b) Conductivity $\sigma$ vs mass fraction of carbon $\phi_m$ in carbon black gels (VXC72R). The solid line corresponds to a power-law fit of the data of the form $\sigma = \tilde{\sigma_0}(\phi_m - \phi_{m,c})^s$, with $\tilde{\sigma_0} = 0.013 \pm 0.002$ mS/cm, $\phi_{m,c} = 0.43 \pm 0.02$ wt% and $s = 2.66 \pm 0.07$.

threshold while rheological measurements are limited by the inertia of the rheometer. We observe that within the error bars of the measurement, the conduction and rigidity percolation thresholds are found to be the same for this grade of carbon black gels $\phi_{m,c} \simeq \phi_{m,r} \simeq 0.44\%$wt. Additional measurements of the viscoelastic moduli at low volume fractions using a strain-controlled rheometer, where inertia effects are non-existent, could help reduce the error bar on the rigidity percolation threshold. Additionally, investigating different grades of carbon black gels would be of interest as the degree of structure present in the carbon black particles can result in a different structure of the percolated network and therefore affect these conclusions.

In Fig. 7-4, we show a cross plot of the elastic modulus vs. the conductivity for the data shown in Fig. 7-3. We observe a correlation between these two parameters and find that a power law fit of the form $G'_0 = K\sigma_0^\alpha$ with $K = 846 \pm 129$ Pa.(cm/mS)$^\alpha$ and $\alpha = 1.53 \pm 0.20$ is in good agreement to the data. The exponent $\alpha$ measured

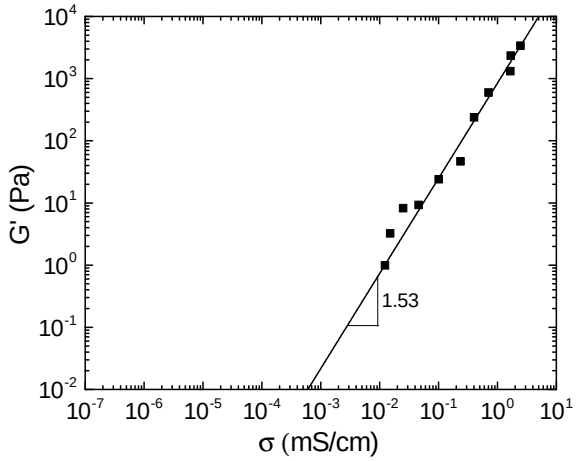


Figure 7-4: Elastic modulus $G'$ of the carbon black gels vs conductivity $\sigma$ in carbon black gels (VXC72R). Each point corresponds to a different mass fraction $\phi_m$. The solid line corresponds to the best power-law fit of the data of the form $G'_0 = K\sigma_0^{\alpha}$, with $K = 846 \pm 129$ Pa.(cm/mS)$^{\alpha}$ and $\alpha = 1.53 \pm 0.20$.

here is close to the one found in section 6.2 where the elasticity and conductivity of a CB were tuned using the shear history of the gel at a fixed mass fraction ($\alpha = 1.65 \pm 0.04$). These preliminary results indicate that the shear history applied to the CB gel is another parameter that can affect the percolation threshold and the percolation dynamics of the CB gel. Further investigation into the effect of shear history on the elasticity and conductivity of the gel is therefore of great relevance.

Overall, these results demonstrate the relevance of simultaneous SAOS measurements and conductivity in studying percolation phenomena in CB gels. This work paves the way for further studies, exploring the effect of the particle interaction, the carbon black particle characteristics and shear history on the percolation thresholds and the critical behavior of the gels close to percolation.

## 7.3 LAOS measurements applied to the study of fatigue in CB gels

In this section, we discuss the use of large amplitude oscillatory shear to study fatigue in CB gels. Perge et al. [303,304] have studied CB gels submitted to large amplitude oscillatory shear stress and showed that at a constant stress amplitude well below its apparent yield stress, the gel displays cyclic fatigue and progressively fluidizes, turning from an elastic solid to a viscous fluid. Our goal is to study this phenomena within the LAOStress framework described by Dimitriou et al. [275] and discuss the signatures of fatigue on the Chebyshev compliance and fluidity coefficients.

### 7.3.1 LAOStress framework

The LAOStress framework for large amplitude oscillatory shear stress described by Dimitriou et al. [275] is the analogue of the LAOS framework presented by Ewoldt et al. [14] and Läuger et al. [305] in the strain-controlled case. Dimitriou et al. [275] have shown that this framework is relevant for the study of elasticviscoplastic (EVP) materials. We begin by noting that we impose a cosinusoidal stress on the material

$$\tau(t) = \tau_0 \cos(\omega t) \tag{7.5}$$

The resulting strain $\gamma(t, \omega, \tau_0)$ can then be decomposed into a Fourier series as follows:

$$\gamma(t, \omega, \tau_0) = \sum_{\text{n odd}} \{J_n'(\omega, \tau_0)\tau_0 \cos(n\omega t) + J_n''(\omega, \tau_0)\tau_0 \sin(n\omega t)\} \tag{7.6}$$

In general, responses in which only odd harmonics are present are considered. This was also the approach taken by Ewoldt et al. [14] and Dimitriou et al. [275]. Even harmonics may arise during transient responses [306] or due to the presence of dynamic wall slip [307]. The formalism described here can be extended to even harmonics if needed. We also neglect any constant strain offsets (corresponding to the $n = 0$ term in Eq. 7.6). The convention of using a cosine wave for the imposed stress is

adopted, because it simplifies the expressions used to determine Chebyshev fitting coefficients [308]. Following the work of Dimitriou et al. [275], we can decompose the strain signal in Eq. 7.6 an into apparent elastic strain $\gamma'$ and an apparent plastic strain $\gamma''$

$$\gamma'(t) = \tau_0 \sum_{\text{n odd}} J'_n(\omega, \tau_0) \cos(n\omega t) \tag{7.7}$$

$$\gamma''(t) = \tau_0 \sum_{\text{n odd}} J''_n(\omega, \tau_0) \sin(n\omega t) \tag{7.8}$$

Having defined $\gamma'$ and $\gamma''$, we can follow the reasoning of Ewoldt et al. [14] and represent these single-valued functions of stress as a series of orthogonal Chebyshev polynomials $T_n(x)$, where $x$ is the scaled stress, $x = \tau(t)/\tau_0$:

$$\gamma'(t) = \tau_0 \sum_{\text{n odd}} J'_n(\omega, \tau_0) \cos(n\omega t) = \tau_0 \sum_{\text{n odd}} \underbrace{J'_n(\omega, \tau_0)}_{c_n} T_n(x) \tag{7.9}$$

$$\dot{\gamma}''(t) = \tau_0 \sum_{\text{n odd}} n\omega J''_n(\omega, \tau_0) \cos(n\omega t) = \tau_0 \sum_{\text{n odd}} \underbrace{n\omega J''_n(\omega, \tau_0)}_{f_n} T_n(x) \tag{7.10}$$

The above representation follows from the identity $T_n(\cos\theta) = \cos(n\theta)$. The resulting material coefficients have units consistent with compliances $c_n(\omega, \tau_0)$ $[\text{Pa}]^{-1}$ and fluidities $f_n(\omega, \tau_0)$ $[\text{Pa.s}]^{-1}$ respectively. Due to the convexity of the third Chebyshev polynomial, positive values of $c_3$ (i.e., increasing compliance) result in stress softening of the apparent elastic stress-strain curve. Positive values of $f_3$ (i.e., increasing fluidity) result in stress-thinning of the apparent plastic strain-rate vs shear stress curve. Conversely, negative values of $c_3$ imply stress-stiffening of the elastic material, while negative values of $f_3$ imply stress-thickening. A number of researchers [Ewoldt et al. [309]; Rogers et al. [310]] have shown that in the limit of a perfectly plastic response, a $1/n$ dependency is observed in the magnitude of the Fourier harmonics, particularly in plastic strain signal $\gamma''(t)$. Therefore, in the case of yielding materials, the Chebyshev coefficients with order $n \geq 5$ can still play a significant role in determining the material response to LAOS.

### 7.3.2 LAOStress behavior of an elastic Bingham fluid with wall slip

Perge et al. [303,304] have shown that CB gels exhibit fatigue under cyclic oscillatory stress and, using ultrasonic velocimetry measurements, they have shown that yielding occurs first near the wall resulting in a series of transient dynamic slip events. Let us investigate the effect of wall slip on the harmonics of the Fourier decomposition for an EVP material. We choose the elastic Bingham fluid to represent the rheology of the fluid:

$$\begin{aligned} \tau &= G\gamma_e \quad \text{if} \quad \tau < \tau_y \\ \dot{\gamma}_p &= \frac{\tau - \tau_y \text{sgn}(\tau)}{\mu_p} \quad \text{if} \quad \tau > \tau_y \end{aligned} \tag{7.11}$$

where $G$ is the elastic shear modulus of the material, $\tau_y$ is the yield stress, $\mu_p$ the plastic viscosity and $\gamma_e$ and $\dot{\gamma}_p$ are the elastic strain and the plastic strain rate respectively. The yield strain is equivalently $\gamma_y = \tau_y/G$. We define a Navier slip law of the form $V_s = \beta\tau$ where $\beta$ is the slip coefficient. We also assume a strain decomposition into a plastic and an elastic components of the form $\gamma = \gamma_e + \gamma_p$.

In a parallel plate geometry, assuming wall slip at both plates, at a given radius, the apparent or measured shear rate $\dot{\gamma}_a$ is given by $\dot{\gamma}_a = \dot{\gamma} + 2V_s/H$ where $H$ is the gap between the plates, and $\dot{\gamma}$ is the true shear rate.

For an imposed cosinusoidal stress on the material [Eq. 7.5], we can distinguish two regimes: above and below the yield stress. Below the yield stress, the apparent strain $\gamma_a$ is given by

$$\gamma_a = \frac{\tau_0}{G}\cos(\omega t) + \frac{2\beta\tau_0}{H\omega}\sin(\omega t) \tag{7.12}$$

In this case, we find that only the first harmonics are present in the apparent strain response and we have $c_1 = 1/G$ and $f_1 = 2\beta/H$. The presence of wall slip manifests as an apparent fluidity in the LAOStress reponse even for a purely elastic material below the yield stress.

Above the yield stress, the apparent strain is given by

$$\gamma_a = \frac{\tau_0}{G}\cos(\omega t) + \frac{2\beta\tau_0}{H\omega}\sin(\omega t) + \frac{\tau_0}{\mu_p\omega}\sin(\omega t) - \sum_{\text{n odd}} \frac{4}{\pi}\frac{(-1)^{\frac{n-1}{2}}}{n}\frac{\tau_y}{\mu_p n\omega}\sin(n\omega t) \quad (7.13)$$

In this case, we find that $c_1 = \frac{1}{G}$, $f_1 = \frac{2\beta}{H} + \frac{(1-4\tau_y/\pi\tau_0)}{\mu_p}$, $f_n = \frac{4}{\pi}\frac{(-1)^{\frac{n-1}{2}}}{n}\frac{\tau_y}{\mu_p n\tau_0}$, $c_n = 0$ for $n \geq 3$. Once again, the presence of wall slip manifests as an added apparent fluidity in the first harmonic. We also note the absence of even harmonics under these assumptions. This analysis shows that an elastic Bingham fluid with linear slip does not exhibit even harmonics. The addition of transience in the slip law such as the introduction of a relaxation time to the slip law might yield even harmonics in the Fourier spectrum [307].

### 7.3.3 Stress amplitude sweeps

Here, we focus on a CB gel composed of VXC72R particles (Cabot) dispersed at 6%wt. in a mineral oil. A stress-controlled torsional rheometer (DHR-3, TA instruments) with a stainless steel cone-plate geometry was used to apply the oscillatory shear stress ($R = 25$ mm). Two cones of different surface roughness were used: a "smooth" 2° cone of RMS roughness $R_q = 30$ nm and a sandblasted "rough" 4° cone of RMS roughness $R_q = 1.7$ $\mu$m. The cone-plate geometry was chosen to run LAOStress measurements to avoid issues associated with this type of measurement in the parallel plate geometry because of the radial shear inhomogeneity [276]. Continuous oscillation stress control was used here to ensure that there are no breaks in the oscillations. This prevents the motor from drifting between measurements when testing soft or low viscosity samples or when the sample fluidizes under the applied load. All measurements were performed at $T = 23$°C. Prior to each test, the sample was presheared at 100 $s^{-1}$ then rapidly brought to $\tau = 0$ Pa and left to equilibrate for 15 min.

In a time-dependent material, a number of experimental problems may come into play when performing LAOStress experiments with a stress-controlled rheometer, particularly due to the inertia of the instrument and the geometry [305]. The most

common problem is that when the sample fluidizes, the stress due to inertia increases sharply while the rheometer keeps the same total stress so that the actual stress felt by the sample falls below the commanded value. While instrument inertia can be an issue for LAOStress measurements, we have limited our measurements to cases where the measured strains are sufficiently small to neglect such effects. We define a dimensionless inertia number $In$, which estimates the relative magnitude of the inertia torque to the sample torque in the cone-plate geometry as follows:

$$In = \frac{3I\omega^2\theta\gamma_0}{2\pi\tau_0 R^3} \tag{7.14}$$

where $I$ is the inertia of the instrument, $\theta$ is the cone angle, $\tau_0$ is the imposed stress amplitude and $\gamma_0$ is the measured strain amplitude. For our measurements, we fin $In < 0.1$ indicating that we can neglect inertial effects.

Stress amplitude sweeps for 0.16 Pa $\leq \tau_0 \leq$ 40 Pa at $\omega = 6.28$ rad/s were performed for the smooth and rough cone geometries and the results are shown in Fig. 7-5. We observe that as the imposed stress amplitude $\tau_0$ increases, the elastic modulus $G'$ decreases and for large stress amplitudes compared to the yield stress ($\tau_0 \geq 15$ Pa), ends up lower than the loss modulus $G''$.

Comparing results obtained with the smooth vs the rough cone, we observe that the gel yields at a higher stress on the rough surface than on the smooth surface. To quantify this observation, we take the intersection of the lines representing the linear viscoelastic region and the yielded region as the apparent yield stress of the fluid [3] and find that $\tau_y^{\text{smooth}} = 5.3$ Pa and $\tau_y^{\text{rough}} = 9.6$ Pa. These results indicate that the roughness of the surface and therefore interfacial phenomena such as wall slip are potentially playing a role in the yielding of the gel.

The elastic Lissajous curves (strain vs. stress) at different points of the stress amplitude sweeps for the smooth and rough SS surface are shown in Fig. 7-6. The bold letters A-F indicate the points labeled in Fig. 7-5. For small imposed stress amplitudes (A,D), the gel behaves like an elastic solid. As the imposed stress amplitude increases, the gel yields and undergoes plastic deformation and the area enclosed by

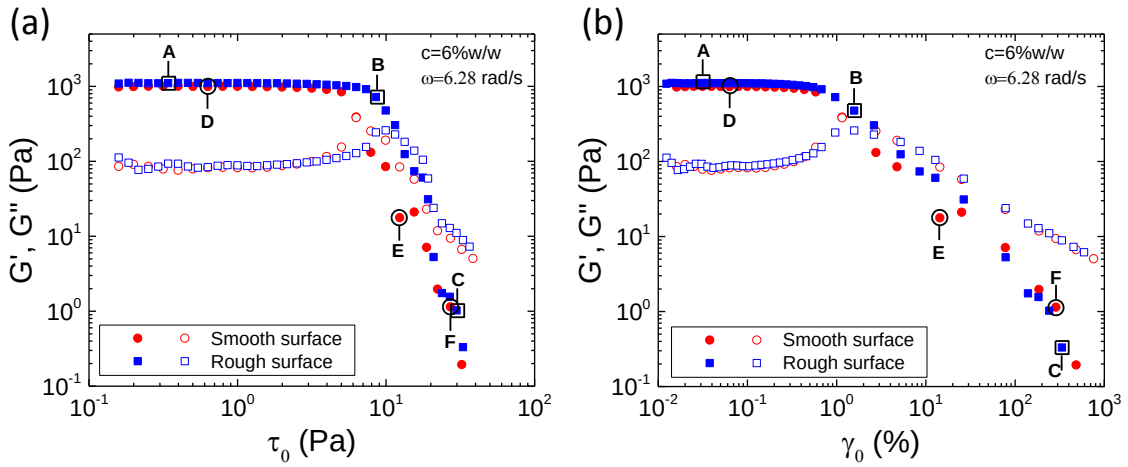


Figure 7-5: Viscoelastic moduli $G'(\omega)$ (closed symbols) and $G''(\omega)$ (open symbols) obtained from stress amplitude sweeps on a smooth and rough SS surface for $\omega = 6.28$ rad/s and a mass fraction $\phi_m = 6\%$wt. of carbon black (VXC72R) in mineral oil at $T = 23°$C. (a) Viscoelastic moduli plotted vs. the imposed stress amplitude $\tau_0$. (b) Viscoelastic moduli plotted vs. the measured strain amplitude $\gamma_0$. The bold letters A-F indicate the points chosen to plot Lissajous curves and Fourier spectrum harmonics in Fig. 7-7 and Fig. 7-6. The letters A-C correspond to the rough surface and in alphabetical order, an imposed stress amplitude $\tau_0 = 0.34, 8.5, 29.7$ Pa with $\tau_y^{\text{rough}} = 9.6$ Pa. This corresponds to $\tau_0/\tau_y^{\text{rough}} = 0.03, 0.88, 3.1$. The letters D-F correspond to the smooth surface and in alphabetical order, an imposed stress amplitude $\tau_0 = 0.63, 13, 29$ Pa with $\tau_y^{\text{smooth}} = 5.3$ Pa. This corresponds to $\tau_0/\tau_y^{\text{smooth}} = 0.12, 2.5, 5.5$.

the Lissajous loop increases indicating greater dissipation is occurring in the gel.

To further understand the yielding behavior of the gel, we analyze our data with the FT rheology package provided by the open source software MITLAOS [14]. The Fourier spectrum harmonics at different points of the stress amplitude sweeps for the smooth and rough SS surface are shown in Fig. 7-7 [The points A-F are labeled on Fig. 7-5]. For both surfaces, we observe that as the gels starts yielding, higher harmonics appear in the Fourier spectrum. While the gel is yielding, we observe the presence of even harmonics, a sign of dynamic slip or transient behavior such as inhomogeneous yielding [275, 303, 307]. Once the gel is fully yielded, the even harmonics disappear and the Fourier spectrum only contains odd harmonics. Fig. 7-8 shows the ratio of the amplitudes of the second and third harmonics $I_2$ and $I_3$ to the

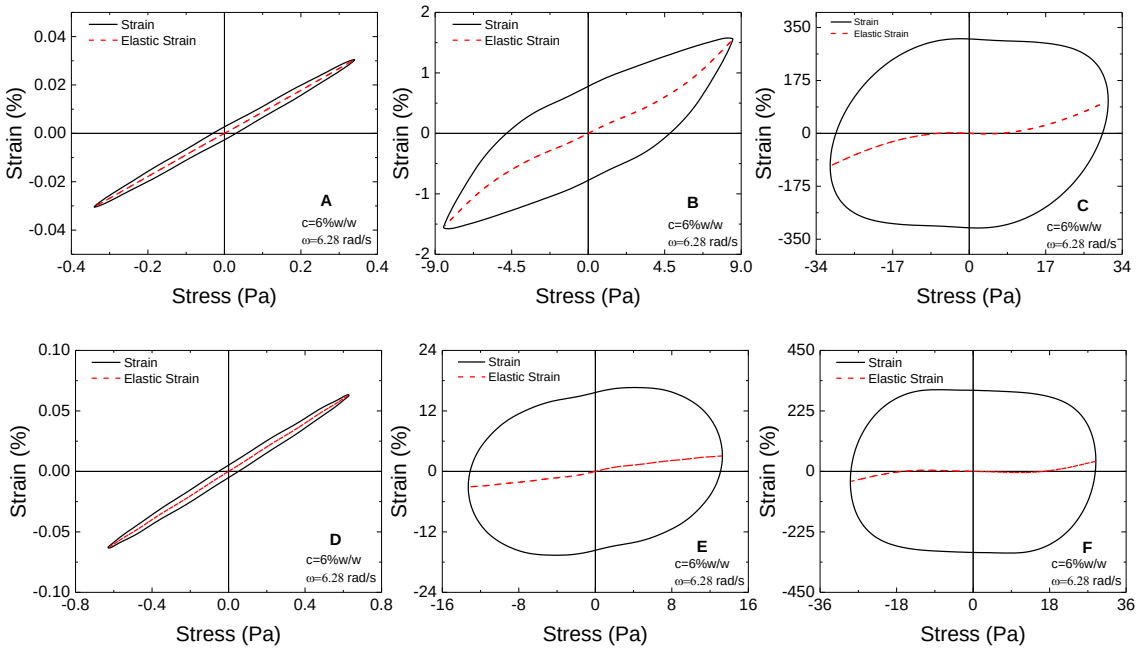


Figure 7-6: Elastic Lissajous curves at different points of the stress amplitude sweeps for the smooth and rough SS surface. The bold letters A-F indicate the points labeled in Fig. 7-5. The dashed red line represents the apparent elastic strain component $\gamma'$ defined in Eq. 7.8. On both surfaces, as the stress amplitude $\tau_0$ increases, the gel transitions from an elastic solid to a yielded fluid. The letters A-C correspond to the rough surface and in alphabetical order, an imposed stress amplitude $\tau_0 = 0.34, 8.5, 29.7$ Pa with $\tau_y^{\text{rough}} = 9.6$ Pa. This corresponds to $\tau_0/\tau_y^{\text{rough}} = 0.03, 0.88, 3.1$. The letters D-F correspond to the smooth surface and in alphabetical order, an imposed stress amplitude $\tau_0 = 0.63, 13, 29$ Pa with $\tau_y^{\text{smooth}} = 5.3$ Pa. This corresponds to $\tau_0/\tau_y^{\text{smooth}} = 0.12, 2.5, 5.5$.

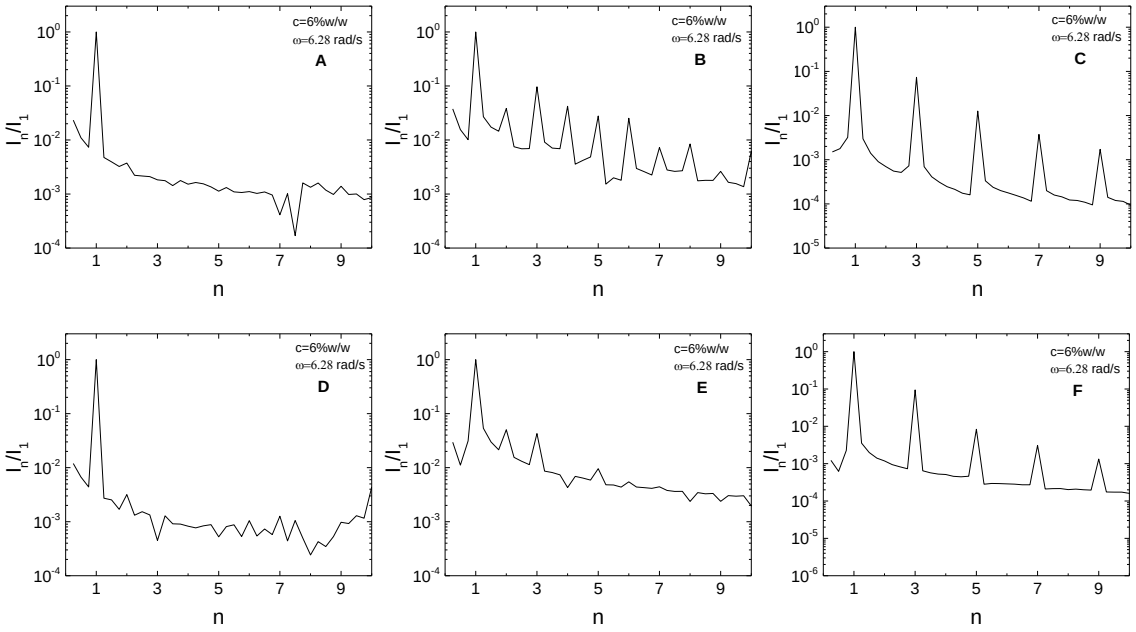


Figure 7-7: Fourier spectra of the non-linear strain response to LAOStress at different points of the stress amplitude sweeps for the smooth and rough SS surface. The bold letters A-F indicate the points labeled in Fig. 7-5. The letters A-C correspond to the rough surface and an imposed stress amplitude $\tau_0 = 0.34, 8.5, 29.7$ Pa in alphabetical order.The letters D-F correspond to the smooth surface and an imposed stress amplitude $\tau_0 = 0.63, 13, 29$ Pa in alphabetical order.

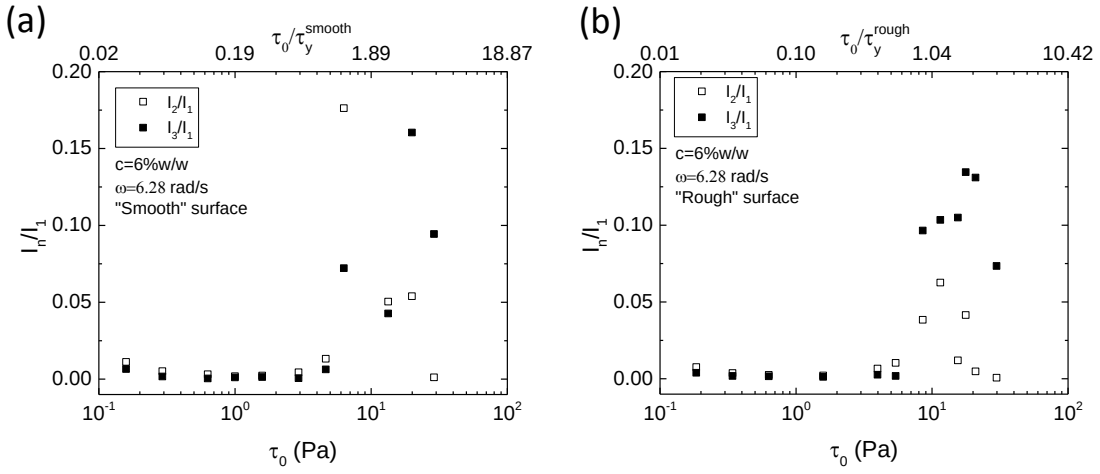


Figure 7-8: Ratio of the amplitude of the second and third harmonic $I_2$ and $I_3$ to the amplitude of the first harmonic $I_1$ as a function of the imposed stress amplitude for the smooth (a) and rough (b) surfaces.

first harmonic $I_1$. We observe that as the gel starts yielding, there is a sharp increase in both the second and third harmonic. In particular, on the smooth surface, close to the yield stress, we observe that the second harmonic can be the dominant non-linear harmonic in the Fourier spectrum. We attribute this behavior to transient behavior occurring as the gel yields heterogeneously and the odd symmetry of the measured strain signal is lost (within one cycle, the properties of the gel change such that one direction of oscillation is not the same as the other). Finally, as observed previously, once the gel fully yields and reaches steady state, only the third harmonic remains and the second harmonic returns to zero.

Next, in Fig. 7-9, we plot the Chebyshev compliance and fluidity ratios $c_3/c_1$ and $f_3/f_1$ vs. the imposed stress amplitude for the rough and smooth surfaces. Since the first Chebyshev compliance and fluidity are positive, the sign of the ratio is the same as the sign of the third coefficient $c_3$ or $f_3$. On the smooth surface, we observe that below the yield stress, we remain in the linear viscoelastic region and the ratios $c_3/c_1$ and $f_3/f_1$ are small and close to zero. Once the stress amplitude exceeds the yield stress, there is an abrupt change that corresponds to an increase of the fluidity ratio that corresponds to stress thinning in the sample. In addition, the compliance ratio first decreases and is negative (corresponding to an apparent stress stiffening) then increases and goes positive corresponding to stress softening of the gel. We note that the region of apparent stress stiffening corresponds to the region where transient effects are dominant and therefore the conclusions in this case should be taken with caution. In general, once the gel fully yields, there is both stress softening and stress thinning behavior observed as expected from the destruction of the CB network. On the rough surface, the behavior is slightly different: the compliance ratio remains only positive and once the yield stress is exceeded increases with the stress amplitude corresponding to stress softening of the gel. Similarly to the smooth surface, the fluidity ratio increases once the stress exceeds the yield stress.

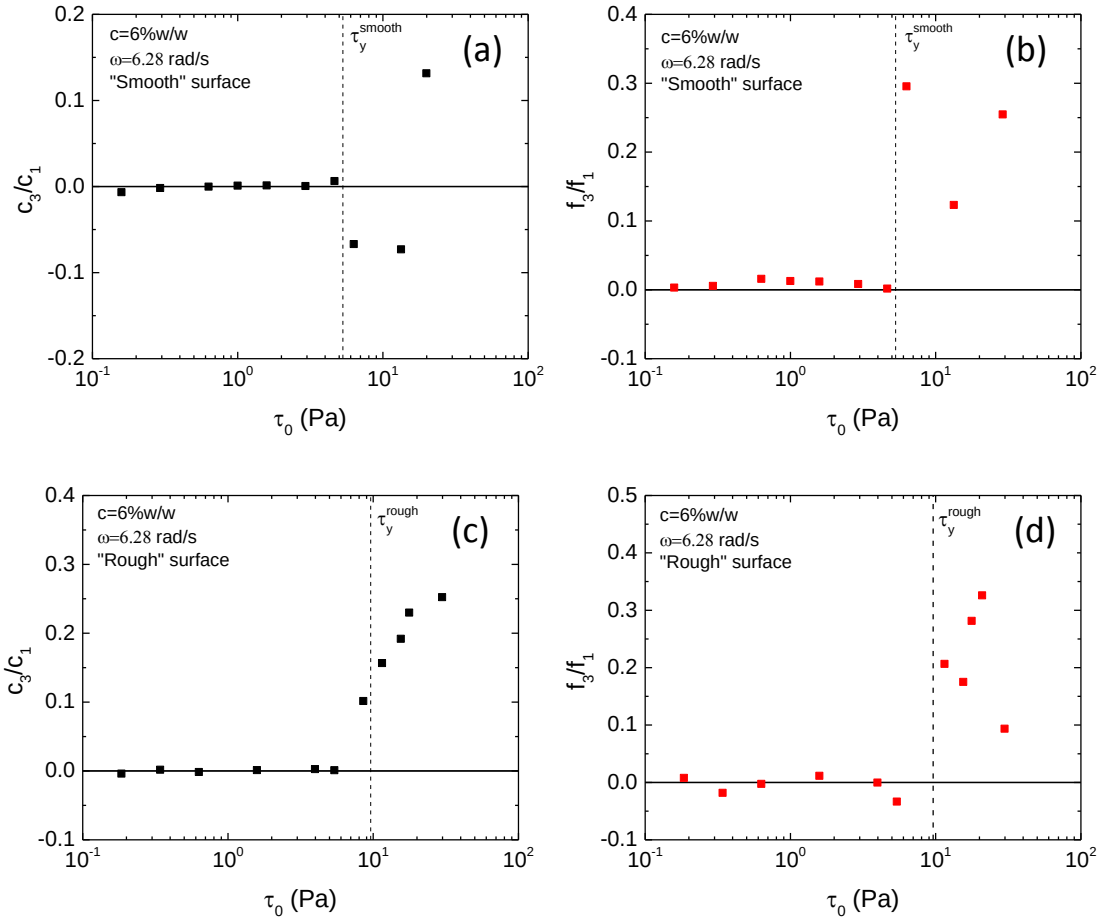


Figure 7-9: Ratio of the third Chebyshev compliance $c_3$ to the first Chebyshev compliance $c_1$ as a function of the imposed stress amplitude $\tau_0$ for the smooth (a) and the rough (c) surfaces. Ratio of the third Chebyshev fluidity $f_3$ to the first Chebyshev fluidity $f_1$ as a function of the imposed stress amplitude $\tau_0$ for the smooth (b) and the rough (d) surfaces. The dashed lines correspond to the yield stress extracted from the amplitude sweep data in Fig. 7-5 for the rough and smooth surfaces.

### 7.3.4 Fatigue of carbon black gels

Perge et al. [303,304] have that under cyclic loading at a constant stress amplitude well below its apparent yield stress, the gel displays fatigue and progressively turns from an elastic solid to a viscous fluid. In this section, we further explore this phenomena by comparing the fatigue behavior between the smooth and rough surfaces. We shall mainly focus on two LAOStress experiments performed at a constant stress amplitude $\tau_0 = 4.2$ Pa ($\tau_0/\tau_y^{\text{smooth}} = 0.79$) and $\tau_0 = 8.0$ Pa ($\tau_0/\tau_y^{\text{rough}} = 0.83$) for the smooth and rough surface respectively. The tests were performed at a constant frequency $\omega = 6.28$ rad/s over 3000 s on the same gel and using the same geometries described in section 7.3.3 at $T = 23°C$.

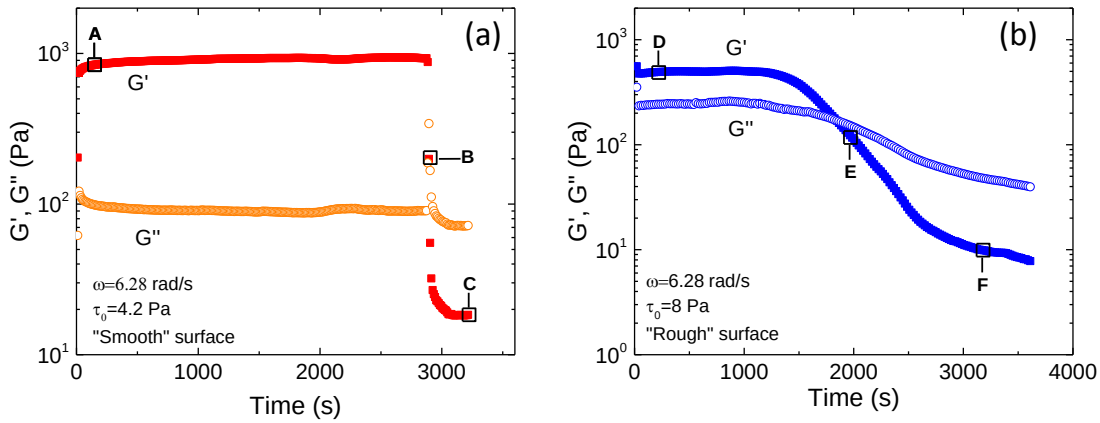


Figure 7-10: Viscoelastic moduli $G'(\omega)$ (closed symbols) and $G''(\omega)$ (open symbols) vs. time obtained from cyclic loading at a constant stress amplitude on a smooth and rough SS surface for $\omega = 6.28$ rad/s and a mass fraction $\phi_m = 6\%$wt. of carbon black (VXC72R) in mineral oil at $T = 23°$C. (a) Viscoelastic moduli vs. time on the smooth SS surface for an imposed stress amplitude $\tau_0 = 4.2$ Pa (b) Viscoelastic moduli vs. time on the rough SS surface for an imposed stress amplitude $\tau_0 = 8.0$ Pa The bold letters A-F indicate the points chosen to plot Lissajous curves and Fourier spectrum harmonics in Fig. 7-12 and Fig. 7-11. The letters A-C correspond to the smooth surface and times corresponding to $t = 221, 2904, 3190$ s in alphabetical order. The letters D-F correspond to the rough surface and times corresponding to $t = 260, 1968, 3370$ s in alphabetical order.

The apparent viscoelastic moduli $G'$ and $G''$ given by the rheometer obtained

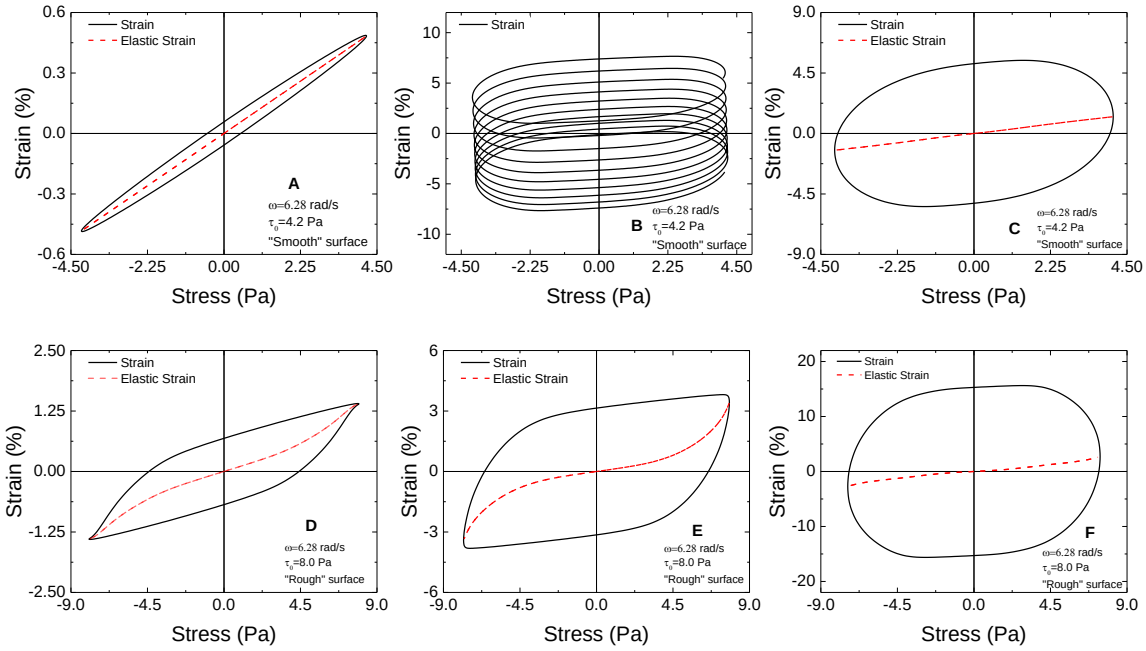


Figure 7-11: Elastic Lissajous curves at different times of the cyclic loading tests for the smooth and rough SS surface. The bold letters A-F indicate the points labeled in Fig. 7-10. The dashed red line represents the apparent elastic strain component $\gamma'$ defined in Eq. 7.8. On both surfaces, the fluid exhibits fatigue and yields under cycling loading.

under cyclic loading of the gel on the smooth and rough surfaces are shown as a function of time in Fig. 7-10. As expected, in both cases, the gel displays fatigue and transitions from an elastic solid with $G' \gg G$" to yielded fluid $G$" $> G'$ at a failure time $t_f = 2880$ s for the smooth surface and $t_f = 1333$ s for the rough surface. However, there is a major difference in the yielding behavior of the gel on the smooth surface vs. the rough surface. On the smooth surface, the gel fails abruptly, experiences a short transient response and reaches steady state within a few cycles. On the other hand, on the rough surface, the transition is more gradual and occurs on a much longer duration.

The elastic Lissajous curves (strain vs. stress) at different times of the cyclic loading tests for the smooth and rough SS surface are shown in Fig. 7-11. The bold letters A-F indicate the points labeled in Fig. 7-10. The letters A-C correspond to the smooth surface and times corresponding to $t = 221, 2904, 3190$ s in alphabetical

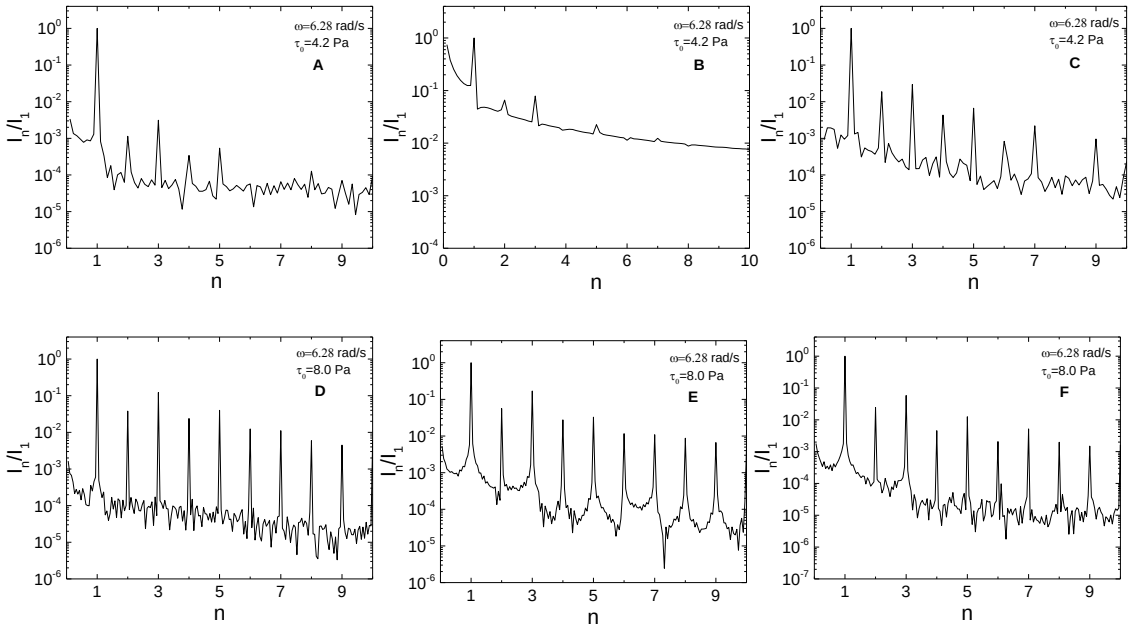


Figure 7-12: Fourier spectra of the non-linear strain response to LAOStress at different times of the cyclic loading tests for the smooth and rough SS surface. The bold letters A-F indicate the points labeled in Fig. 7-10.

order. The letters D-F correspond to the rough surface and times corresponding to $t = 260, 1968, 3370$ s in alphabetical order. On the smooth surface, at small times, the gel behaves like a rigid elastic solid. As $t > t_f$, the gel yields and undergoes plastic deformation as shown by the increase in the area of the Lissajous loop. The abrupt yielding on the smooth surface is accompanied with a strong transient response as shown in the B case in Fig. 7-11. On the rough surface, the gel starts out partially yielded ($(\tau_0/\tau_y^{\text{rough}} = 0.83)$) i.e. not in the linear viscoelastic region but continues to plastically deform as time increases and exceeds $t_f$.

To further understand the fatigue behavior of the gel, we analyze our data with the FT rheology package provided by the open source software MITLAOS [14]. The Fourier spectrum harmonics at different points of the stress amplitude sweeps for the smooth and rough SS surface are shown in Fig. 7-12 [The points A-F are labeled on Fig. 7-10]. We notice the presence of a weak second and fourth harmonic in the Fourier spectrum of the smooth surface and an increase in the amplitude of the odd harmonics once the gel yields. On the rough surface, both even and odd harmonics

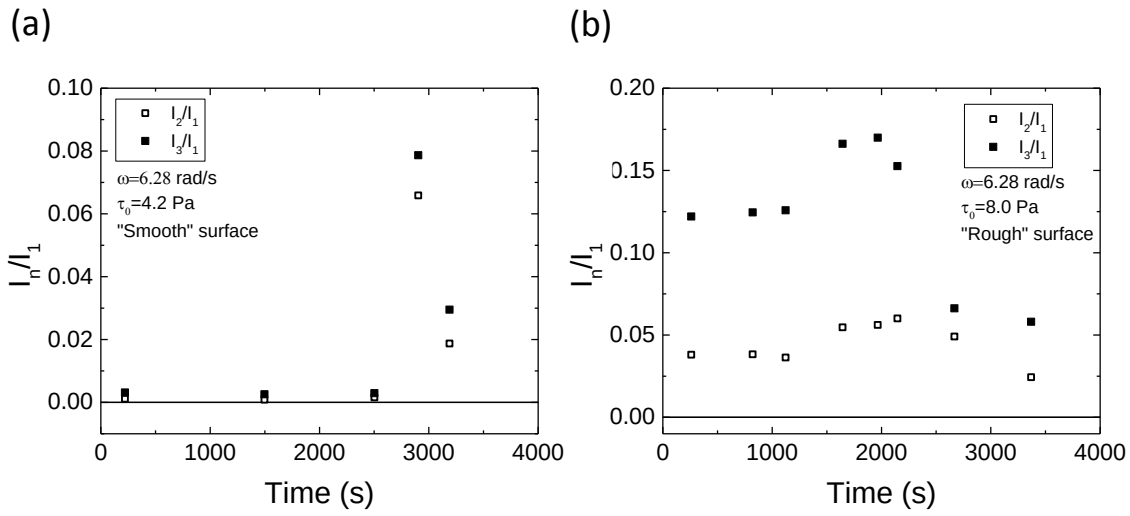


Figure 7-13: Ratio of the amplitude of the second and third harmonic $I_2$ and $I_3$ to the amplitude of the first harmonic $I_1$ as a function of time in the cyclic loading tests for the smooth (a) and rough (b) surfaces.

are present in relatively equal amounts indicating that transient behavior or dynamic slip are occurring. This is unsurprising since on the rough surface, the gel starts in a semi-yielded state ($\tau_0/\tau_y^{\text{rough}} = 0.83$) and we have discussed in section 7.3.3 that as the gel starts to yield, even harmonics tend to appear. Fig. 7-13 shows the ratio of the amplitudes of the second and third harmonics $I_2$ and $I_3$ to the first harmonic $I_1$ as a function of time for the smooth and rough surface. On the smooth surface, the gel starts in the linear viscoelastic region (both $I_2/I_1$ and $I_3/I_1$ are close to zero) then fails abruptly and this failure is associated with a strong transience that manifests in a large increase in $I_2/I_1$ and $I_3/I_1$ over the short duration of the yielding. On the rough surface, the gel displays some non-linearities from the start as it is partially yielded (both $I_2/I_1$ and $I_3/I_1$ are non-zero). As $t$ exceeds $t_f$, both the second and third harmonic ratio increase in the yielding region before decreasing once the gel is fully yielded.

We plot the Chebyshev compliance and fluidity ratios $c_3/c_1$ and $f_3/f_1$ against time for the cyclic loading tests on the rough and smooth surfaces in Fig. 7-14. On the smooth surface, we again note that the gel starts in the linear viscoelastic region then fails abruptly and reaches steady state. As the gel fails, there is a alot of transience

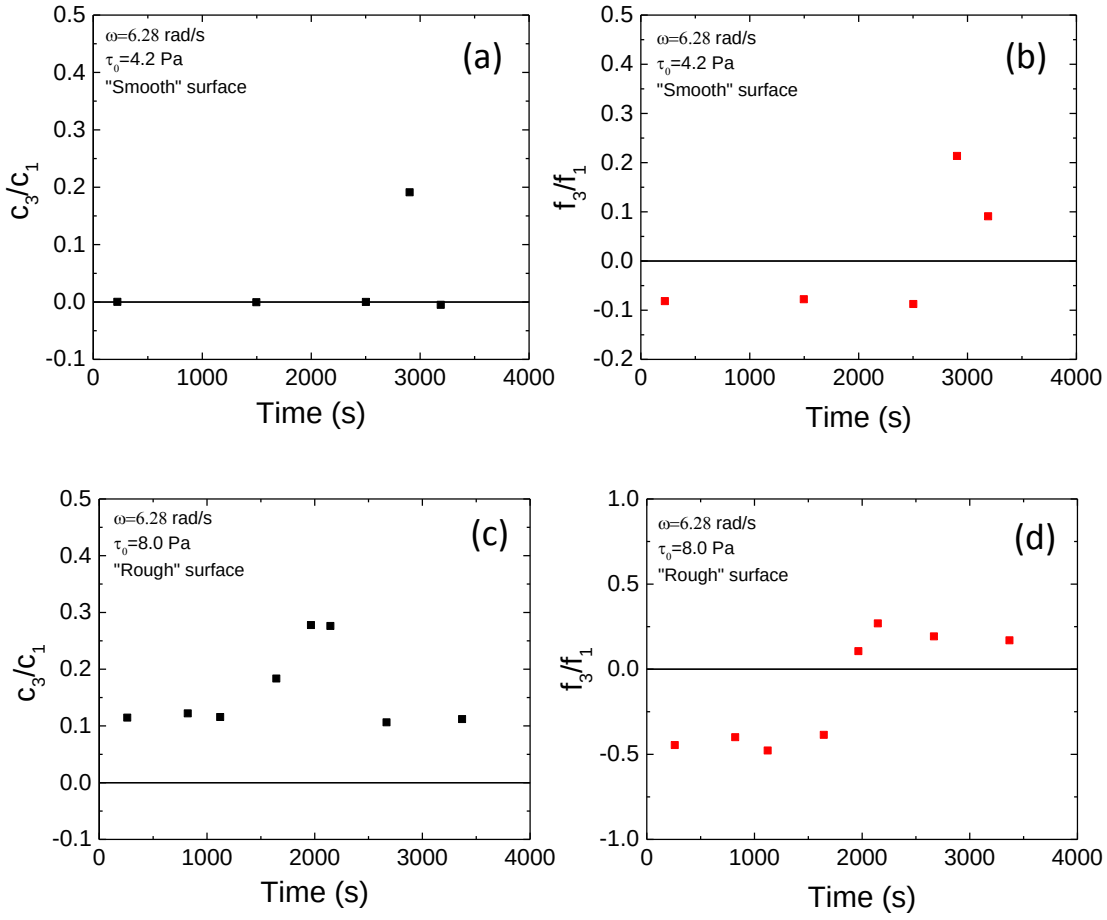


Figure 7-14: Ratio of the third Chebyshev compliance $c_3$ to the first Chebyshev compliance $c_1$ as a function of time in the cyclic loading tests for the smooth (a) and the rough (c) surfaces. Ratio of the third Chebyshev fluidity $f_3$ to the first Chebyshev fluidity $f_1$ as a function of time in the cyclic loading tests for the smooth (b) and the rough (d) surfaces.

(see point B in Fig. 7-11) that is associated with an apparent stress softening. We note that in the prior to yield, the gel displays a weak stress thickening then once the gel yields, the gel exhibits stress thinning. On the rough surface, the gel initially exhibits stress softening ($c_3/c_1 > 0$) that increases as it starts yielding before decreasing post yield. Additionally, the gel initially exhibits stress thickening ($f_3/f_1 < 0$) before the onset of the yielding process. As the yielding occurs, $f_3/f_1$ slowly increases and changes sign as the gel stress thins.

These observations lead us to propose two different yielding scenarios for the fatigue of CB gels on rough and smooth surfaces. In both cases, the onset of failure occurs near the interface and leads to dynamic slip behavior that manifests in the appearance of even harmonics in the Fourier spectrum. On the smooth surface, the gel adheres poorly and it yields abruptly across the whole interface at the same time creating a lubrication layer and a portion of the gel that flows as a plug. This is corroborated by the apparent stress thinning behavior post yield ($f_3/f_1 > 0$) and the short duration of the yielding process in comparison to the rough surface. On the rough surface, the gel will tend to adhere more to the interface and as a consequence, the gel will not yield uniformly at the interface but rather start at the weakest point then the yielding will propagate to the rest of the interface and the bulk. This behavior is corroborated by the longer duration of yielding, the presence of dynamic slip events and the apparent stress thinning of the gel during the yielding process ($f_3/f_1 > 0$). These scenarios are in agreement with ultrasound velocimetry measurements performed by Perge et al. [303,304] that also show that on the "rough" surface of their Couette cell bob, the gel first yields at a specific location on the interface and then the yielding propagates to the rest of the interface and the bulk of the gel. The work of Gibaud et al. [304] also discuss the dependence of the failure time with the amplitude of the imposed cyclic stress. They show that the failure time can be fit empirically by either an exponential decreasing function of stress $t_f \sim \exp(-\tau_0)$ (delayed yielding model) or by a power law $t_f \sim \tau_0^{-\alpha}$ (Basquin model [311]). According to the Basquin model, CB gels are prompt to accumulate damage and are much more sensitive to stress than asphalt or metals [304]. According to the delayed failure model, the carbon

black particles have a weaker interaction with the walls than between themselves which justifies that the gel yields first at the wall and then in bulk [304]. Future studies should probe the dependence of the failure time on the applied cyclic stress amplitude on both rough and smooth surfaces to further understand the driving mechanism behind the observed fatigue.

To sum up, we investigated the effect of the surface roughness on the fatigue of CB gels. Our results confirm the observation that fatigue is linked to adhesive failure at the interface and that surface roughness affects the rapidity of the failure process. These conclusions indicate that the second and third harmonic ratios $I_2/I_1$ and $I_3/I_1$ are good predictors of the onset of failure due to fatigue as dynamic slip and transient events occur. Additionally, the fluidity ratio $f_3/f_1$ is another indicator of the onset of fatigue as the gel transitions from stress thickening ($f_3/f_1 < 0$) to stress thinning behavior ($f_3/f_1 > 0$) during the yield process. Accurate predictiors of the onset of fatigue are important for applications such as semi-solid flow batteries where cyclic loading is common (e.g. intermittent flow) and where fatigue will result in a decrease of the conductivity of the slurry. An interesting area for future work is testing whether conductivity measurements during the fatigue process can be good predictors for the onset of fatigue. As discussed in Chapter 6, conductivity measurements have a higher resolution than mechanical measurements, particularly in low deformation regimes and therefore could be a useful tool for the study of fatigue.

# Chapter 8

# Gravity-induced Flow Cell Design (GIFcell)

## 8.1 Introduction

Low-cost, scalable energy storage is crucial to the integration of sustainable but intermittent energy generation technologies such as wind and solar into the electric power infrastructure. Redox flow batteries are among the technologies that may meet these needs, due to their ability to decouple stored energy from power, inherent scalability, and potential for low cost [118, 120, 132]. Existing flow batteries designed to operate with low energy density aqueous solution flow electrodes of 1-2 M redox active concentration (also termed catholyte and anolyte) [135, 312], are relatively complex electrochemical-mechanical systems in which a high part count has historically compromised reliability and cost. Despite about thirty years of development, the basic architecture of the flow battery has not changed. With the advent of high energy density flow electrodes, such as the semi-solid lithium ion suspensions pioneered by Duduta et al. [121] and the electronically-conductive lithium polysulfide solution/precipitation flow electrodes developed by Fan et al. [34], opportunities to re-invent the conventional flow battery have arisen. We are motivated by these new flow electrode capabilities to explore potentially more efficient, passively driven, compact, simpler and lower-cost flow battery architectures.

Here, we develop and demonstrate one such concept, a pumpless design that utilizes gravity to induce flow (Fig. 8-1) referred to herein as a gravity-induced flow cell (GIFcell) [136]. Conceptually analogous to an hourglass of variable tilt angle, gravitational force causes flow of energy-dense electrodes through a centrally positioned electrochemical stack. Reversal of flow is carried out by physically inverting the GIFcell. Each half-cycle of the battery, whether charge or discharge, may be conducted with multiple passes, or in theory a single pass (i.e., "stoichiometric" flow) [222]. In this chapter, we identify the most important design parameters for such a flow battery through modeling and experiment, and demonstrate how an understanding of the rheology and wall slip behavior of the energy-dense, rheologically complex non-flow electrodes can be used to guide cell design and operation.

For stationary flow battery applications, a more energy-dense chemistry not only reduces system size, but can lower system cost and improve efficiency and reliability. As shown by Chen et al. [136], the mechanical loss in operating the GIFcell is a very small fraction of the stored electrochemical energy of the battery. This is not surprising since a fundamental advantage of electrochemical storage is its much higher energy density compared to mechanical approaches (e.g., pumped hydroelectric storage). Although the GIFcell can be scalable to large size without sacrificing this fundamental mechanical efficiency, the availability of compact modular flow cells permits new design flexibility, including highly networked architectures not possible with conventional flow batteries. Systems of large total energy could be composed of parallel/series networks of individual cells, each of which has variable power output (through tilt angle) and can be easily switched, providing redundancy and improving the reliability of the network.

## 8.2 Cell design

Although the GIFcell concept can in principle be applied broadly to the expanding number of flowable, energy-storing solutions and suspensions [34, 121, 125], we focus here on high energy density flow electrodes which will tend to have higher viscosities

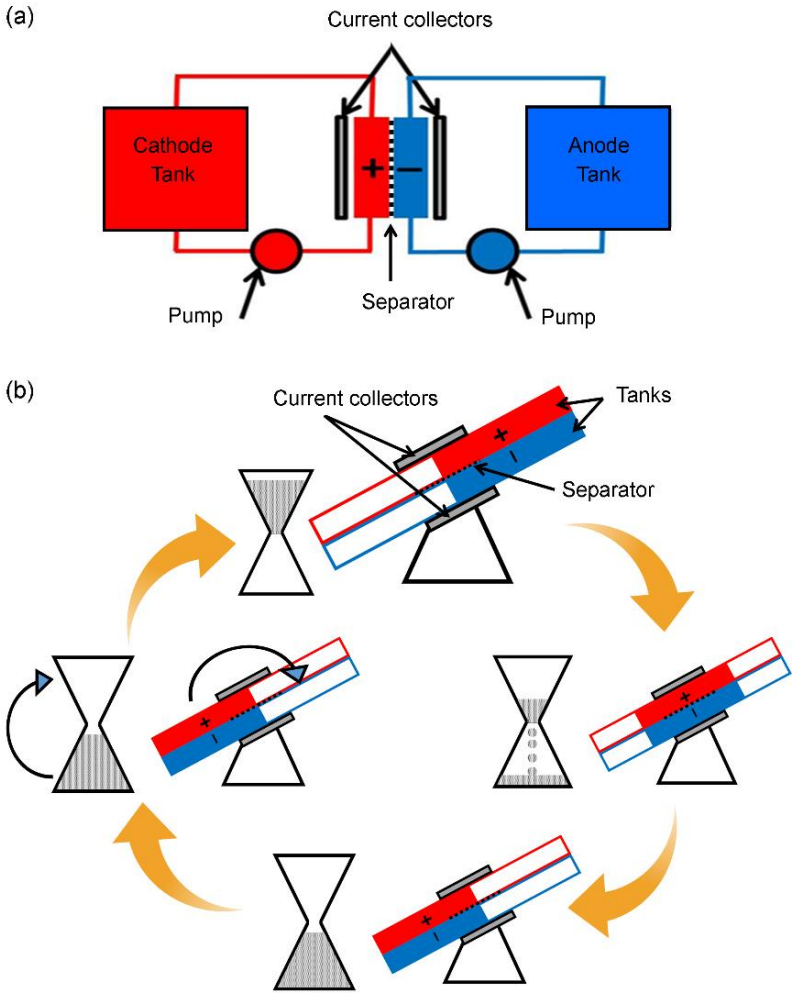


Figure 8-1: Conventional redox flow battery design versus new scheme. (a) A conventional redox flow battery consists of two fluid tanks, from which catholyte and anolyte are mechanically pumped through the electrochemical cell stack. (b) The gravity-induced flow cell (GIFcell) has an operational principle analogous to that of an hourglass, relying on gravity to move the catholyte and anolyte through the power-extracting stack. The flow rate is controlled by tilt angle, cell design, and surface engineering for fluid slip. Electrochemical performance such as power and efficiency is controlled by the flow rate, stack design, and the inherent properties of the flow electrodes. Reversal of flow by flipping the GIFcell allows switching between charge and discharge cycles as well as multiple-pass operation during in either half-cycle.

compared to typical aqueous flow electrolytes of low molar concentration, such as vanadium redox solutions (20-70 cP) [34]. Furthermore, non-Newtonian rheology is likely to be the rule rather than the exception at high concentrations of redox active species. To illustrate the special considerations that must be taken into account when designing for complex rheology, we use lithium-sulfur as the experimental chemistry. As the positive electrode, we use the electronically-conductive lithium polysulfide suspensions developed by Fan et al. [34], wherein percolating nanocarbon suspensions provide an extended, in-situ, current collector network enabling charge-transfer throughout the volume of the flow electrode. For the negative electrode, we use a stationary lithium metal foil as was used by Fan et al. [34]. This "half-flow-cell" design in which only the cathode flows allows the operation of the GIFcell to be evaluated in a simpler design than a "full-flow cell" (our ultimate goal) in which both electrodes flow.

Fig. 8-2 shows a lab-scale prototype of the GIFcell design. A GIFcell computer-aided design (CAD) model (excluding fasteners) is shown in Fig. 8-2(c). The casing was 3D-printed from an ABS-like polymer proprietary to the manufacturer (Somos WaterShedXC 11122, DSM). Gaskets and fasteners were made from ethylene propylene diene monomer (M-Class) rubber (EPDM), Teflon, or stainless steel, each of which was separately shown to be chemically non-reactive with the flow catholyte and lithium metal anode over the duration of the experimental tests. Gold-sputtered stainless steel plates were used as the current collectors, with a current collector area of 2 $cm^2$ being used for a single channel of electrode thickness $H = 1.6$ mm, $W = 10$ mm and $L = 75$ mm. Here, a porous carbon current collector is not used, since the suspended carbon provides both electronic conductivity and surface area for charge transfer. The volume of flow electrode that occupies the space between current collectors, which we refer to as an "aliquot" [222], is 0.32 $cm^3$. The total electrolyte volume per channel is 3.75 aliquots (1.2 $cm^3$).

Similarly to the suspensions discussed in chapter 4, the sulfur flow electrode does not contain solid elemental sulfur but rather contains $Li_2S_8$, which is completely soluble in the solvent phase. A very high specific capacity of 1000 mAh/g is obtained

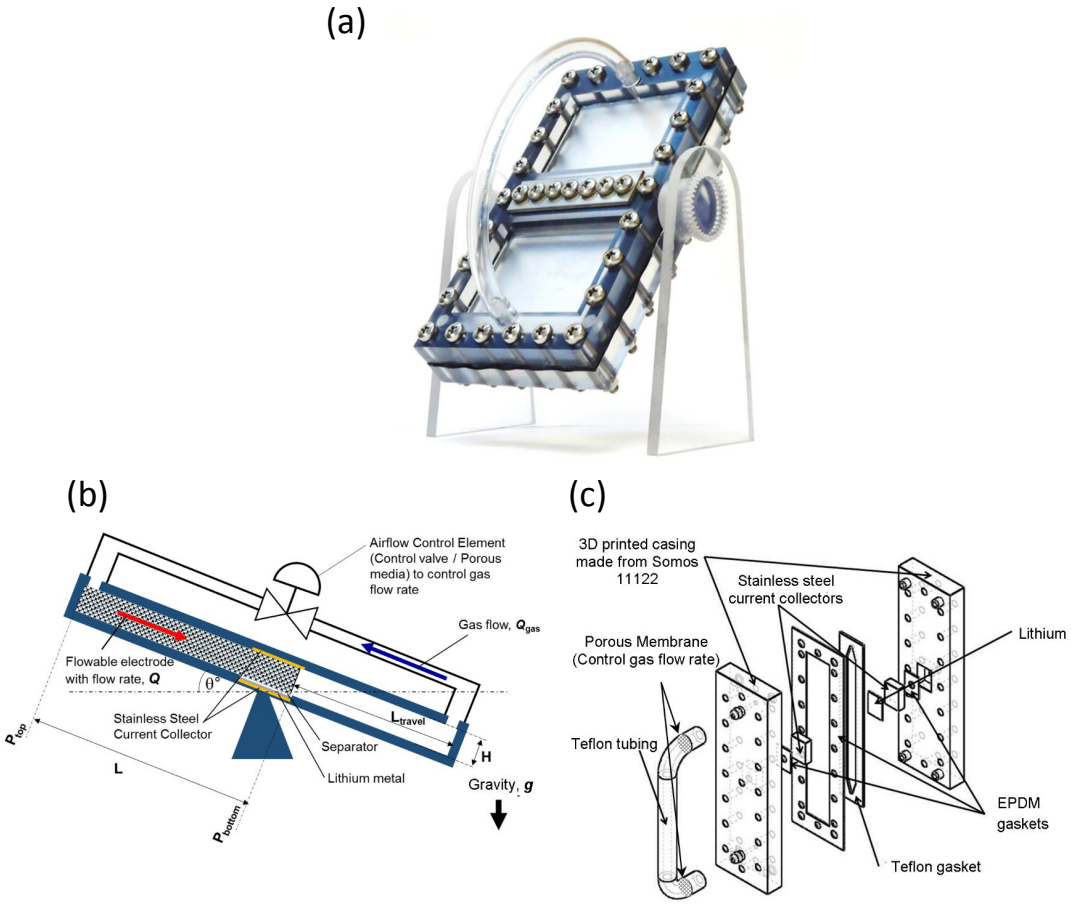


Figure 8-2: (a) First generation laboratory-scale prototype of gravity-induced flow cell (GIFcell) fabricated by 3-dimensional printing of major components. The design is a half-flow-cell with flowing catholyte and stationary Li metal counter-electrode. The internal volume ratio of storage "tanks" to electrochemical stack is $\sim 4:1$, and flow channel has high width to thickness aspect ratio. (b) Schematic of improved design combining gravity feed with passive gas flow rate controller. The notations used are the flow modeling parameters. (c) Exploded view of components for the GIFcell design in (b).

since the sulfur positive electrode is cycled between the composition limits $Li_2S_8$ (dissolved) and $Li_2S$ (solid); the incorporation of the nanoscale conductor network permits charge-transfer throughout the volume of the electrode and allow sulfur utilization over both the solution-phase and precipitation (of $Li_2S$) regimes. However, in the flow cell experiments, the range of the cathode reaction was limited to the fully-soluble regime between $Li_2S_8$ and $Li_2S_6$, to minimize rheological changes that accompany the precipitation of solid $Li_2S$. Thus the overall cell reaction used is $2Li + 3Li_2S_8 \rightarrow 4\ Li_2S_6$.

## 8.3 Flow electrode design

In this section, we discuss the choice of the flow electrode in terms of solvent choice and carbon loading for the GIFcell. The basic formulation of the semi-solid flow cathode consists of a solution phase containing $Li_2S_8$ dissolved in a glyme solvent, with 0.5 M LiTFSI and 1 wt% of $LiNO_3$ being added as the supporting salt and solid electrolyte interphase (SEI) formation additive, respectively, and into which is dispersed ¡1% by volume of a nanoscale carbon. At low concentrations (0.5-2.0 vol%) of the percolating carbon network, electronic conductivities of 2.5-18 mS/cm are achievable in the flow electrode, which exceed typical ionic conductivities for the nonaqeuous electrolyte. These flow electrodes have a viscoplastic rheology wherein the fluid has a finite yield stress as well as shear-thinning behavior. Typically, a Bingham plastic [Eq. 1.2] or Herschel Bulkley model [Eq. 1.3] are used to model the rheology of the fluids. For flow modeling, using the Bingham model makes for more tractable equations but if the material is shear-thinning, the Bingham model fit will tend to overestimate the yield stress. A compromise between simpler flow equations and good accuracy for fits can be made if we use a piecewise Bingham model over the range of shear rates of interest where we define a transition stress $\tau_t$ above which we allow the yield stress and plastic viscosity to change while keeping the function piecewise continuous. The equation for the piecewise Bingham model is given by

$$\dot{\gamma} = 0 \quad \text{if} \quad \tau < \tau_y$$

$$\tau = \tau_y + \mu_p \dot{\gamma} \quad \text{if} \quad \tau > \tau_y \tag{8.1}$$

$$\tau = \tau_y' + \mu_p' \dot{\gamma} \quad \text{if} \quad \tau > \tau_t \tag{8.2}$$

For a shear-thinning material, the piecewise Bingham model will provide a more accurate fit than the Bingham model while keeping linear plastic terms for simpler flow equations.

Rheology and electrochemical performance are strongly dependent on composition. Solvent choice is a trade-off between volatility, viscosity and electrochemical function; within the glyme family, diglyme showed the highest capacity and lowest polarization [Fig. 8-3(a)], but has too high a vapor pressure for consistent experimentation (Table 8.1). Exchange current density measurements of $Li_2S_6$ solutions show an order of magnitude decrease in interfacial reaction rate on glassy carbon between the endmembers diglyme and tetraglyme. On the other hand, all three glymes tested have similar viscosities at a constant carbon black loading [Fig. 8-3(b)]. Therefore, the triglyme electrolyte was chosen as the most suitable compromise between low volatility and facile electrochemical kinetics.

| **Solvent** | **Vapor Pressure (mm Hg) 20°C** | **Ionic Conductivity (mS/cm) 25°C** | | **Viscosity (mPa.s)** |
|---|---|---|---|---|
| | | 0.5M LiTFSI, 1wt% $LiNO_3$ | 0.5M LiTFSI,1wt% $LiNO_3$, 2.5M $Li_2S_8$ | 0.5M LiTFSI,1wt% $LiNO_3$, 2.5M $Li_2S_8$ |
| Diglyme | 3 | 5 | 3.31 | 9 |
| Triglyme | 0.9 | 3.7 | 3.09 | 17 |
| Tetraglyme | 2.14 | 2.14 | 2.00 | 25 |

Table 8.1: Vapor pressures of the glyme-solvent family, and the ionic conductivities and viscosities of 2.5 M lithium polysulfide ($Li_2S_8$) solution with the additives (0.5M LiTFSI and 1wt% $LiNO_3$) with various solvent of the glyme family.

The yield stress and viscosity of the semi-solid catholyte are most strongly depen-

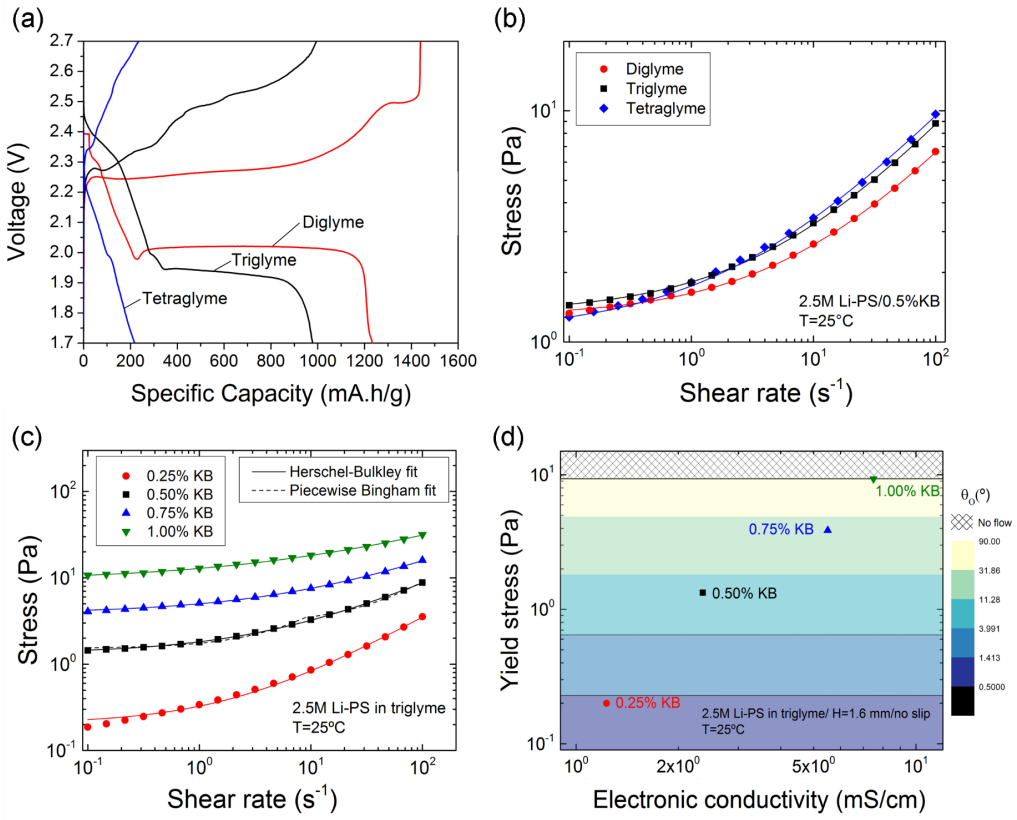


Figure 8-3: Selection criteria for an optimal polysulfide flow catholyte based on electrochemical and rheological considerations. (a) Voltage-capacity profile for Li metal/Li-polysulfide suspension (Li/Li-PS) electrochemical couples tested in a stationary cell configuration (Swagelok cell) at C/5 rate. Of the three glyme solvents for which results are shown, triglyme offers optimal tradeoff between volatility and electrochemical performance. In all cases the catholyte consists of a 2.5 M Li-PS suspension containing 1 vol% ketjen black for electronic conductivity, 0.5 M LiTFSI salt, and 1 wt% $LiNO_3$ additive for anode passivation. (b) Slip-corrected flow curves measured at 25°C show similar rheology behavior for the three suspensions, indicating that carbon content dominates rheological behavior. (c) Effect of Ketjenblack (KB) loading (vol%) on the slip-corrected flow curves measured at 25°C for 2.5 M Li-PS triglyme suspensions. The experimentally measured profiles are fitted to the Herschel-Bulkley model (solid lines) and the piecewise Bingham plastic model (dashed line). (d) Relationship between the yield stress and electronic conductivity for the triglyme suspensions as a function of KB loading, showing that both increase with KB loading. The color contour scale shows the calculated tilt angle for onset of flow ($\theta_O$) in a GIFcell as a function of the yield stress, at constant flow channel thickness of $H = 1.6$ mm and assuming no-slip boundary conditions.

dent on the carbon black content, as shown in Fig. 8-3(c) for the triglyme solvent. The yield stress increases by a factor of 100 between 0.25% and 1% carbon by volume, which strongly limits gravitational flow. However, higher nano-carbon content also increases electronic conductivity, which in turn can improve electrochemical kinetics. Fig. 8-3(d) shows the yield stress vs. electronic conductivity of the flow electrode using triglyme solvent. Separate experimentation showed that adequate electrochemical kinetics could be achieved over a range of carbon contents, and that the limiting factor is yield stress-controlled gravitational flow. Assuming a stress-free interface with no slip of the fluid at the wall, the wall shear-stress in the flow electrode $\tau_w$ is given by:

$$\tau_w = \rho g \sin(\theta) \frac{H}{2} \tag{8.3}$$

where $\tau_w$ is the shear stress at the wall, $\rho$ is the density of the suspension, $g$ is the acceleration due to gravity, $H$ is the thickness of the fluid film, and $\theta$ is the angle of the GIFcell from the horizontal plane (to which gravity is normal). The notations for the GIFcell are shown in Fig. 8-2(b). The critical angle for the onset of flow, $\theta_O$, occurs when the shear stress at the wall, $\tau_w$, reaches the yield stress of the suspension, $\tau_w = \tau_y$, and is given by:

$$\theta_O = \sin^{-1}\left(\frac{2\tau_y}{\rho g H}\right) \tag{8.4}$$

Fig. 8-3(d) shows color contours giving the critical flow angle corresponding to the yield stresses shown, assuming $H = 1.6$ mm. In order to allow for a wide range of flow angles ($\theta_O \leq 15°$), the carbon loading was thus chosen to be 0.5 vol%. This 0.5 vol% carbon flow electrode, containing 2.5 M S/L of $Li_2S_8$ in triglyme with 0.5 M LiTFSI and 1 wt% $LiNO_3$, has nearly identical electronic and ionic conductivity of $\sim$ 2.5 mS/cm, and is an ideal mixed-conductor. The suspension was measured to have the following Herschel-Bulkley parameters (curve fit to $R^2 = 0.99$): Yield stress is $\tau_y = 1.33$ Pa, consistency is $K = 4.48$ Pa.s$^n$ and power-law index is $n = 0.59$. For simpler flow modeling, a piecewise Bingham model is also fit to the rheometric data in Fig. 8-3(c) to $R^2 = 0.99$. A kink at the transition stress is a consequence of this model as seen in Fig. 8-3(b).

Despite designing the suspension for flow in the absence of wall slip, the introduction of high slip surfaces is beneficial as it allows the carbon black containing suspension to flow unyielded as a plug even at lower tilt angles, permitting flow control and higher electrochemical efficiency over a wider range of operating conditions [222]. We explore the impact of wall slip on flow cell design using an analytical model and corroborating experiments. Surfaces of low energy and those with which the suspension has a high contact angle are likely to exhibit stronger slip at the wall [151]. For the glyme-based flow cathodes used here, PTFE (Teflon) proved to be a useful high slip surface, as characterized in Fig. 8-4. To examine the impact of wall slip on cell design, two model surfaces were compared; a stainless steel surface exhibiting no wall slip and the Teflon surface. Using a torsional rheometer with a parallel plate geometry, the slip velocity was determined using the multiple gap slip correction model proposed by Yoshimura & Prud'homme [139] and discussed in chapter 4. The slip velocity $V_s$ of our model suspension is shown in Fig. 8-4 as a function of the applied shear stress $\tau$ for the stainless steel and Teflon surfaces. The stainless steel surface was found to exhibit no wall slip within the range of stress accessible through the measurement. For the Teflon surface, above a critical stress $\tau_c$, a finite slip velocity that increases linearly with applied stress was observed. The critical stress $\tau_c$ is associated with the work needed for adhesive failure at the wall surface and onset of slip. Chen et al [136] show in their work that a droplet of the polysulfide catholyte was able to glide freely on a Teflon surface but not on the acrylonitrile butadiene styrene (ABS) material from which the flow cell bodies were fabricated (by 3D printing). The advancing and receding contact angles of a 0.5 vol% KB suspension on the Teflon were found to be 71.4° and 70.9° respectively.

Wall slip behavior was modeled using a critical slip model [313] given by:

$$\begin{aligned} V_s &= 0 \quad \text{if} \quad \tau < \tau_c \\ V_s &= \beta(\tau - \tau_c) \quad \text{if} \quad \tau > \tau_c \end{aligned} \tag{8.5}$$

where $\tau_c$ is the critical stress for onset of slip and $\beta$ is the slip coefficient. A fit

of this model to the experimental data on the Teflon surface is shown in Fig. 8-4 ($R^2 = 0.95$); the critical stress and slip coefficient were found to be $\tau_c$=0.78 Pa and $\beta = 205$ $\mu$m.Pa$^{-1}$.s$^{-1}$ respectively.

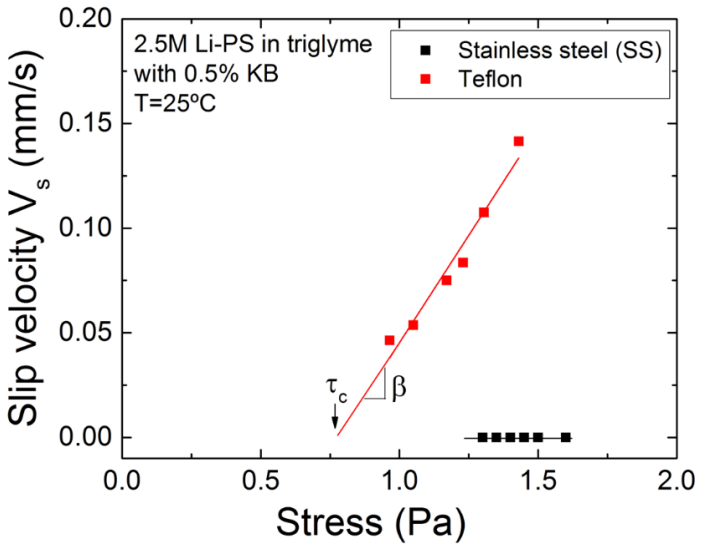


Figure 8-4: Measured slip velocity of the suspension vs. applied shear stress at 25°C for flow on Teflon and stainless steel surfaces, showing the much greater slip velocity on the former. The critical slip model [Eq. 8.5] was fitted as shown by the solid lines.

## 8.4 Modeling the flow in the cell

With these parameters in hand, the impact of slip on the flow velocity vs. tilt angle behavior of the rectangular flow channel can be modeled. Flow of the suspension in a channel of gap $H$ (the distance between the current collectors), length $L$, and width $W$ was modeled [Fig. 8-2(b)]. The geometry of the cell has $H \ll L$, $W \ll L$, and flow is assumed to be two-dimensional with no fingering instabilities or capillary effects such as contact line-pinning. Two slip boundary conditions were modeled, either no-slip or the critical slip model described above. The equation of motion for the yield stress fluid is solved analytically [137] and the volumetric flow rate, $Q$ (cm$^3$/s), was obtained as a function of the model parameters.

In the presence of wall slip, there are three flow regimes in the general case depending on the value of the wall shear stress $\tau_w$: For $\tau_w < \tau_c$, the suspension does not flow and $Q = 0$. For $\tau_c < \tau_w < \tau_y$, the suspension slips and flows as an unyielded plug and the flow rate is given by:

$$Q = \beta W H(\tau_w - \tau_c) \tag{8.6}$$

where $\tau_y$ is the yield stress extracted from the fit of the piecewise Bingham model. For $\tau_w \geq \tau_y$, the suspension yields and the flow is due to a mix of plastic flow in the bulk and wall slip. In this case, the flow rate is given by [137]:

$$Q = \frac{WH^2\tau_y}{6\mu_p}\left[\frac{\tau_w}{\tau_y} - \frac{3}{2} + \frac{1}{2}(\frac{\tau_y}{\tau_w})^2\right] + \beta W H(\tau_w - \tau_c) \tag{8.7}$$

A piecewise Bingham model was used to account for shear thinning over the range of shear rates from which the rheology data was measured by updating the Bingham model parameters $\tau_y$ & $\mu_p$ to $\tau_y'$ & $\mu_p'$ respectively if $\tau_w > \tau_t$. Knowing the flow rate $Q$, the flow time for one complete pass of the flow electrode, $t_{\text{pass}}$ was obtained as the time to flow the full volume of suspension from the upper "tank" to the lower "tank":

$$t_{\text{pass}} = \frac{WHL_{\text{travel}}}{Q} \tag{8.8}$$

where $L_{\text{travel}}$ is the distance traveled by the suspension.

For operation of the cell, the most important parameters are $t_{\text{pass}}$, which determines the charging or discharging time that is available during a single pass, and the sensitivity of the flow rate to the tilt angle, which affects how precisely the flow kinetics can be controlled. Fig. 8-5(a) shows the flow time for one pass as a function of the tilt angle $\theta$ for a GIFcell design with $H = 1.6$ mm, $W = 10$ mm and $L = 75$ mm, modeled for a zero-slip surface and for a Teflon respectively. The three flow regimes described above are outlined in the figure. We note that using a Teflon surface is beneficial in that the range of angles over which flow is neither too fast nor zero, i.e., the "elbow" of the curve, is broadened. Without wall slip, the transition from no

flow to very rapid flow occurs over only about 5°. Taking a tilt angle of $\theta = 10°$, for the case of Teflon surfaces the calculated time for one pass is 3.9 min. Experimentally, a time of 3 min was observed, which is in reasonably good agreement with the model. However, the flow rate remains highly sensitive to tilt angle; for just a one degree increase in tilt angle to $\theta = 11°$, the flow time decreases from 3.9 to 2.6 min. Furthermore, a $t_{\text{pass}}$ on the order of minutes may simply be too fast relative to the charge/discharge kinetics of the cell: a 3 min discharge corresponds to a 20 C-rate for single-pass charging or discharging. Thus, it is desirable to both slow down the flow rate and decrease the angular dependence of flow rate at the target rates.

One approach to achieve a slower flow rate of the suspension is to decrease the gap $H$. Fig. 8-5(b) shows the effect of decreasing $H$ for a GIFcell for the same dimension cell with $W = 10$ mm and $L = 75$ mm, modeled for a Teflon surface. The main result of decreasing the gap is to reduce the range of flowable angles by increasing the critical angle for onset of flow (Eq. 8.4). For the range of flowable angles, the flow time for one pass is increased, but remains less than an hour for realistic values of the gap. In addition, the slope of the curve remains steep close to the onset of flow making the design difficult to control precisely in this regime.

A simple and precise approach for further decreasing the flow rate is to add further resistance in the form of gas flow control [Fig. 8-2(b) and 8-2(c)]. Assuming incompressible (low Mach number) gas flow, mass conservation dictates that the suspension flow rate is equal to the gas flow rate (i.e. $Q_{gas} = Q$). Either an actively controlled pneumatic resistor element such as a valve, or a passive element such as a porous flow restrictor, could in principle be used. We modeled the effect of gas flow control as follows: neglecting the inertia of the gas (low Reynolds number), the flow resistance of the gas-flow control element is defined as:

$$\alpha = \frac{\Delta P(Q)}{Q} \tag{8.9}$$

where $\Delta P(Q)$ is the pressure drop across the control element for a flow rate, $Q$, of gas through the element. $\alpha$ has units of Pa.s.mm$^{-3}$ and adds a tunable feedback loop

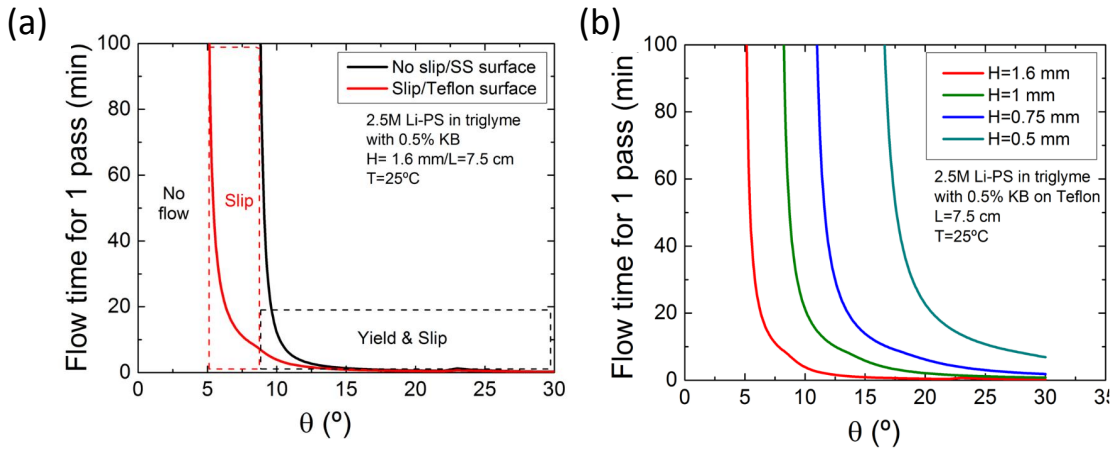


Figure 8-5: Flow modeling results showing the effects of adjustable parameters in the GIFcell design on flow characteristics for a 2.5 M Li-PS suspension in triglyme (0.5vol% KB, 0.5 M LiTFSI and 1wt% $LiNO_3$). (a) Modeling results showing flow time for a single pass vs. tilt angle $\theta$. The effect of added slip from a Teflon surface on flow time shows that increasing slip permits flow at lower angles. The desired behavior for the GIFcell is controlled, slow flow rates (long flow time) at easily controlled tilt angles. (b) Effect of flow channel thickness $H$ on the flow time for one pass, showing that decreasing $H$ slows the flow rate at fixed angle.

parameter to the cell that aids in controlling the flow rate of the suspension. As the flow rate of the suspension increases, the pressure drop in the element increases and is imposed as a back pressure on the fluid and slows it down. In the case of flow through a porous medium such as a porous membrane or solid plug of a permeable medium, $\alpha$ is given by:

$$\alpha = \frac{L_{porous}}{\mu_{gas}\kappa A_{porous}} \tag{8.10}$$

where $\mu_{gas}$ is the dynamic viscosity of the gas (in our case, Argon), $L_{porous}$, $A_{porous}$, $\kappa$ are the thickness, cross-sectional area and permeability of the membrane or solid, respectively. With the additional back-pressure due to the resistance to gas-flow acting on the suspension, the shear stress at the wall is given by:

$$\tau_w = \left[\rho g \sin\theta - \alpha Q\right]\frac{H}{2} \tag{8.11}$$

The three regimes described previously are still present, and assuming wall slip is present, the angle for onset of flow remains similar to the no gas-flow control case and is now given by:

$$\theta_F = \sin^{-1}\left(\frac{2\tau_c}{\rho g H}\right) \tag{8.12}$$

In the slip regime ($\tau_c < \tau_w < \tau_y$), the flow rate is now given by:

$$Q = \frac{\beta W H\left[\rho g \sin\theta \frac{H}{2} - \tau_c\right]}{1 + \frac{\alpha}{L}\frac{\beta W H^2}{2}} \tag{8.13}$$

When the material yields ($\tau_w > \tau_y$), the flow rate is given by Eq. 8.7, where the shear stress at the wall is given by Eq. 8.11. This defines an implicit equation for the flow rate that can be solved numerically once the design parameters are specified. The effect of adding gas-flow control in the design on the flow time for one pass is shown in Fig. 8-6 for different flow resistance $\alpha$ in a GIFCell design with $H = 1.6$ mm, $W = 10$ mm, $L = 75$ mm, and assuming the optimal suspension is flowing over a Teflon surface. We observe that adding the gas-flow control element does not affect the critical angle for onset of flow, but allows the flow time to be increased significantly over a wide range of flowable angles. In particular, tuning of the gas-flow control element decreases the flow rate in the slip regime as shown in Eq. 8.13 and increases the angle for onset of yield ($\tau_w = \tau_y$), therefore promoting plug flow. For example, at $\theta = 10°$, the flow time for one pass is 7.5, 26.4 and 212 min for $\alpha = 10^{-1}, 10^{0}\&10^{1}$ Pa.s.mm$^{-3}$ respectively. These times demonstrate the benefit of incorporating a gas-flow control element in the design of the GIFcell in order to impose longer flow times and to improve flow rate control.

## 8.5 Scaling of mechanical loss with GIFcell size

In this section, we analyze the mechanical energy consumed in operating the GIFcell as a function of its size. The mechanical energy per unit mass to tilt the cell by an

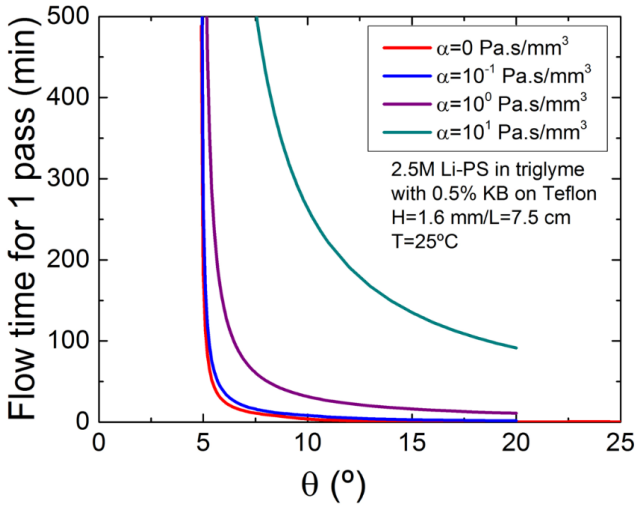


Figure 8-6: Effect of introducing gas flow control on the flow time for one pass. Gas flow resistance of the control element is defined as $\alpha = \Delta P(Q)/Q$ where $\Delta P(Q)$ is the pressure drop across the control element for a flow rate $Q$ of gas through the element. $\alpha$ has units of Pa.s.mm$^{-3}$. Results show that gas flow control reduces the slope of the curves at long flow times, decreasing the sensitivity of flow rate to tilt angle and facilitating flow-rate control over a wide range of tilt angles.

angle $2\theta$ is given by:

$$e_{mechanical} = gL_{\text{travel}} \sin\theta \tag{8.14}$$

where $L_{\text{travel}}$ is the length of the electrolyte chamber or "tank" as illustrated in Fig. 8-2(b) and $g$ is the gravitational force constant. As a starting point, consider that the mechanical energy for 25 flips of the prototype GIFcell is 0.032 J/g, which is in the order of about $10^{-4}$ of the electrochemical energy extracted for this system. Table 8.2 shows how the ratio of mechanical energy to electrochemical energy scales with tank length $L_{tank}$, assuming 25 tilt operations are needed to fully charge or discharge the cell. It is seen that a GIFcell could in principle be several meters long while retaining high mechanical efficiency. The other adjustable parameters are the energy density of the suspension, which could increase by a factor of 2 or 3 while remaining within the sulfur solubility limit, and the number of tilts required, which could decrease; both would further decrease the mechanical losses from those shown.

| | | | | | |
|---|---|---|---|---|---|
| **$L_{tank}$ (m)** | 0.07 (lab scale) | 0.1 | 1 | 10 | 100 |
| **Mechanical to electrochemical energy ratio** | 0.023% | 0.032% | 0.32% | 3.2% | 32% |

Table 8.2: The effect of tank length $L_{tank}$ on the ratio of mechanical energy to electrochemical energy, assuming 25 tilt operations are needed to fully charge or discharge the cell.

In practice, as the system scales up, the angle of operation will not remain the same to keep the same residence time in the electroactive region. In addition, less flips are needed to extract the total amount of energy available in the cell. As such, a finer analysis of the scaling of the mechanical losses with system size may ultimately be needed.

## 8.6 Conclusion

In this section, we demonstrate a gravity-fed design for flow batteries, the GIFcell, which has a low part count and is well-suited for high energy density, non-Newtonian flow electrodes. Using a model lithium polysulfide-nanocarbons suspension that exemplifies a rheologically complex flow electrode, a high energy efficiency prototype GIFcell was designed, modeled, and experimentally demonstrated by Chen et al. [136]. Through modeling of the rheological and wall slip properties of the suspensions, we demonstrate that the use of high-slip surfaces and gas-flow control allow optimal control of the residence time in the electro-active region. The results illustrate the integration of flow electrode electrochemical design, cell mechanical design, and development of electrochemical operation protocols for such devices.

# Chapter 9

# Conclusions and Outlook

The central focus of this thesis has been to develop an understanding of electro-active yield stress (EAYS) fluids and the application of this understanding to explore the design of devices using them. This work investigated two representative case studies of such devices using viscoplastic fluids: 1) small rapidly-actuated hydraulic valves using electrorheological fluids applied to centimeter-scale robotics and 2) semi-solid flow batteries using suspensions of percolated networks of carbon black flowing in millifluidic channels. Using these examples, we have focused on three goals: 1) developing a better understanding of the rheological and electrical properties of the fluids at the material level through experimental characterization (Chapters 2, 4, 6 and 7); 2) using the improved understanding of the flow of EAYS fluids to develop device-level predictive models of the key performance metrics, leading to a better understanding of the device design and operation space (Chapter 3 and 8); 3) developing novel methods and instrumentation to design new characterization tools to explore interactions between the rheology and the electrical properties of the EAYS fluids (Chapter 3 and 5). At the completion of this work, we arrive at the following conclusions:

When designing devices using active suspensions such as electrorheological or magnetorheological fluids in flow mode, the phenomenon of yield hardening must be considered. Specifically, the local densification in the suspension microstructure reported in Chapter 2, must be taken into account in systems modeling, since it controls the magnitude of the yield pressure that must be achieved to induce flow in

the device. We have shown in chapter 2 that the complex interdependencies between the electrostatic interactions, the hydrodynamic forces and the channel geometry can be modeled by understanding the ratio of the particle aggregation time scale to the convective flow time scale and linked to the permeability of the chained microstructures that assemble in the channel, when a transverse electric field is applied to the flow. The understanding of flow-induced densification and saturation is important in optimizing parameters such as channel length and switching time in ER-fluidic valve design. With the physical understanding of the densification that occurs in channel flow, we can model and predict the performance in channel flow using a characterization of the dependence of the yield stress on particle volume fraction performed in wall-driven flow, thus allowing us to reconcile the discrepancies observed in the two modes of flow.

In addition, in chapter 3, we explored the design space of ER valves with a focus on defining performance metrics for the valves and understanding how design parameters such as the electric field, channel aspect ratio and electrode surface roughness affect the valve performance. We identified the power efficiency and holding pressure of the valves as performance metrics of interest and demonstrated that a trade-off exists between them in terms of valve aspect ratio. We also showed that enhancing electrode surface roughness can improve both the efficiency and holding pressure of the valve and can be an interesting area for further study. This work paves the way for the use of rapid-switching millifluidic ER valves in small hydraulic robotic applications.

We also discussed methods to characterize the rheology and wall slip of semi-solid flow electrodes in chapter 4. We emphasized the importance of wall slip correction in obtaining accurate rheology data and slip laws and explored the impact of various design parameters on the rheology and slip of the suspensions. Quantifying the rheology and wall slip behavior of the flow electrodes is crucial for flow modeling in cell prototypes as demonstrated in a new gravity-driven flow cell architecture: the GIF-cell (Chapter 8). Through modeling of the rheological and wall slip properties of the suspensions, we demonstrated that the use of high-slip surfaces and gas flow control allow optimal control of the residence time in the electro-active region of the cells.

This work emphasized the importance of integrating rheological characterization and flow modeling to the mechanical and electrochemical design of flow cells in order to improve their performance.

We have also introduced a new rheo-electric apparatus designed for conventional stress-controlled rheometers (Chapter 5). This apparatus can be used to accurately measure the conductivity of strongly conductive materials under flow at the same time as the viscometric properties of the gel are measured. The use of gold-sputtered plates and a liquid metal alloy (EGaIn) to close the electrical circuit allow for accurate electrical measurements on a wide variety of strongly conductive complex fluids, which demonstrate the versatility of the EGaIn rheo-electric test fixture. Benchmark tests on CB gels have allowed us to illustrate the high sensitivity of the apparatus even at low strains, and to determine the transient and steady-state behavior of CB gels by comparing the simultaneous electrical and mechanical response (Chapter 6). Furthermore, by taking into account shear inhomogeneity, wall slip and the existence of a measurable contact resistance, we have shown that the correction methods first introduced to extract true bulk rheological measurements from parallel plate rheometry data can be formally extended to analyze electrical data. The latter analysis should be used as a reference for future electrical characterization of other conductive complex fluids such as conductive silver pastes, carbon nanotube nanocomposites, conductive inks, etc. More generally, the low friction rheo-electric apparatus we have designed for stress-controlled rheometers paves the way for wider use of rheo-electrical measurements in the broad soft matter community. In particular, the EGaIn apparatus enables two-electrode electrochemical tests to be performed under flow, which is of primary importance for flow batteries, where the systematic characterization of cell performance under flow in a controlled environment is crucial for cell design and optimization.

There are several potential avenues for continuing this work - both at the material and device level. First, further exploration of the effect of electrode surface roughness remains to be performed. In addition, we need to develop a better understanding of the effect of temperature on the yield stress and current density of ER fluids. This

is particularly important for ER valve design as it may limit the maximum size of ER valves. As the size of the valves increases (and thus the surface area to volume ratio decreases), the heat generated by ohmic losses can raise the temperature of the fluid (if not dissipated correctly) and cause the leakage current to increase. This in turn could further increase the temperature of the fluid causing a runaway current to develop and the electrical losses in the valves to dramatically rise. A study coupling an understanding of the effect of temperature on the current density coupled with a device level exploration of heat dissipation mechanisms in ER valves is a natural extension of the goals of this work. Furthermore, the integration of ER valves in robotic application remains an open challenge. While using ER fluids allows the valves to become solid-state components with no moving parts, additional research into solid-state pumps is needed to complete the hydraulic circuit. An interesting area of further exploration could be the development of solid state ER pumps and actuators.

Regarding the rheo-electric test fixture, further testing on other conductive complex fluids such as silver inks or carbon nanotube composites is an interesting area for further exploration. Specifically, the recovery time of the conductivity and therefore of the microstructure after shear remains a rich area for further study. In addition, while this work has focused on performing accurate measurements, we have not explored modeling of the conductivity under flow. Gaining an deeper understanding of the material parameters that affect conductivity of complex fluids under flow is a growing area of interest. In particular, developing quantitative laws that can be used to model the decrease of conductivity with increasing shear can be of interest to guide semi-solid flow cell design by predicting the associated efficiency loss. A coupled electrochemical-rheological model of semi-solid flow cells taking into account the conductivity loss under flow remains to be formulated. Developing such a model would be the analog of the work carried out in the present work in terms of translating the rheological and slip characterization to flow models for the cells. On the fundamental side, the rheo-electric test fixture paves the way for its use as an additional probe of the microstructure and additional testing particularly for transient shear may lead to

the discovery of new physics in attractive colloidal gels. Further studies on the role of shear history and thixotropy using rheo-electric measurements can help elucidate the role a deformable microstructure plays in driving the evolution of these complex non-linear effects.

For flow cell design, we have observed that high slip interfaces can help improve the performance of flow cells. The development of such interfaces such as Liquid Impreganted Surfaces (LIS) developed by Varanasi et al. [314] for flow cell applications could potentially prove useful. Although challenges associated with the low electronic conductivity of the lubricant films may compromise performance, modeling the coupling between the extent of the slip layer to the apparent conductivity and validating the models using the rheo-electric test fixture could be of use for the development of such surfaces.

# Bibliography


[1] H. A. Barnes, "The yield stress -a review or 'panta rei'- everything flows?," *Journal of Non-Newtonian Fluid Mechanics*, vol. 81, pp. 133–178, 1999.

[2] N. J. Balmforth, I. A. Frigaard, and G. Ovarlez, "Developments in Viscoplastic Fluid Mechanics," *Annual Review of Fluid Mechanics*, vol. 46, pp. 121–146, 2014.

[3] D. Bonn, J. Paredes, M. M. Denn, L. Berthier, T. Divoux, and S. Manneville, "Yield Stress Materials in Soft Condensed Matter," *arXiv*, vol. 1502.05281, pp. [cond–mat.soft], 2015.

[4] M. Cloitre, R. Borrega, and L. Leibler, "Rheological aging and rejuvenation in microgel pastes," *Physical Review Letters*, vol. 85, pp. 4819–4822, Nov 2000.

[5] P. Ballesta and G. Petekidis, "Creep and aging of hard-sphere glasses under constant stress," *Phys. Rev. E*, vol. 93, p. 042613, Apr 2016.

[6] P. Coussot, "Yield stress fluid flows: A review of experimental data," *Journal of Non-Newtonian Fluid Mechanics*, vol. 211, pp. 31–49, 2014.

[7] P. Coussot, *Rheometry of Pastes, Suspensions, and Granular Materials: Applications in Industry and Environment*. John Wiley and Sons Inc., 2005.

[8] M. Kogan, L. Ducloué, J. Goyon, X. Chateau, O. Pitois, and G. Ovarlez, "Mixtures of foam and paste: Suspensions of bubbles in yield stress fluids," *Rheologica Acta*, vol. 52, pp. 237–253, 2013.

[9] G. A. van Aken, "Aeration of emulsions by whipping," *Colloids and Surfaces A: Physicochemical and Engineering Aspects*, vol. 190, no. 3, pp. 333 – 354, 2001.

[10] P. Coussot, "Rheophysics of pastes: a review of microscopic modelling approaches," *Soft Matter*, vol. 3, pp. 528–540, 2007.

[11] C. Chang, Q. D. Nguyen, and H. P. Rønningsen, "Isothermal start-up of pipeline transporting waxy crude oil," *Journal of Non-Newtonian Fluid Mechanics*, vol. 87, no. 23, pp. 127–154, 1999.

[12] C. J. Dimitriou, *The rheological complexity of waxy crude oils: Yielding, thixotropy and shear heterogeneities*. PhD thesis, Massachusetts Institute of Technology, 2013.

[13] R. H. Ewoldt, C. Clasen, A. E. Hosoi, and G. H. McKinley, "Rheological fingerprinting of gastropod pedal mucus and synthetic complex fluids for biomimicking adhesive locomotion," *Soft Matter*, vol. 3, pp. 634–643, 2007.

[14] R. H. Ewoldt, *Nonlinear viscoelastic materials : bioinspired applications and new characterization measures by.* PhD thesis, Massachusetts Institute of Technology, 2009.

[15] K. Kamrin and L. Mahadevan, "Soft catenaries," *Journal of Fluid Mechanics*, vol. 691, pp. 165–177, 1 2012.

[16] R. T. Bonnecaze and M. Cloitre, *High Solid Dispersions*, ch. Micromechanics of Soft Particle Glasses, pp. 117–161. Berlin, Heidelberg: Springer Berlin Heidelberg, 2010.

[17] J. Mewis and N. J. Wagner, *Colloidal suspension rheology.* Cambridge University Press, 2011.

[18] I. A. Gutowski, D. Lee, J. R. Bruyn, and B. J. Frisken, "Scaling and mesostructure of carbopol dispersions," *Rheologica Acta*, vol. 51, no. 5, pp. 441–450, 2012.

[19] K. N. Nordstrom, E. Verneuil, P. E. Arratia, A. Basu, Z. Zhang, A. G. Yodh, J. P. Gollub, and D. J. Durian, "Microfluidic rheology of soft colloids above and below jamming," *Physical Review Letters*, vol. 105, p. 175701, Oct. 2010.

[20] P. G. Roberts and A. H. Barnes, "New measurements of the flow-curves for carbopol dispersions without slip artefacts," *Rheologica Acta*, vol. 40, no. 5, pp. 499–503, 2001.

[21] L. Bécu, S. Manneville, and A. Colin, "Yielding and flow in adhesive and non-adhesive concentrated emulsions," *Physical Review Letters*, vol. 96, p. 138302, Apr 2006.

[22] T. Mason, J. Bibette, and D. Weitz, "Yielding and flow of monodisperse emulsions," *Journal of Colloid and Interface Science*, vol. 179, no. 2, pp. 439 – 448, 1996.

[23] S. Cohen-Addad, R. Höhler, and O. Pitois, "Flow in foams and flowing foams," *Annual Review of Fluid Mechanics*, vol. 45, no. 1, pp. 241–267, 2013.

[24] K. Krishan, A. Helal, R. Höhler, and S. Cohen-Addad, "Fast relaxations in foam," *Physical Review E*, vol. 82, no. 1, p. 011405, 2010.

[25] A. V. Agafonov and A. G. Zakharov, "Electrorheological fluids," *Russian Journal of General Chemistry*, vol. 80, no. 3, pp. 567–575, 2010.

[26] T. Hao, *Electrorheological Fluids: The Non-aqueous Suspensions.* Elsevier, 2005.

[27] P. Sheng and W. Wen, "Electrorheological Fluids: Mechanisms, Dynamics, and Microfluidics Applications," *Annual Review of Fluid Mechanics*, vol. 44, pp. 143–174, 2012.

[28] T. C. Halsey, "Electrorheological fluids - structure and dynamics," *Advanced Materials*, vol. 5, no. 10, pp. 711–718, 1993.

[29] M. Ocalan, *Magnetorheological Fluids for Extreme Environments : Stronger, Lighter, Hotter*. PhD thesis, Massachusetts Institute of Technology, 2011.

[30] R. Tao, "Super-strong magnetorheological fluids," *Journal of Physics: Condensed Matter*, vol. 13, no. 50, pp. R979–R999, 2001.

[31] M. Cloitre, R. Borrega, F. Monti, and L. Leibler, "Structure and flow of polyelectrolyte microgels: from suspensions to glasses," *Comptes Rendus Physique*, vol. 4, no. 2, pp. 221–230, 2003.

[32] S. P. Meeker, R. T. Bonnecaze, and M. Cloitre, "Slip and flow in soft particle pastes," *Physical Review Letters*, vol. 92, no. 19, p. 198302, 2004.

[33] T. Amari, "Flow properties and electrical conductivity of carbon black-linseed oil suspension," *Journal of Rheology*, vol. 34, p. 207, 1990.

[34] F. Y. Fan, W. H. Woodford, Z. Li, N. Baram, K. C. Smith, A. Helal, G. H. McKinley, W. Craig Carter, and Y. M. Y.-M. Chiang, "Polysulfide flow batteries enabled by percolating nanoscale conductor networks," *Nano Letters*, vol. 14, pp. 2210–2218, 2014.

[35] H. Block, J. P. Kelly, A. Qin, and T. Watson, "Materials and mechanisms in electrorheology," *Langmuir*, vol. 6, no. 1, pp. 6–14, 1990.

[36] M. Parthasarathy and D. J. Klingenberg, "Electrorheology: Mechanisms and models," *Materials Science and Engineering: R: Reports*, vol. 17, no. 2, pp. 57 – 103, 1996.

[37] H. Block and J. P. Kelly, "Electro-rheology," *Journal of Physics D: Applied Physics*, vol. 21, no. 12, p. 1661, 1988.

[38] R. T. Bonnecaze and J. F. Brady, "Yield stresses in electrorheological fluids," *Journal of Rheology*, vol. 36, no. January 1992, pp. 73–115, 1992.

[39] D. J. Klingenberg, "Particle polarization and nonlinear effects in electrorheological suspensions," *MRS Bulletin*, vol. 23, pp. 30–34, 8 1998.

[40] W. M. Winslow, "Induced Fibration of Suspensions," *Journal of Applied Physics*, vol. 20, no. 12, pp. 1137–1140, 1949.

[41] L.-X. Gao, J.-L. Chen, X.-W. Han, S.-X. Yan, Y. Zhang, W.-Q. Zhang, and Z.-W. Gao, "Electro-response characteristic of starch hydrogel crosslinked with glutaraldehyde," *Journal of Biomaterials Science, Polymer Edition*, vol. 26, no. 9, pp. 545–557, 2015.

[42] C. Gracia-Fernández, S. Gómez-Barreiro, A. Álvarez-García, J. López-Beceiro, and R. Artiaga, "Electrorheological behaviour of a starch-oil system," *Rheologica Acta*, vol. 53, no. 8, pp. 655–661, 2014.

[43] L. Xu, X. Shi, and Q. Wang, "Preparation and properties of nano-crystalline cellulose electro-rheological fluid.," in *Materials Science Forum*, vol. 815, 2014.

[44] H. J. Choi, T. W. Kim, M. S. Cho, S. G. Kim, and M. S. Jhon, "Electrorheological characterization of polyaniline dispersions," *European Polymer Journal*, vol. 33, no. 5, pp. 699–703, 1997.

[45] A. Lengálová, V. Pavlínek, P. Sáha, J. Stejskal, T. Kitano, and O. Quadrat, "The effect of dielectric properties on the electrorheology of suspensions of silica particles coated with polyaniline," *Physica A: Statistical Mechanics and its Applications*, vol. 321, no. 3, pp. 411–424, 2003.

[46] S. Wu, F. Zeng, and J. Shen, "The Electrorheological Properties of Polypyrrole Suspensions," *Polymer Journal*, vol. 30, no. 6, pp. 451–454, 1998.

[47] H. S. Chae, W. L. Zhang, S. H. Piao, and H. J. Choi, "Synthesized palygorskite/polyaniline nanocomposite particles by oxidative polymerization and their electrorheology," *Applied Clay Science*, vol. 107, pp. 165–172, 2015.

[48] K. Lu, R. Shen, X. Wang, G. Sun, and W. Wen, "The electrorheological fluids with high shear stress," *International Journal of Modern Physics B*, vol. 19, no. 07n09, pp. 1065–1070, 2005.

[49] K. Di, Y. Zhu, X. Yang, and C. Li, "Electrorheological behavior of copper phthalocyanine-doped mesoporous TiO2 suspensions," *Journal of colloid and interface science*, vol. 294, no. 2, pp. 499–503, 2006.

[50] H. Block, K. M. W. Goodwin, E. M. Gregson, and S. M. Walker, "Stimulated resonance between electrical and shear fields by a colloidal system," *Nature*, vol. 275, pp. 632–634, Oct. 1978.

[51] C. Wu, Y. Chen, and H. Conrad, "Electrorheology of a zeolite/silicone oil suspension with DC and AC fields," *Journal of Physics D: Applied Physics*, vol. 31, no. 8, p. 960, 1998.

[52] P. Sheng and W. Wen, "Electrorheology: Statics and dynamics," *Solid State Communications*, vol. 150, no. 21-22, pp. 1023–1039, 2010.

[53] Z. Song, Y. Cheng, J. Wu, J. Guo, and G. Xu, "Influence of volume fraction on the yield behavior of giant electrorheological fluid," *Applied Physics Letters*, vol. 101, pp. 23–26, 2012.

[54] W. Wen, X. Huang, S. Yang, K. Lu, and P. Sheng, "The giant electrorheological effect in suspensions of nanoparticles," *Nature materials*, vol. 2, no. November, pp. 727–730, 2003.

[55] W. Wen, X. Huang, and P. Sheng, "Electrorheological fluids: structures and mechanisms," *Soft Matter*, vol. 4, p. 200, 2008.

[56] H. J. Choi, J. W. Kim, M. S. Cho, C. A. Kim, and M. S. Jhon, "Characteristics of a Yield Stress Scaling Function for Electrorheological Fluids," *International Journal of Modern Physics B*, vol. 16, no. 24, pp. 2636–2642, 2002.

[57] Y. P. Seo and Y. Seo, "Analysis of giant electrorheological fluids," *Journal of colloid and interface science*, vol. 402, pp. 90–93, 2013.

[58] F. E. Filisko, "Current Developments in Electrorheological Materials," in *Smart Materials*, CRC Press, Nov. 2008.

[59] Y. D. Liu and H. J. Choi, "Electrorheological fluids: smart soft matter and characteristics," *Soft Matter*, pp. 11961–11978, 2012.

[60] S. R. Kumbhar, S. Maji, and B. Kumar, "Research on smart materials for automotive applications," *Journal of Automobile Engineering and Applications*, vol. 1, no. 1, pp. 6–10, 2014.

[61] D. E. Eastman, *Design of semi-active variable impedance materials using field-responsive fluids*. PhD thesis, Massachusetts Institute of Technology, 2004.

[62] R. Stanway and J. L. Sproston, "Electro-Rheological Fluids: A Systematic Approach to Classifying Modes of Operation," *Journal of Dynamic Systems, Measurement, and Control*, vol. 116, pp. 498–504, 1994.

[63] L. Bitman, Y. T. Choi, S. B. Choi, and N. M. Wereley, "Electrorheological damper analysis using an Eyring-plastic model," *Smart Materials and Structures*, vol. 14, no. 1, p. 237, 2005.

[64] W. A. Bullough, A. R. Johnson, A. Hosseini-Sianaki, J. Makin, and R. Firoozian, "The electro-rheological clutch: design, performance characteristics and operation," *Proceedings of the Institution of Mechanical Engineers, Part I: Journal of Systems and Control Engineering*, vol. 207, no. 2, pp. 87–95, 1993.

[65] S. M. Chen and W. A. Bullough, "CFD study of the flow in a radial electrorheological fluid clutch," *Journal of Intelligent Material Systems and Structures*, vol. 21, no. 15, pp. 1569–1574, 2010.

[66] S. B. Choi and M. S. Cho, "Control performance of hydraulic servo valves utilising electrorheological fluids," *International Journal of Vehicle Design*, vol. 38, p. 196, 2005.

[67] S.-B. Choi, J.-Y. Yook, M.-K. Choi, Q. H. Nguyen, Y.-S. Lee, and M.-S. Han, "Speed control of DC motor using electrorheological brake system," *Journal of Intelligent Material Systems and Structures*, vol. 18, no. 12, pp. 1191–1196, 2007.

[68] S. Chonan, M. Tanaka, T. Naruse, and T. Hayase, "Development of an electrorheological active buffer for railway vehicles-estimation of the capacity from prototype performance," *Smart Materials and Structures*, vol. 13, no. 5, p. 1195, 2004.

[69] J. P. Coulter, K. D. Weiss, and J. D. Carlson, "Engineering Applications of Electrorheological Materials," *Journal of Intelligent Material Systems and Structures*, vol. 4, pp. 248–259, Apr. 1993.

[70] H. P. Gavin, "Multi-duct ER dampers," *Journal of Intelligent Material Systems and Structures*, vol. 12, no. 5, pp. 353–366, 2001.

[71] N. M. Wereley, J. Lindler, N. Rosenfeld, and Y.-T. Choi, "Biviscous damping behavior in electrorheological shock absorbers," *Smart Materials and Structures*, vol. 13, no. 4, p. 743, 2004.

[72] M. Kamelreiter, W. Kemmetmüller, and A. Kugi, "Digitally controlled electrorheological valves and their application in vehicle dampers," *Mechatronics*, vol. 22, no. 5, pp. 629–638, 2012.

[73] D. J. Klingenberg and C. F. Zukoski, "Studies on the steady-shear behavior of electrorheological suspensions," *Langmuir*, vol. 6, no. 20, pp. 15–24, 1990.

[74] X. Niu, W. Wen, and Y.-K. Lee, "Micro valves using nanoparticle-based giant electrorheological fluid," *The 13th International Conference on Solid-State Sensors, Actuators and Microsystems, 2005. Digest of Technical Papers. TRANSDUCERS '05.*, vol. 1, pp. 652–655, 2005.

[75] K. Yoshida, M. Kikuchi, J. H. Park, and S. Yokota, "Fabrication of micro electro-rheological valves (ER valves) by micromachining and experiments," *Sensors and Actuators, A: Physical*, vol. 95, pp. 227–233, 2002.

[76] K. Krivenkov, S. Ulrich, and R. Bruns, "Extending the operation range of electrorheological actuators for vibration control through novel designs," *Journal of Intelligent Material Systems and Structures*, vol. 23, no. 12, pp. 1323–1330, 2012.

[77] Y. Liu, R. Davidson, and P. Taylor, "Touch sensitive electrorheological fluid based tactile display," *Smart Materials and Structures*, vol. 14, no. 6, p. 1563, 2005.

[78] L. Liu, X. Niu, W. Wen, and P. Sheng, "Electrorheological fluid-actuated flexible platform," *Applied Physics Letters*, vol. 88, no. 17, 2006.

[79] X. Niu, L. Liu, W. Wen, and P. Sheng, "Hybrid approach to high-frequency microfluidic mixing," *Physical Review Letters*, vol. 97, p. 044501, Jul 2006.

[80] R. H. Ewoldt, P. Tourkine, G. H. McKinley, and A. E. Hosoi, "Controllable adhesion using field-activated fluids," *Physics of Fluids*, vol. 23, no. 7, p. 073104, 2011.

[81] S. A. Lira and J. A. Miranda, "Field-controlled adhesion in confined magnetorheological fluids," *Physical Review E*, vol. 80, no. 4, p. 046313, 2009.

[82] W. Kim, S. Lee, Y. Kim, and E. Lee, "The electromechanical principle of electrorheological fluid-assisted polishing," *International Journal of Machine Tools and Manufacture*, vol. 43, no. 1, pp. 81–88, 2003.

[83] D. Golini, S. D. Jacobs, V. Kordonski, and P. Dumas, "Precision optics fabrication using magnetorheological finishing," in *Advanced Materials for optics and precision structures*, vol. 1, pp. 251–274, 1997.

[84] K. Yoshida, T. Ide, J.-w. Kim, and S. Yokota, "A microgripper using flexible electro-rheological valves," in *World Automation Congress (WAC), 2010*, pp. 1–6, IEEE, 2010.

[85] R. J. Samson, G. W. Mulholland, and J. W. Gentry, "Structural analysis of soot agglomerates," *Langmuir*, vol. 3, no. 2, pp. 272–281, 1987.

[86] V. Trappe, E. Pitard, L. Ramos, A. Robert, H. Bissig, and L. Cipelletti, "Investigation of q-dependent dynamical heterogeneity in a colloidal gel by x-ray photon correlation spectroscopy," *Phys. Rev. E*, vol. 76, p. 51404, 2007.

[87] *Carbon black user's guide, ICBA "http://www.carbon-black.org"*.

[88] V. Trappe and D. A. Weitz, "Scaling of the viscoelasticity of weakly attractive particles," *Physical Review Letters*, vol. 85, no. c, pp. 449–452, 2000.

[89] V. Trappe, V. Prasad, L. Cipelletti, P. N. Segre, and D. A. Weitz, "Jamming phase diagram for attractive particles," *Nature*, vol. 411, no. June, pp. 772–775, 2001.

[90] M. van der Waarden, "Stabilization of carbon-black dispersions in hydrocarbons," *Journal of Colloid Science*, vol. 5, pp. 317–325, 1950.

[91] A. S. Negi and C. O. Osuji, "New insights on fumed colloidal rheology - Shear thickening and vorticity-aligned structures in flocculating dispersions," *Rheologica Acta*, vol. 48, pp. 871–881, 2009.

[92] C. O. Osuji, C. Kim, and D. A. Weitz, "Shear thickening and scaling of the elastic modulus in a fractal colloidal system with attractive interactions," *Phys. Rev. E*, vol. 77, pp. 8–11, 2008.

[93] C. O. Osuji and D. A. Weitz, "Highly anisotropic vorticity aligned structures in a shear thickening attractive colloidal system," *Soft Matter*, vol. 4, pp. 1388–1392, 2008.

[94] B. Ho, *An Experimental Study on the Structure-Property Relationship of Composite Fluid Electrodes for Use In High Energy Density Semi-Solid Flow Cells.* PhD thesis, Massachusetts Institute of Technology, 2011.

[95] T. Denaro, V. Baglio, M. Girolamo, V. Antonucci, F. Matteucci, R. Ornelas, *et al.*, "Investigation of low cost carbonaceous materials for application as counter electrode in dye-sensitized solar cells," *Journal of Applied Electrochemistry*, vol. 39, no. 11, pp. 2173–2179, 2009.

[96] K. B. Hatzell, M. Boota, and Y. Gogotsi, "Materials for suspension (semi-solid) electrodes for energy and water technologies," *Chem. Soc. Rev.*, vol. 44, pp. 8664–8687, 2015.

[97] J. B. Donnet, *Carbon Black: Science and Technology, Second Edition.* Taylor & Francis, 1993.

[98] V. Grenard, *Structuration et fluidification de gels de noir de carbone.* PhD thesis, ENS Lyon, 2012.

[99] T. C. Bond and R. W. Bergstrom, "Light absorption by carbonaceous particles: An investigative review," *Aerosol science and technology*, vol. 40, no. 1, pp. 27–67, 2006.

[100] P. Chỳlek, G. Videen, D. Ngo, R. G. Pinnick, and J. D. Klett, "Effect of black carbon on the optical properties and climate forcing of sulfate aerosols," *Journal of Geophysical Research: Atmospheres*, vol. 100, no. D8, pp. 16325–16332, 1995.

[101] A. I. Medalia, "Morphology of aggregates: VI. effective volume of aggregates of carbon black from electron microscopy; application to vehicle absorption and to die swell of filled rubber," *Journal of Colloid and Interface Science*, vol. 32, no. 1, pp. 115–131, 1970.

[102] K.-M. Jäger and D. H. McQueen, "Fractal agglomerates and electrical conductivity in carbon black polymer composites," *Polymer*, vol. 42, no. 23, pp. 9575–9581, 2001.

[103] D. Pantea, H. Darmstadt, S. Kaliaguine, and C. Roy, "Electrical conductivity of conductive carbon blacks: influence of surface chemistry and topology," *Applied Surface Science*, vol. 217, no. 1, pp. 181–193, 2003.

[104] K. M. Yearsley, M. R. Mackley, F. Chinesta, and A. Leygue, "The rheology of multiwalled carbon nanotube and carbon black suspensions," *Journal of Rheology*, vol. 56, p. 1465, 2012.

[105] S. Brunauer, P. H. Emmett, and E. Teller, "Adsorption of gases in multimolecular layers," *Journal of the American chemical society*, vol. 60, no. 2, pp. 309–319, 1938.

[106] S. Y. Nof, *Handbook of Industrial Robotics, Volume 1.* John Wiley & Sons, 1999.

[107] M. Raibert, K. Blankespoor, G. Nelson, R. Playter, and T. Team, "Bigdog, the rough-terrain quadruped robot," in *Proceedings of the 17th World Congress*, vol. 17, pp. 10822–10825, 2008.

[108] Y.-M. Han, K.-M. Sung, J. W. Sohn, and S.-B. Choi, "Performance comparison of electrorheological valves with two different geometric configurations : cylinder and plate," *Proc. IMechE*, vol. 223, pp. 573–581, 2008.

[109] Y.-M. Han, Q.-H. Nguyen, and S.-B. Choi, "Unsteady flow modeling of an electrorheological valve system with experimental validation," *Smart Materials and Structures*, vol. 18, p. 085005, 2009.

[110] Y. S. Jeon, Y. M. Han, Q. H. Nguyen, and S. B. Choi, "Unsteady laminar flow analysis of ER valve systems: Modeling and simulation," *Journal of Physics: Conference Series*, vol. 149, p. 012012, 2009.

[111] J. W. Kim, K. Yoshida, K. Kouda, and S. Yokota, "A flexible electro-rheological microvalve (FERV) based on SU-8 cantilever structures and its application to microactuators," *Sensors and Actuators, A: Physical*, vol. 156, pp. 366–372, 2009.

[112] W. H. Kuo, Y. C. Lin, T. N. Wu, J. Guo, Y. N. Chen, and Y. Shiao, "Study on the Controllable Characteristics of Electrorheological Valve Using Serial Multi-electrode," *Tamkang Journal of Science & Engineering*, vol. 12, no. 3, pp. 351–358, 2009.

[113] D. J. Laser and J. G. Santiago, "A review of micropumps," *Journal of Micromechanics and Microengineering*, vol. 14, pp. R35–R64, 2004.

[114] X. Niu, W. Wen, and Y. K. Lee, "Electrorheological-fluid-based microvalves," *Applied Physics Letters*, vol. 87, no. 2005, pp. 1–3, 2005.

[115] *ARPA-E FOA DE-FOA-0000290: Grid-Scale Rampable Intermittent Dispatchable Storage (GRIDS).*

[116] M. Carbajales-Dale, C. J. Barnhart, and S. M. Benson, "Can we afford storage? a dynamic net energy analysis of renewable electricity generation supported by energy storage," *Energy & Environmental Science*, vol. 7, no. 5, pp. 1538–1544, 2014.

[117] S. Chu and A. Majumdar, "Opportunities and challenges for a sustainable energy future," *Nature*, vol. 488, no. 7411, pp. 294–303, 2012.

[118] B. Dunn, H. Kamath, and J.-M. Tarascon, "Electrical energy storage for the grid: A battery of choices," *Science*, vol. 334, no. 6058, pp. 928–935, 2011.

[119] D. Elliott, "A balancing act for renewables," *Nature Energy*, 2015.

[120] Z. Yang, J. Zhang, M. C. W. Kintner-Meyer, X. Lu, D. Choi, J. P. Lemmon, and J. Liu, "Electrochemical energy storage for green grid," *Chemical Reviews*, vol. 111, no. 5, pp. 3577–3613, 2011. PMID: 21375330.

[121] M. Duduta, B. Ho, V. C. Wood, P. Limthongkul, V. E. Brunini, W. Craig Carter, and Y. M. Chiang, "Semi-solid lithium rechargeable flow battery," *Advanced Energy Materials*, vol. 1, pp. 511–516, 2011.

[122] F. R. Brushett, J. T. Vaughey, and A. N. Jansen, "An all-organic non-aqueous lithium-ion redox flow battery," *Advanced Energy Materials*, vol. 2, no. 11, pp. 1390–1396, 2012.

[123] T. Janoschka, N. Martin, U. Martin, C. Friebe, S. Morgenstern, H. Hiller, M. D. Hager, and U. S. Schubert, "An aqueous, polymer-based redox-flow battery using non-corrosive, safe, and low-cost materials," *Nature*, vol. 527, pp. 78–81, Nov. 2015.

[124] Y. Lu, J. B. Goodenough, and Y. Kim, "Aqueous cathode for next-generation alkali-ion batteries," *Journal of the American Chemical Society*, vol. 133, no. 15, pp. 5756–5759, 2011.

[125] Z. Li, K. C. Smith, Y. Dong, N. Baram, F. Y. Fan, J. Xie, P. Limthongkul, W. Craig Carter, and Y.-M. Chiang, "Aqueous semi-solid flow cell: demonstration and analysis.," *Physical Chemistry Chemical Physics : PCCP*, vol. 15, pp. 15833–9, 2013.

[126] J.-Y. Luo, W.-J. Cui, P. He, and Y.-Y. Xia, "Raising the cycling stability of aqueous lithium-ion batteries by eliminating oxygen in the electrolyte," *Nat Chem*, vol. 2, pp. 760–765, sep 2010.

[127] Z. Li, D. Young, K. Xiang, W. C. Carter, and Y.-M. Chiang, "Towards high power high energy aqueous sodium-ion batteries: The NaTi2(PO4)3/Na0.44MnO2 system," *Advanced Energy Materials*, vol. 3, no. 3, pp. 290–294, 2013.

[128] J. Whitacre, A. Tevar, and S. Sharma, "Na4Mn9O18 as a positive electrode material for an aqueous electrolyte sodium-ion energy storage device," *Electrochemistry Communications*, vol. 12, no. 3, pp. 463 – 466, 2010.

[129] J. Whitacre, T. Wiley, S. Shanbhag, Y. Wenzhuo, A. Mohamed, S. Chun, E. Weber, D. Blackwood, E. Lynch-Bell, J. Gulakowski, C. Smith, and D. Humphreys, "An aqueous electrolyte, sodium ion functional, large format energy storage device for stationary applications," *Journal of Power Sources*, vol. 213, pp. 255 – 264, 2012.

[130] M. Pasta, C. D. Wessells, R. A. Huggins, and Y. Cui, "A high-rate and long cycle life aqueous electrolyte battery for grid-scale energy storage," *Nat Commun*, vol. 3, p. 1149, oct 2012.

[131] C. D. Wessells, R. A. Huggins, and Y. Cui, "Copper hexacyanoferrate battery electrodes with long cycle life and high power," *Nat Commun*, vol. 2, p. 550, nov 2011.

[132] R. M. Darling, K. G. Gallagher, J. A. Kowalski, S. Ha, and F. R. Brushett, "Pathways to low-cost electrochemical energy storage: a comparison of aqueous and nonaqueous flow batteries," *Energy Environ. Sci.*, vol. 7, pp. 3459–3477, 2014.

[133] C. P. De Leon, A. Frias-Ferrer, J. González-García, D. A. Szánto, and F. C. Walsh, "Redox flow cells for energy conversion," *Journal of Power Sources*, vol. 160, no. 1, pp. 716–732, 2006.

[134] G. L. Soloveichik, "Flow batteries: Current status and trends," *Chemical Reviews*, vol. 115, no. 20, pp. 11533–11558, 2015.

[135] A. Z. Weber, M. M. Mench, J. P. Meyers, P. N. Ross, J. T. Gostick, and Q. Liu, "Redox flow batteries: a review," *Journal of Applied Electrochemistry*, vol. 41, no. 10, pp. 1137–1164, 2011.

[136] X. Chen, B. J. Hopkins, A. Helal, F. Y. Fan, K. C. Smith, Z. Li, A. H. Slocum, G. H. McKinley, W. C. Carter, and Y.-M. Chiang, "A low-dissipation, pumpless, gravity-induced flow battery," *Energy Environ. Sci.*, 2016.

[137] R. B. Bird, R. C. Armstrong, and O. Hassager, *Dynamics of Polymeric Liquids. Vol. 1, 2nd Ed. : Fluid Mechanics.* John Wiley and Sons Inc., 1987.

[138] C. W. Macosko, "Rheology: principles, measurements, and applications," *Advances in interfacial engineering series*, 1994.

[139] A. Yoshimura and R. K. Prud'homme, "Wall Slip Corrections for Couette Disk Viscometers and Parallel," *Journal of Rheology*, vol. 32, no. l, pp. 53–67, 1988.

[140] H. A. Barnes and Q. D. Nguyen, "Rotating vane rheometry  a review," *Journal of Non-Newtonian Fluid Mechanics*, vol. 98, no. 1, pp. 1 – 14, 2001.

[141] N. Q. Dzuy and D. V. Boger, "Yield stress measurement for concentrated suspensions," *Journal of Rheology*, vol. 27, no. 4, pp. 321–349, 1983.

[142] G. Ovarlez, S. Cohen-Addad, K. Krishan, J. Goyon, and P. Coussot, "On the existence of a simple yield stress fluid behavior," *Journal of Non-Newtonian Fluid Mechanics*, vol. 193, pp. 68–79, Mar. 2013.

[143] D. C. Cheng, "Yield stress: a time-dependent property and how to measure it," *Rheologica Acta*, vol. 25, no. 5, pp. 542–554, 1986.

[144] J. Mewis and N. J. Wagner, "Thixotropy," *Advances in Colloid and Interface Science*, vol. 147148, pp. 214 – 227, 2009. Colloids, polymers and surfactants.Special Issue in honour of Brian Vincent.

[145] E. C. Bingham, *Fluidity and plasticity*, vol. 2. McGraw-Hill Book Company, Incorporated, 1922.

[146] W. H. Herschel and R. Bulkley, "Model for time dependent behavior of fluids," in *Proc. American Society of Testing Materials*, vol. 26, p. 621, 1926.

[147] M. M. Denn and D. Bonn, "Issues in the flow of yield-stress liquids," *Rheologica Acta*, vol. 50, no. 4, pp. 307–315, 2011.

[148] P. Coussot, Q. Nguyen, H. Huynh, and D. Bonn, "Viscosity bifurcation in thixotropic, yielding fluids," *Journal of Rheology (1978-present)*, vol. 46, no. 3, pp. 573–589, 2002.

[149] H. A. Barnes, "A review of the slip (wall depletion) of polymer solutions, emulsions and particle suspensions in viscometers: its cause, character, and cure," *International Journal of Multiphase Flow*, vol. 22, p. 132, 1996.

[150] R. Buscall, "Letter to the Editor: Wall slip in dispersion rheometry," *Journal of Rheology*, vol. 54, no. 6, pp. 1177–1183, 2010.

[151] D. M. Huang, C. Sendner, D. Horinek, R. R. Netz, and L. Bocquet, "Water slippage versus contact angle: A quasiuniversal relationship," *Physical Review Letters*, vol. 101, pp. 1–4, Nov. 2008.

[152] E. Lauga, M. Brenner, and H. Stone, *Springer Handbook of Experimental Fluid Mechanics*, ch. 19 Microfluidics: The No-Slip Boundary Condition, pp. 1219–1240. Berlin, Heidelberg: Springer Berlin Heidelberg, 2007.

[153] B. K. Aral and D. M. Kalyon, "Effects of temperature and surface roughness on time-dependent development of wall slip in steady torsional flow of concentrated suspensions," *Journal of Rheology*, vol. 38, no. 4, pp. 957–972, 1994.

[154] H. J. Walls, S. B. Caines, A. M. Sanchez, and S. A. Khan, "Yield stress and wall slip phenomena in colloidal silica gels," *Journal of Rheology*, vol. 47, no. 4, pp. 847–868, 2003.

[155] W. B. Russel and M. C. Grant, "Distinguishing between dynamic yielding and wall slip in a weakly flocculated colloidal dispersion," *Colloids and Surfaces A: Physicochemical and Engineering Aspects*, vol. 161, no. 2, pp. 271–282, 2000.

[156] A. D. Stickland, A. Kumar, T. E. Kusuma, P. J. Scales, A. Tindley, S. Biggs, and R. Buscall, "The effect of premature wall yield on creep testing of strongly flocculated suspensions," *Rheologica Acta*, vol. 54, pp. 337–352, 2015.

[157] J. Persello, A. Magnin, J. Chang, J. M. Piau, and B. Cabane, "Flow of colloidal aqueous silica dispersions," *Journal of Rheology*, vol. 38, pp. 1845–1870, 1994.

[158] F. Pignon, A. Magnin, and J.-M. Piau, "Thixotropic colloidal suspensions and flow curves with minimum: Identification of flow regimes and rheometric consequences," *Journal of Rheology*, vol. 40, no. 4, pp. 573–587, 1996.

[159] D. M. Kalyon, P. Yaras, B. Aral, and U. Yilmazer, "Rheological behavior of a concentrated suspension: A solid rocket fuel simulant," *Journal of Rheology*, vol. 37, no. 1, pp. 35–53, 1993.

[160] D. M. Kalyon, "Apparent slip and viscoplasticity of concentrated suspensions," *Journal of Rheology*, vol. 49, p. 621, 2005.

[161] R. Pal, "Slippage during the flow of emulsions in rheometers," *Colloids and Surfaces A: Physicochemical and Engineering Aspects*, vol. 162, no. 1, pp. 55–66, 2000.

[162] J. Plucinski, R. K. Gupta, and S. Chakrabarti, "Wall slip of mayonnaises in viscometers," *Rheologica acta*, vol. 37, no. 3, pp. 256–269, 1998.

[163] N. D. Denkov, V. Subramanian, D. Gurovich, and A. Lips, "Wall slip and viscous dissipation in sheared foams: Effect of surface mobility," *Colloids and Surfaces A: Physicochemical and Engineering Aspects*, vol. 263, no. 1, pp. 129–145, 2005.

[164] J. R. Seth, M. Cloitre, and R. T. Bonnecaze, "Influence of short-range forces on wall-slip in microgel pastes," *Journal of Rheology*, vol. 52, p. 1241, 2008.

[165] V. Bertola, F. Bertrand, H. Tabuteau, D. Bonn, and P. Coussot, "Wall slip and yielding in pasty materials," *Journal of Rheology*, vol. 47, no. 5, pp. 1211–1226, 2003.

[166] J. M. Franco, C. Gallegos, and H. A. Barnes, "On slip effects in steady-state flow measurements of oil-in-water food emulsions," *Journal of Food Engineering*, vol. 36, no. 1, pp. 89–102, 1998.

[167] J. R. Seth, C. Locatelli-Champagne, F. Monti, R. T. Bonnecaze, and M. Cloitre, "How do soft particle glasses yield and flow near solid surfaces?," *Soft Matter*, vol. 8, p. 140, 2012.

[168] C. S. Nickerson and J. A. Kornfield, "A "cleat" geometry for suppressing wall slip," *Journal of Rheology*, vol. 49, no. 4, pp. 865–874, 2005.

[169] D. Bonn, S. Rodts, M. Groenink, S. Rafaï, N. Shahidzadeh-Bonn, and P. Coussot, "Some Applications of Magnetic Resonance Imaging in Fluid Mechanics: Complex Flows and Complex Fluids," *Annual Review of Fluid Mechanics*, vol. 40, pp. 209–233, 2008.

[170] P. Coussot, L. Tocquer, C. Lanos, and G. Ovarlez, "Macroscopic vs. local rheology of yield stress fluids," *Journal of Non-Newtonian Fluid Mechanics*, vol. 158, pp. 85–90, 2009.

[171] J.-B. Salmon, L. Bécu, S. Manneville, and A. Colin, "Towards local rheology of emulsions under Couette flow using dynamic light scattering," *The European Physical Journal E*, vol. 10, no. 3, pp. 209–221, 2003.

[172] T. Gallot, C. Perge, V. Grenard, M.-A. Fardin, N. Taberlet, and S. Manneville, "Ultrafast ultrasonic imaging coupled to rheometry: Principle and illustration," *Review of Scientific Instruments*, vol. 84, p. 45107, 2013.

[173] S. Manneville, L. Bécu, and A. Colin, "High-frequency ultrasonic speckle velocimetry in sheared complex fluids," *Eur. Phys. J. AP*, vol. 28, pp. 361–373, 2004.

[174] G. Degré, P. Joseph, P. Tabeling, S. Lerouge, M. Cloitre, and A. Ajdari, "Rheology of complex fluids by particle image velocimetry in microchannels," *Applied Physics Letters*, vol. 89, no. 2, p. 024104, 2006.

[175] P. Tapadia and S.-Q. Wang, "Direct visualization of continuous simple shear in non-Newtonian polymeric fluids," *Physical Review Letters*, vol. 96, no. 1, p. 016001, 2006.

[176] I. Cohen, B. Davidovitch, A. B. Schofield, M. P. Brenner, and D. A. Weitz, "Slip, yield, and bands in colloidal crystals under oscillatory shear," *Physical Review Letters*, vol. 97, no. 21, p. 215502, 2006.

[177] D. Derks, H. Wisman, A. Van Blaaderen, and A. Imhof, "Confocal microscopy of colloidal dispersions in shear flow using a counter-rotating cone–plate shear cell," *Journal of Physics: Condensed Matter*, vol. 16, no. 38, p. S3917, 2004.

[178] N. Koumakis, M. Laurati, S. U. Egelhaaf, J. F. Brady, and G. Petekidis, "Yielding of Hard-Sphere Glasses during Start-Up Shear," *Physical Review Letters*, vol. 108, no. 9, p. 98303, 2012.

[179] B. Rajaram and A. Mohraz, "Microstructural response of dilute colloidal gels to nonlinear shear deformation," *Soft Matter*, vol. 6, no. 10, p. 2246, 2010.

[180] Y. L. Yeow, Y. K. Leong, and A. Khan, "Non-Newtonian flow in parallel-disk viscometers in the presence of wall slip," *Journal of Non-Newtonian Fluid Mechanics*, vol. 139, pp. 85–92, 2006.

[181] J. G. Cao, J. P. Huang, and L. W. Zhou, "Structure of electrorheological fluids under an electric field and a shear flow: Experiment and computer simulation," *Journal of Physical Chemistry B*, vol. 110, pp. 11635–11639, 2006.

[182] X. Tang, W. H. Li, X. J. Wang, and P. Q. Zhang, "Structure Evolution of Electrorheological Fluids under Flow Conditions," *International Journal of Modern Physics B*, vol. 13, pp. 1806–1813, June 1999.

[183] Y. Pappas and D. J. Klingenberg, "Simulations of magnetorheological suspensions in Poiseuille flow," *Rheologica Acta*, vol. 45, pp. 621–629, 2006.

[184] Y. Tian, X. Zhu, J. Jiang, Y. Meng, and S. Wen, "Structure factor of electrorheological fluids in compressive flow," *Smart Materials and Structures*, vol. 19, p. 105024, 2010.

[185] M. Gurka, R. Petricevic, S. Schneider, and S. Ulrich, "Characterization of Step Response Time and Bandwidth of Electrorheological Fluids," *Journal of Intelligent Material Systems and Structures*, vol. 22, pp. 1745–1748, 2011.

[186] Y. J. Jang, M. S. Suh, M. S. Yeo, and S. B. Choi, "The Numerical Analysis of Channel Flows of ER Fluids," *Journal of Intelligent Material Systems and Structures*, vol. 7, pp. 604–609, Sep. 1996.

[187] H. G. Lee and S. B. Choi, "Dynamic properties of an ER fluid under shear and flow modes," *Materials & Design*, vol. 23, pp. 69–76, 2002.

[188] M. Nakano, R. Aizawa, and Y. Asako, "Steady and transient responses of electrheological suspensions passing through a rectangular channel," *International Journal of Modern Physics B*, vol. 10, pp. 2965–2972, Oct. 1996.

[189] Y. J. Nam, M. K. Park, and R. Yamane, "Dynamic responses of electrorheological fluid in steady pressure flow," *Experiments in Fluids*, vol. 44, pp. 915–926, 2008.

[190] B. Qian, G. H. McKinley, and A. E. Hosoi, "Structure evolution in electrorheological fluids flowing through microchannels," *Soft Matter*, vol. 9, no. 10, pp. 2889–2898, 2013.

[191] "RheOil4.0 datasheet," *ERF Production Würzburg GmbH Product Information on RheOil 4.0, http://www.erfgmbh.de*, 2008.

[192] Y. Reichert and H. Böse, "Novel electrorheological fluids with polymer particles containing organic dopants," in *Electro-Rheological Fluids and Magneto-Rheological Suspensions*, pp. 338–347, WORLD SCIENTIFIC, may 2011.

[193] S. Schneider and S. Eibl, "Review of the ER effect of polyurethane-based ER fluids," *Applied Rheology*, vol. 18, no. 2, pp. 23956 (1–8), 2008.

[194] M. Gurka, L. Johnston, and R. Petricevic, "New Electrorheological Fluids – Characteristics and Implementation in Industrial and Mobile Applications," *Journal of Intelligent Material Systems and Structures*, vol. 21, pp. 1531–1535, 2010.

[195] G. Ovarlez, L. Tocquer, F. Bertrand, and P. Coussot, "Rheopexy and tunable yield stress of carbon black suspensions," *Soft Matter*, vol. 9, no. 23, p. 5540, 2013.

[196] C. J. Gow and C. F. Zukoski IV, "The electrorheological properties of polyaniline suspensions," *Journal of Colloid and Interface Science*, vol. 136, pp. 175–188, Apr. 1990.

[197] L. Marshall, C. F. Zukoski, and J. W. Goodwin, "Effects of electric fields on the rheology of non-aqueous concentrated suspensions," *Journal of the Chemical Society, Faraday Transactions 1*, vol. 85, no. 9, pp. 2785–2795, 1989.

[198] X. D. Pan and G. H. McKinley, "Simultaneous measurement of viscoelasticity and electrical conductivity of an electrorheological fluid," *Langmuir*, vol. 14, no. 11, pp. 985–989, 1998.

[199] K. P. S. Parmar, Y. Méheust, B. Schjelderupsen, and J. O. Fossum, "Electrorheological suspensions of laponite in oil: Rheometry studies," *Langmuir*, vol. 24, no. 20, pp. 1814–1822, 2008.

[200] X. Chateau, G. Ovarlez, and K. L. Trung, "Homogenization approach to the behavior of suspensions of noncolloidal particles in yield stress fluids," *Journal of Rheology*, vol. 52, no. May 2013, pp. 489–506, 2008.

[201] I. M. Krieger and T. J. Dougherty, "A Mechanism for Non-Newtonian Flow in Suspensions of Rigid Spheres," *Transactions of The Society of Rheology (1957-1977)*, vol. 3, no. 1, pp. 137–152, 1959.

[202] S. Mueller, E. W. Llewellin, and H. M. Mader, "The rheology of suspensions of solid particles," *Proceedings of the Royal Society of London A: Mathematical, Physical and Engineering Sciences*, vol. 466, pp. 1201–1228, Feb. 2010.

[203] L. Heymann, S. Peukert, and N. Aksel, "On the solid-liquid transition of concentrated suspensions in transient shear flow," *Rheologica Acta*, vol. 41, no. 4, pp. 307–315, 2002.

[204] Johnsen, C. Chevalier, A. Lindner, R. Toussaint, E. Clément, K. J. Måløy, E. G. Flekkøy, and J. Schmittbuhl, "Decompaction and fluidization of a saturated and confined granular medium by injection of a viscous liquid or gas," *Physical Review E*, vol. 78, no. 5, pp. 1–12, 2008.

[205] B. Abu-Jdayil, "Response time of an ER-fluid under shear and flow modes," *Journal of Physics: Conference Series*, vol. 412, pp. 012009 (1–8), 2013.

[206] J. C. Hill and T. H. V. Steenkiste, "Response times of electrorheological fluids," *Journal of Applied Physics*, vol. 70, pp. 1207–1211, 1991.

[207] S. Ergun, "Fluid through packed columns," *Chemical Engineering Progress*, vol. 48, no. 2, pp. 89–94, 1952.

[208] A. Tamayol and M. Bahrami, "Transverse permeability of fibrous porous media," *Physical Review E*, vol. 83, no. 4, pp. 1–9, 2011.

[209] P. C. Carman, "Fluid flow through granular beds," *Transactions, Institution of Chemical Engineers, London*, vol. 15, pp. 150–166, 1937.

[210] J. Kozeny, "Ueber kapillare Leitung des Wassers im Boden," *Sitzungsber Akad. Wiss., Wien*, vol. 136, pp. 271–306, 1927.

[211] T. D. Truong, S. E. Semercigil, and Ö. F. Turan, "Towards a Valveless Electro-Rheological Valve," in *15th Australian Fluid Mechanics Conference*, 2004.

[212] A. Simmonds, "Electro-rheological valves in a hydraulic circuit," *IEE Proceedings D Control Theory and Applications*, vol. 138, no. 4, p. 400, 1991.

[213] H. Sahin, X. Wang, and F. Gordaninejad, "Magneto-rheological fluid flow through complex valve geometries," *International Journal of Vehicle Design*, vol. 63, pp. 241–255, 2013.

[214] K. Yoshida, T. Ide, K. Joon-wan, and S. Yokota, "A microgripper using electro-rheological fluid," *2009 Iccas-Sice*, vol. 1, pp. 2987–2990, 2009.

[215] N. Masami, M. Shuji, and H. Katsuya, "PWM flow rate control of ER valve & its application to ER actuator control," *International Journal of Modern Physics B*, vol. 13, pp. 2168–2175, 1999.

[216] Q. H. Nguyen, S. B. Choi, Y. S. Lee, and M. S. Han, "An analytical method for optimal design of MR valve structures," *Smart Materials and Structures*, vol. 18, p. 095032, 2009.

[217] M. Whittle, R. Firoozian, D. J. Peel, and W. A. Bullough, "Electrorheological relaxation times derived from pressure response experiments in the flow mode," *Journal of Non-Newtonian Fluid Mechanics*, vol. 57, pp. 1–25, apr 1995.

[218] S. B. Choi, T. H. Lee, Y. S. Lee, and M. S. Han, "Control performance of an electrorheological valve based vehicle anti-lock brake system, considering the braking force distribution," *Smart Materials and Structures*, vol. 14, no. 6, p. 1483, 2005.

[219] G. Georgiades and S. Oyadiji, "Voltage control characteristics of electrorheological fluid valves," *International Journal of Vehicle Design*, vol. 33, p. 218, 2003.

[220] G. Georgiades and S. O. Oyadiji, "Effects of Electrode Geometry on the Performance of Electrorheological Fluid Valves," *Journal of Intelligent Material Systems and Structures*, vol. 14, pp. 105–111, feb 2003.

[221] T.-S. Wei, F. Y. Fan, A. Helal, K. C. Smith, G. H. McKinley, Y.-M. Chiang, and J. A. Lewis, "Biphasic Electrode Suspensions for Li-Ion Semi-solid Flow Cells with High Energy Density, Fast Charge Transport, and Low-Dissipation Flow," *Advanced Energy Materials*, vol. 5, 2015.

[222] K. C. Smith, Y.-M. Chiang, and W. Craig Carter, "Maximizing Energetic Efficiency in Flow Batteries Utilizing Non-Newtonian Fluids," *Journal of the Electrochemical Society*, vol. 161, no. 4, pp. 486–496, 2014.

[223] G. Ovarlez, S. Rodts, X. Chateau, and P. Coussot, "Phenomenology and physical origin of shear localization and shear banding in complex fluids," *Rheologica Acta*, vol. 48, pp. 831–844, 2009.

[224] M. P. Godfrin, A. Tiwari, A. Bose, and A. Tripathi, "Phase and steady shear behavior of dilute carbon black suspensions and carbon black stabilized emulsions," *Langmuir*, vol. 30, no. 51, pp. 15400–15407, 2014.

[225] M. F. Ashby, *Materials Selection in Mechanical Design, 4th Edition*. Elsevier, 2010.

[226] A. Mohraz, E. R. Weeks, and J. A. Lewis, "Structure and dynamics of biphasic colloidal mixtures," *Phys. Rev. E*, vol. 77, p. 060403, June 2008.

[227] S. K. Rhodes, R. H. Lambeth, J. Gonzales, J. S. Moore, and J. A. Lewis*, "Cationic comb polymer superdispersants for colloidal silica suspensions," *Langmuir*, vol. 25, no. 12, pp. 6787–6792, 2009.

[228] J. N. Israelachvili, "Chapter 6 - van der waals forces," in *Intermolecular and Surface Forces (Third Edition)* (J. N. Israelachvili, ed.), pp. 107 – 132, San Diego: Academic Press, 2011.

[229] L. Zhang, Y. Jiang, Y. Ding, M. Povey, and D. York, "Investigation into the antibacterial behaviour of suspensions of ZnO nanoparticles (ZnO nanofluids)," *Journal of Nanoparticle Research*, vol. 9, no. 3, pp. 479–489, 2007.

[230] Y. Zhao, S. Wang, C. Zhao, and D. Xia, "Synthesis and electrochemical performance of licopo4 micron-rods by dispersant-aided hydrothermal method for lithium ion batteries," *Rare Metals*, vol. 28, no. 2, pp. 117–121, 2009.

[231] H. Wang, X. Qiao, J. Chen, X. Wang, and S. Ding, "Mechanisms of PVP in the preparation of silver nanoparticles," *Materials Chemistry and Physics*, vol. 94, no. 2-3, pp. 449 – 453, 2005.

[232] J. Zhang, D. Jiang, and Q. Lin, "Poly(vinyl pyrrolidone), a dispersant for non-aqueous processing of silicon carbide," *Journal of the American Ceramic Society*, vol. 88, no. 4, pp. 1054–1056, 2005.

[233] G. H. McKinley, "A Hitchhikers Guide to complex fluids," *Rheology Bulletin*, vol. 84, pp. 14–17, 2015.

[234] P. J. Lu and D. A. Weitz, "Colloidal Particles: Crystals, Glasses, and Gels," *Annu. Rev. Condens. Matter Phys.*, vol. 4, pp. 217–233, 2013.

[235] T. Divoux, M.-A. Fardin, S. Manneville, and S. Lerouge, "Shear Banding of Complex Fluids," *Annual Review of Fluid Mechanics*, vol. 48, pp. 81–103, 2016.

[236] M.-A. Fardin, T. J. Ober, V. Grenard, T. Divoux, S. Manneville, G. H. McKinley, and S. Lerouge, "Interplay between elastic instabilities and shear-banding: three categories of Taylor-Couette flows and beyond," *Soft Matter*, vol. 8, no. 39, pp. 10072–10089, 2012.

[237] M.-A. Fardin and S. Lerouge, "Instabilities in wormlike micelle systems," *European Physical Journal E: Soft Matter*, vol. 35, no. 9, pp. 1–29, 2012.

[238] J. V. DeGroot, C. W. Macosko, T. Kume, and T. Hashimoto, "Flow-Induced Anisotropic SALS in Silica-Filled PDMS Liquids," *Journal of Colloid and Interface Science*, vol. 166, pp. 404–413, 1994.

[239] V. Grenard, N. Taberlet, and S. Manneville, "Shear-induced structuration of confined carbon black gels: Steady-state features of vorticity-aligned flocs," *Soft Matter*, vol. 7, p. 10, 2010.

[240] A. Montesi, A. A. Peña, and M. Pasquali, "Vorticity alignment and negative normal stresses in sheared attractive emulsions," *Physical Review Letters*, vol. 92, p. 58303, 2004.

[241] S. Pujari, S. Rahatekar, J. W. Gilman, K. K. Koziol, A. H. Windle, and W. R. Burghardt, "Shear-induced anisotropy of concentrated multiwalled carbon nanotube suspensions using x-ray scattering," *Journal of Rheology*, vol. 55, no. 5, p. 1033, 2011.

[242] A. P. R. Eberle and L. Porcar, "Flow-SANS and Rheo-SANS applied to soft matter," *Current Opinion in Colloid and Interface Science*, vol. 17, no. 1, pp. 33–43, 2012.

[243] P. T. Callaghan, "Rheo NMR and shear banding," *Rheologica Acta*, vol. 47, pp. 243–255, 2008.

[244] S. Manneville, "Recent experimental probes of shear banding," *Rheologica Acta*, vol. 47, pp. 301–318, 2008.

[245] I. Alig, P. Pötschke, D. Lellinger, T. Skipa, S. Pegel, G. R. Kasaliwal, and T. Villmow, "Establishment, morphology and properties of carbon nanotube networks in polymer melts," *Polymer*, vol. 53, no. 1, pp. 4–28, 2012.

[246] W. Bauhofer, S. C. Schulz, A. E. Eken, T. Skipa, D. Lellinger, I. Alig, E. J. Tozzi, and D. J. Klingenberg, "Shear-controlled electrical conductivity of carbon nanotubes networks suspended in low and high molecular weight liquids," *Polymer*, vol. 51, no. 22, pp. 5024–5027, 2010.

[247] S. Capaccioli, D. Prevosto, A. Best, A. Hanewald, and T. Pakula, "Applications of the rheo-dielectric technique," *Journal of Non-Crystalline Solids*, vol. 353, pp. 4267–4272, 2007.

[248] J. Crawshaw and G. Meeten, "Shear-induced changes of electrical conductivity in suspensions," *Rheologica Acta*, vol. 46, no. 2, pp. 183–193, 2006.

[249] U. Genz, J. A. Helsen, and J. Mewis, "Dielectric spectroscopy of Reversibly floculated dispersions during flow," *Journal of Colloids & Interface Science*, vol. 165, pp. 212–220, 1994.

[250] J. Mewis, L. M. de Groot, and J. A. Helsen, "Dielectric Behaviour of Flowing Thixotropic Suspensions.," *Colloids and Surfaces*, vol. 22, pp. 271–289, 1987.

[251] N. Lou, Y. Wang, X. Li, H. Li, P. Wang, C. Wesdemiotis, A. P. Sokolov, and H. Xiong, "Dielectric relaxation and rheological behavior of supramolecular polymeric liquid," *Macromolecules*, vol. 46, no. 8, pp. 3160–3166, 2013.

[252] H. Watanabe, T. Sato, K. Osaki, M.-L. M.-L. Yao, and A. Yamagishi, "Rheological and Dielectric Behavior of a Styrene-Isoprene-Styrene Triblock Copolymer in Selective Solvents. 2. Contribution of Loop-Type Middle Blocks to Elasticity and Plasticity," *Macromolecules*, vol. 30, no. 19, pp. 5877–5892, 1997.

[253] H. Watanabe, T. Sato, Y. Matsumiya, T. Inoue, and K. Osaki, "Rheodielectrics: Its applicability," *Nihon Reoroji Gakkaishi*, vol. 27, no. 2, pp. 121–125, 1999.

[254] I. Alig, T. Skipa, M. Engel, D. Lellinger, S. Pegel, and P. Pötschke, "Electrical conductivity recovery in carbon nanotube-polymer composites after transient shear," *Physica Status Solidi (B) Basic Research*, vol. 244, no. 11, pp. 4223–4226, 2007.

[255] I. Alig, T. Skipa, D. Lellinger, and P. Pötschke, "Destruction and formation of a carbon nanotube network in polymer melts: Rheology and conductivity spectroscopy," *Polymer*, vol. 49, pp. 3524–3532, 2008.

[256] B. H. Cipriano, A. K. Kota, A. L. Gershon, C. J. Laskowski, T. Kashiwagi, H. a. Bruck, and S. R. Raghavan, "Conductivity enhancement of carbon nanotube and nanofiber-based polymer nanocomposites by melt annealing," *Polymer*, vol. 49, no. 22, pp. 4846–4851, 2008.

[257] S. B. Kharchenko, J. F. Douglas, J. Obrzut, E. A. Grulke, and K. B. Migler, "Flow-induced properties of nanotube-filled polymer materials," *Nature Materials*, vol. 3, no. 8, pp. 564–568, 2004.

[258] S. C. Schulz and W. Bauhofer, "Shear influenced network dynamics and electrical conductivity recovery in carbon nanotube/epoxy suspensions," *Polymer*, vol. 51, no. 23, pp. 5500–5505, 2010.

[259] L. Madec, M. Youssry, M. Cerbelaud, P. Soudan, D. Guyomard, and B. Lestriez, "Non-aqueous carbon black suspensions for lithium-based redox flow batteries: rheology and simultaneous rheo-electrical behavior.," *Physical chemistry chemical physics : PCCP*, vol. 15, pp. 14476–86, 2013.

[260] L. Madec, M. Youssry, M. Cerbelaud, P. Soudan, D. Guyomard, and B. Lestriez, "Electronic vs Ionic Limitations to Electrochemical Performance in Li4Ti5O12-Based Organic Suspensions for Lithium-Redox Flow Batteries," *Journal of the Electrochemical Society*, vol. 161, no. 5, pp. 693–699, 2014.

[261] H. Watanabe, Y. Matsumiya, M. Kakiuchi, and Y. Aoki, "Rheo-dielectric Behavior of Carbon Black Suspensions.," *Nihon Reoroji Gakkaishi*, vol. 29, no. 2, pp. 77–80, 2001.

[262] M. Youssry, L. Madec, P. Soudan, M. Cerbelaud, D. Guyomard, and B. Lestriez, "Formulation of flowable anolyte for redox flow batteries: Rheo-electrical study," *Journal of Power Sources*, vol. 274, pp. 424–431, Jan. 2015.

[263] L. Madec, M. Youssry, M. Cerbelaud, P. Soudan, D. Guyomard, and B. Lestriez, "Surfactant for Enhanced Rheological, Electrical, and Electrochemical Performance of Suspensions for Semisolid Redox Flow Batteries and Supercapacitors," *ChemPlusChem*, vol. 80, 2014.

[264] T. Gibaud, D. Frelat, and S. Manneville, "Heterogeneous yielding dynamics in a colloidal gel," *Soft Matter*, vol. 6, pp. 3482–3488, 2010.

[265] V. Grenard, T. Divoux, N. Taberlet, and S. Manneville, "Timescales in creep and yielding of attractive gels," *Soft Matter*, vol. 10, p. 1555, 2014.

[266] Z. Liu, Y. Song, J. Zhou, and Q. Zheng, "Simultaneous measurement of rheological and conductive properties of carbon black filled ethylene-tetrafluorothylene copolymer," *Journal of Materials Science*, vol. 42, no. 20, pp. 8757–8759, 2007.

[267] R. B. Bird and A. J. Giacomin, "Who conceived the "complex viscosity"?," *Rheologica Acta*, vol. 51, pp. 481–486, 2012.

[268] A. Gemant, "The conception of a complex viscosity and its application to dielectrics," *Transactions of the Faraday Society*, vol. 31, pp. 1582–1590, 1935.

[269] A. Bard and L. Faulkner, *Electrochemical methods: Fundamentals and Applications*. John Wiley and Sons Inc., 2001.

[270] M. D. Dickey, R. C. Chiechi, R. J. Larsen, E. A. Weiss, D. A. Weitz, and G. M. Whitesides, "Eutectic gallium-indium (EGaIn): A liquid metal alloy for the formation of stable structures in microchannels at room temperature," *Advanced Functional Materials*, vol. 18, no. 7, pp. 1097–1104, 2008.

[271] M. T. Shaw and Z. Z. Liu, "Single-point determination of nonlinear rheological data from parallel-plate torsional flow," *Applied Rheology*, vol. 16, no. 2, pp. 70–79, 2006.

[272] M. Abramowitz and I. A. Stegun, *Handbook of Mathematical Functions*. New York: Dover Publications, 1972.

[273] C. Clasen, "Determining the true slip of a yield stress material with a sliding plate rheometer," *Rheologica Acta*, vol. 51, pp. 883–890, 2012.

[274] S. Zahirovic, A. S. Lubansky, Y. Leong Yeow, and D. V. Boger, "Obtaining the steady shear rheological properties and apparent wall slip velocity data of a water-in-oil emulsion from gap-dependent parallel plate viscometry data," *Rheologica Acta*, vol. 48, pp. 221–229, 2009.

[275] C. J. Dimitriou, R. H. Ewoldt, and G. H. McKinley, "Describing and prescribing the constitutive response of yield stress fluids using large amplitude oscillatory shear stress (LAOStress)," *Journal of Rheology*, vol. 57, no. 1, p. 27, 2013.

[276] J. J. Stickel, J. S. Knutsen, and M. W. Liberatore, "Response of elastoviscoplastic materials to large amplitude oscillatory shear flow in the parallel-plate and cylindrical-Couette geometries," *Journal of Rheology*, vol. 57, no. 6, pp. 1569–1596, 2013.

[277] N. A. Bharadwaj and R. H. Ewoldt, "Single-point parallel disk correction for asymptotically nonlinear oscillatory shear," *Rheologica Acta*, vol. 54, no. 3, pp. 223–233, 2015.

[278] J. Sprakel, S. B. Lindström, T. E. Kodger, and D. A. Weitz, "Stress Enhancement in the Delayed Yielding of Colloidal Gels," *Physical Review Letters*, vol. 106, p. 248303, 2011.

[279] N. Koumakis, E. Moghimi, R. Besseling, W. C. K. Poon, J. F. Brady, and G. Petekidis, "Tuning colloidal gels by shear," *Soft Matter*, vol. 11, pp. 4640–4648, 2015.

[280] M. Cross and A. Kaye, "Simple procedures for obtaining viscosity/shear rate data from a parallel disc viscometer," *Polymer*, vol. 28, pp. 435–440, 1987.

[281] J. P. Clerc, G. Giraud, J. M. Laugier, and J. M. Luck, "The electrical conductivity of binary disordered systems, percolation clusters, fractals and related models," *Advances in Physics*, vol. 39, no. 3, pp. 191–309, 1990.

[282] S. Kirkpatrick, "Percolation and Conduction," *Reviews of Modern Physics*, vol. 45, no. 4, pp. 574–588, 1973.

[283] J. P. Straley, "Critical exponents for the conductivity of random resistor lattices," *Physical Review B*, vol. 15, no. 12, pp. 5733–5737, 1977.

[284] I. Balberg, "Tunneling and Nonuniversal Conductivity in composite materials," *Physical Review Letters*, vol. 59, no. 12, pp. 1305–1308, 1987.

[285] I. Balberg, "A comprehensive picture of the electrical phenomena in carbon black-polymer composites," *Carbon*, vol. 40, no. 2, pp. 139–143, 2002.

[286] Z. Rubin, S. A. Sunshine, M. B. Heaney, I. Bloom, and I. Balberg, "Critical behavior of the electrical transport properties in a tunneling-percolation system," *Physical Review B*, vol. 59, no. 19, pp. 12196–12199, 1999.

[287] T. Divoux, C. Barentin, and S. Manneville, "From transient fluidization processes to Herschel-Bulkley behavior in simple yield stress fluids," *Soft Matter*, vol. 7, pp. 8409–8418, 2011.

[288] T. Bauer, J. Oberdisse, and L. Ramos, "Collective rearrangement at the onset of flow of a polycrystalline hexagonal columnar phase," *Physical Review Letters*, vol. 97, p. 258303, 2006.

[289] M. Siebenbürger, M. Ballauf, and T. Voigtmann, "Creep in colloidal glasses," *Physical Review Letters*, vol. 108, p. 255701, 2012.

[290] T. Brenner, S. Matsukawa, K. Nishinari, and R. Johannsson, "Failure in a soft gel: Delayed failure and the dynamic yield stress," *Journal of Non-Newtonian Fluid Mechanics*, vol. 196, pp. 1–7, 2013.

[291] M. Leocmach, C. Perge, T. Divoux, and S. Manneville, "Creep and Fracture of a Protein Gel under Stress," *Physical Review Letters*, vol. 113, p. 38303, 2014.

[292] J. Colombo and E. Del Gado, "Stress localization, stiffening, and yielding in a model colloidal gel," *Journal of Rheology*, vol. 58, pp. 1089–1116, 2014.

[293] A. Kyrlidis, R. M. Sawka, G. D. Moeser, P. A. Kossyrev, and N. J. Hardman, "High surface area and low structure carbon blacks for energy storage applications," 2014.

[294] Cabot, *Sales specification: Vulcan XC72R*, 2008.

[295] Cabot, *Sales specification: Elftex 8*, 2008.

[296] Cabot, *Sales specification: Monarch 120*, 2003.

[297] P.-G. De Gennes, "On a relation between percolation theory and the elasticity of gels," *Journal de Physique Lettres*, vol. 37, no. 1, pp. 1–2, 1976.

[298] S. Feng, P. N. Sen, B. I. Halperin, and C. J. Lobb, "Percolation on two-dimensional elastic networks with rotationally invariant bond-bending forces," *Phys. Rev. B*, vol. 30, pp. 5386–5389, Nov 1984.

[299] Y. Kantor and I. Webman, "Elastic properties of random percolating systems," *Phys. Rev. Lett.*, vol. 52, pp. 1891–1894, May 1984.

[300] M. Michels, J. Brokken-Zijp, W. Groenewoud, and A. Knoester, "Systematic study of percolative network formation and effective electric response in low-concentration carbon black/polymer composites," *Physica A: Statistical Mechanics and its Applications*, vol. 157, no. 1, pp. 529–534, 1989.

[301] D. Stauffer, A. Coniglio, and M. Adam, "Gelation and Critical Phenomena," *Advances in Polymer Science*, vol. 44, pp. 104–158, 1982.

[302] B. Nigro, C. Grimaldi, P. Ryser, F. Varrato, G. Foffi, and P. J. Lu, "Enhanced tunneling conductivity induced by gelation of attractive colloids," *Phys. Rev. E*, vol. 87, p. 062312, Jun 2013.

[303] C. Perge, N. Taberlet, T. Gibaud, and S. Manneville, "Time dependence in large amplitude oscillatory shear: a rheo-ultrasonic study of fatigue dynamics in a colloidal gel," *Eprint*, vol. 1331, p. 21, 2014.

[304] T. Gibaud, C. Perge, S. B. Lindström, N. Taberlet, and S. Manneville, "Multiple yielding processes in a colloidal gel under large amplitude oscillatory stress," *Soft Matter*, pp. 1701–1712, 2016.

[305] J. Läuger and H. Stettin, "Differences between stress and strain control in the non-linear behavior of complex fluids," *Rheologica acta*, vol. 49, no. 9, pp. 909–930, 2010.

[306] K. Atalik and R. Keunings, "On the occurrence of even harmonics in the shear stress response of viscoelastic fluids in large amplitude oscillatory shear," *Journal of Non-Newtonian Fluid Mechanics*, vol. 122, no. 13, pp. 107 – 116, 2004. {XIIIth} International Workshop on Numerical Methods for Non-Newtonian Flows.

[307] M. D. Graham, "Wall slip and the nonlinear dynamics of large amplitude oscillatory shear flows," *Journal of Rheology*, vol. 39, no. 4, pp. 697–712, 1995.

[308] R. H. Ewoldt, "Defining nonlinear rheological material functions for oscillatory shear," *Journal of Rheology (1978-present)*, vol. 57, no. 1, pp. 177–195, 2013.

[309] R. H. Ewoldt and G. H. McKinley, "On secondary loops in LAOS via self-intersection of Lissajous–Bowditch curves," *Rheologica Acta*, vol. 49, no. 2, pp. 213–219, 2010.

[310] S. A. Rogers, B. M. Erwin, D. Vlassopoulos, and M. Cloitre, "A sequence of physical processes determined and quantified in LAOS: Application to a yield stress fluid," *Journal of Rheology*, vol. 55, no. 2, pp. 435–458, 2011.

[311] O. Basquin, "The exponential law of endurance tests," in *Proc. Astm*, vol. 10, pp. 625–630, 1910.

[312] W. Wang, Q. Luo, B. Li, X. Wei, L. Li, and Z. Yang, "Recent progress in redox flow battery research and development," *Advanced Functional Materials*, vol. 23, no. 8, pp. 970–986, 2013.

[313] L. L. Ferrás, J. M. Nóbrega, and F. T. Pinho, "Analytical solutions for Newtonian and inelastic non-Newtonian flows with wall slip," *Journal of Non-Newtonian Fluid Mechanics*, vol. 175-176, pp. 76–88, 2012.

[314] B. R. Solomon, K. S. Khalil, and K. K. Varanasi, "Drag reduction using lubricant-impregnated surfaces in viscous laminar flow," *Langmuir*, vol. 30, no. 36, pp. 10970–10976, 2014.